

DISSERTATION

Control of Unbalance and Self-Exciting Forces by Active Magnetic Bearings

ausgeführt zum Zwecke der Erlangung des akademischen Grades
eines Doktors der technischen Wissenschaften
unter der Leitung von

o. Univ. Prof. Dr. Helmut Springer
Institut für Maschinendynamik und Meßtechnik, E303

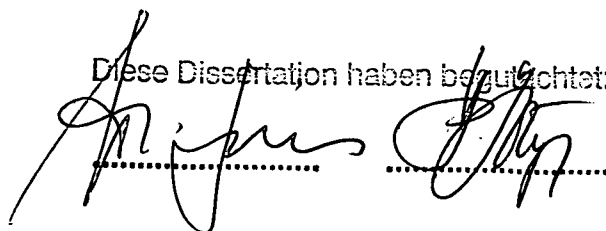
eingereicht an der Technischen Universität Wien
Fakultät für Maschinenbau

von

Dipl.-Ing. Martin Hirschmanner
A-1030 Wien, Keilgasse 8/16

Wien, im September 2003

Diese Dissertation haben begutachtet:


.....

To Birgit,
who took me to Vienna
and back again

...

1. SEITE VON
PROF. SPRINGER ✓
U

dann dasulgen:

Deutsche Kurzfassung

Das Ziel dieser Dissertation ist es, einen adaptiven Regler zur Unterdrückung zirkulatorischer Kreuzkopplungskräfte, der am Institut für Maschinendynamik und Messtechnik entwickelt wurde, mit einem Unwuchtkompensationsalgorithmus, der in der Literatur beschrieben wird, zu kombinieren.

In dieser Dissertation wird das Verhalten eines starren Rotors beschrieben, der in zwei aktiven Magnetlagern gelagert ist sowie von zwei Arten von Kräften zu Schwingungen angeregt und durch drei Algorithmen geregelt wird. Die betrachteten Anregungen sind, die Unwuchtanregung, die eine drehzahlsynchrone, harmonische Anregung darstellt, und eine nichtkonservative zirkulatorische Kreuzkopplungsanregung, die einen destabilisierenden Prozess repräsentiert. Die drei Regelalgorithmen sind ein zeitdiskreter PID-Regler, ein adaptiver Kreuzkopplungskompensationsalgorithmus (adaptive cross-coupling control, ACCC) und ein Unwuchtkompensationsalgorithmus, der in diskreter (discrete harmonic control, DHC) und kontinuierlichen Form (continuous harmonic control, CHC) vorliegt.

Diese Dissertation besteht aus zwei Teilen. Im ersten Teil werden der Rotor und die aktiven Magnetlager modelliert, während im zweiten Teil die Regelalgorithmen hergeleitet und ihr Verhalten, insbesondere ihre Interaktion untereinander, mittels numerischen Simulationen studiert wird. Alle drei Algorithmen werden als zeitdiskrete Prozesse analysiert und implementiert. Die zeitkontinuierlichen Gegenstücke sind ebenfalls beschrieben um ein leichteres Verstehen der Wirkungsweisen zu ermöglichen.

Die Ergebnisse in zusammengefasster Form sind: der PID-Regler ist für einen stabilen Betrieb des Rotors in Magnetlagern notwendig. Der ACCC-Algorithmus stabilisiert den Rotor wenn dieser durch starke Kreuzkopplungskräfte destabilisiert wird. Wenn der Rotor gleichzeitig durch Unwuchtschwingungen angeregt wird, bewirkt dieser jedoch starke Rotorschwingungen. Die Unwuchtkompensationsregelung reduziert deutlich die Auswirkungen der Unwuchtanregung, unabhängig davon, ob der ACCC-Algorithmus eingesetzt

wird oder nicht. Mit der Reduktion der Unwuchtauswirkungen verschwinden auch die starken Rotorvibrationen, die durch den ACCC-Algorithmus hervorgerufen werden. Für einen durch Kreuzkopplungskräfte destabilisierten Rotor ist der ACCC-Algorithmus für den Betrieb notwendig, während eine zusätzliche Unwuchtkompensationregelung die negativen Auswirkungen des ACCC-Algorithmus beseitigt und darüber hinaus die Unwuchtschwingungen reduziert.

Abstract

The goal of this thesis is to combine an adaptive cross-coupling control scheme, developed at the Institute for Machine Dynamics and Measurement, with an unbalance control scheme, described in the literature, and study the interaction between these two algorithms.

In this doctoral dissertation, the behavior of a rigid rotor is described which is supported by active magnetic bearings (AMBs) and is excited by two sources of vibration and controlled by three control algorithms. The sources of vibration are the mass unbalance excitation which is a harmonic excitation synchronous to the rotational speed and a nonconservative cross-coupling excitation representing a destabilizing process. The three control algorithms are, a discrete-time PID (proportional integral differential) control, an adaptive cross-coupling control (ACCC) algorithm, and an unbalance control algorithm either discrete harmonic control (DHC) or continuous harmonic control (CHC).

This thesis consists of two parts. In the first part, rotor and active magnetic bearings are modelled while in the second part the control algorithms are developed and their behavior is studied by numerical simulations as they operate independently or interact with each other. All three algorithms are analyzed and implemented as discrete-time control algorithms; the continuous-time counterparts are also included in the thesis for easier understanding of the operational principles.

Summarizing the result, the PID controller is necessary for a stable operation of the AMB-supported rotor. The ACCC control stabilizes the rotor when it is destabilized by a nonconservative cross-coupling force, but causes a high rotor vibration level when unbalance excitation acts on the rotor at the same time. The unbalance control can substantially reduce the effects of unbalance excitation regardless of adaptive cross-coupling control. With the reduction of the unbalance effects, the high vibration level from the ACCC algorithm disappears. So, for an unstable cross-coupling excited rotor, the ACCC is necessary

for operation, while the additional unbalance control diminishes the negative effects of the ACCC algorithm without influencing the positive effects of the ACCC and furthermore, it can reduce unbalance vibrations.

Contents

Deutsche Kurzfassung	iii
Abstract	v
Preface	xi
Nomenclature	xiii
General Conventions	xiii
Indexing Rules	xiii
Notation	xiv
Symbols	xvi
1. Introduction	1
2. Numerical Simulation Model	4
2.1. The Rotor	4
2.2. The Magnetic Bearing	6
I. Modelling	9
3. AMB Modelling	10
3.1. Introduction	10
3.2. The Nonlinear Simple AMB Model	14
3.3. The Linearized Simple AMB Model	17
3.3.1. The Linear Magnetic Bearing with an Input Voltage . . .	17
3.3.2. Underlying Current Controller	19
3.3.3. Pulse-Width-Modulation Controlled Switching Amplifier	22
3.3.4. Design of the Underlying Current Controller	26

4. The Linearized Rigid Rotor Model	30
4.1. Introduction	30
4.2. Equations of Motion in Center Coordinates	31
4.3. Transformations of Displacements and Forces	33
4.4. Nonconservative Cross-Coupling Forces	35
4.5. Preloading the Magnetic Bearings	37
4.6. Rotor Magnetic Bearing Assembly	39
4.6.1. Eigenvalues of the Simple Model	41
4.6.2. Eigenvalues of the Complex Model	42
4.7. 2DoF Model	43
 II. Control	 44
5. Stabilizing Feedback Loop Control	45
5.1. Introduction	45
5.2. Feedback Loop	46
5.3. Continuous-Time PID Control	49
5.4. Discrete-Time PID Control	51
5.5. 2DoF Model	55
 6. Adaptive Cross-Coupling Control	 58
6.1. Introduction	58
6.2. Influence of the Cross-Coupling on the System	61
6.3. On-line Parameter Estimation	65
6.4. Reference Force Concept	67
6.4.1. Compensation Current and Reference Position Filtering	69
6.5. Adaptive Cross-Coupling Control (ACCC)	70
6.6. 2DoF Model with Adaptive Cross-Coupling Control	70
6.7. Simulation Results 2DoF Model	72
6.7.1. Autonomous 2DoF System with Nonzero Initial Condi- tions	73
6.7.2. 2DoF System with Noise Excitation	75
6.7.3. 2DoF System with Unbalance Excitation	78
6.8. Analysis of the 2DoF System with Unbalance Excitation	88
6.8.1. Analytic Solution of the On-Line Estimator for a Con- stant Whirl Radius	88
6.8.2. Prediction of Estimator Oscillations	89

6.9. Simulation Results 4DoF System	94
6.9.1. Autonomous 4DoF System with Nonzero Initial Condi- tions	95
6.9.2. 4DoF System with Noise Excitation	95
6.9.3. 4DoF System with Unbalance Excitation	97
7. Unbalance Control	104
7.1. Introduction	104
7.2. Ideal Unbalance Control	109
7.3. Discrete Harmonic Control	112
7.3.1. Harmonic Response of a Linear Time Invariant System .	112
7.3.2. Discrete Harmonic Control Algorithm (DHC)	113
7.3.3. Calculation of Fourier Coefficients	117
7.3.4. Application to a Magnetic Bearing System	118
7.3.5. Simulation Results for Displacement Nulling	121
7.3.6. Simulation Results for Current Nulling	126
7.3.7. Simulation Results for Force Nulling	129
7.4. Continuous Harmonic Control	133
7.4.1. Stability Analysis	134
7.4.2. Comparison of DHC and CHC for Displacement Nulling	136
8. Combination of Unbalance and Cross-Coupling Control	140
8.1. Introduction	140
8.2. Simulation Results for DHC and Adaptive Cross-Coupling Con- trol	141
8.2.1. Displacement Nulling and ACCC	141
8.2.2. Current Nulling and ACCC	149
8.2.3. Force Nulling and ACCC	151
8.3. Simulation Results for CHC and Adaptive Cross-Coupling Con- trol	153
8.3.1. Displacement Nulling and ACCC	153
8.3.2. Rotor Run-Ups	156
9. Conclusions and Outlook	162
A. Appendix	165
A.1. Some Concepts of Linear Algebra, Rotor Dynamics and Con- troller Design	165

A.1.1. Complex Notation for 2DoF Rotor Dynamics	165
A.2. Discrete-Time (Digital) Control	166
A.2.1. Discrete-Time State Space	166
A.2.2. z-Transform	168
A.2.3. q-Transform (Tustin Approximation)	168
A.3. The Reluctance Network AMB-Model	170
A.4. Change in the Total Energy of a System with Cross-Coupling Excitation	174
A.5. Least-Squares Estimation	175
A.5.1. Projection Theorem	175
A.5.2. Discrete Least-Squares	177
A.5.3. Continuous Least-Squares	179

Preface

I started this work in May 2000 at the Institute for Machine Dynamics and Measurement at Vienna University of Technology. One of the first steps was to collect all the necessary data to develop a simulation model which behaves similar to the actual test rig available at the institute's laboratory. I tried to maintain a balance between finding general relationships and using the actual numerical values for the parameters. A more scientific approach would have been to hide the actual parameters in the appendix, but this would have obscured the fact that all of the simulations are carried out for the specific test rig data.

After the data collection, I tried to get an insight into the nature of the rotor and magnetic bearing model by deriving quite sophisticated models. I simulated a nonlinear rotor model derived from Euler's equations of rotational motion, but it turned out that the nonlinearity is negligible even for very high displacements. The next step was to investigate the behavior of the magnetic bearing. I derived a reluctance network model, which includes coordinate coupling effects due to back iron fluxes. Then I incorporated magnetic hysteresis effects in a one-dimensional flux magnetic bearing model. It turned out, however, that all these effects are small compared to the uncertainty of the material permeability. After studying the nature of the rotor and the magnetic bearings, I decided to stick to a quite simple model of the magnetic bearing and rigid rotor.

I would like to thank all my colleagues at the Institute for Machine Dynamics and Measurement at Vienna University of Technology, especially Dipl.-Ing. ALEXANDER SCHULZ for reading and commenting on the section about power amplifiers, Dipl.-Ing. STEFAN ENGLEDER for proof-reading my thesis and giving valuable advice about the readability and understandability of my writing, Dr. HORST ECKER who was always willing to discuss various problems, Dipl.-Ing. NORBERT STEINSCHADEN who provided a starting point for this investigation, Mrs. KARIN MATSCHIR who had always an open-ear for non-scientific

problems and typed most of my literature references, and last but not least Prof. Dr. HELMUT SPRINGER who was more a friend and advisor than a boss.

Furthermore, I would like to thank Prof. Dr. HANNS PETER JÖRGL from the Institute for Maschine and Process Automation, who was my second supervisor, Dr. SIEGFRIED SILBER from Johannes Kepler University of Linz for his valuable advice on power amplifiers, and Prof. JOSIAH D. KNIGHT from Duke University, North Carolina, for his linguistic advice.

Dipl.-Ing. Martin Hirschmanner

Nomenclature

General Conventions

Variable	Example	Font
Scalar	<i>a</i>	italic letter (usually lowercase)
Vector	a	bold face lowercase letter
Matrix	A	bold face capital letter

Indexing Rules

Generally subscripts are used for identifying symbols. As an example, the static magnetic bearing force vector is given as follows

$$\mathbf{f}_{MB,0} = \begin{bmatrix} \mathbf{f}_{MBA,0} \\ \mathbf{f}_{MBB,0} \end{bmatrix} = \begin{bmatrix} f_{MBAx,0} \\ f_{MBAy,0} \\ f_{MBBx,0} \\ f_{MBBy,0} \end{bmatrix}.$$

The symbol \mathbf{f}_{MB} is the force vector for the magnetic bearing forces. The additional ,0 indicates that it is the static force vector. The subscript *A* or *B* indicates the selector of higher importance (bearing station *A* or *B*) and the subscript *x* or *y* indicates the selector of lower importance (*x* or *y*-direction). As an additional example, the same force vector in center coordinates is given;

$$\mathbf{f}_{MBc,0} = \begin{bmatrix} \mathbf{m}_{MB,0} \\ \mathbf{f}_{MBx_c,0} \end{bmatrix} = \begin{bmatrix} m_{MBx,0} \\ m_{MB y,0} \\ f_{MBx_c,0} \\ f_{MB y_c,0} \end{bmatrix}.$$

The additional subscript *c* indicates center coordinates and is written immediately after the main symbol. It is only necessary in the symbol for the complete vector, because the symbols for the vector components already indicate

the center coordinates. The next example shows the rotor position vector in bearing, measurement, and center coordinates.

$$\mathbf{x}_b = \begin{bmatrix} x_A \\ y_A \\ x_B \\ y_B \end{bmatrix} \quad \mathbf{x}_m = \begin{bmatrix} x_{mA} \\ y_{mA} \\ x_{mB} \\ y_{mB} \end{bmatrix} \quad \mathbf{x}_c = \begin{bmatrix} \alpha \\ \beta \\ x_c \\ y_c \end{bmatrix}$$

Finally, three current vectors are given, first the position current vector, second the control current vector for all four coils of bearing A , and third the actual currents in all four coils of bearing A .

$$\mathbf{i}_x = \begin{bmatrix} \mathbf{i}_{xA} \\ \mathbf{i}_{xB} \end{bmatrix} = \begin{bmatrix} i_{Ax} \\ i_{Ay} \\ i_{Bx} \\ i_{By} \end{bmatrix} \quad \mathbf{i}_{cA} = \begin{bmatrix} i_{cA1} \\ i_{cA2} \\ i_{cA3} \\ i_{cA4} \end{bmatrix} \quad \mathbf{i}_A = \begin{bmatrix} i_{A1} \\ i_{A2} \\ i_{A3} \\ i_{A4} \end{bmatrix}$$

Notation

Symbol	Description
\mathbb{R}	field of real numbers
\mathbb{C}	field of complex numbers
\in	belong to
$:=$	defined as
\cong	approximately equal to
\triangleq	correspond to
\gg	much greater than
\ll	much less than
j	$\sqrt{-1}$, imaginary unit
\mathbf{I}	identity matrix
$\mathbf{0}$	zero matrix or vector

(continued on next page)

Symbol	Description
$\mathbf{1}$	matrix or vector of ones
\mathbf{A}^T	transpose of \mathbf{A}
\mathbf{A}^{-1}	inverse of \mathbf{A}
\mathbf{A}^{-T}	shorthand of $(\mathbf{A}^{-1})^T$
$\bar{\sigma}(\mathbf{A})$	maximum singular value of \mathbf{A}
$\ \mathbf{A}\ _p$	p norm of \mathbf{A}
$\langle \mathbf{x}, \mathbf{y} \rangle$	inner product of \mathbf{x} and \mathbf{y}
t, τ	continuous-time
$a(t)$	continuous-time signal
\dot{a}, \ddot{a}	first and second time derivative of $a(t)$
s	variable of the Laplace transform
$\hat{a}(s)$	Laplace transform of $a(t)$
k, κ	sample number
$a(kT_s)$	sampled continuous-time signal
$a(k)$	discrete-time signal
z	variable of the z-transform
$\hat{a}(z)$	z-transform of $a(kT_s)$
$\hat{\mathbf{a}}_1$	vector of speed synchronous Fourier coefficients of a
\hat{a}_{1s}	speed synchronous sine coefficient of a
\hat{a}_{1c}	speed synchronous cosine coefficient of a
q	variable of the Tustin approximation transform
$G(s)$	Laplace transfer function
$\mathbf{G}(s)$	Laplace transfer matrix
$G(z)$	z-transfer function

(continued on next page)

Symbol	Description
T_{BA}	transformation matrix from A to B
$\delta(\cdot)$	(1) continuous dirac impulse function $\delta(0) = \infty$ (2) discrete dirac impulse function $\delta(0) = 1$
$\sigma(k)$	discrete-time unit step function

Symbols

Symbol	Matlab	Description
α, β, γ	alpha, ...	Kardan position angles of the rigid rotor
$\lambda(t)$	lambda	time variant forgetting factor
μ	mu	(1) relative magnetic permeability (2) parameter of CHC control
ϕ	phi	magnetic flux
A	A	area
$\hat{A}(\Omega)$	mhatA	control gain matrix for harmonic control
B	B	flux density (induction)
D	mD	damping matrix
d_i	vd_i	current disturbance
d_m		measurement noise
f	vf	force vector
f_g	vf_g	weight force vector
f_{MB}	vf_MB	magnetic bearing force vector
f_n	vf_n	nonconservative cross-coupling force vector
f_{ub}	vf_ub	unbalance force vector in bearing coordinates

(continued on next page)

Symbol	Matlab	Description
\mathbf{G}	mG	gyroscopic matrix
$\mathbf{G}_{x/f}(s)$		force to position transfer matrix of the rotor supported by the AMBs.
$\mathbf{G}_{x/i}(s)$		current to position transfer matrix of the rotor supported by the AMBs.
H	H	magnetic field strength
i	i	current
i_0	i_0	bias current
\mathbf{i}_A	vi_A	current vector of bearing A
i_{Ax}	i_Ax	control current for the x-direction in bearing A
$i_{B1,0}$	i_B10	bias current for coil 1, bearing B
\mathbf{i}_c	vi_c	vector of control currents
i_{ck}	i_ck	control current for coil k
\mathbf{i}_h	vi_h	harmonic control vector added to the AMB control current
\mathbf{i}_n	vi_n	additional control current from the adaptive cross-coupling control
$i_{k,0}$	i_k0	bias current for coil k
\mathbf{i}_x	vi_x	vector of control currents for bearings A and B (both directions)
\mathbf{i}_{xA}	vi_xA	vector of control currents (both directions)
J	J	moment of inertia
\mathbf{K}	mK	symmetric stiffness matrix
k_i	k_i	current coefficient
k_{iAx}	k_iAx	current coefficient bearing A, x-direction

(continued on next page)

Symbol	Matlab	Description
\mathbf{K}_i	mK_i	current coefficient matrix
$\mathbf{K}_{f/i}(s)$	mK_fi	dynamic current coefficient matrix (transfer matrix)
$\mathbf{K}_{f/x}(s)$	mK_fx	dynamic position coefficient matrix (transfer matrix)
k_s	k_s	position coefficient
\mathbf{K}_s	mK_s	position coefficient matrix
m	m	mass
\mathbf{M}	mM	mass matrix
$\mathbf{M}(s)$		transfer matrix of the measurement device including any measurement filters and calculations; it is assumed to be \mathbf{T}_{mb}
\mathbf{N}	mN	skew-symmetric stiffness matrix
$\tilde{\mathbf{n}}$	vtilden	estimated parameter vector
n_1	n_1	cross-coupling coefficient 1
$\tilde{\mathbf{N}}_b$	mtildeN_b	estimated cross-coupling stiffness matrix
N_w	N_w	number of coil windings
ω		natural frequency
Ω	Omega	rotational speed
\mathcal{P}	P	magnetic permeance
\mathbf{P}	mP	gain matrix of the estimator
\mathbf{P}_D	mP_D	differential gain matrix
\mathbf{P}_I	mP_I	integral gain matrix
\mathbf{P}_P	mP_P	proportional gain matrix
p_{ui}	p_ui	proportional gain of the underlying current controller

(continued on next page)

Symbol	Matlab	Description
\mathcal{R}	Rel	magnetic reluctance
\mathcal{R}	mRel	magnetic reluctance matrix
R	R	ohmic resistance
$\mathbf{R}(z)$		z-transfer matrix of the discrete-time controller
\mathbf{r}	vr	reference value vector, usually equal to $\mathbf{0}$
$\hat{\mathbf{T}}(\Omega)$	mhatT	influence coefficient matrix
T_h	T_h	sample time of the discrete harmonic control
T_{MB}	T_MB	time constant of the magnetic bearing
T_s	T_s	sample time of the stabilizing (PID) control
T_{sw}	T_sw	switching time of the PWM controlled power amplifiers
u	u	voltage
\mathbf{u}_A	vu_A	voltage vector of bearing A
u_{max}	u_max	maximum voltage
ζ		damping ratio
\mathbf{x}	vx	position vector
x_A	x_A	subscript for bearing station A
x_{Am}	x_Am	subscript for sensor station A
x_B	x_B	subscript for bearing station B
\mathbf{x}_b	vx_b	rotor position vector in bearing coordinates
\mathbf{x}'_b		measured rotor position in bearing coordinates with additional harmonic control vector
x_c	x_c	subscript for center of gravity

(continued on next page)

Symbol	Matlab	Description
x_c	vx_c	subscript for center coordinates
x_h	vx_h	harmonic control vector added to the measured rotor position signal x_b
x_m	vx_m	subscript for sensor (measured) coordinates
x_N	x_N	subscript for plane of cross-coupling force
x_p	x_p	general position at the rotor

1. Introduction

Active magnetic bearings (AMBs) are well established in modern turbomachinery. Their obvious benefits like contact free suspension and the lack of a lubrication system encourage the use of magnetic bearings in vacuum and high speed technology. Since the levitation in an AMB is inherently unstable, a stabilizing controller is needed and thus control theory issues have been introduced into the field of rotor dynamics.

The development of active magnetic bearings has also ignited substantial research in actively controlling the movement of the rotor itself. A widely researched issue is the control of mass unbalance excitations, especially with the so-called open-loop methods. Another important topic in standard rotor dynamics is the instability of rotors which occur in various applications. There are several constructive measures discussed in the literature to prevent unstable behavior, but only very few researchers have tried to use active elements for this purpose.

At the Institute for Machine Dynamics and Measurement a control algo-

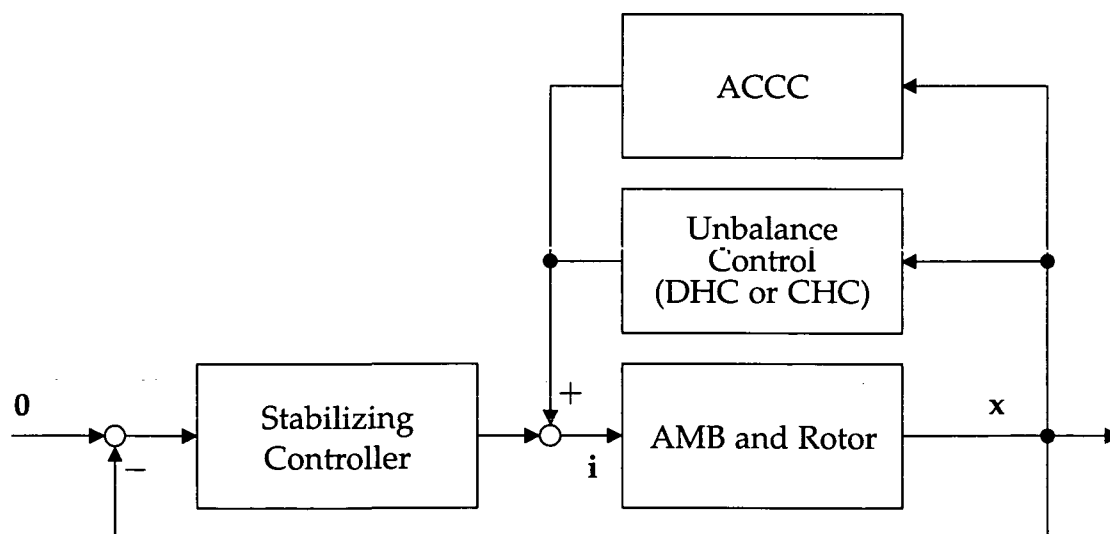


Figure 1.1.: Block diagram of the system

rithm for stabilizing nonconservative cross-coupling excitations has been developed and tested. This algorithm is named "adaptive cross-coupling control" (ACCC). The main goal of this thesis has been to combine this algorithm with an open-loop unbalance control algorithm called "recursive gain scheduled algorithm" in the literature. It has turned out that a more appropriate name for this algorithm is "discrete harmonic control (DHC)" and there is a similar unbalance control algorithm, which is named "continuous harmonic control (CHC)" in this thesis. The system with the two control algorithms is depicted in figure 1.1. The questions posed are:

- Is it possible to combine unbalance and adaptive cross-coupling control algorithms?
- How do they influence each other?
- Which phenomena will occur?

It should be pointed out that AMBs are only one possible choice for the actuators and that the control algorithms could also be used with different actuators.

This thesis is subdivided into nine chapters. A more detailed introduction including a comprehensive literature review is given at the beginning of each chapter. The contents of the chapters are as follows.

In chapter 2, the numerical values of the simulation model are summarized. The position of this chapter reflects the actual research process which also began with the collection of these values.

In chapter 3, the active magnetic bearing is modelled and linearized. For the linearized model, Laplace transfer matrices are derived. Special attention is paid to include the magnetic bearing inductance and the underlying current controller in the model. Additionally, the behavior of the pulse-width-modulation controlled switching amplifier is studied and some hints are given for the design of the underlying current controller.

In chapter 4, the linearized model for the rigid rotor is described. It is shown that any distribution of cross-coupling forces along the rotor can be described with three independent parameters. The rotor is combined with the AMBs. Three types of system models are given: a simple model neglecting the inductance of the AMBs, a complex model including the inductance of the AMBs, and a simple two degrees of freedom (2DoF) model. The eigenvalues of all three models are calculated.

In chapter 5, the stabilizing feedback loop controller is described in the continuous-time and the discrete-time domain. The influence of the sampling time on the discrete-time controlled system is studied. The eigenvalues of all three *controlled* AMB-rotor models are calculated.

In chapter 6, the behavior of the system with cross-coupling excitation is studied and the stability margins are calculated. The adaptive cross-coupling control (ACCC) is derived. The behavior of the rotor with this control algorithm is studied for the simple 2DoF model and for the complex 4DoF model and various excitation cases.

In chapter 7, three possible goals of unbalance control are posed, indicated as "current nulling", "force nulling" and "position nulling". An open-loop method, which is called discrete harmonic control (DHC) and a closed-loop method called continuous harmonic control (CHC) are derived, and the similarities between these two methods are analyzed. Both methods can be used to reach all three goals; this is shown by various simulations.

In chapter 8, the unbalance and the cross-coupling control algorithms are combined. If necessary, the unbalance control schemes are adapted to work together with the adaptive cross-coupling control. It is possible to achieve all goals of unbalance control together with the adaptive cross-coupling control.

In chapter 9, conclusions are drawn and an outlook for possible future research is given.

2. Data of the Numerical Simulation Model

2.1. The Rotor

A numerical simulation model of a rigid rotor supported by active magnetic bearings is used for testing the developed control algorithms. The parameters of the model are chosen to represent a test rig at the Institute for Machine Dynamics and Measurement, which has been designed by Markus Nagl. His assembly drawing is shown in figure 2.1. For the simulation as a stiff rotor, important values are given in table 2.1 (The values correspond to the rotor with laminations). The dimensions of the rotor are taken from the original construction drawings. Values for mass, moment of inertia, and the position of the center of gravity have been calculated by O. Lang and are taken from his thesis [Lan97].

Table 2.1.: Design parameters of the rotor

Property	Symbol	Value	Unit
total mass	m	28.768	kg
lateral moment of inertia	J_l	0.8632	kg m ²
polar moment of inertia	J_p	0.02188	kg m ²
position of the center of gravity	z_C	0.0	m
position of bearing station A	z_A	-0.239	m
position of sensor station A	z_{mA}	-0.190	m
position of bearing station B	z_B	0.241	m
position of bearing station B	z_{mB}	0.192	m

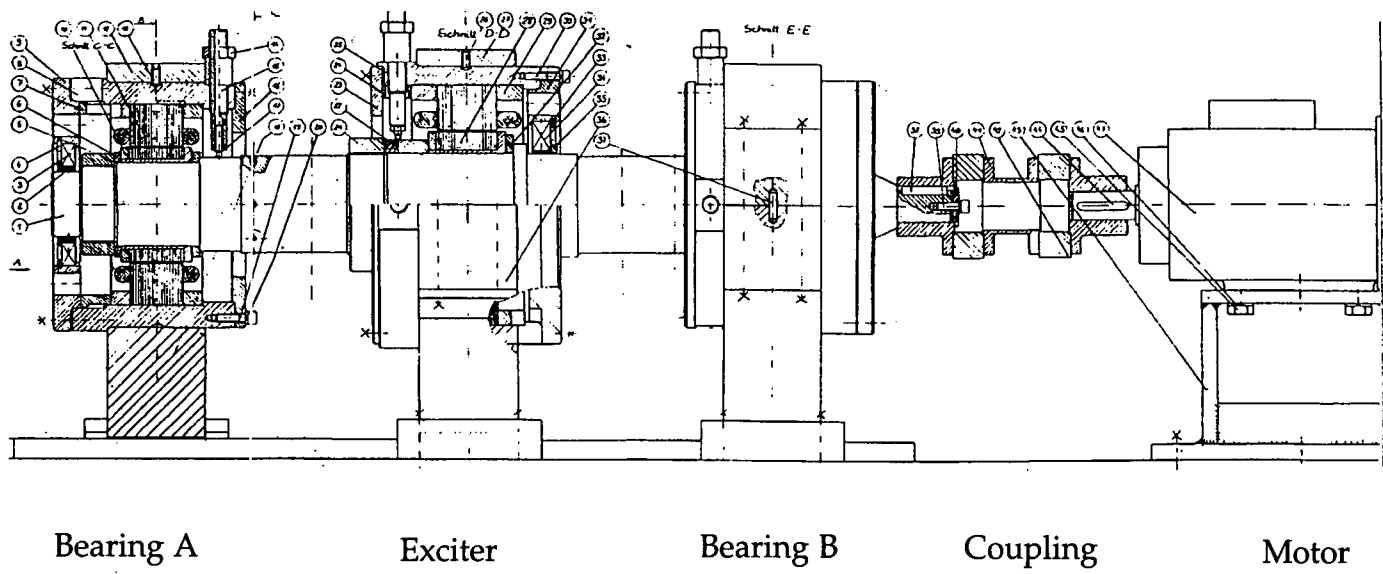


Figure 2.1.: Design drawing of the test rig, taken from [Lan97]

2.2. The Magnetic Bearing

The magnetic bearings used in the test rig are of the type RL90 produced by MECOS Traxler. In table 2.2, the geometrical and electrical design parameters of the Magnetic bearings are shown. These values are either taken from the design drawing or measured. Unfortunately, no data is available about the relative permeability of the rotor and stator material. From the identified position and current coefficient of the magnetic bearing in [Lan97], however, a value of $\mu = 3000$ seems reasonable. The ohmic resistance of the coil windings and the permeability of stator and rotor material are estimated.

Table 2.2.: Design parameters of the magnetic bearing

Property	Symbol	Value	Unit
axial length of the pole shoes	l_p	44	mm
axial length of the rotor sheets	l_{rt}	42	mm
outer diameter of the stator	$d_{a,st}$	158	mm
inner diameter of the stator	$d_{i,st}$	118	mm
half angle between two poles	α_p	22.5	°
width of the pole shoes (tangential)	w_p	17	mm
inner diameter of the pole shoes	d_p	90	mm
cross section of a pole shoe	$A_p = w_p l_p$	697	mm ²
length of the flux path in the pole shoes	$l_{\phi,p} = \frac{1}{2} (d_{i,st} - d_p)$	14	mm
cross section of the back iron	$A_b = \frac{1}{2} (d_{a,st} - d_{i,st}) l_p$	820	mm ²
mean diameter back iron	$d_b = \frac{1}{2} (d_{a,st} + d_{i,st})$	138	mm
length of the flux path in the back iron	$l_{\phi,b} = \frac{\pi}{8} d_b + \frac{1}{2} (d_b - d_{i,st})$	64.19	mm

(continued on next page)

Table 2.2.: (continued)

Property	Symbol	Value	Unit
total length of the flux path in the stator	$l_{\phi,st} = 2l_{\phi p} + l_{\phi b}$	92.19	mm
outer diameter of the rotor sheets	$d_{a,rt}$	89	mm
inner diameter of the backup bearing	$d_{i,bk}$	89.5	mm
inner diameter of the rotor sheets	$d_{i,rt}$	68	mm
diameter of the flux path in the rotor sheets	$d_{\phi,rt} = \frac{1}{2} (d_{a,rt} + d_{i,rt})$	78.5	mm
cross section of the rotor sheets	$A_{rt} = \frac{1}{2} (d_{a,rt} - d_{i,rt}) l_{rt}$	441	mm ²
length of the flux path in the rotor	$l_{\phi,rt} = \frac{1}{8} d_{\phi,rt} \pi$	30.83	mm
length of the air gap (center position)	$l_g = \frac{1}{2} (d_p - d_{a,rt})$	0.5	mm
maximum orbit radius	$r_{o,max} = \frac{1}{2} (d_p - d_{i,bk})$	0.25	mm
number of coil windings for one pole	N_p	65	
number of coil windings for one actuator	$N_w = 2N_p$	130	
diameter of coil windings wire	d_{ww}	1.06	mm
length of coil windings wire (one actuator)	l_{ww}	24	m

(continued on next page)

Table 2.2.: (continued)

Property	Symbol	Value	Unit
specific ohmic resistance (copper)	ρ_{ww}	0.017	$\mu\Omega \text{ m}$
ohmic resistance of one actuator (calculated)		0.46	Ω
ohmic resistance of one actuator and cables (estimated)	R	0.8	Ω
permeability of vacuum	μ_0	40π	$\mu\text{H/m}$
relative permeability stator	μ_{st}	3000	
relative permeability rotor	μ_{rt}	3000	
inductance of one actuator (calculated air-gap only, no back iron)	$(N_w^2 \mu_0 A_g) / (2l_g)$	14.802	mH
inductance of one actuator (calculated, no back iron)	$L_0 = N_w^2 / \mathcal{R}_0$	14.182	mH
nominal maximum current	i_{max}	8	A
nominal bias current	i_0	4	A
nominal maximum control current	$i_{c,max}$	4	A
nominal maximum force	$f_{max} = 4 \frac{i_0 N_w^2 \cos \alpha}{\mathcal{R}_0^2 \mu_0 A_g} i_{c,max}$	803.38	N

3. Modelling of the Magnetic Bearing

3.1. Introduction

The modelling of an active magnetic bearing can be divided into two parts. The first part is to describe the relationships among the electrical properties (like coil current and coil voltage), the magnetic properties (like magnetic flux, flux density and magnetic field strength), and the mechanical properties (like forces acting on the rotor). The second part is to choose how the magnetic bearing is controlled and to find an input-output relationship between the control variable and the magnetic bearing force. This may also include the choice of a stationary operating point and a linearization of the input-output relationship. The distinction of these two parts is not always drawn in the literature; sometimes only the first part is regarded as modelling process and sometimes both parts are combined, depending on the focus of the work.

Finite elements model The first part of the modelling process consists mainly of the calculation of the magnetic field in the AMB. This would usually lead to a three-dimensional field calculation, but, to the author's knowledge, in no publication a three-dimensional magnetic field calculation is considered. The first simplification is to assume a constant magnetic field density along one of the three spatial directions and thus reducing the three-dimensional field calculation to a two-dimensional one. One method to calculate the two-dimensional field is by means of finite elements. Unfortunately, finite elements are not very well suited for dynamical calculations due to the high computational demands. Therefore, the calculations are usually carried out for a stationary rotor, neglecting magnetic hysteresis effects, and assuming sinusoidal or constant coil currents. The results from the finite element calculations are not directly useful for controller design or numerical simulation of the overall rotor behavior; they are used for deriving the coefficients of a linearized input-

output relationship, for the verification of simpler models or the calculation of losses.

Reluctance network model The next possible simplification in the calculation of the magnetic field in the AMB is to use a reluctance network. The two-dimensional AMB is divided into sections where the magnetic field is assumed to be constant along a second spatial direction resulting in a one-dimensional reluctance element describing the relationship between magnetic flux and magnetic field strength in this section of the AMB. The one-dimensional reluctance elements are combined to a two-dimensional network similar to an electrical network. The resulting equations are simple enough to be used in a simulation of the overall rotor behavior, even when magnetic hysteresis is included in the model. Other applications are the optimization of current control schemes, calculation of linearized parameters or precise force calculations. However, the reluctance network model is still too complex for the rotor-position controller design.

One-dimensional field model The simplest magnetic field calculation is applicable when only single flux loops are considered. The result is a one-dimensional field calculation for every magnetic actuator of the AMB. Neither coupling between actuators nor leakage effects can be included in the model. This is the most frequently used model and in spite of all simplifications it can describe the magnetic bearing behavior quite well in the usual operational range. Further simplifications can only be reached by neglecting the magnetic material hysteresis, using a linear relationship between magnetic field strength and flux density (constant material permeability) or setting the iron core permeability to infinity.

Control variable The second part of the modelling process starts with choosing the control variable. The most commonly used approach is to use the coil current as control variable which is called "current control scheme". This implies the assumption that the current can be injected into the coils. In practical applications, a current source where the current is independent of the electrical load is not available. Usually, a controllable voltage source is used and controlled in a way that the actual current is as close as possible to the needed (control-) current. This scheme is called "underlying current controller" and the current controller as well as the power amplifiers are included in the mag-

netic bearing model. In the literature, the current controller is often seen as part of the power amplifiers and is not explicitly mentioned. Another possible choice for the control variable is the coil voltage which is called "voltage control scheme". This approach describes the actual behavior of the AMB much better than the current control scheme, but leads to a more difficult input-output relationship and thus to a higher sophisticated global controller design. The choice of the control variable influences the overall modelling process. In general, only static relationships are derived for current control, while voltage control usually leads to dynamical equations.

Linearization and push-pull scheme Even with the simplest magnetic field and force calculation the resulting bearing model is described by nonlinear algebraic or differential equations. Although there are many nonlinear rotor control schemes described for AMBs in the literature, the most commonly used control schemes are linear controllers; therefore, the input-output relationship of the AMB has to be linearized. This is done by choosing an operating point at which the equations are linearized (bias linearization). A better linearity of the bearing characteristics can be achieved by controlling two opposing actuators in a push-pull scheme.

Literature review The early papers describing AMBs in a rotor-dynamic context like [SL76, Ulb79, Zam81] exclusively use the one-dimensional field formulation together with a current control based linearization. This approach is described e.g. in the book of Schweitzer et al. [STB93].

Knight et al. [KXM92] apply a two-dimensional finite element method to study the behavior of a single and two opposing horseshoe actuators and compare the numerical results with experiments. Magnetic saturation of the iron core without hysteresis is included in the model. They calculate and measure static forces for a given current when the rotor is displaced from the center position and find out that not only a force component in the direction of displacement exists but also a force component perpendicular to the displacement. This cross-coupling effect is purely nonlinear and should not be mixed up with the nonconservative cross-coupling effect as discussed later in this thesis.

Maslen et al. [MM94, MM95] describe how to apply a reluctance network model to calculate the static AMB forces depending on the coil currents. The magnetic material is assumed to be linear. The resulting equations are also

used to find a certain current control law by which the AMB forces are linear and decoupled for a specific rotor position. This is viewed to be especially useful for asymmetric bearings and to achieve fault tolerance to coil failures. Fault tolerance to coil failures is only possible when initially more coils are included in the AMB than would be necessary for magnetic suspension. In Meeker et al. [MMN96, Mee96], the reluctance network model is augmented to include eddy currents, fringing, and leakage effects. This model is used to calculate the frequency response from applied voltage to coil current and the coil inductance for an AMB with a fixed rotor position. The results are compared with a simple network model and with experiments. The augmented network model is superior to the simple network model especially at frequencies higher than 1000 Hz. The most recent paper from this group of authors is by Noh et al. [NMMK00]. Additionally to the effects considered by Meeker, magnetic hysteresis and a switching power amplifier is also included in the model. They calculate the magnetic field and the resulting coil currents by a numerical simulation, but again only for a stationary rotor.

Gähler et al. [GF94] also develop a reluctance network model; nonlinearities in the material are not considered. Contrary to the work by Maslen, Meeker, Noh et al., they derive the network equations with the help of standard methods of electric circuit theory (graph theory). The details are not given in the paper [GF94], but similar calculations can be found in the appendix A.3 of this thesis. The resulting set of equations is more convenient to use than the ones by Maslen, but the results calculated from these equations should be identical. Gähler et al. use the network model to calculate the AMB force from static currents as well as from measured fluxes. The fluxes are measured in some parts of the AMB and the actual force is calculated; the AMB is employed as a "force sensor". In additional papers from the same group [FGN96, AN99], the application of this force measurement principle is described and quantitative errors in comparison to a strain gauge measurement and finite elements calculation are given.

Schmidt et al. [SPS96] compare results from finite elements and reluctance network calculations. The material is assumed to have a linear magnetic field strength to flux density relationship, thus saturation and hysteresis effects are neglected. They calculate static forces and linearized parameters for the current control scheme. Schlager [Sch97b] and Springer [SSP98] use a reluctance network including magnetic material hysteresis to model the magnetic bearing. They simulate the behavior of a 2DoF rotor suspended in a voltage controlled AMB for unbalance and shock loads.

Antila et al. [ALT98, ALA98, Ant98] use finite elements and reluctance network calculations to calculate the static linearized parameters of the AMB especially when magnetic saturation occurs; additional to the current and position stiffness the dynamic inductance of the coils and the cross-coupling coefficients are also evaluated. The reluctance network model is used to include magnetic hysteresis and eddy currents which are not included in the finite elements calculation. These results are compared with measurements.

Na et al. [NP01, NP00c, NP00a, NP00b] pick up the idea of fault tolerance from Maslen et al. as mentioned above. They use, among other differences, the reluctance network model not only for finding a specific current control law in the case of a coil failure, but also for a dynamical simulation of the rotor and AMB behavior.

In [Hir01], the author of this thesis develops a reluctance network model to calculate the AMB force and also describes a simulation model. However, it turns out that the increased accuracy due to the network model has almost no effect on the qualitative behavior of the AMB in the usual operational range and is small compared to the uncertainties of the material parameters. For that reason, the AMB model is derived from a one-dimensional field calculation in this thesis. (The equations for the reluctance network model can be found in the appendix A.3.) This nonlinear model is used for the numerical simulations. For the controller design and stability considerations, a linearized model is employed. This linearized model is derived from the voltage control scheme and used together with an underlying current controller. The resulting model described by a system of ordinary differential equations combines the accuracy of the voltage controlled AMB model with the usability of the current controlled AMB model. Additionally, it offers some design hints for the underlying current controller and power amplifiers, which are also considered here. To the author's knowledge, this approach cannot be found in the literature.

3.2. The Nonlinear Simple AMB Model

The one-dimensional model of the AMB is shown in figure 3.1. This simple model also implies the neglect of leakage fluxes and coupling among the four

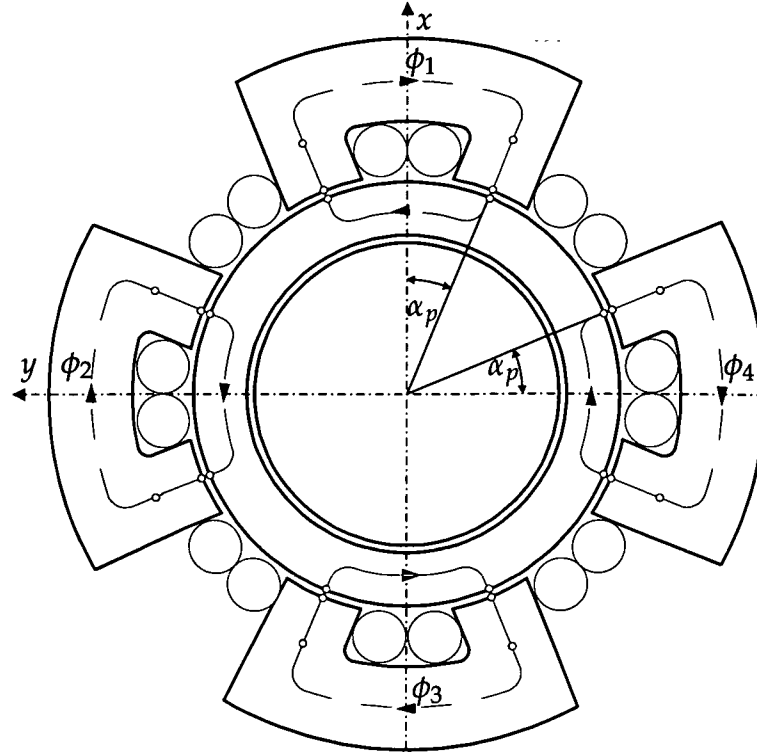


Figure 3.1.: The simple actuator model

actuators¹. The induction law

$$u = Ri + N_w \frac{d}{dt} \phi ,$$

Ampere's loop law

$$iN_w = \Theta = \oint \mathbf{H} d\mathbf{l}$$

and the relationship between the air gap force and the flux density

$$\mathbf{f} = \frac{1}{2\mu_0} \iint |\mathbf{B}|^2 d\mathbf{A}$$

are the basis for the differential equations of the AMB. The differential equations describing the characteristics of one opposite pair of the four actuators are derived in the following. Each of the circuits is divided into three magnetic path resistances, one for the rotor, denoted by the subscript *rt*, one for

¹ In this thesis, the term magnetic actuator refers to a part of the magnetic bearing.

the stator, denoted by the subscript st , and one for the two air gaps, denoted by the subscript g . After several algebraic calculations, the following relations can be obtained

$$\begin{aligned} \frac{d}{dt} \begin{bmatrix} \phi_1 \\ \phi_3 \end{bmatrix} &= -\frac{R}{N_w^2} \begin{bmatrix} l_{\phi,rt}H_{rt}(\phi_1) + l_{\phi,st}H_{st}(\phi_1) + \frac{2(l_g - x \cos \alpha_p)}{\mu_0 A_g} \phi_1 \\ l_{\phi,rt}H_{rt}(\phi_3) + l_{\phi,st}H_{st}(\phi_3) + \frac{2(l_g + x \cos \alpha_p)}{\mu_0 A_g} \phi_3 \end{bmatrix} + \frac{1}{N_w} \begin{bmatrix} u_1 \\ u_3 \end{bmatrix} \\ \begin{bmatrix} i_1 \\ i_3 \\ f_x \end{bmatrix} &= \begin{bmatrix} l_{\phi,rt}H_{rt}(\phi_1) + l_{\phi,st}H_{st}(\phi_1) + \frac{2(l_g - x \cos \alpha_p)}{\mu_0 A_g} \phi_1 \\ l_{\phi,rt}H_{rt}(\phi_3) + l_{\phi,st}H_{st}(\phi_3) + \frac{2(l_g + x \cos \alpha_p)}{\mu_0 A_g} \phi_3 \\ (\phi_1^2 - \phi_3^2) \frac{\cos \alpha_p}{\mu_0 A_g} \end{bmatrix}. \end{aligned} \quad (3.1)$$

Although the relationship between the magnetic flux and the magnetic field strength is nonlinear in the rotor and the stator, material hysteresis is neglected in this model. Assuming that the relationship between the magnetic field strength H and the magnetic flux ϕ is linear, that is

$$l_{\phi,rt}H_{rt}(\phi_1) + l_{\phi,st}H_{st}(\phi_1) + \frac{2(l_g - x \cos \alpha_p)}{\mu_0 A_g} \phi_1 = \mathcal{R}_{act}(x) \phi_1,$$

where

$$\mathcal{R}_{act}(x) := \frac{l_{\phi,rt}}{\mu_{rt}\mu_0 A_{rt}} + \frac{l_{\phi,st}}{\mu_{st}\mu_0 A_{st}} + \frac{2(l_g - x \cos \alpha_p)}{\mu_0 A_g},$$

equation (3.1) simplifies to

$$\begin{aligned} \frac{d}{dt} \begin{bmatrix} \phi_1 \\ \phi_3 \end{bmatrix} &= -\frac{R}{N_w^2} \begin{bmatrix} \mathcal{R}_{act}(x) & 0 \\ 0 & \mathcal{R}_{act}(-x) \end{bmatrix} \begin{bmatrix} \phi_1 \\ \phi_3 \end{bmatrix} + \frac{1}{N_w} \begin{bmatrix} u_1 \\ u_3 \end{bmatrix} \\ \begin{bmatrix} i_1 \\ i_3 \\ f_x \end{bmatrix} &= \begin{bmatrix} \frac{1}{N_w} \mathcal{R}_{act}(+x) \phi_1 \\ \frac{1}{N_w} \mathcal{R}_{act}(-x) \phi_3 \\ (\phi_1^2 - \phi_3^2) \frac{\cos \alpha_p}{\mu_0 A_g} \end{bmatrix}. \end{aligned} \quad (3.2)$$

In equation (3.2), the magnetic bearing force is written in terms of magnetic fluxes. It will also be useful to write the force in terms of the coil currents, that is

$$f_x = \left(\frac{i_1^2}{\mathcal{R}_{act}(x)^2} - \frac{i_3^2}{\mathcal{R}_{act}(-x)^2} \right) \frac{N_w^2 \cos \alpha_p}{\mu_0 A_g}.$$

When the rotor is at the center position ($x = 0$) this simplifies to

$$f_x|_{x=0} = (i_1^2 - i_3^2) \frac{N_w^2 \cos \alpha_p}{\mathcal{R}_0^2 \mu_0 A_g},$$

where

$$\mathcal{R}_0 := \mathcal{R}_{act}(0) = \frac{l_{\phi,rt}}{\mu_{rt}\mu_0 A_{rt}} + \frac{l_{\phi,st}}{\mu_{st}\mu_0 A_{st}} + \frac{2l_g}{\mu_0 A_g}.$$

3.3. The Linearized Simple AMB Model

3.3.1. The Linear Magnetic Bearing with an Input Voltage

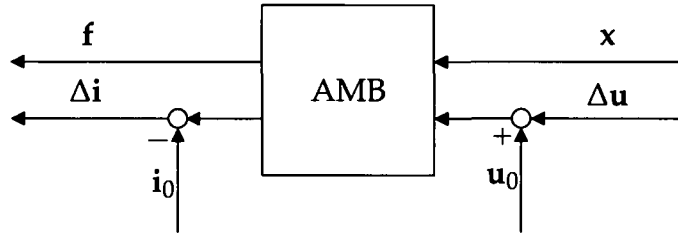


Figure 3.2.: Linearizing the AMB

In this section, the equations are written for all four actuators/coils. They are valid for bearing *A* as well as for bearing *B* of the rigid rotor (see figure 2.1). In order to derive a linearized model, a static equilibrium state has to be found. At this equilibrium point the inputs (the position and the voltage) are set to a fixed value. Usually the position is set to the center position, i.e. $x_0 = y_0 = 0$. The input voltage is set to the so-called bias voltage $u_{1,0}$ to $u_{4,0}$. The equilibrium condition

$$\frac{d}{dt}\phi = 0$$

leads to

$$\begin{bmatrix} \phi_{1,0} \\ \phi_{2,0} \\ \phi_{3,0} \\ \phi_{4,0} \end{bmatrix} = \frac{N_w}{R\mathcal{R}_0} \begin{bmatrix} u_{1,0} \\ u_{2,0} \\ u_{3,0} \\ u_{4,0} \end{bmatrix}.$$

The bias fluxes $\phi_{1,0}$ to $\phi_{4,0}$ represent the solutions for the equilibrium point. It is useful to define bias currents $i_{1,0} := \frac{u_{1,0}}{R}$ to $i_{4,0} := \frac{u_{4,0}}{R}$. We now define the deviations of the actual values for fluxes, voltages, currents and forces from the static equilibrium (bias) values by

$$\begin{aligned}\Delta u_k &:= u_k - u_{k,0} & \Delta \phi_k &:= \phi_k - \phi_{k,0} & \Delta i_k &:= i_k - i_{k,0} \\ \Delta f_x &:= f_x - f_{x,0} & \Delta f_y &:= f_y - f_{y,0} & \Delta x &:= x - x_0 & \Delta y &:= y - y_0\end{aligned}$$

where $k \in \{1, 2, 3, 4\}$. The linearized model for the deviated values is derived by approximating the nonlinear differential equations by a Taylor series and neglecting all terms of higher order. The linearized equations have the form

$$\begin{aligned}\frac{d}{dt} \begin{bmatrix} \Delta \phi_1 \\ \Delta \phi_2 \\ \Delta \phi_3 \\ \Delta \phi_4 \end{bmatrix} &= -\frac{R\mathcal{R}_0}{N_w^2} \begin{bmatrix} \Delta \phi_1 \\ \Delta \phi_2 \\ \Delta \phi_3 \\ \Delta \phi_4 \end{bmatrix} + \frac{1}{N_w} \begin{bmatrix} \Delta u_1 \\ \Delta u_2 \\ \Delta u_3 \\ \Delta u_4 \end{bmatrix} + \frac{2 \cos \alpha_p}{N_w \mathcal{R}_0 \mu_0 A_g} \begin{bmatrix} u_{1,0} & 0 \\ 0 & u_{2,0} \\ -u_{3,0} & 0 \\ 0 & -u_{4,0} \end{bmatrix} \begin{bmatrix} \Delta x \\ \Delta y \end{bmatrix} \\ \begin{bmatrix} \Delta i_1 \\ \Delta i_2 \\ \Delta i_3 \\ \Delta i_4 \end{bmatrix} &= \frac{\mathcal{R}_0}{N_w} \begin{bmatrix} \Delta \phi_1 \\ \Delta \phi_2 \\ \Delta \phi_3 \\ \Delta \phi_4 \end{bmatrix} + \frac{2 \cos \alpha_p}{R \mathcal{R}_0 \mu_0 A_g} \begin{bmatrix} -u_{1,0} & 0 \\ 0 & -u_{2,0} \\ u_{3,0} & 0 \\ 0 & u_{4,0} \end{bmatrix} \begin{bmatrix} \Delta x \\ \Delta y \end{bmatrix} \\ \begin{bmatrix} \Delta f_x \\ \Delta f_y \end{bmatrix} &= \frac{2 N_w \cos \alpha_p}{R \mathcal{R}_0 \mu_0 A_g} \begin{bmatrix} u_{1,0} & 0 & -u_{3,0} & 0 \\ 0 & u_{2,0} & 0 & -u_{4,0} \end{bmatrix} \begin{bmatrix} \Delta \phi_1 \\ \Delta \phi_2 \\ \Delta \phi_3 \\ \Delta \phi_4 \end{bmatrix}.\end{aligned}$$

When the bias voltages are added to the input voltages and the bias currents are subtracted from the actual coil currents as shown in figure 3.2, these linearized equations represent a proper description for the system. The bias currents (voltages) of the AMB are chosen in section 4.5 to carry the weight of the rotor. Therefore, the resulting magnetic bearing force is the deviation from the static equilibrium value. From now on, only the deviation values are considered, and, for the sake of simplicity, the prefix Δ is dropped. With the following abbreviations

$$\begin{aligned}L_0 &:= \frac{N_w^2}{\mathcal{R}_0}, \\ k_{sx} &:= 4 \frac{(i_{1,0}^2 + i_{3,0}^2) N_w^2 \cos^2 \alpha_p}{\mathcal{R}_0^3 \mu_0^2 A_g^2},\end{aligned}$$

$$k_{i1} := 2 \frac{i_{1,0} N_w^2 \cos \alpha_p}{\mathcal{R}_0^2 \mu_0 A_g},$$

(the other constants k_{i2} to k_{i4} and k_{sy} are calculated accordingly), and the relationship

$$(k_{i1}^2 + k_{i3}^2) = 4 \frac{(i_{1,0}^2 + i_{3,0}^2) N_w^4 \cos^2 \alpha_p}{\mathcal{R}_0^4 \mu_0^2 A_g^2} = k_{sx} L_0,$$

the transformation into the Laplace domain of the linearized equations yields

$$\hat{\mathbf{i}}(s) = \mathbf{G}_{i/u}(s) \hat{\mathbf{u}}(s) + \mathbf{G}_{i/x}(s) \hat{\mathbf{x}}(s) \quad (3.3)$$

$$\hat{\mathbf{f}}(s) = \mathbf{G}_{f/u}(s) \hat{\mathbf{u}}(s) + \mathbf{G}_{f/x}(s) \hat{\mathbf{x}}(s) \quad (3.4)$$

with the corresponding transfer matrices for a four actuator model

$$\begin{aligned} \mathbf{G}_{i/u}(s) &:= \mathbf{I} \frac{1}{sL_0 + R} \\ \mathbf{G}_{i/x}(s) &:= \begin{bmatrix} -k_{i1} & 0 \\ 0 & -k_{i2} \\ k_{i3} & 0 \\ 0 & k_{i4} \end{bmatrix} \frac{s}{sL_0 + R} \\ \mathbf{G}_{f/u}(s) &:= \begin{bmatrix} k_{i1} & 0 & -k_{i3} & 0 \\ 0 & k_{i2} & 0 & -k_{i4} \end{bmatrix} \frac{1}{(sL_0 + R)} \\ \mathbf{G}_{f/x}(s) &:= \begin{bmatrix} k_{sx} & 0 \\ 0 & k_{sy} \end{bmatrix} \frac{1}{2 \left(s \frac{L_0}{R} + 1 \right)}. \end{aligned}$$

3.3.2. The Linear Actuator with an Input Current (underlying current controller)

In most AMB applications, the coil voltages are controlled by an underlying current controller. This controller is usually a simple proportional gain controller and the coil voltages are

$$\hat{\mathbf{u}}(s) = p_{ui} \left(\hat{\mathbf{i}}_c(s) - \hat{\mathbf{i}}(s) - \hat{\mathbf{d}}_i(s) \right) \quad (3.5)$$

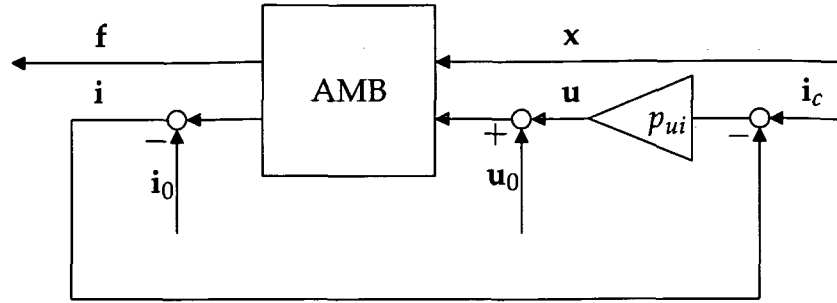


Figure 3.3.: AMB with underlying current controller

with \mathbf{i}_c as the vector of control currents and \mathbf{d}_i as the current measurement noise. From (3.3) and (3.5) we get for the current

$$\hat{\mathbf{i}}(s) = \mathbf{T}_{i/i_c}(s) \hat{\mathbf{i}}_c(s) - \mathbf{T}_{i/i_c}(s) \hat{\mathbf{d}}_i(s) + \mathbf{T}_{i/x}(s) \hat{\mathbf{x}}(s) \quad (3.6)$$

where

$$\mathbf{T}_{i/i_c}(s) := \mathbf{I} \frac{p_{ui}}{R + p_{ui}} \frac{1}{s \frac{L_0}{R + p_{ui}} + 1}$$

$$\mathbf{T}_{i/x}(s) := \begin{bmatrix} -k_{i1} & 0 \\ 0 & -k_{i2} \\ k_{i3} & 0 \\ 0 & k_{i4} \end{bmatrix} \frac{s}{s \frac{L_0}{R + p_{ui}} + 1} \frac{1}{R + p_{ui}}.$$

The actual coil voltage is given by

$$\hat{\mathbf{u}}(s) = \mathbf{T}_{u/i_c}(s) \hat{\mathbf{i}}_c(s) - \mathbf{T}_{u/i_c}(s) \hat{\mathbf{d}}_i(s) + \mathbf{T}_{u/x}(s) \hat{\mathbf{x}}(s)$$

with the transfer matrices

$$\mathbf{T}_{u/i_c}(s) := \mathbf{I} \frac{p_{ui} R}{R + p_{ui}} \frac{\left(s \frac{L_0}{R} + 1 \right)}{s \frac{L_0}{R + p_{ui}} + 1}$$

$$\mathbf{T}_{u/x}(s) := \begin{bmatrix} k_{i1} & 0 \\ 0 & k_{i2} \\ -k_{i3} & 0 \\ 0 & -k_{i4} \end{bmatrix} \frac{p_{ui}}{R + p_{ui}} \frac{s}{s \frac{L_0}{R + p_{ui}} + 1}.$$

Finally, the magnetic bearing force is given by

$$\hat{\mathbf{f}}(s) = \mathbf{T}_{f/i_c}(s) \hat{\mathbf{i}}_c(s) - \mathbf{T}_{f/i_c}(s) \hat{\mathbf{d}}_i(s) + \mathbf{T}_{f/x}(s) \hat{\mathbf{x}}(s)$$

with the transfer matrices

$$\mathbf{T}_{f/i_c}(s) := \begin{bmatrix} k_{i1} & 0 & -k_{i3} & 0 \\ 0 & k_{i2} & 0 & -k_{i4} \end{bmatrix} \frac{p_{ui}}{R + p_{ui}} \frac{1}{s \frac{L_0}{R + p_{ui}} + 1}$$

$$\mathbf{T}_{f/x}(s) := \begin{bmatrix} k_{sx} & 0 \\ 0 & k_{sy} \end{bmatrix} \frac{1}{s \frac{L_0}{R + p_{ui}} + 1}.$$

To improve the linearity of the AMB, it is controlled by a push-pull scheme such that the control currents are

$$\begin{aligned} i_{c1} &= i_x & i_{c3} &= -i_x \\ i_{c2} &= i_y & i_{c4} &= -i_y \end{aligned}$$

With the definitions

$$k_{ix} := k_{i1} + k_{i3} = 2 \frac{(i_{1,0} + i_{3,0}) N_w^2 \cos \alpha_p}{\mathcal{R}_0^2 \mu_0 A_g}$$

and

$$k_{iy} := k_{i2} + k_{i4} = 2 \frac{(i_{2,0} + i_{4,0}) N_w^2 \cos \alpha_p}{\mathcal{R}_0^2 \mu_0 A_g},$$

we get the AMB force (neglecting the current measurement noise) as

$$\hat{\mathbf{f}}(s) = \frac{1}{sT_{MB} + 1} \left(\frac{p_{ui}}{R + p_{ui}} \begin{bmatrix} k_{ix} & 0 \\ 0 & k_{iy} \end{bmatrix} \begin{bmatrix} \hat{i}_x \\ \hat{i}_y \end{bmatrix} + \begin{bmatrix} k_{sx} & 0 \\ 0 & k_{sy} \end{bmatrix} \begin{bmatrix} \hat{x} \\ \hat{y} \end{bmatrix} \right). \quad (3.7)$$

The time constant of the current controlled magnetic bearing is

$$T_{MB} := \frac{L_0}{R + p_{ui}}. \quad (3.8)$$

From equation (3.7) it can be seen that a high proportional gain p_{ui} of the underlying current controller always improves the AMB performance. Since the current measurement noise to force transfer matrix is the same as the

control current to force transfer matrix, a higher bandwidth for $T_{f/i_c}(s)$ also increases the noise level in the resulting forces. The $T_{u/i_c}(s)$ transfer matrix has the characteristics of a lead element. Higher frequencies are amplified more than lower frequencies. This effect increases with higher p_{ui} as well as the overall amplification.

The state space form of the linearized AMB with underlying current controller is given by

$$\frac{d}{dt} \begin{bmatrix} \phi_1 \\ \phi_2 \\ \phi_3 \\ \phi_4 \end{bmatrix} = -\frac{R+p_{ui}}{L_0} \begin{bmatrix} \phi_1 \\ \phi_2 \\ \phi_3 \\ \phi_4 \end{bmatrix} + \frac{p_{ui}}{N_w} \begin{bmatrix} 1 & 0 \\ 0 & 1 \\ -1 & 0 \\ 0 & -1 \end{bmatrix} \begin{bmatrix} i_x \\ i_y \end{bmatrix} + \frac{R+p_{ui}}{N_w L_0} \begin{bmatrix} k_{i1} & 0 \\ 0 & k_{i2} \\ -k_{i3} & 0 \\ 0 & -k_{i4} \end{bmatrix} \begin{bmatrix} x \\ y \end{bmatrix}$$

$$\begin{bmatrix} f_x \\ f_y \end{bmatrix} = \frac{N_w}{L_0} \begin{bmatrix} k_{i1} & 0 & -k_{i3} & 0 \\ 0 & k_{i2} & 0 & -k_{i4} \end{bmatrix} \begin{bmatrix} \phi_1 \\ \phi_2 \\ \phi_3 \\ \phi_4 \end{bmatrix}.$$

Calculating the transfer matrices from this state space form will lead to the same results as before.

3.3.3. Pulse-Width-Modulation Controlled Switching Amplifier

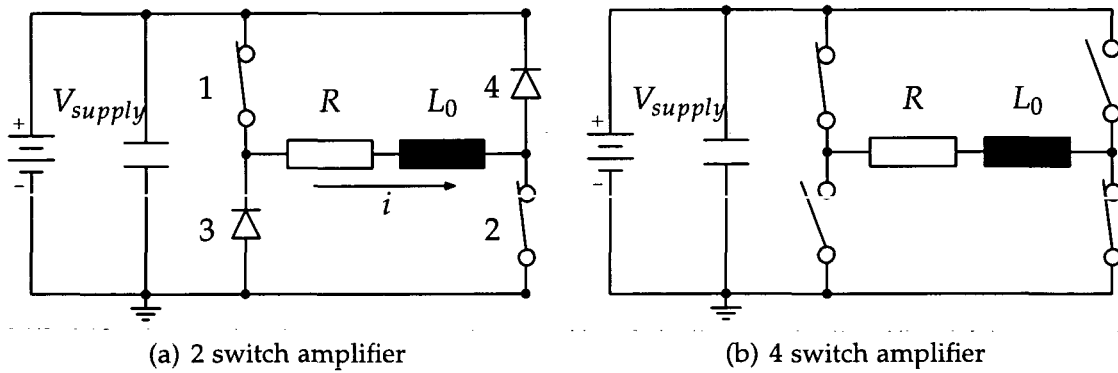


Figure 3.4.: Two types of dc-to-dc converters

To generate the necessary voltages, power amplifiers have to be used. In the previous section, it has been assumed that the coil voltage is proportional to

the current error. This behavior can be realized very easily with linear amplifiers. However, due to the low efficiency of linear amplifiers, switching amplifiers are used for most modern magnetic bearing applications.

In figure 3.4, two variants of dc-to-dc converters are drawn. The variant shown in figure 3.4a is usually used, since in most AMB applications only unipolar output current is required. It is cheaper because only two active switches (metal oxide semiconductor field effect transistor, MOS-FET) are needed and the two diodes work as "passive switches". The circuit can assume three states. In the first state, the switches 1 and 2 are closed while the two passive switches 3 and 4 are "open"; positive voltage is applied to the coil. In the second state, switches 1 and 2 are open while the passive switches 3 and 4 are "closed"; negative voltage is applied to the coil. In the third state, switch 1 is open while switch 2 is closed; no supply voltage is applied on the coil. In this state, the load current stays approximately constant and therefore the electromagnetic emission of the coils is minimal; all measurements should take place during this period. The variant figure 3.4b shows an identical behavior; it is used when bipolar coil current is needed. For a detailed description of the functionality, the reader is asked to refer to e.g. [CCI⁺97].

The dc-to-dc converter can either work with a fixed switching frequency or without one. Designs without a fixed switching frequency have some advantages but a substantial disadvantage; they cannot be synchronized with the measurements and therefore there is no way to reduce measurement noise by selecting the measurement time. Some of the possible operating principles are described in [Sch95, KMH90]. The most common method of controlling the switching amplifier is the pulse width modulation approach.

An ideal dc-to-dc converter is considered with perfect switches and constant supply voltage, for all further calculations. Reformulating equation (3.3) and (3.5) for a single actuator of the AMB and the rotor at center position ($x, y = 0$) the system is

$$\hat{i}(s) = \frac{1}{sL_0 + R} \hat{u}(s) . \quad (3.9)$$

The voltage $u(t)$ is now given as a pulse-width-modulation controlled voltage

$$u(t) = \text{PWM}(e(t_k))$$

depending on the current error

$$e(t) = i_c(t) - i(t) .$$

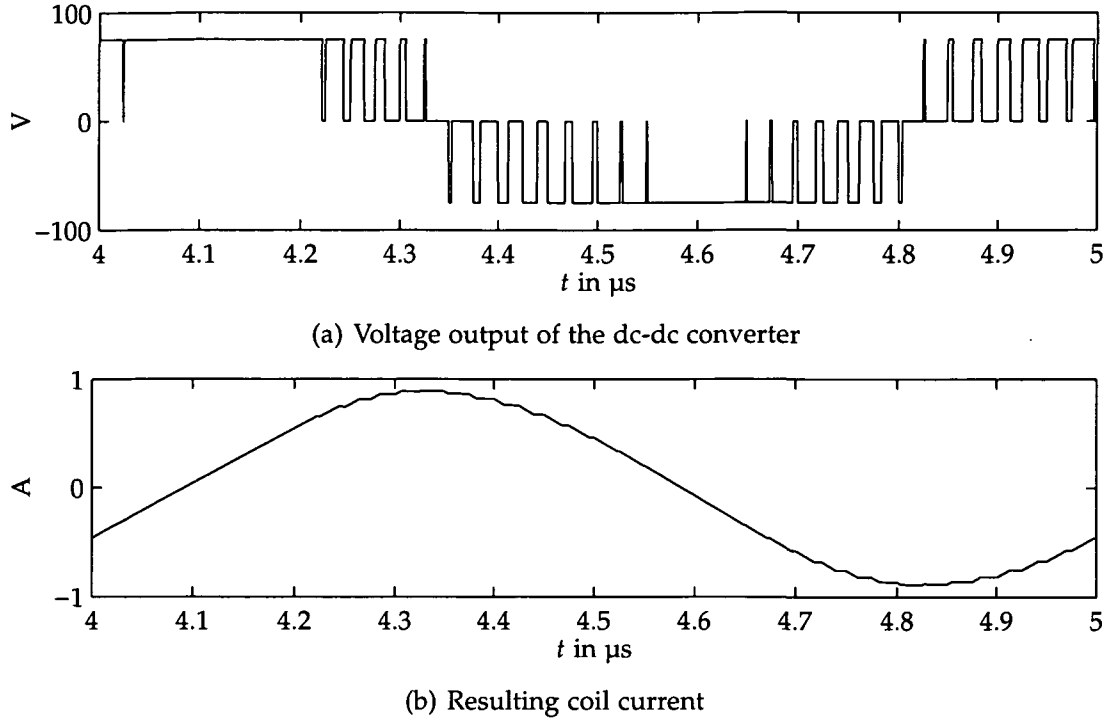


Figure 3.5.: Typical output voltage of a PWM controlled amplifier and resulting coil current

The PWM operator is characterized by a periodic sampling with period T_{sw} at discrete instants t_k (i.e., $t_{k+1} = t_k + T_{sw}$). For the sake of simplicity, it is assumed that the absolute value of the maximum voltage is u_{max} and the minimum voltage is $-u_{max}$. Following [SRBPRLA92], the voltage output of the PWM controlled dc-to-dc converter is described by

$$\text{PWM}(e(t_k)) := \begin{cases} u_{max} \text{sign}(e(t_k)) & \text{for } t_k < t \leq t_k + \tau(e(t_k)) T_{sw} \\ 0 & \text{otherwise} \end{cases}$$

where

$$\tau(e(t_k)) := \begin{cases} 1 & \text{for } |e(t_k)| > \frac{u_{max}}{p_{ui}} \\ \left| \frac{p_{ui}}{u_{max}} e(t_k) \right| & \text{for } |e(t_k)| \leq \frac{u_{max}}{p_{ui}} \end{cases}$$

τ is known as the duty ratio and p_{ui} will be addressed as the amplifier gain.

In figure 3.5, a typical simulation result for the system equation (3.9) is plotted. The parameters for the simulation are $u_{max} = 75$ V, $p_{ui} = 150$ V/A, $L_0 = 14.18$ mH, and $R = 0.8$ Ω . The control current is a sine wave with a frequency of 1000 Hz and an amplitude of 1 A.

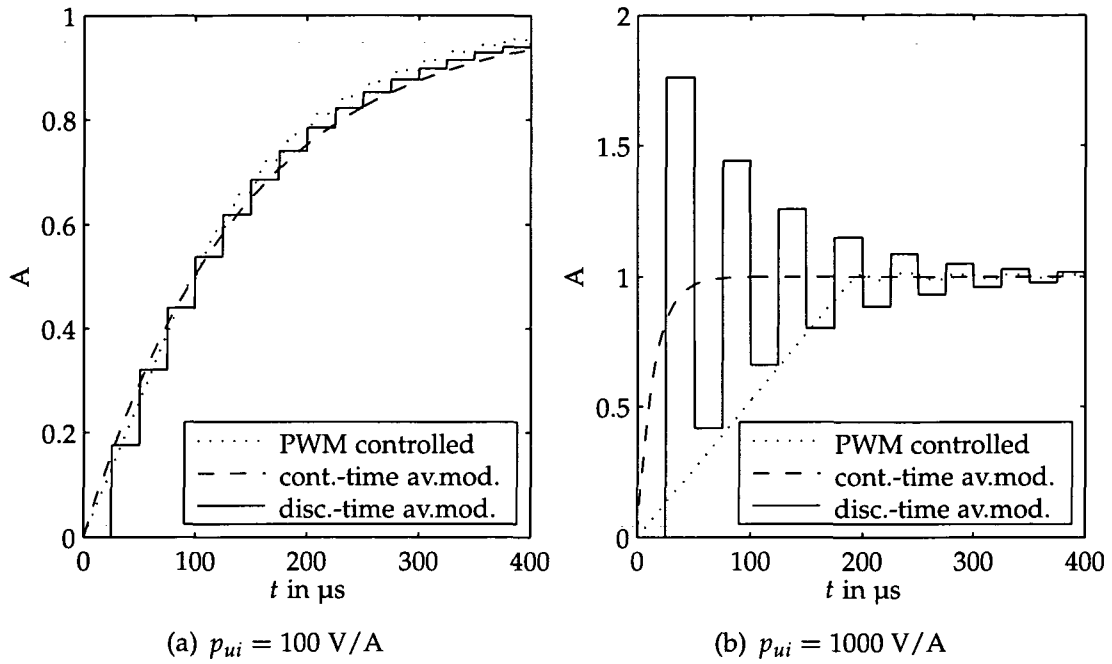


Figure 3.6.: Step responses of different dc-to-dc converter models

It is shown in [SRBPRLA92] that, under certain conditions and assuming that the switching frequency $1/T_{sw}$ is much higher than the natural frequencies of the converter system², the dc-to-dc converter can be described by the so-called average controlled system

$$\begin{aligned}
 \hat{i}(s) &= \frac{1}{sL_0 + R} \hat{u}(s) \\
 e(t) &= i_c(t) - i(t) \\
 u(t) &= u_{max} \text{sat}(e(t))
 \end{aligned} \tag{3.10}$$

where

$$\text{sat}(e(t)) := \begin{cases} \text{sign}(e(t)) & \text{for } |e(t)| > \frac{u_{max}}{p_{ui}} \\ \frac{p_{ui}}{u_{max}} e(t) & \text{for } |e(t)| \leq \frac{u_{max}}{p_{ui}} \end{cases}$$

² This also implies that the sampling frequency of a global discrete-time controller should be much lower than the switching frequency.

For small values of $e(t)$, the average model simplifies to

$$\begin{aligned}\hat{i}(s) &= \frac{1}{sL_0 + R} \hat{u}(s) \\ e(t) &= i_c(t) - i(t) \\ u(t) &= p_{ui} e(t)\end{aligned}\tag{3.11}$$

which is equivalent to equation (3.6). It is worth to note that the average controlled system has not the same value for the resulting coil current $i(t)$ as the PWM controlled system, even at the discrete-time instants t_k .

The average model does not describe the effects connected to the discretization of the model with the switching frequency $1/T_{sw}$. A method to overcome this drawback is to discretize equation (3.11). In figure 3.6, the step response of the PWM controlled dc-to-dc converter equation (3.9) is compared to the average model without saturation (equ. (3.11)) and to a discrete version of the average model without saturation.

The dashed line is the response of the continuous model and the stair case function is the response of the discrete version. The simulations are done for a value of $p_{ui} = 100 \text{ V/A}$ (fig. 3.6a) and a value of $p_{ui} = 1000 \text{ V/A}$ (fig. 3.6b). The switching frequency $1/T_{sw}$ is 40 kHz as in the thesis of A. Schulz [Sch].

For the low amplifier gain, all three models behave very similar; the discrete model describes the behavior of the PWM controlled model a little bit better. For the high amplifier gain, the discrete model behaves qualitatively different compared to the other models since the step response is oscillating. In the PWM controlled model, the saturation effect is preventing this oscillation, while the continuous model does not show this behavior at all.

3.3.4. Design of the Underlying Current Controller

The problem that arises at this point is the choice of p_{ui} . For the average model, it seems as if it would be the best to set p_{ui} simply to infinity. But is this still true with the actual PWM controlled model? (It should be noted here that current measurement noise is not taken into consideration.) In figure 3.7, simulations are shown for different values of p_{ui} and a switching frequency of 40 kHz. As the control current a discrete sine wave is chosen with a small amplitude of 0.2 A. The frequency of the sine wave is 2094.4 rad/s which corresponds to the maximum rotational speed of the rotor and the sample time of the sine wave is 100 μs which is the same as the sample time of the position controller of the AMB/rotor system.

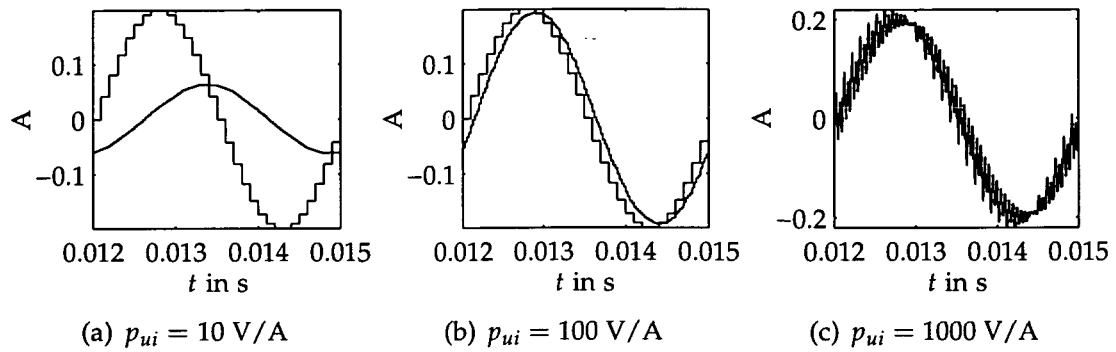


Figure 3.7.: Response of the PWM controlled actuator to a harmonic signal with amplitude 0.2 A and frequency of 2094.4 rad/s

In figure 3.7a, the amplifier gain is too small and the current cannot follow the control current, but the amplifier gain is high enough to follow the control current in 3.7b. In 3.7c, the very high amplifier gain only marginally increases performance, but also increases the so-called current ripple in the actual current. Such a high amplifier gain is more or less a bang-bang control scheme and the main advantage of the PWM-scheme, the low current ripple, is totally lost.

The simulations shown in figure 3.8 are carried out with the same parameters as before, only the amplitude of the control current is set to the maximum value of 4 A. Figure 3.8a is almost the same as 3.7a. For higher amplifier gains, the results are different. The amplifier reaches its maximum voltage and therefore also the maximum current slew rate. A further increase of p_{ui} neither improves the performance nor increases the current ripple.

For the choice of the amplifier gain, the following problem arises. If the

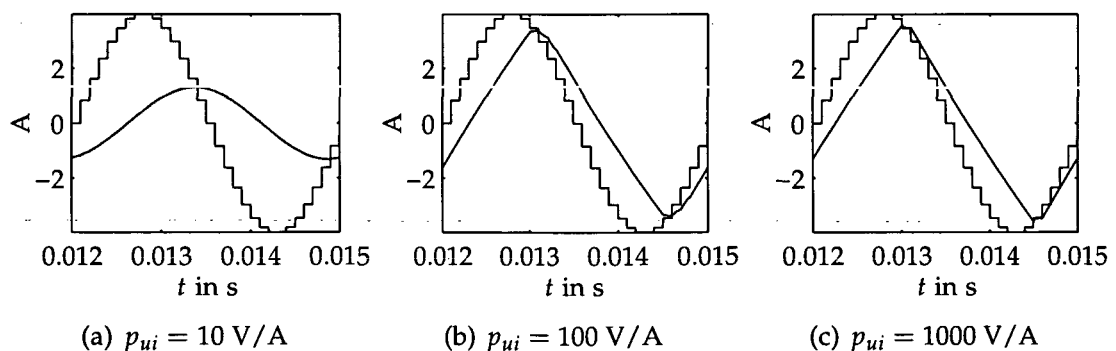


Figure 3.8.: Response of the PWM controlled actuator to a harmonic signal with amplitude 4 A and frequency of 2094.4 rad/s

amplifier gain is chosen so that no saturation is occurring at the maximum current amplitude, the performance for low amplitudes may be bad. Since a higher amplifier gain never decreases performance the choice for the amplifier gain should be as high as needed, but not higher, so that the resulting current ripples are as low as possible.

As there is no exact design process for choosing the gain p_{ui} , it is more or less a trial and error procedure. The starting point for the actual value used in the simulations is to allow a maximum deviation ζ of $\left| \frac{\hat{i}_x(j\Omega)}{i_x(j\Omega)} \right|$ to the static value $k_{ix} \frac{p_{ui}}{R+p_{ui}}$ at the maximum rotational frequency Ω . The maximum deviation is (at center position $x = y = 0$)

$$\zeta := \frac{\left| \frac{\hat{i}_x(j\Omega)}{i_x(j\Omega)} \right|}{k_{ix} \frac{p_{ui}}{R+p_{ui}}} = \frac{1}{\sqrt{\left(\Omega \frac{L_0}{R+p_{ui}} \right)^2 + 1}} .$$

Solving this equation for p_{ui} gives

$$p_{ui} = \frac{\Omega L_0}{\sqrt{\frac{1}{\zeta^2} - 1}} - R .$$

For $\Omega = 2094 \text{ rad/s} \hat{=} 20000 \text{ r/min}$ and $\zeta = 0.95$, the value $p_{ui} = 89.6 \text{ V/A}$ is obtained. The actual chosen value of the underlying current control gain is set to

$$p_{ui} = 100 \text{ V/A} ,$$

which results in a magnetic bearing time constant of

$$T_{MB} = 140.7 \text{ } \mu\text{s} .$$

Current measurement noise is not included in the previous considerations. A higher amplifier gain also increases the resulting noise level in the coil current, so basically the same conclusion, namely to choose the gain as high as needed but not higher, also arises from noise considerations. Contrary to many other control problems a high noise and oscillation level in the control variable (the PWM signal) does not damage the control element (the switching amplifier), since the switching frequency is fixed.

Maximum Pulse Width

Finally, a few words have to be said about the maximum pulse width. There are two reasons to restrict the duty ratio to a value lower than one and thereby the maximum pulse width to a value lower than T_{sw} :

- The specific dc-to-dc converter design needs a minimum time with a defined voltage output. This is the case e.g. in the bootstrap design where the high side switches have to be in open state for a minimum amount of time to charge the capacitors of the bootstrap circuits of the gate drivers.
- All measurements in the system are synchronized with the switching frequency of the amplifier, and these are carried out during the period where the amplifier output is zero. In this way the disturbance caused by high magnetic field changes is minimized (See also [Sch95]).

A maximum pulse width lower than one can be described with the average model simply by multiplying the maximum voltage with the maximum pulse width.

4. The Linearized Rigid Rotor Model

4.1. Introduction

Without any linearization, the equations of motion of a rigid rotor are difficult to derive in an exact manner from Euler's equations for a gyroscope. So, in almost every book on rotor dynamics, the position tilting angles of the rotor are assumed to be small a priori, and all trigonometric functions of these angles are linearized. With the assumption of small tilting angles of the rotor axis, the derivation of the linearized equations of motion is rather easy and several approaches are used. For example, Schweitzer et al. [STB93] use Lagrange's equations and Gasch et al. [GNP02] insert a linearized relationship between the rotor angles and the angular momentum into the Euler's equations. In both books, the additional assumption is used that the rotational speed is constant.

Genta [Gen93] derives the equations of motion including static and dynamic mass unbalance applying Lagrange's equations. In his derivations, the rotational speed is not assumed to be constant and the resulting equations are the same as from other authors for the case without dynamic unbalance. Genta also uses the small displacement assumption from the beginning, but claims that a fully nonlinear derivation of the equations of motion and subsequent linearization will lead to the same result.

Beside the unbalance excitation, nonconservative cross-coupling excitation is considered in this thesis. This cross-coupling excitation is seen as a general concept, valid for various types of destabilizing processes, especially fluid to structure interactions as, for example, fluid film bearings, annular seals, steam to blade interaction, and furthermore, partially filled centrifuges, or internal damping sources in the shaft. In the rotor-dynamic literature (e.g. [GNP02, Chi93]), cross-coupling excitations are described in a linearized way by calculating the cross-coupling force as a product of the rotor displacement vector

with a skew-symmetric stiffness matrix. The coefficients of the cross-coupling stiffness matrix in general depend on the rotational speed and other operational parameters of rotating machinery.

The derivations, assumptions and resulting equations in this chapter are very similar to those in [Lan97]. As the results are very important for the following calculations, the derivation is repeated here. In addition, the results including the magnetic bearing characteristics and a reduction to a 2DoF model are presented.

4.2. Equations of Motion in Center Coordinates

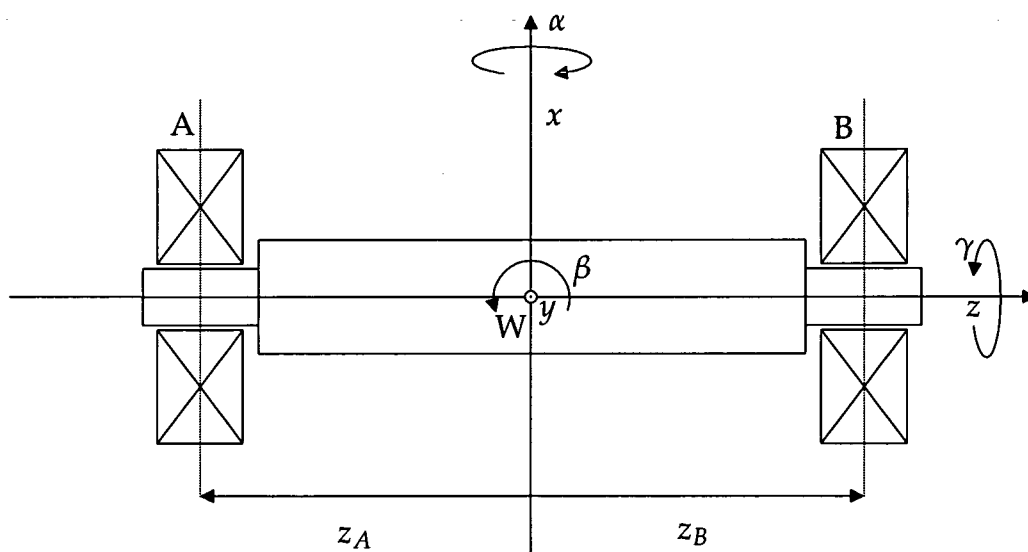


Figure 4.1.: The rigid rotor model

For the derivation of the linearized rigid rotor model, we use the following assumptions:

- The rotational axis is parallel to the axis of inertia (no dynamic unbalance). The rotation of the body around this axis can be described with the angle $\gamma(t)$ where $\gamma(0) = 0$ and $\frac{d}{dt}\gamma(t) = \Omega(t)$. (The assumption that Ω is constant is not necessary.)
- The location of the rotational axis is described by the position of one point on the rotational axis and the angle α about which we have to

rotate the z -axis around the x -axis and the angle β about which we have to rotate this axis around the y -axis to get the axis of rotation. (For a detailed description of these so-called cardan angles see e.g. [Sch86].)

- The angles α and β are considered small ($|\alpha| \ll 1$ and $|\beta| \ll 1$), so that the angle between the projection of the rotational axis on the x, z -plane and the x -axis is approximately β , and the angle between the projection of the rotational axes on the y, z -plane and the z -axis is approximately α .
- There is no displacement considered of the rigid rotor in z -direction.
- The coordinates x_c, y_c and $z_c = 0$ describe the point W on the rotational axis which is closest to the center of gravity CG . The distance between W and CG is the eccentricity e .
- $\gamma(t)$ is the given angle of rotation and is not influenced by α, β, x_c , and y_c .

With these assumptions, the linearized equations of motion for the rigid rotor shown in figure 4.1 can be written in the following form

$$\mathbf{M}_c \ddot{\mathbf{x}}_c + \mathbf{G}_c \dot{\mathbf{x}}_c = \mathbf{f}_u + \mathbf{f}_c.$$

The center coordinate vector \mathbf{x}_c is defined as

$$\mathbf{x}_c := [\alpha \quad \beta \quad x_c \quad y_c]^T,$$

the mass matrix \mathbf{M}_c , and the skew-symmetric gyroscopic matrix \mathbf{G}_c for center coordinates are defined as

$$\mathbf{M}_c := \begin{bmatrix} J_l & 0 & 0 & 0 \\ 0 & J_l & 0 & 0 \\ 0 & 0 & m & 0 \\ 0 & 0 & 0 & m \end{bmatrix} \quad \mathbf{G}_c := \Omega \begin{bmatrix} 0 & J_p & 0 & 0 \\ -J_p & 0 & 0 & 0 \\ 0 & 0 & 0 & 0 \\ 0 & 0 & 0 & 0 \end{bmatrix},$$

the pseudo-external force due to static mass unbalance \mathbf{f}_u

$$\mathbf{f}_u := me \begin{bmatrix} 0 \\ 0 \\ \Omega^2 \cos \gamma + \dot{\Omega} \sin \gamma \\ \Omega^2 \sin \gamma - \dot{\Omega} \cos \gamma \end{bmatrix},$$

and the sum of external forces and moments \mathbf{f}_c acting on the rotor with respect to W

$$\mathbf{f}_c := [m_x \quad m_y \quad f_{x_c} \quad f_{y_c}]^T.$$

4.3. Transformations of Displacements and Forces

With the center coordinate vector, the position of any point P along the axis of rotation with a z-coordinate z_P is given. Using the assumptions of small α and β , the x_P and y_P coordinates are determined by

$$\begin{bmatrix} x_P \\ y_P \end{bmatrix} = \begin{bmatrix} 0 & z_P & 1 & 0 \\ -z_P & 0 & 0 & 1 \end{bmatrix} \begin{bmatrix} \alpha \\ \beta \\ x_c \\ y_c \end{bmatrix}. \quad (4.1)$$

A force vector $[f_{Px} \ f_{Py}]^T$ acting on the rotor at a point P with a z-coordinate z_P can be transformed into the equivalent force system with respect to point W by

$$\begin{bmatrix} m_x \\ m_y \\ f_{x_c} \\ f_{y_c} \end{bmatrix} = \begin{bmatrix} 0 & -z_P \\ z_P & 0 \\ 1 & 0 \\ 0 & 1 \end{bmatrix} \begin{bmatrix} f_{Px} \\ f_{Py} \end{bmatrix}. \quad (4.2)$$

Using equations (4.1) and (4.2), the transformation matrices from center to bearing coordinates can be defined. The bearing coordinate vector is defined as the rotor displacements at the two bearing stations, that is

$$\mathbf{x}_b := [x_A \ y_A \ x_B \ y_B]^T.$$

Expanding (4.1), the transformation from center to bearing coordinates is given by

$$\mathbf{x}_b = \mathbf{T}_{bc} \mathbf{x}_c \quad (4.3)$$

where

$$\mathbf{T}_{bc} := \begin{bmatrix} 0 & z_A & 1 & 0 \\ -z_A & 0 & 0 & 1 \\ 0 & z_B & 1 & 0 \\ -z_B & 0 & 0 & 1 \end{bmatrix}.$$

The forces acting at the bearing stations are combined to the vector

$$\mathbf{f}_b := [f_{Ax} \ f_{Ay} \ f_{Bx} \ f_{By}]^T$$

and can be transformed to forces and moments with respect to point W by equation (4.2), that is

$$\mathbf{f}_c = \mathbf{T}_{bc}^T \mathbf{f}_b$$

where

$$\mathbf{T}_{bc}^T = \begin{bmatrix} 0 & -z_A & 0 & -z_B \\ z_A & 0 & z_B & 0 \\ 1 & 0 & 1 & 0 \\ 0 & 1 & 0 & 1 \end{bmatrix}.$$

With the inverse of the transformation matrix \mathbf{T}_{bc}

$$\mathbf{T}_{bc}^{-1} = \mathbf{T}_{cb} = \frac{1}{z_A - z_B} \begin{bmatrix} 0 & -1 & 0 & 1 \\ 1 & 0 & -1 & 0 \\ -z_B & 0 & z_A & 0 \\ 0 & -z_B & 0 & z_A \end{bmatrix}$$

and the transposed matrix \mathbf{T}_{bc}^{-T} of the inverse, the equations of motion can be transformed to bearing coordinates in the form

$$\begin{aligned} \mathbf{T}_{bc}^{-T} \mathbf{M}_c \mathbf{T}_{bc}^{-1} \ddot{\mathbf{x}}_b + \mathbf{T}_{bc}^{-T} \mathbf{G}_c \mathbf{T}_{bc}^{-1} \dot{\mathbf{x}}_b &= \mathbf{f}_b + \mathbf{T}_{bc}^{-T} \mathbf{f}_u \\ \mathbf{M}_b \ddot{\mathbf{x}}_b + \mathbf{G}_b \dot{\mathbf{x}}_b &= \mathbf{f}_b + \mathbf{f}_{ub} \end{aligned}$$

where the resulting mass matrix in bearing coordinates is

$$\mathbf{M}_b = \frac{1}{(z_A - z_B)^2} \begin{bmatrix} J_l + mz_B^2 & 0 & -J_l - mz_A z_B & 0 \\ 0 & J_l + mz_B^2 & 0 & -J_l - mz_A z_B \\ -J_l - mz_A z_B & 0 & J_l + mz_A^2 & 0 \\ 0 & -J_l - mz_A z_B & 0 & J_l + mz_A^2 \end{bmatrix}, \quad (4.4)$$

the resulting gyroscopic matrix in bearing coordinates is

$$\mathbf{G}_b = \frac{1}{(z_A - z_B)^2} \begin{bmatrix} 0 & \Omega J_p & 0 & -\Omega J_p \\ -\Omega J_p & 0 & \Omega J_p & 0 \\ 0 & -\Omega J_p & 0 & \Omega J_p \\ \Omega J_p & 0 & -\Omega J_p & 0 \end{bmatrix},$$

and the vector of unbalance forces transformed to bearing coordinates is given by

$$\mathbf{f}_{ub} = \frac{me}{z_A - z_B} \begin{bmatrix} -z_B (\dot{\Omega} \sin \gamma + \Omega^2 \cos \gamma) \\ -z_B (-\dot{\Omega} \cos \gamma + \Omega^2 \sin \gamma) \\ z_A (\dot{\Omega} \sin \gamma + \Omega^2 \cos \gamma) \\ z_A (-\dot{\Omega} \cos \gamma + \Omega^2 \sin \gamma) \end{bmatrix}.$$

4.4. Nonconservative Cross-Coupling Forces

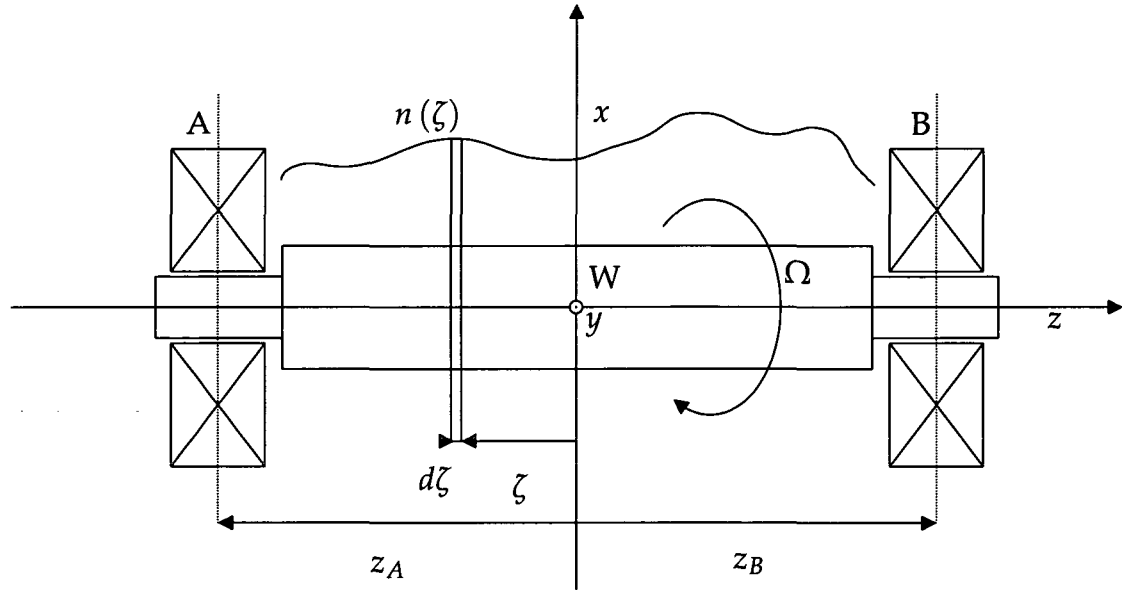


Figure 4.2.: Local nonconservative cross-coupling stiffness density distribution

It is assumed that an unknown distribution of nonconservative cross-coupling forces are acting perpendicular to the rotor axis. The cross-coupling force density $\frac{df_{n\zeta}}{d\zeta}$ at an arbitrary z -position ζ in local ζ -coordinates of the rotor is given by

$$\frac{df_{n\zeta}}{d\zeta} := - \begin{bmatrix} 0 & n(\zeta) \\ -n(\zeta) & 0 \end{bmatrix} \begin{bmatrix} x_\zeta \\ y_\zeta \end{bmatrix}.$$

The parameter $n(\zeta)$ is the local nonconservative cross-coupling coefficient or stiffness density and is depicted in figure 4.2. A positive coefficient $n(\zeta)$ induces a forward whirl and a negative coefficient a backward whirl of the rotor axis (for $\Omega > 0$).

With equation (4.1) and equation (4.2), the cross-coupling force density can

be transformed to center coordinates

$$\begin{aligned} \frac{d\mathbf{f}_{nc}}{d\zeta} &= \begin{bmatrix} 0 & -\zeta \\ \zeta & 0 \\ 1 & 0 \\ 0 & 1 \end{bmatrix} \begin{bmatrix} 0 & n(\zeta) \\ -n(\zeta) & 0 \end{bmatrix} \begin{bmatrix} 0 & \zeta & 1 & 0 \\ -\zeta & 0 & 0 & 1 \end{bmatrix} \mathbf{x}_c \\ &= n(\zeta) \begin{bmatrix} 0 & \zeta^2 & \zeta & 0 \\ -\zeta^2 & 0 & 0 & \zeta \\ -\zeta & 0 & 0 & 1 \\ 0 & -\zeta & -1 & 0 \end{bmatrix} \mathbf{x}_c. \end{aligned}$$

Transforming this into bearing coordinates yields

$$\frac{d\mathbf{f}_{nb}}{d\zeta} = -n(\zeta) \begin{bmatrix} 0 & v^2 & 0 & -uv \\ -v^2 & 0 & uv & 0 \\ 0 & -uv & 0 & u^2 \\ uv & 0 & -u^2 & 0 \end{bmatrix} \mathbf{x}_b$$

where

$$u := \frac{(\zeta - z_A)}{(z_A - z_B)} \quad \text{and} \quad v := \frac{(\zeta - z_B)}{(z_A - z_B)}.$$

By integrating the stiffness density matrix along the z -direction of the rotor, one gets a skew-symmetric cross-coupling stiffness matrix \mathbf{N}_b in bearing coordinates with three independent parameters n_1, n_2, n_3 in the form

$$\mathbf{f}_{nb} = -\mathbf{N}_b \mathbf{x}_b = - \begin{bmatrix} 0 & n_1 & 0 & n_2 \\ -n_1 & 0 & -n_2 & 0 \\ 0 & n_2 & 0 & n_3 \\ -n_2 & 0 & -n_3 & 0 \end{bmatrix} \begin{bmatrix} x_A \\ y_A \\ x_B \\ y_B \end{bmatrix}. \quad (4.5)$$

For a single discrete cross-coupling force at a point P with z -coordinate z_P and the local cross-coupling stiffness n , the cross-coupling force density is

$$n(\zeta) = n \delta(\zeta - z_P)$$

with the continuous dirac impulse function δ . The resulting cross-coupling matrix is then

$$\mathbf{N}_b = n \begin{bmatrix} 0 & v^2 & 0 & -uv \\ -v^2 & 0 & uv & 0 \\ 0 & -uv & 0 & u^2 \\ uv & 0 & -u^2 & 0 \end{bmatrix}$$

where

$$u := \frac{z_P - z_A}{z_A - z_B} \quad \text{and} \quad v := \frac{z_P - z_B}{z_A - z_B} .$$

4.5. Preloading the Magnetic Bearings

The magnetic bearing force in terms of control current and rotor position is given by equation (3.7) in the Laplace domain for a single AMB. This equation is extended for two magnetic bearings to

$$\hat{\mathbf{f}}(s) = \mathbf{K}_{f/i}(s) \hat{\mathbf{i}}_x(s) + \mathbf{K}_{f/x}(s) \hat{\mathbf{x}}_b(s) \quad (4.6)$$

where \mathbf{i}_x is the control current vector for both bearings

$$\mathbf{i}_x := [i_{Ax} \ i_{Ay} \ i_{Bx} \ i_{By}]^T ,$$

$\mathbf{K}_{f/i}$ is the dynamic current coefficient matrix, given by

$$\mathbf{K}_{f/i}(s) := \frac{1}{sT_{MB} + 1} \frac{p_{ui}}{R + p_{ui}} \begin{bmatrix} k_{iAx} & & & \\ & k_{iAy} & & \\ & & k_{iBx} & \\ & & & k_{iBy} \end{bmatrix} ,$$

and $\mathbf{K}_{f/x}$ is the dynamic position coefficient matrix or dynamic magnetic bearing stiffness matrix, given by

$$\mathbf{K}_{f/x}(s) := \frac{1}{sT_{MB} + 1} \begin{bmatrix} k_{sAx} & & & \\ & k_{sAy} & & \\ & & k_{sBx} & \\ & & & k_{sBy} \end{bmatrix} ,$$

with the time constant T_{MB} being equal for both bearings and axes.

In the common magnetic bearing literature, the magnetic bearing time constant T_{MB} is assumed to be zero. This is equivalent to the use of $\mathbf{K}_{f/i}(0)$ and $\mathbf{K}_{f/x}(0)$. Since we will also use this assumption sometimes, we will write for the static current and position coefficient matrix

$$\mathbf{K}_i := \mathbf{K}_{f/i}(0) \quad \mathbf{K}_s := \mathbf{K}_{f/x}(0) .$$

The use of \mathbf{K}_i and \mathbf{K}_s is consistent with the AMB literature and is slightly easier to read.

The numerical values for the geometric and electrical parameters of the magnetic bearings are given in chapter 2. The only unknown parameters are the bias currents. Since for a horizontal machine the magnetic bearing rotor system is preloaded with the static rotor weight, the bias currents must be able to carry this weight. Usually the bias current is simply set to half of the maximum allowed current (which is usually the current where magnetic saturation occurs) and the force to lift the weight is provided by the controller [STB93]. This is not really correct, since the weight shifts the working point away from the zero force point. Since the weight force for each bearing is about 17% of the maximum force the bearing can supply, neglecting this working point shift will result in a significant deviation of the actual position coefficients from the calculated ones (see [SW]).

First the calculation of the bias currents and AMB coefficients are carried out for one bearing. The bias currents for the two actuators in y -direction (actuator 2 and 4 in figure 3.1) are chosen to be $-i_0$. To generate a force in x -direction without changing the current coefficient, the bias current in actuator 1 should be $i_{1,0} = i_0 + i_{0f}$ and in actuator 3 should be $i_{3,0} = i_0 - i_{0f}$. The static force in x -direction f_x is then

$$f_{x,0} = 4i_{0f} i_0 \frac{N_w^2 \cos \alpha_p}{\mathcal{R}_0^2 \mu_0 A_g}$$

and so i_{0f} becomes

$$i_{0f} = f_{x,0} \frac{\mathcal{R}_0^2 \mu_0 A_g}{4i_0 N_w^2 \cos \alpha_p}.$$

The bias currents for one magnetic bearing are chosen to be

$$\mathbf{i}_0 = [i_0 + i_{0f} \quad -i_0 \quad i_0 - i_{0f} \quad -i_0]^T. \quad (4.7)$$

The negative sign of the bias currents $i_{2,0}$ and $i_{4,0}$ indicate that an NNSS pole scheme¹ is used in the magnetic bearing; this does not change the behavior of the simple actuator model but influences the behavior of higher sophisticated models. With this choice for the bearing bias currents, we get for the current coefficients

$$k_{ix} = 4 \frac{i_0 N_w^2 \cos \alpha_p}{\mathcal{R}_0^2 \mu_0 A_g} \quad k_{iy} = -4 \frac{i_0 N_w^2 \cos \alpha_p}{\mathcal{R}_0^2 \mu_0 A_g}$$

¹ There are two possible pole configurations, the classical NNSS scheme where two north poles are followed by two south poles, and the NSNS scheme where a north pole is always followed by a south pole.

and for the position coefficients

$$k_{sx} = 8 \frac{(i_0^2 + i_{0f}^2) N_w^2 \cos^2 \alpha_p}{\mathcal{R}_0^3 \mu_0^2 A_g^2} \quad k_{sy} = 8 \frac{i_0^2 N_w^2 \cos^2 \alpha_p}{\mathcal{R}_0^3 \mu_0^2 A_g^2} .$$

The shift of the working point only changes the position coefficient of the bearing; the current coefficients are unchanged, because the static current to force relationship is linear at the center position.

The weight force carried by each bearing can be found by transforming the weight to bearing coordinates

$$\begin{aligned} \mathbf{f}_{gb} &= \mathbf{T}_{bc}^{-T} \mathbf{f}_{gc} = \mathbf{T}_{bc}^{-T} [0 \quad 0 \quad -mg \quad 0]^T \\ &= [f_{gAx} \quad f_{gAy} \quad f_{gBx} \quad f_{gBy}]^T = [-141.7 \text{ N} \quad 0 \quad -140.5 \text{ N} \quad 0]^T . \end{aligned}$$

To lift the weight, the static forces of both magnetic bearings have to be

$$f_{Ax,0} = -f_{gAx} \quad \text{and} \quad f_{Bx,0} = -f_{gBx} . \quad (4.8)$$

Therefore, using the numerical values of the simulation model, the current and the stiffness coefficient matrix respectively are

$$\begin{aligned} \mathbf{K}_i &= \begin{bmatrix} 199.07 & & & \\ & -199.07 & & \\ & & 199.07 & \\ & & & -199.07 \end{bmatrix} \text{ N/A} \\ \mathbf{K}_s &= \begin{bmatrix} 1.4665 & & & \\ & 1.4222 & & \\ & & 1.4657 & \\ & & & 1.4222 \end{bmatrix} \text{ MN/m} . \end{aligned}$$

4.6. Rotor Magnetic Bearing Assembly

The equations of motion of the rigid rotor in bearing coordinates including nonconservative cross-coupling stiffness have now the form

$$\mathbf{M}_b \ddot{\mathbf{x}}_b + \mathbf{G}_b \dot{\mathbf{x}}_b + \mathbf{N}_b \mathbf{x}_b = \mathbf{f}_b + \mathbf{f}_{ub} .$$

With the rotor being supported by active magnetic bearings, the weight of the rotor is lifted by the static nonlinear magnetic bearing forces (see equ. (4.8)), so it is not included in the force vector \mathbf{f}_b . The remaining forces \mathbf{f}_b acting on the rotor in bearing coordinates are

$$\mathbf{f}_b = \mathbf{f}_{MB} + \mathbf{f}_{db} ,$$

where \mathbf{f}_{MB} is the linearized deviation of the magnetic bearing forces from the static values $\mathbf{f}_{MB,0}$ and \mathbf{f}_{db} are additional disturbance forces acting on the rotor.

The forces of both magnetic bearings are combined in one vector named \mathbf{f}_{MB} . These forces can be described by the corresponding Laplace transfer matrix equation (4.6) or by the differential equations of the magnetic bearings

$$\frac{d}{dt}\mathbf{f}_{MB} = \frac{1}{T_{MB}} (-\mathbf{f}_{MB} + \mathbf{K}_i \mathbf{i}_x + \mathbf{K}_s \mathbf{x}_b) .$$

In this equation, the bearing forces instead of the bearing fluxes are used as state space variables; this reduces the number of state variables by a factor two.

Since the rotor position has to be measured, we also need a relationship between the state vector \mathbf{x}_b and the sensor signals (the position of the axis of rotation at the sensor locations z_{mA} and z_{mB}). The sensor signal is

$$\mathbf{x}_m = \mathbf{T}_{mb}\mathbf{x}_b$$

with

$$\mathbf{T}_{mb} = \mathbf{T}_{mc}\mathbf{T}_{cb} = \mathbf{T}_{bm}^{-1} = \frac{1}{z_A - z_B} \begin{bmatrix} z_{mA} - z_B & 0 & z_A - z_{mA} & 0 \\ 0 & z_{mA} - z_B & 0 & z_A - z_{mA} \\ z_{mB} - z_B & 0 & z_A - z_{mB} & 0 \\ 0 & z_{mB} - z_B & 0 & z_A - z_{mB} \end{bmatrix} .$$

For collocations of sensors and bearings, the transformation matrix \mathbf{T}_{mb} is equal to the identity matrix

$$\mathbf{T}_{mb} = \mathbf{I} \quad \text{for} \quad z_{mA} = z_A, \quad z_{mB} = z_B .$$

When \mathbf{x}_b is calculated from the sensor signals

$$\mathbf{x}_b = \mathbf{T}_{bm}\mathbf{x}_m$$

with

$$\mathbf{T}_{bm} = \mathbf{T}_{bc}\mathbf{T}_{cm} = \frac{1}{z_{mA} - z_{mB}} \begin{bmatrix} z_A - z_{mB} & 0 & z_{mA} - z_A & 0 \\ 0 & z_A - z_{mB} & 0 & z_{mA} - z_A \\ z_B - z_{mB} & 0 & z_{mA} - z_B & 0 \\ 0 & z_B - z_{mB} & 0 & z_{mA} - z_B \end{bmatrix}$$

we assume that this calculation is exact and that we "measure" \mathbf{x}_b directly. Other possible approaches might be to write the system in sensor coordinates instead of bearing coordinates or to include an output equation in the rotor AMB system. Both alternative approaches, however, make the handling of the equations more difficult and do not have significant advantages.

The equations of motion for the rotor supported by active magnetic bearings can either be written as a system of first order differential equations in the form

$$\frac{d}{dt} \begin{bmatrix} \mathbf{f}_{MB} \\ \dot{\mathbf{x}}_b \\ \mathbf{x}_b \end{bmatrix} = \begin{bmatrix} -\frac{1}{T_{MB}} \mathbf{I} & 0 & -\frac{1}{T_{MB}} \mathbf{K}_s \\ -\mathbf{M}_b^{-1} & -\mathbf{M}_b^{-1} \mathbf{G}_b & -\mathbf{M}_b^{-1} \mathbf{N}_b \\ 0 & \mathbf{I} & 0 \end{bmatrix} \begin{bmatrix} \mathbf{f}_{MB} \\ \dot{\mathbf{x}}_b \\ \mathbf{x}_b \end{bmatrix} + \begin{bmatrix} \frac{1}{T_{MB}} \mathbf{K}_i & 0 \\ 0 & \mathbf{M}_b^{-1} \\ 0 & 0 \end{bmatrix} \begin{bmatrix} \mathbf{i}_x \\ \mathbf{f}_{ub} + \mathbf{f}_{db} \end{bmatrix} \quad (4.9)$$

or with the corresponding Laplace transfer matrices

$$\hat{\mathbf{x}}_b(s) = \mathbf{G}_{x/f}(s) (\hat{\mathbf{f}}_{ub}(s) + \hat{\mathbf{f}}_{db}(s)) + \mathbf{G}_{x/i}(s) \hat{\mathbf{i}}_x(s)$$

where

$$\begin{aligned} \mathbf{G}_{x/f}(s) &:= \left(s^2 \mathbf{M}_b + s \mathbf{G}_b + \mathbf{N}_b - \mathbf{K}_{f/x}(s) \right)^{-1} \\ \mathbf{G}_{x/i}(s) &:= \mathbf{G}_{x/f}(s) \mathbf{K}_{f/i}(s) . \end{aligned}$$

To avoid confusion, this model is referred to as "complex model".

For large $1/T_{MB}$ in relation to the excitation frequencies and the other eigenvalues of the system, the differential equations of the magnetic bearing can be neglected and one gets the well known system of second order differential equations

$$\mathbf{M}_b \ddot{\mathbf{x}}_b + \mathbf{G}_b \dot{\mathbf{x}}_b + (\mathbf{N}_b - \mathbf{K}_s) \mathbf{x}_b = \mathbf{K}_i \mathbf{i}_x + \mathbf{f}_{db} + \mathbf{f}_{ub} \quad (4.10)$$

or

$$\hat{\mathbf{x}}_b(s) = \left(s^2 \mathbf{M}_b + s \mathbf{G}_b + \mathbf{N}_b - \mathbf{K}_s \right)^{-1} \left(\hat{\mathbf{f}}_{ub}(s) + \hat{\mathbf{f}}_{db}(s) + \mathbf{K}_i \hat{\mathbf{i}}_x(s) \right) .$$

This model is referred to as "simple model".

4.6.1. Eigenvalues of the Simple Model

For the simple model equation (4.10), the poles λ_i of the system for $\mathbf{N}_b = 0$ and $\mathbf{G}_b = 0$ are the square roots of the generalized eigenvalues of \mathbf{M} and \mathbf{K} or the solutions of

$$\det \left(\mathbf{K}_s + \lambda_i^2 \mathbf{M}_b \right) = 0 .$$

Assuming that the center of gravity is located at the mid-span position between the two bearings i.e. $z_A = -z_B$ and that the stiffness coefficients of both bearings are equal i.e. $k_{sAx} = k_{sBx} = k_{sx}$, $k_{sAy} = k_{sBy} = k_{sy}$, the poles of the system are

$$\begin{aligned}\lambda_{1,2} &= \pm \sqrt{\frac{2k_{sx}}{m}} = \pm 319.257 \text{ s}^{-1} & \lambda_{3,4} &= \pm \sqrt{\frac{2k_{sy}}{m}} = \pm 314.444 \text{ s}^{-1} \\ \lambda_{5,6} &= \pm \sqrt{\frac{2k_{sx}z_A^2}{J_l}} = \pm 442.335 \text{ s}^{-1} & \lambda_{7,8} &= \pm \sqrt{\frac{2k_{sy}z_A^2}{J_l}} = \pm 435.666 \text{ s}^{-1}.\end{aligned}$$

The actual poles of equation (4.10)

$$\begin{aligned}\lambda_{1,2} &= \pm 319.252 \text{ s}^{-1} & \lambda_{3,4} &= \pm 314.438 \text{ s}^{-1} \\ \lambda_{5,6} &= \pm 442.342 \text{ s}^{-1} & \lambda_{7,8} &= \pm 435.674 \text{ s}^{-1}\end{aligned}$$

differ only very slightly from the symmetrical configuration. The occurrence of eigenvalues with positive real parts indicates that the system is not stable.

4.6.2. Eigenvalues of the Complex Model

For the poles of the complex model equation (4.9), we have to solve

$$\det \left(\begin{bmatrix} -\frac{1}{T_{MB}}\mathbf{I} & \mathbf{0} & \frac{1}{T_{MB}}\mathbf{K}_s \\ -\mathbf{M}_b^{-1} & -\mathbf{M}_b^{-1}\mathbf{G}_b & -\mathbf{M}_b^{-1}\mathbf{N}_b \\ \mathbf{0} & \mathbf{I} & \mathbf{0} \end{bmatrix} - \lambda_i \mathbf{I} \right) = 0$$

for λ_i . The values are given in table 4.1. The first eight poles are close to those of the simple model. There are four additional poles which correspond to the magnetic bearing characteristic and have the approximate value of $\lambda_{9...12} \approx -1/T_{MB}$.

Table 4.1.: The poles of the complex AMB/rotor model

Pole	value s ⁻¹	Pole	value s ⁻¹
λ_1	312.46	λ_2	-326.86
λ_3	307.84	λ_4	-321.81
λ_5	423.25	λ_6	-450.16
λ_7	429.55	λ_8	-457.30
λ_9	-7080.84	λ_{10}	-7080.01
λ_{11}	-7093.36	λ_{12}	-7093.79

4.7. Two Degrees of Freedom Model

It will be useful to have a simpler model with fewer degrees of freedom that behaves similar to equation (4.10). Under the assumption that $x_A = x_B = x_c$ and $y_A = y_B = y_c$, $\alpha = \beta = 0$ and $i_{Ax} = i_{Bx} = i_x$ and $i_{Ay} = i_{By} = i_y$, we can use the transformation

$$\mathbf{x}_b = \mathbf{R} \begin{bmatrix} x_c \\ y_c \end{bmatrix}$$

where

$$\mathbf{R} := \begin{bmatrix} 1 & 0 & 1 & 0 \\ 0 & 1 & 0 & 1 \end{bmatrix}^T,$$

to reduce the 4DoF model to a 2DoF Model. The transformation of the simple 4DoF system

$$\mathbf{R}^T \mathbf{M}_b \mathbf{R} \begin{bmatrix} \ddot{x}_c \\ \ddot{y}_c \end{bmatrix} + \mathbf{R}^T (\mathbf{N}_b - \mathbf{K}_s) \mathbf{R} \begin{bmatrix} x_c \\ y_c \end{bmatrix} = \mathbf{R}^T \mathbf{K}_i \mathbf{R} \begin{bmatrix} i_x \\ i_y \end{bmatrix} + \mathbf{R}^T \mathbf{f}_{ub} + \mathbf{R}^T \mathbf{f}_{db}$$

leads to

$$\begin{bmatrix} m & 0 \\ 0 & m \end{bmatrix} \begin{bmatrix} \ddot{x}_c \\ \ddot{y}_c \end{bmatrix} + \left(\begin{bmatrix} 0 & n \\ -n & 0 \end{bmatrix} - \begin{bmatrix} k_{sAx} + k_{sBx} & 0 \\ 0 & k_{sAy} + k_{sBy} \end{bmatrix} \right) \begin{bmatrix} x_c \\ y_c \end{bmatrix} = \frac{p_{ui}}{R + p_{ui}} \begin{bmatrix} k_{iAx} + k_{iBx} & 0 \\ 0 & k_{iAy} + k_{iBy} \end{bmatrix} \begin{bmatrix} i_x \\ i_y \end{bmatrix} + \begin{bmatrix} \Omega^2 \cos \gamma + \dot{\Omega} \sin \gamma \\ \Omega^2 \sin \gamma - \dot{\Omega} \cos \gamma \end{bmatrix} + \mathbf{R}^T \mathbf{f}_{db}. \quad (4.11)$$

There is no gyroscopic effect in the 2DoF system since $\mathbf{R}^T \mathbf{G}_b \mathbf{R} = \mathbf{0}$. The cross-coupling parameter n is calculated by

$$n := n_1 + 2n_2 + n_3$$

which is the same as the integration of the cross-coupling density along the rotor, i.e.

$$n = \int_{-\infty}^{\infty} n(\zeta) d\zeta.$$

Part II.

Control

5. Stabilizing Feedback Loop Control

5.1. Introduction

One of the most significant disadvantages of magnetic levitation and suspension is that these levitations are usually unstable. This fundamental fact has already been proved by S. Earnshaw in [Ear39], and is known as "Earnshaw's theorem". It states that no stationary object made of charges, magnets, and masses in a fixed configuration can be held in stable equilibrium by any combination of static electric, magnetic, or gravitational forces [GG97]. The only way around Earnshaw's theorem is to violate the assumptions on which the theorem is based. Using diamagnetism is one way to levitate objects [Bra39a, Bra39b], but has no technical relevance yet. For an interesting review of such experiments, the reader is asked to refer to [BG97]. Another famous approach is to use superconducting materials, but technical realizations are still very rare.

The most often used principle of magnetic levitation is to feed back the object position and change the magnetic field in a way to stabilize the levitation. One of the earliest publications describing magnetic bearings are carried out by Beams et al. In [BB39], the magnetic forces are only used to support a mechanical bearing, but in [BYM46] small solid steel spheres are fully suspended in a magnetic field; two degrees of freedom are passively stabilized, and an analog proportional-derivative (PD) controller is used together with an inductive position measurement to actively stabilize the third degree of freedom. The PD control scheme is also widely used for the suspension of rigid as well as flexible rotors in active magnetic bearings. Because of the similarity with mechanical spring-damper elements, the PD control is easy to understand. Usually an integral part is added to the PD scheme to achieve steady state accuracy (see [STB93]).

For a simple rigid rotor AMB model as shown in equation (4.10), the rotor

position and the rotor velocity are the states of the system. So, a PD controller can also be viewed as a state feedback controller where the velocity states are generated from differentiation of the position states. The differentiation has some important disadvantages which are mentioned later in this thesis; a different approach for the calculation of the velocity states is to use an observer. Ulbrich [Ulb79] employs the Ricatti equation to find an optimal state feedback (LQR, linear quadratic regulator) controller and uses it together with an optimal observer to control a rigid rotor. Bleuler [Ble84] starts from a similar controller structure combined with a Luenberger observer and develops an optimal decentral controller and a decentral observer to reduce the computational load for the rotor controller. There are numerous other publications in which optimal linear controllers like an LQR controller are coupled with optimal linear observers like a Kalman filter. This combination is usually called LQG (linear quadratic gaussian) controller. A good review of the available publications in 1991 is included in the PhD-thesis by Maslen [Mas91]. Other modern linear control approaches, which have drawn some attention recently, are H_∞ and μ -synthesis control (see for example [KB92, NI96, LGH98]).

5.2. Feedback Loop

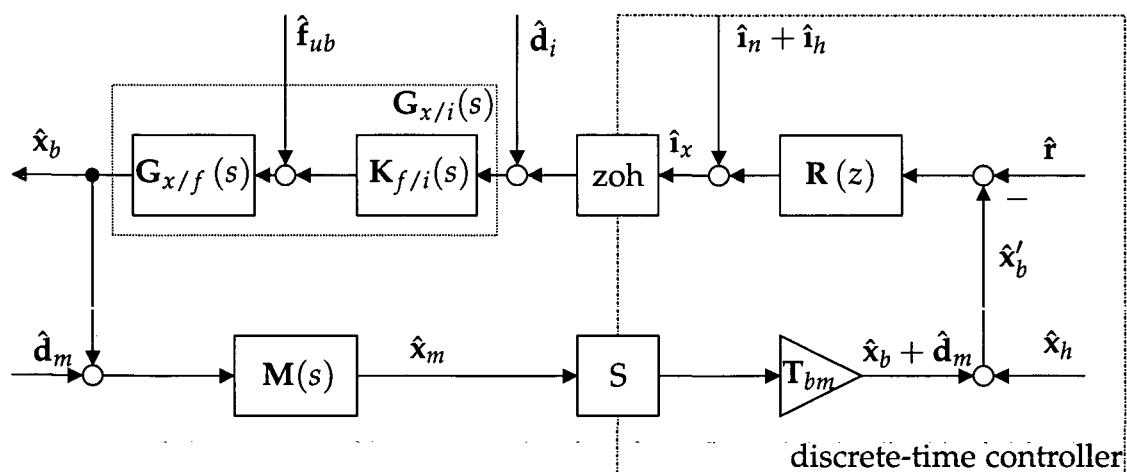


Figure 5.1.: The feedback control loop

Figure 5.1 illustrates the components of the discrete-time controller feedback loop. The loop is divided into a discrete-time part and a continuous-time part.

At the boundary, the translation from discrete-time to continuous-time is done by a zero order hold block (denoted by zoh) and a sample block S vice versa. The measured rotor position x_m in measurement coordinates is converted back to bearing coordinates with the transformation matrix T_{bm} ; it is assumed that this conversion as well as the measurement itself are perfect ($M(s) = T_{mb}$).

The system figure 5.1 is a mixed discrete-time and continuous-time system. As long as only the input-output relationships between discrete-time signals are investigated, the input-output relationship is described by z -transfer matrices. For the input-output of relationship from continuous-time to discrete-time signals, there is no *exact* transfer matrix relationship. However, if the continuous signals have only frequency components significantly smaller than the Nyquist frequency $f_{Ny} = 1/2T_s$, the use of the equivalent discrete-time signals with the corresponding z -transfer matrices is a good approximation. This means that from the relationship

$$\hat{y}(s) = \hat{G}(s) \hat{u}(s), \quad \text{with} \quad \hat{y}(s) = \mathcal{L}(y(t)) \quad \hat{u}(s) = \mathcal{L}(u(t)),$$

follows the approximation

$$\hat{y}(z) \cong \hat{G}(z) \hat{u}(z)$$

with

$$\hat{y}(z) = \mathcal{Z}(y(kT_s)) \quad \hat{u}(z) = \mathcal{Z}(u(kT_s)) \quad k = 0, 1, \dots, \infty.$$

So, basically the calculation of the input-output relationship is the same for the continuous and the discrete signals. This has the additional benefit that, if we assume a continuous-time system, we only have to exchange the z -transfer matrices with the corresponding Laplace transfer matrices.

When we neglect the dynamics of the measurement device $M(s)$, only one continuous-time transfer matrix is outside the discrete-time part of the control loop, namely the current to displacement transfer matrix $G_{x/i}(s)$. The corresponding z -transfer matrix can be calculated with

$$G_{x/i}(z) = \frac{z}{z-1} \mathcal{Z} \left\{ \mathcal{L}^{-1} \left\{ \frac{1}{s} G_{x/i}(s) \right\} \right\}.$$

It is worth to note that

$$G_{x/i}(s) = G_{x/f}(s) K_{f/i}(s), \quad \text{but} \quad G_{x/i}(z) \neq G_{x/f}(z) K_{f/i}(z).$$

The control law is given by

$$\hat{\mathbf{i}}_x(z) = \mathbf{R}(z) (\hat{\mathbf{r}}(z) - \hat{\mathbf{x}}_b(z)) + \hat{\mathbf{i}}_n(z) + \hat{\mathbf{i}}_h(z) \quad (5.1)$$

where $\hat{\mathbf{i}}_x(z)$ is the control current vector for both bearings, $\mathbf{R}(z)$ is the controller transfer matrix, $\hat{\mathbf{r}}(z)$ is the reference value vector, $\hat{\mathbf{x}}_b(z)$ is the measured rotor position vector, $\hat{\mathbf{i}}_n(z)$ is the additional control current vector for cross-coupling control, and $\hat{\mathbf{i}}_h(z)$ is the additional control current vector for harmonic control. For further discussion (see [ZDG96]), it is convenient to define the input open-loop transfer matrix, \mathbf{L}_i , and the output open-loop transfer matrix, \mathbf{L}_o (the function argument z is omitted), as,

$$\mathbf{L}_i := \mathbf{R}\mathbf{G}_{x/i}, \quad \mathbf{L}_o := \mathbf{G}_{x/i}\mathbf{R},$$

respectively. The input sensitivity matrix $\mathbf{S}_i(z)$ and the output sensitivity matrix are defined as

$$\mathbf{S}_i(z) := (\mathbf{I} + \mathbf{L}_i(z))^{-1}, \quad \mathbf{S}_o(z) := (\mathbf{I} + \mathbf{L}_o(z))^{-1}.$$

The input and output complementary sensitivity matrices are defined as

$$\begin{aligned} \mathbf{T}_i &:= \mathbf{I} - \mathbf{S}_i = \mathbf{L}_i(\mathbf{I} + \mathbf{L}_i)^{-1} \\ \mathbf{T}_o &:= \mathbf{I} - \mathbf{S}_o = \mathbf{L}_o(\mathbf{I} + \mathbf{L}_o)^{-1}. \end{aligned}$$

The input-output relationship of the signals in system shown in figure 5.1 is described by

$$\begin{bmatrix} \hat{\mathbf{x}}_b \\ \hat{\mathbf{x}}'_b \\ \hat{\mathbf{i}}_x \end{bmatrix} = \begin{bmatrix} \mathbf{T}_o & -\mathbf{T}_o & \mathbf{S}_o\mathbf{G}_{x/i} & \mathbf{S}_o\mathbf{G}_{x/i} & \mathbf{S}_o\mathbf{G}_{x/f} \\ \mathbf{T}_o & \mathbf{S}_o & \mathbf{S}_o\mathbf{G}_{x/i} & \mathbf{S}_o\mathbf{G}_{x/i} & \mathbf{S}_o\mathbf{G}_{x/f} \\ \mathbf{R}\mathbf{S}_o & -\mathbf{R}\mathbf{S}_o & \mathbf{S}_i & -\mathbf{T}_i & -\mathbf{R}\mathbf{S}_o\mathbf{G}_{x/f} \end{bmatrix} \begin{bmatrix} \hat{\mathbf{r}} \\ \hat{\mathbf{x}}_h + \hat{\mathbf{d}}_m \\ \hat{\mathbf{i}}_n + \hat{\mathbf{i}}_h \\ \hat{\mathbf{d}}_i \\ \hat{\mathbf{f}}_{ub} \end{bmatrix}. \quad (5.2)$$

For the continuous-time inputs $\hat{\mathbf{d}}_i$, $\hat{\mathbf{d}}_m$, and $\hat{\mathbf{f}}_{ub}$, equation (5.2) is just an approximation. Additionally the approximation that

$$\mathbf{G}_{x/i}(z) \cong \mathbf{G}_{x/f}(z) \mathbf{K}_{f/i}(z)$$

is used in equation (5.2) for the transfer matrices with input signal $\hat{\mathbf{f}}_{ub}$.

Although equation (5.2) is written with transfer matrices the actual calculations of the input-output behavior is done with state space equations. Another

issue in the calculation of the transfer matrices is the numerical imperfect zero pole cancellations. For example, the numerical calculation of T_o with

$$T_o = G_{x/i} R (I + G_{x/i} R)^{-1}$$

would deliver an unstable system, since $G_{x/i}$ is unstable, while a numerical calculation with

$$T_o = (R^{-1} G_{x/i}^{-1} + I)^{-1}$$

delivers a stable system. For various other calculations, the following identities may come handy

$$T_o = L_o S_o = G_{x/i} S_i R = S_o L_o$$

$$T_i = L_i S_i = R S_o G_{x/i} = S_i L_i .$$

5.3. Continuous-Time PID Control

The rotor supported by active magnetic bearings is coherently unstable as indicated by the poles with positive real parts of equation (4.9) and (4.10). Therefore a stabilizing controller is needed. There are many different ways of designing a stabilizing controller for the linearized system. Most modern linear control concepts for MIMO systems are based on a state feedback controller coupled with a state observer (see e.g. [ZDG96]).

Mechanical engineers, however, do still prefer a PD control scheme, because the principle is highly analogous to changing the stiffness and the damping in a mechanical spring mass system. The idea behind this is to measure the position of a mechanical system and calculate the velocity by differentiating the position. This is a simple state observer, since the position and the velocity are also the states of the system equation (4.10). With the "observed" states, a feedback controller can be designed so that the closed-loop has the desired damping and eigenfrequency characteristics (pole placement see [STB93]).

Lang [Lan97] has designed a PID controller by augmenting the simple model, described by equation (4.10), with an integral state and setting $\Omega = 0$ and $N = 0$. The resulting system in state space form is

$$\frac{d}{dt} \begin{bmatrix} \dot{x}_b \\ x_b \\ \int_0^t x_b d\tau \end{bmatrix} = \begin{bmatrix} 0 & M_b^{-1} K_s & 0 \\ I & 0 & 0 \\ 0 & I & 0 \end{bmatrix} \begin{bmatrix} \dot{x}_b \\ x_b \\ \int_0^t x_b d\tau \end{bmatrix} + \begin{bmatrix} M_b^{-1} K_i \\ 0 \\ 0 \end{bmatrix} i_x$$

with the augmented state vector \mathbf{z}

$$\mathbf{z} = \begin{bmatrix} \dot{\mathbf{x}}_b & \mathbf{x}_b & \int_0^t \mathbf{x}_b d\tau \end{bmatrix}^T.$$

Lang used an LQR algorithm, which minimizes the cost functional

$$J = \int_0^\infty \left(\mathbf{z}^T \mathbf{W}_z \mathbf{z} + \mathbf{i}_x^T \mathbf{W}_i \mathbf{i}_x \right) dt$$

where \mathbf{W}_z and \mathbf{W}_i are weighting matrices, to calculate the optimal state feedback controller

$$\mathbf{i}_x = - [\mathbf{P}_D \quad \mathbf{P}_P \quad \mathbf{P}_I] \mathbf{z}.$$

The resulting control law in the Laplace domain is given by

$$\hat{\mathbf{i}}_x(s) = -\mathbf{R}(s) \hat{\mathbf{x}}_b(s) = - \left(s\mathbf{P}_D + \mathbf{P}_P + \frac{1}{s}\mathbf{P}_I \right) \hat{\mathbf{x}}_b(s) \quad (5.3)$$

where $\mathbf{R}(s)$ is the controller transfer matrix. The numerical values for \mathbf{P}_P , \mathbf{P}_I and \mathbf{P}_D are as follows

$$\mathbf{P}_P = \begin{bmatrix} 25450.3 & 0 & 75.7595 & 0 \\ 0 & -25135.8 & 0 & -75.2596 \\ 74.9087 & 0 & 25442.5 & 0 \\ 0 & -75.2596 & 0 & -25133.2 \end{bmatrix} \text{ A/m} \quad (5.4)$$

$$\mathbf{P}_I = \begin{bmatrix} 160000 & 0 & 3.7642 & 0 \\ 0 & -160000 & 0 & 0 \\ -3.7642 & 0 & 160000 & 0 \\ 0 & 0 & 0 & -160000 \end{bmatrix} \text{ A/ms} \quad (5.5)$$

$$\mathbf{P}_D = \begin{bmatrix} 52.3681 & 0 & 8.5144 & 0 \\ 0 & -52.0436 & 0 & -8.462 \\ 8.5126 & 0 & 52.0664 & 0 \\ 0 & -8.462 & 0 & -51.7492 \end{bmatrix} \text{ As/m} . \quad (5.6)$$

Inserting the PID controller into the simple system equations (4.10), the controlled simple system can be written as

$$\mathbf{M}_b \ddot{\mathbf{x}}_b + (\mathbf{G}_b + \mathbf{K}_i \mathbf{P}_D) \dot{\mathbf{x}}_b + (\mathbf{N}_b - \mathbf{K}_s + \mathbf{K}_i \mathbf{P}_P) \mathbf{x}_b + \mathbf{K}_i \mathbf{P}_I \int_0^t \mathbf{x}_b d\tau = \mathbf{f}_{db} + \mathbf{f}_{ub}.$$

(5.7)

The poles of the PID controlled simple system for $\Omega = 0$ and $N_b = 0$ are given in table 5.1 together with the corresponding undamped natural frequencies and the damping ratios; the values are rounded to three significant digits. The poles λ_5 to λ_8 correspond to the mechanical natural frequencies of the motion in x and y direction, λ_9 to λ_{12} to the natural frequencies of the tilting motion in the x, z -plane and y, z -plane, and λ_1 to λ_4 to the integral part of the controller.

Table 5.1.: Poles of continuous-time controlled simple model

pole	value s^{-1}	natural frequency	value Hz	damping ratio	value
λ_1	-9.09		1.45		1.0
λ_2	-9.09		1.45		1.0
λ_3	-9.13		1.45		1.0
λ_4	-9.13		1.45		1.0
$\lambda_{5,6}$	$-413 \pm 268i$	ω_{1y}	78.4	ζ_{1y}	0.839
$\lambda_{7,8}$	$-416 \pm 266i$	ω_{1x}	78.6	ζ_{1x}	0.842
$\lambda_{9,10}$	$-573 \pm 372i$	ω_{2y}	109	ζ_{2y}	0.839
$\lambda_{11,12}$	$-576 \pm 369i$	ω_{2x}	109	ζ_{2x}	0.842

5.4. Discrete-Time PID Control

The continuous PID controller has one major drawback: it can not be realized. This might seem surprising, since there are numerous so-called PID controllers in use today. All these devices have in common that they behave only approximately as a PID controller for lower frequencies and quite different for higher frequencies. The most common way to implement a PID controller today is a digital approximation. There is almost no advantage of an analog design especially since the cost for digital components have decreased dramatically.

With the forward difference quotient, we can find a simple discrete-time

approximation of the continuous PID controller from equation (5.3), which is

$$\begin{bmatrix} \mathbf{x}_I(k+1) \\ \mathbf{x}_D(k+1) \end{bmatrix} = \begin{bmatrix} \mathbf{I} & \mathbf{0} \\ \mathbf{0} & \mathbf{0} \end{bmatrix} \begin{bmatrix} \mathbf{x}_I(k) \\ \mathbf{x}_D(k) \end{bmatrix} + \begin{bmatrix} T_s \mathbf{I} \\ \mathbf{I} \end{bmatrix} \mathbf{x}_b(kT_s)$$

$$\mathbf{i}_x(kT_s) = \begin{bmatrix} \mathbf{P}_I & -\frac{1}{T_s} \mathbf{P}_D \end{bmatrix} \begin{bmatrix} \mathbf{x}_I(k) \\ \mathbf{x}_D(k) \end{bmatrix} + \left(\frac{1}{T_s} \mathbf{P}_D + \mathbf{P}_P \right) \mathbf{x}_b(kT_s) .$$

The properties of the discrete-time PID controller are mainly influenced by the sample time T_s . A smaller sample time improves the controller performance but also increases the hardware cost and may lead to numerical problems in the realization of the control algorithm.

Choosing the sample time is not as trivial as it seems to be. As a rule of the thumb (see [Ack88]) the sample time T_s for discretizing a linear system should be

$$T_s \leq \frac{\pi}{4 \max(|\lambda_i|)}$$

where λ_i stands for the poles of the system. For the simple model, the value of T_s would be 1776 μs and even the complex model could be stabilized by a discrete controller with this sample time, since the unstable poles are already included in the simple model.

The discretized PID controller, however, has to use a sample time smaller than 800 μs to be stable. As shown in simulations, good performance is accomplished with a sample time smaller than 100 μs . This is due to the continuous design process of the PID controller. So the sample time is set to

$$T_s = 100 \mu\text{s} .$$

In figures 5.2 and 5.3, the continuous PID controlled simple system, the discrete PID controlled simple system $T_{MB} = 0$, and the discrete PID controlled complex system $T_{MB} > 0$ are compared. They show the frequency response plots of the (1,1)-element of the transfer matrices $\mathbf{S}_o \mathbf{G}_{x/i}$ —that are, the transfer functions from i_{Ax} to x_A —and the continuous-time equivalent for the continuous PID control. In figure 5.2 the sample time T_s is 800 μs and in figure 5.3 T_s is 100 μs .

Especially in the magnitude plot figure 5.2a we see that for the sample time $T_s = 800 \mu\text{s}$ the difference between the discrete-time controlled simple model and the discrete-time controlled complex model is very large; the complex model and therefore also the real system is close to instability. For smaller sample times, the influence of the magnetic bearing time constant is much lower as

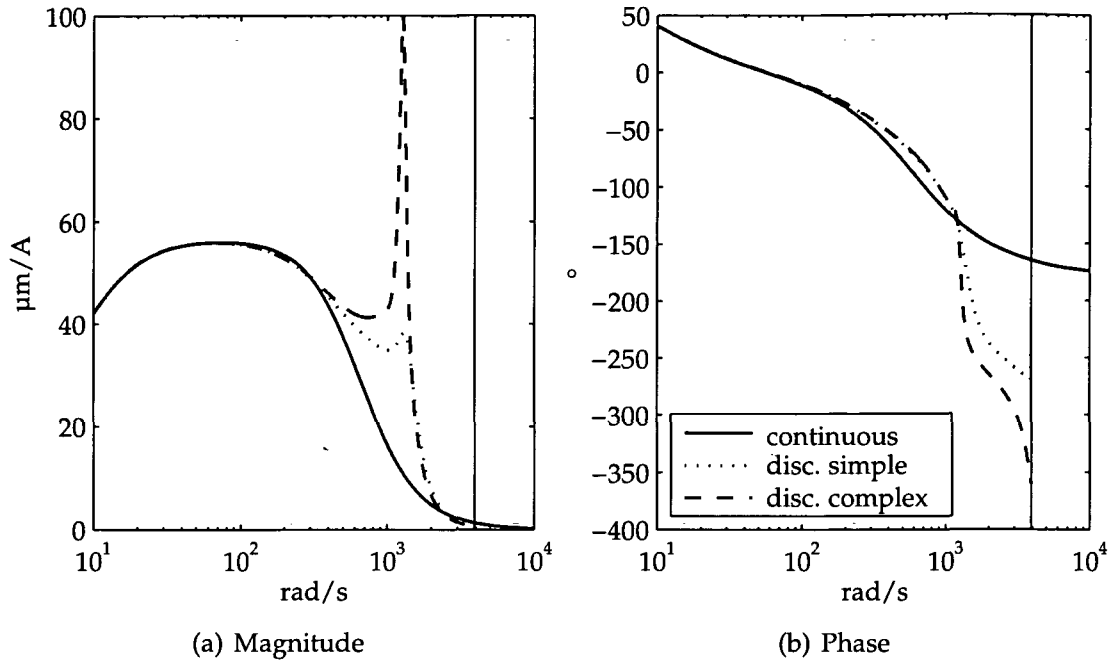


Figure 5.2.: Frequency response plots of (1,1)-element of the transfer matrix $S_o G_{x/i}$ for continuous PID control and discrete PID control with $T_s = 800 \mu s$

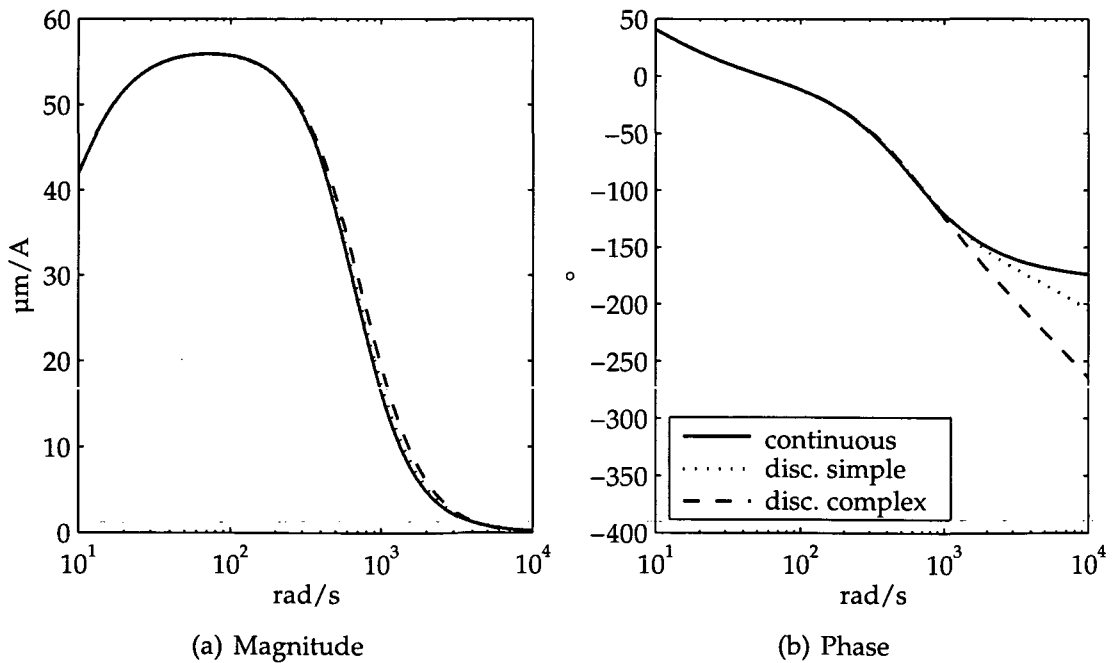


Figure 5.3.: Frequency response plots of (1,1)-element of the transfer matrix $S_o G_{x/i}$ for continuous PID control and discrete PID control with $T_s = 100 \mu s$

shown in figure 5.3. All three models have a similar magnitude response, but there is still a significant phase lag corresponding to the discretization and the magnetic bearing dynamics; neglecting the magnetic bearing time constant, however, might be reasonable, i.e. the simple model may be sufficient.

A big advantage of the PID controller is its relatively high robustness in comparison to e.g. an LQG controller (LQR control combined with a Kalman filter). Since the rotational speed and the cross-coupling parameters are changing we need some robustness of the basic control even if we add adaptive cross-coupling control. This is the reason why an LQG controller approach is not used here. Instead of the PID controller, a design process including the robustness issue could be used (e.g. H_∞). In table 5.2, the poles of the simple model with the discrete-time PID controller can be seen. To make comparisons with the continuous-time system easier, we use the equivalent poles as a solutions of $z = e^{sT_s}$. In comparison to the continuous-time system, we see four additional poles, λ_{13} to λ_{16} , corresponding to the differential part of the controller. The "mechanical" natural frequencies have also changed and are now a little bit higher than in the continuous case.

In table 5.3, we have the equivalent poles of the discrete-time PID controlled complex model, where the magnetic bearing time constant is greater than zero (see equation (3.8)). We see four additional poles λ_{17} to λ_{20} corresponding

Table 5.2.: Poles of discrete-time controlled simple system

equiv. pole	value s^{-1}	equiv. nat. fr.	value Hz	equiv. dmp.ratio	value
λ_1	-9.09		1.45		1.0
λ_2	-9.09		1.45		1.0
λ_3	-9.14		1.45		1.0
λ_4	-9.14		1.45		1.0
$\lambda_{5,6}$	$-443 \pm 264i$	ω_{1y}	82.1	ζ_{1y}	0.859
$\lambda_{7,8}$	$-446 \pm 262i$	ω_{1x}	82.3	ζ_{1x}	0.862
$\lambda_{9,10}$	$-632 \pm 362i$	ω_{2y}	116	ζ_{2y}	0.868
$\lambda_{11,12}$	$-637 \pm 359i$	ω_{2x}	116	ζ_{2x}	0.871
λ_{13}	-27200		4330		1.0
λ_{14}	-27200		4340		1.0
λ_{15}	-30800		4900		1.0
λ_{16}	-30900		4910		1.0

Table 5.3.: Poles of discrete-time controlled complex system

equiv. pole	value s^{-1}	equiv. nat. fr.	value Hz	equiv. dmp.ratio	value
λ_1	-9.09		1.45		1.0
λ_2	-9.09		1.45		1.0
λ_3	-9.14		1.45		1.0
λ_4	-9.14		1.45		1.0
$\lambda_{5,6}$	$-495 \pm 263i$	ω_{1y}	89.2	ζ_{1y}	0.883
$\lambda_{7,8}$	$-499 \pm 260i$	ω_{1x}	89.6	ζ_{1x}	0.887
$\lambda_{9,10}$	$-766 \pm 348i$	ω_{2y}	134	ζ_{2y}	0.911
$\lambda_{11,12}$	$-774 \pm 340i$	ω_{2x}	135	ζ_{2x}	0.916
λ_{13}	-4380		697		1.0
λ_{14}	-4400		701		1.0
λ_{15}	-5230		832		1.0
λ_{16}	-5240		834		1.0
$\lambda_{17,18}$	$-42200 + 31400i$		8370		0.802
$\lambda_{19,20}$	$-45100 + 31400i$		8750		0.820

to the magnetic time constant T_{MB} . The poles λ_{17} to λ_{20} are not conjugate complex pairs as one might assume. The reason for this is the transformation $z = e^{sT_s}$. The magnetic bearing time constant has also a high impact on the poles λ_{13} to λ_{16} , corresponding to the differential part of the controller, as they are moved to a much lower frequency range.

5.5. Two Degrees of Freedom Model

In section 4.7, we derived a two degrees of freedom version of the simple model. For $n = 0$, the two degrees of freedom are decoupled and we can write (4.11) in the form

$$\begin{bmatrix} m & 0 \\ 0 & m \end{bmatrix} \begin{bmatrix} \ddot{x}_c \\ \ddot{y}_c \end{bmatrix} - \begin{bmatrix} k_{sAx} + k_{sBx} & 0 \\ 0 & k_{sAy} + k_{sBy} \end{bmatrix} \begin{bmatrix} x_c \\ y_c \end{bmatrix} = \frac{p_{ui}}{R + p_{ui}} \begin{bmatrix} k_{iAx} + k_{iBx} & 0 \\ 0 & k_{iAy} + k_{iBy} \end{bmatrix} \begin{bmatrix} i_x \\ i_y \end{bmatrix} + \begin{bmatrix} f_x \\ f_y \end{bmatrix}$$

where f_x is the sum of all external and unbalance forces in x -direction and f_y in y -direction, respectively. The reduced continuous PD controller for two degrees of freedom (the integral term is neglected) is

$$\begin{bmatrix} \dot{i}_x \\ \dot{i}_y \end{bmatrix} = \frac{1}{2} \mathbf{R}^T \mathbf{P}_P \mathbf{R} \begin{bmatrix} x_c \\ y_c \end{bmatrix} + \frac{1}{2} \mathbf{R}^T \mathbf{P}_D \mathbf{R} \begin{bmatrix} \dot{x}_c \\ \dot{y}_c \end{bmatrix}$$

with

$$\frac{1}{2} \mathbf{R}^T \mathbf{P}_P \mathbf{R} = \begin{bmatrix} p_{Px} & 0 \\ 0 & p_{Py} \end{bmatrix} \quad \frac{1}{2} \mathbf{R}^T \mathbf{P}_D \mathbf{R} = \begin{bmatrix} p_{Dx} & 0 \\ 0 & p_{Dy} \end{bmatrix}.$$

The factor $1/2$ is needed to get similar poles for the 2DoF PD controlled model and the continuous PID controlled 4DoF simple model. The controlled system can be written as

$$\begin{aligned} \ddot{x}_c + 2\zeta_x \omega_x \dot{x}_c + \omega_x^2 x_c &= \frac{1}{m} f_x \\ \ddot{y}_c + 2\zeta_y \omega_y \dot{y}_c + \omega_y^2 y_c &= \frac{1}{m} f_y \end{aligned} \quad (5.8)$$

with

$$\begin{aligned} \omega_h &= \sqrt{\frac{\frac{p_{ui}}{R+p_{ui}} (k_{iAh} + k_{iBh})}{m} p_{Ph} - (k_{sAh} + k_{sBh})} \\ \zeta_h &= \frac{\frac{p_{ui}}{R+p_{ui}} (k_{iAh} + k_{iBh}) p_{Dh}}{2m\omega_h} \end{aligned}$$

where $h \in \{x, y\}$.

A further simplification can be obtained by making the system symmetric. The parameters for the symmetric system are the mean values of the parameters of system equation (5.8)

$$\begin{aligned} p_P &= \frac{|p_{Py}| + |p_{Px}|}{2} & p_D &= \frac{|p_{Dx}| + |p_{Dy}|}{2} \\ k_i &= \frac{|k_{iAx} + k_{iBx}| + |k_{iAy} + k_{iBy}|}{2} & k_s &= \frac{|k_{sAx} + k_{sBx}| + |k_{sAy} + k_{sBy}|}{2} \end{aligned}$$

(The absolute values are necessary when the parameters of both equations have different signs.) Then the stiffness and the damping parameter of both directions are

$$k = p_P \frac{p_{ui}}{R + p_{ui}} k_i - k_s \quad \text{and} \quad c = p_D \frac{p_{ui}}{R + p_{ui}} k_i,$$

and the resulting natural frequency and damping ratio are given by, respectively

$$\omega_0 = \sqrt{\frac{k}{m}} = \frac{\omega_x + \omega_y}{2} \quad \text{and} \quad \zeta = \frac{c}{2\sqrt{km}} = \frac{\zeta_x + \zeta_y}{2}.$$

The resulting system can be written as

$$\begin{aligned} \ddot{x}_c + 2\zeta\omega_0\dot{x}_c + \omega_0^2 x_c &= \frac{1}{m}f_x \\ \ddot{y}_c + 2\zeta\omega_0\dot{y}_c + \omega_0^2 y_c &= \frac{1}{m}f_y \end{aligned}$$

with the parameter values

$$m = 28.768 \text{ kg} \quad k = 7.2161 \text{ kN/mm} \quad c = 24.111 \text{ kN s/m}$$

and the natural frequency and damping ratio, respectively

$$\omega_0 = 501 \text{ rad s}^{-1} \triangleq 79.7 \text{ Hz} \quad \zeta = 0.837.$$

6. Adaptive Cross-Coupling Control

6.1. Introduction

Destabilizing cross-coupling excitations are a well known phenomenon in rotor dynamics. Usually the destabilizing effect can be reduced by design measures, as for example

- replacing the source of the cross-coupling excitation, e.g. replace plain journal bearings by tilting-pad bearings,
- including additional damping sources like squeeze film dampers,
- influencing the source of the cross-coupling excitation, e.g. inject a tangentially directed flow in the rotor stator clearance (see [MFB88, Mus88, MB89]),
- introduce honey-comb seals instead of common plain labyrinth seals, etc.

A good overview of the various design alternatives is given in the book by Childs [Chi93].

Beside the design measures, active control methods which prevent instability due to cross-coupling excitation may also be very helpful; they may either be cheaper than design methods, especially when the rotor is already equipped with actuators, or design measures may not be sufficient to stabilize the rotor or can not be realized due to some other constraints. However, there is very little literature about cross-coupling control.

Matsushita et al. [MTY⁺88, MTY⁺90] describe the cross-coupling control of a partially filled centrifuge which is unstable within a certain rotational speed range. They assume that the resulting unstable whirl vibrates with the 2nd natural frequency of the rotor; so they use a tuning filter centered at this

frequency to pick up only the unstable vibrations. The output of the tuning filter is multiplied with a counter acting cross-coupling stiffness α and applied to the rotor by the magnetic bearings; the cross-coupling control is switched on before the rotor reaches the critical speed range and switched off afterwards. This approach has some important drawbacks. First, one has to have a good guess of the actual cross-coupling parameters in order to choose the right value of α ; it seems that this is basically a trial and error approach. Second, one must know the speed range where the rotor becomes unstable. Third, it is not quite clear why the tuning filter is needed, since the actual control is just a counter acting cross-coupling force; maybe it makes the system more robust with respect to variations of α , and therefore the frequency of the cross-coupling whirl must be known.

The papers of Ulbrich et al. also discuss the control of partially filled centrifuges. In [UAC96], the authors derive a detailed model of the flexible rotor with the centrifuge including the fluid components and calculate the stability margins of the system. In [UCA97], the authors suggest to use the calculated fluid forces to counteract on the actual rotor, which worked well in the numerical simulation. In [UCA00], the authors present three possible approaches to stabilize the centrifuge. In the first approach, two sets of parameters are used for the basic PD control where one parameter set shifts the unstable region to a higher operational speed. In a run-up operation, the PD controller parameter set is switched to the second set, when the unstable rotational speed region is reached, and switched back, when it is passed. The second approach utilizes a velocity cross-coupling control to stabilize the system. This approach is based on the observation that, for the given system, the fluid forces are in phase with the rotor position velocities. The velocity cross-coupling control is plugged into the system model and the control parameter is chosen in a way that the system is stable. This control parameter depends on the rotational frequency and on the filling ratio of the centrifuge. In the third approach, an observer is used to identify the states of a simplified fluid model; these states are used in a state feedback controller to stabilize the system. Also in this approach the controller parameters have to be adjusted for every operating point, i.e. rotational frequency and filling ratio of the centrifuge. Since the work by Ulbrich et al. is based on a very detailed model of the centrifuge including the interacting fluid components, it is not clear how proper a simple excitation model, using a skew-symmetric cross-coupling stiffness matrix introduced in the rotor model, would approximate the actual behavior of the system.

Wurmsdobler et al. [WJ96, WJS96, Wur97a, Wur97b] use a discrete-time adaptive state space controller for stabilizing a rigid rotor with cross-coupling excitation modelled by a skew-symmetric stiffness matrix. No additional excitations like mass unbalance are considered. Wurmsdobler's approach is based on a Kalman filter as a state observer together with an identification process of the system parameters and Kalman filter parameters; this results in a total of 96 parameters to be identified. Based on the identified parameters the parameters of a state feedback controller are computed, such that the poles of the closed-loop system are at predefined values (pole placement). The main advantage of this approach is that it utilizes a well established adaptive control method. The drawbacks are that it poses a high computational load on the actual controller hardware and a total of 96 parameters are estimated while only one parameter (a single cross-coupling stiffness) is changed in the example simulated by the authors. However, other parameters may also change without the need for additional controller complexity; it should be easy to use this approach for a distributed cross-coupling force along the rotor axis.

Another interesting approach is described by Liao et al. [LGKK00]. They consider a 2DoF Jeffcott rotor supported by journal bearings. The use of journal bearings results in a stiffness matrix with skew-symmetric components which induce an unstable behavior of the rotor above a certain rotational speed. Additional to the cross-coupling excitation, mass unbalance excitation is present in the system. The starting point for the controller design is that, as long as the rotor is stable, the rotor position and the rotor velocity oscillate with the frequency of the unbalance excitation, i.e. the rotational speed. The applied so-called "phase-locked delayed feedback control" calculates the difference between the actual values and the values which have been measured a period ago. These differences of the velocity as well as the rotor position are amplified and fed back into the system. So the controller is only active when instability occurs, and can be seen as an increase in stiffness and damping. Again, the controller parameters are calculated from the known system parameters, including the cross-coupling parameters. The advantage of this approach is that the system is unchanged as long as it is stable. Unfortunately, measurement noise is not included in the numerical simulations, which will probably turn on the phase-locked control all the time.

The control approach used in this thesis has been first employed by Kienberger [KE94, Kie94]. The basic idea is to identify only the cross-coupling stiffness parameter with a continuous-time least-squares algorithm. As a reference for the estimation parameter the cross-coupling forces are used in the

derivation of the estimation process and exchanged with the magnetic bearing forces in the actual estimation process. Kienberger has successfully tested this approach in a numerical simulation. Lang et al. [LWS95, LWS96b, LWS96a, Lan97] carried out numerical simulations and experiments on a test rig to validate and improve the algorithm; as in the work by Kienberger only a single source of cross-coupling excitation is considered. Steinhardt [Ste96] uses the simulation model of Lang to stabilize a flexible rotor with cross-coupling excitation. However, the adaptation of the algorithm for the flexible rotor is described very rudimentarily.

6.2. Influence of the Cross-Coupling on the System

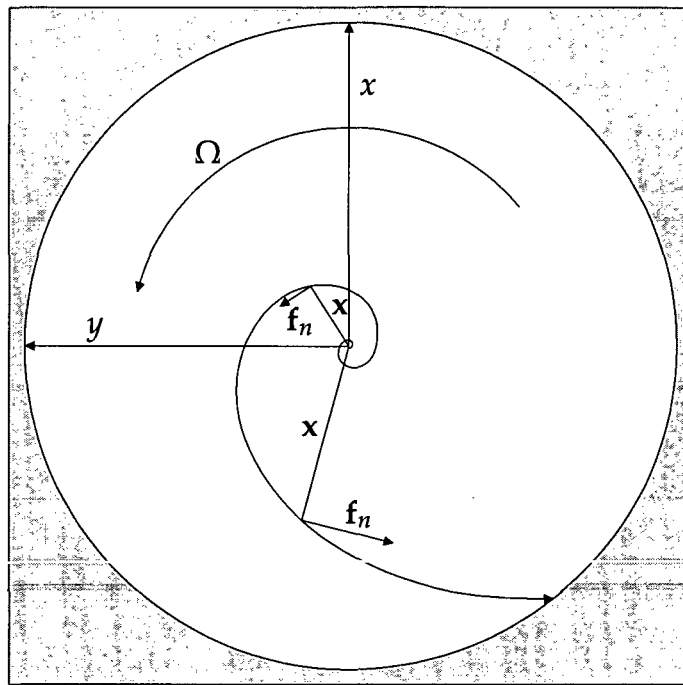


Figure 6.1.: Orbit of a rotor excited by a cross-coupling force

It has already been mentioned that self-exciting cross-coupling forces can be described approximately by a linear relationship between the displacement

vector and the cross-coupling force vector with a skew-symmetric matrix.

$$\mathbf{f}_n = -\mathbf{N}\mathbf{x}, \quad \mathbf{N} = -\mathbf{N}^T.$$

Nonconservative forces may drive a system to instability. Although it is hard to prove this analytically, the reason is quite obvious. In figure 6.1, we see the orbit of a rotor which is excited by a cross-coupling force. As the rotor is displaced, a force acts on the rotor which is perpendicular and proportional in magnitude to the rotor displacement vector. This drives the rotor away from the center position on a spiral orbit; the center position is unstable.

If we look at the energy stored in the system we might get a better insight into the stability problem. For a second order system,

$$\mathbf{M}\ddot{\mathbf{x}} + \mathbf{D}\dot{\mathbf{x}} + (\mathbf{K} + \mathbf{N})\mathbf{x} = \mathbf{0}$$

with symmetric \mathbf{M} , \mathbf{D} and \mathbf{K} and a skew-symmetric \mathbf{N} , we can write the total (kinetic plus potential) energy in the system as

$$E = \frac{1}{2}\dot{\mathbf{x}}^T \mathbf{M} \dot{\mathbf{x}} + \frac{1}{2}\mathbf{x}^T \mathbf{K} \mathbf{x}.$$

The time derivative of the total energy (for a more detailed derivation see appendix A.4),

$$\dot{E} = -\dot{\mathbf{x}}^T \mathbf{D} \dot{\mathbf{x}} + \mathbf{x}^T \mathbf{N} \dot{\mathbf{x}} = -W_d + W_n, \quad (6.1)$$

consists of the dissipative work W_d and the excitation work W_n . The system is unstable when the exciting work exceeds the dissipative work. Unfortunately, this relationship is not really helpful, because \mathbf{x} and $\dot{\mathbf{x}}$ have to be known to calculate the energy change, whereas the stability of the system is independent of \mathbf{x} and $\dot{\mathbf{x}}$.

In section 4.4, we have derived the cross-coupling stiffness matrix for the 4DoF rigid rotor. It has been shown that the matrix \mathbf{N}_b consists of only three independent parameters n_1 , n_2 and n_3 for any distribution of cross-coupling forces along the rotor. A good impression of the influence of the three independent cross-coupling parameters can be seen from the change they impose to the system poles in the complex plane.

The poles are calculated for the discrete-time PID controlled complex model. Instead of the poles of the corresponding z -transfer matrix $\mathbf{T}_o(z)$ we use the poles of the q -transformed transfer matrix $\mathbf{T}_o^\#(q)$ (see section A.2.3). This q -transformed transfer matrix is stable if all poles are in the open left half plane.

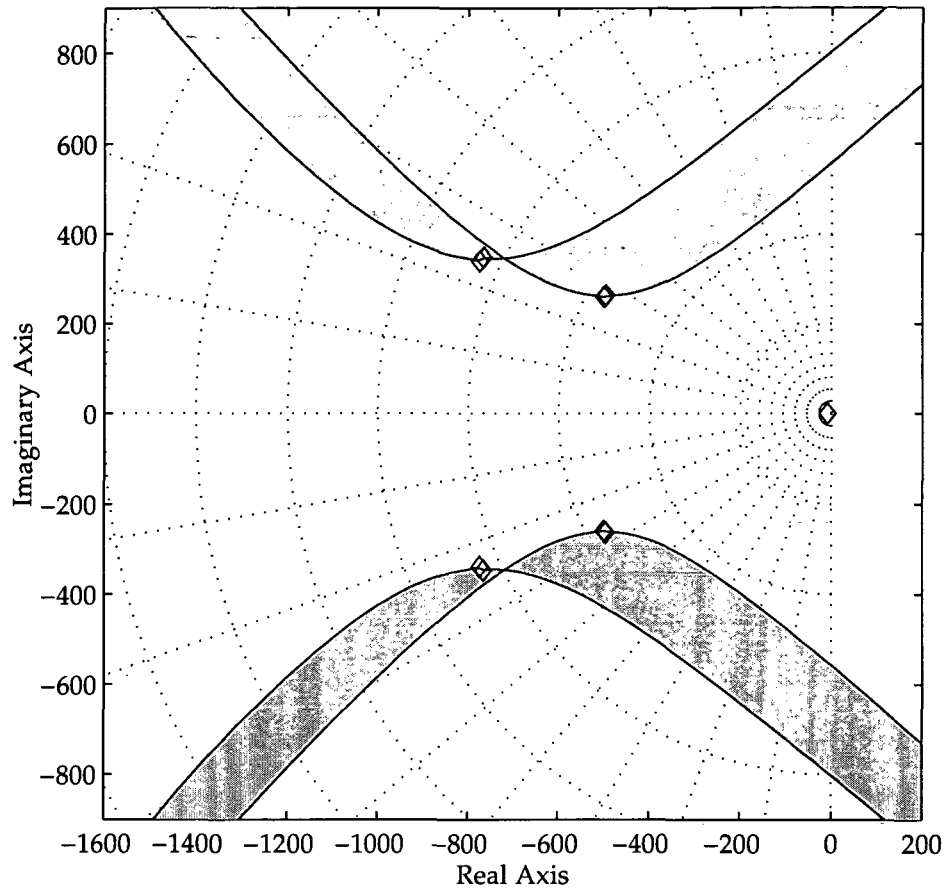
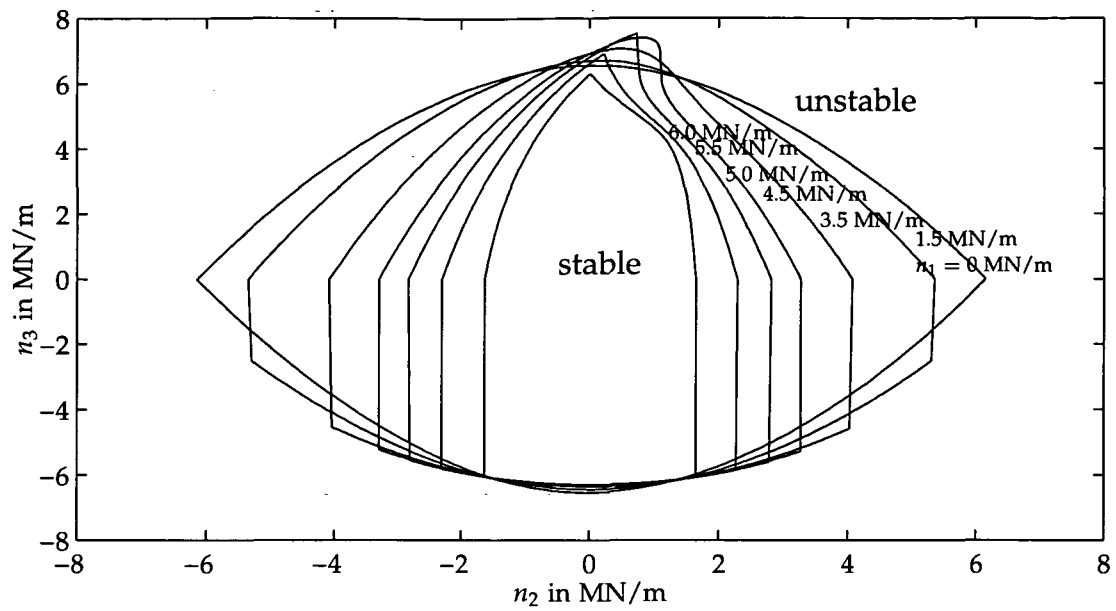
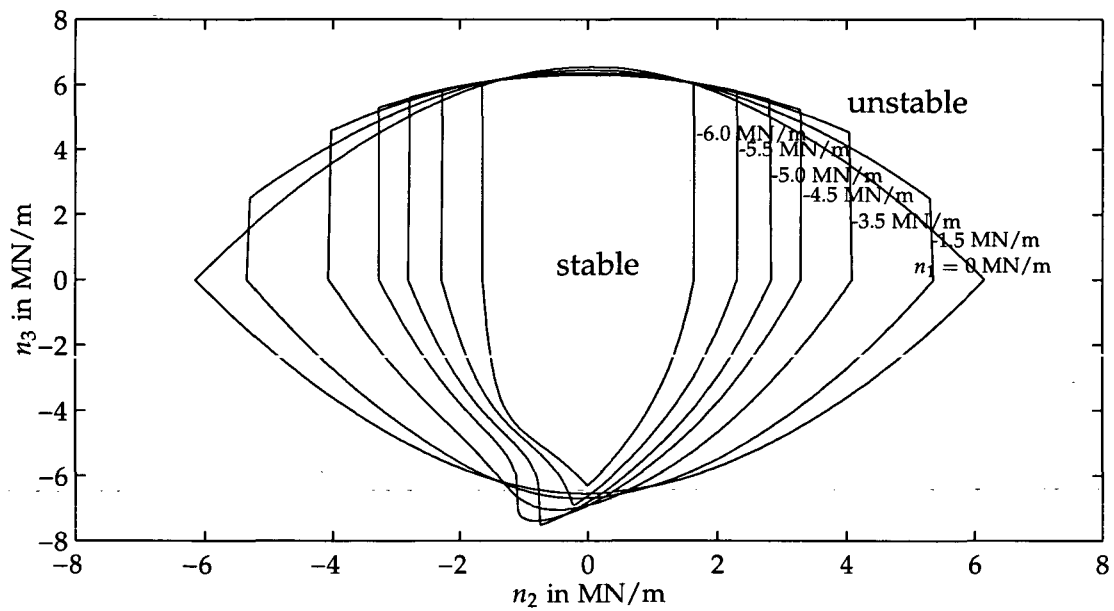


Figure 6.2.: Root locus of $T_o^{\#}(q)$ for variations of the parameters n_1 , n_2 , and n_3

In figure 6.2, the poles of $T_o^{\#}(q)$ are plotted for variations of the parameters n_1 , n_2 and n_3 in the range of -20 MN/m to +20 MN/m. The diamonds in figure 6.2 are the poles for $n_1 = n_2 = n_3 = 0$ while for any other value the poles are points inside the grey bands. It is interesting that the varying poles stay in a narrow band which crosses the imaginary axis approximately between the undamped natural mechanical frequencies. If n_1 and n_3 are set to zero and only n_2 is varied the band degrades to two lines (root locus) which are also the borders of the bands.

A second possibility to describe the stability behavior of the system is to plot the stable region for the three independent parameters; this is shown in the figures 6.3 and 6.4.

Figure 6.3.: Stability margins for $n_1 \geq 0$ Figure 6.4.: Stability margins for $n_1 \leq 0$

6.3. On-line Parameter Estimation

Numerous different mechanisms may be the source of cross-coupling forces (see [GNP02, Chi93]). For most of these mechanisms, the cross-coupling coefficients depend on the operating conditions of rotating machinery. The matrix \mathbf{N} can change with time and this might also happen very fast, e.g. due to a fast run-up or run-down operation. An instability during such an operation may lead to a catastrophic failure of a machine.

The basic idea behind the proposed control algorithm is to use the linearity between the cross-coupling force and the displacement, that is

$$\mathbf{f}_n(t) = -\mathbf{N} \mathbf{x}(t).$$

For any matrix \mathbf{N} , we can also write

$$\mathbf{f}_n(t) = \mathbf{X}(t) \mathbf{n}$$

since

$$\begin{bmatrix} \mathbf{n}_1^T \\ \mathbf{n}_2^T \\ \vdots \\ \mathbf{n}_n^T \end{bmatrix} \begin{bmatrix} x_1 \\ x_2 \\ \vdots \\ x_n \end{bmatrix} = \begin{bmatrix} \mathbf{x}^T & 0 & \cdots & 0 \\ 0 & \mathbf{x}^T & \cdots & 0 \\ \vdots & \vdots & \ddots & \vdots \\ 0 & 0 & \cdots & \mathbf{x}^T \end{bmatrix} \begin{bmatrix} \mathbf{n}_1 \\ \mathbf{n}_2 \\ \vdots \\ \mathbf{n}_n \end{bmatrix}$$

with \mathbf{n}_i^T as the row vectors of \mathbf{N} . If some parameters n_{ik} are equal to other parameters n_{jl} or equal to zero the size of the matrix $\mathbf{X}(t)$ can be reduced. For our special case of the rigid rotor with three independent parameters (see equ. (4.5)),

$$\mathbf{f}_{nb} = \begin{bmatrix} -y_A(t) & -y_B(t) & 0 \\ x_A(t) & x_B(t) & 0 \\ 0 & -\dot{y}_A(t) & -\dot{y}_B(t) \\ 0 & x_A(t) & x_B(t) \end{bmatrix} \begin{bmatrix} n_1 \\ n_2 \\ n_3 \end{bmatrix}$$

holds.

The goal is to calculate a parameter vector $\hat{\mathbf{n}}_t$ which is the best estimate based on measurements of $\mathbf{X}(t)$ and $\mathbf{f}_n(t)$ within the time interval $t \geq 0$;

$$\|\mathbf{f}_n(t) - \mathbf{X}(t) \hat{\mathbf{n}}_t\| \leq \|\mathbf{f}_n(t) - \mathbf{X}(t) \mathbf{n}\| \quad \text{for all } \mathbf{n} \in \mathbb{R}^n.$$

The properties of the used norm $\|\cdot\|$ define what is meant by "best estimate". If the square root of an inner product $\|\mathbf{x}\| = \sqrt{\langle \mathbf{x}, \mathbf{x} \rangle}$ is used as a norm (see

definition A.3 in the appendix), we can apply the projection theorem (see theorem A.4) to calculate the "best estimate" $\tilde{\mathbf{n}}_t$ of \mathbf{n} . The special inner product

$$\langle \mathbf{x}(t), \mathbf{y}(t) \rangle = \int_{s=0}^t e^{-\int_s^t \lambda(r) dr} \mathbf{x}^T(s) \mathbf{y}(s) ds.$$

finally leads to the algorithm as described by Slotine and Lee [SL91], that is

$$\frac{d}{dt} \tilde{\mathbf{n}}(t) = \mathbf{P}(t) \mathbf{X}^T(t) (\mathbf{f}_n(t) - \mathbf{X}(t) \tilde{\mathbf{n}}(t)) \quad (6.2)$$

$$\frac{d}{dt} \mathbf{P}(t) = \lambda(t) \mathbf{P}(t) - \mathbf{P}(t) \mathbf{X}^T(t) \mathbf{X}(t) \mathbf{P}(t). \quad (6.3)$$

For a more detailed discussion, see section A.5 where the discrete-time equivalent is described. Instead of $\tilde{\mathbf{n}}_t$, which has been the best estimate of the constant parameter vector \mathbf{n} based on the measurements from 0 to t , we now use $\tilde{\mathbf{n}}(t)$. This indicates that the actual parameter vector $\mathbf{n}(t)$ may change with time and $\tilde{\mathbf{n}}(t)$ is now an estimate of this parameter vector, but not necessarily the "best" estimate, because we assumed a constant parameter vector \mathbf{n} in the derivation of the algorithm. The actual quality of the estimate is determined by the behavior of $\mathbf{n}(t)$ and the forgetting factor $\lambda(t)$.

Slotine and Lee suggest a time varying forgetting factor¹

$$\lambda(t) = \lambda_0 \left(1 - \frac{\|\mathbf{P}(t)\|}{K_0} \right).$$

Unfortunately, Slotine and Lee do not specify the appropriate norm for the algorithm. A quite simple approach is to use the induced 1-norm $\|\mathbf{P}(t)\|_1$, that is

$$\left\| \begin{bmatrix} p_{11} & \cdots & p_{1n} \\ \vdots & \ddots & \vdots \\ p_{n1} & \cdots & p_{nn} \end{bmatrix} \right\|_1 = \max_{1 \leq j \leq n} \sum_{i=1}^n |p_{ij}| \quad (\text{column sum}).$$

The forgetting factor $\lambda(t)$ is quickly disposing old data for fast changes in the system output (indicated by a small $\|\mathbf{P}(t)\|$) and slowly for little changes in the system output. λ_0 represents the maximum forgetting rate and K_0 the upper bound of $\|\mathbf{P}(t)\|$.

¹ The used norm $\|\mathbf{P}(t)\|$ is a different norm than for deriving equation (6.2), because it is not a function norm but a norm of the matrix $\mathbf{P}(t)$ at the time t .

6.4. Reference Force Concept

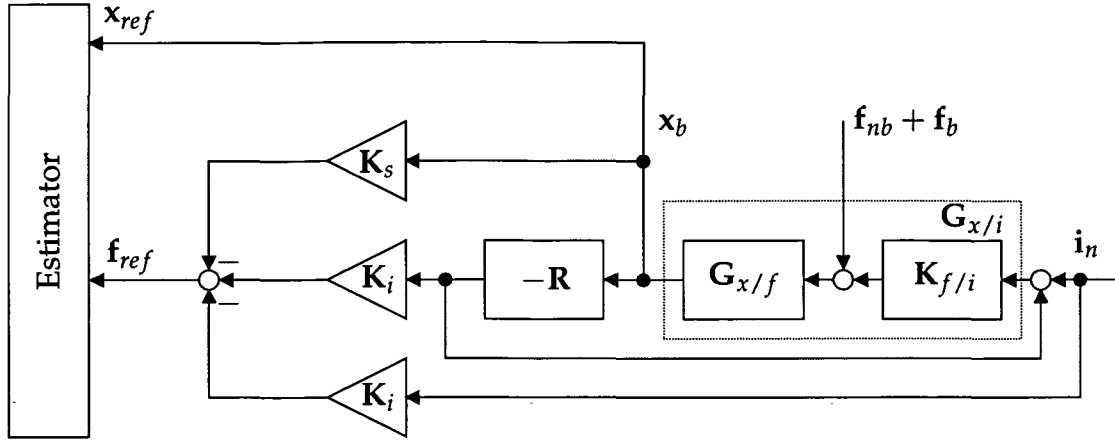


Figure 6.5.: Reference force transfer function

In the preceding section, the on-line estimation algorithm for \mathbf{n} has been derived assuming that the cross-coupling forces \mathbf{f}_n can be measured. Since this is not the case, the negative magnetic bearing forces—calculated with the assumption that T_{MB} is equal to zero—are used as reference forces instead of the actual cross-coupling forces, that is

$$\mathbf{f}_{ref}(t) := -\mathbf{K}_i \mathbf{i}_x(t) - \mathbf{K}_s \mathbf{x}_b(t) . \quad (6.4)$$

Assuming that $\hat{\mathbf{i}}_h = 0$ and $\hat{\mathbf{r}} = 0$, equation (5.1) is written as

$$\hat{\mathbf{i}}_x(z) = -\mathbf{R}(z) \hat{\mathbf{x}}_b(z) + \hat{\mathbf{i}}_n(z)$$

and the reference force vector is given by

$$\hat{\mathbf{f}}_{ref}(z) = \mathbf{K}_i \mathbf{R}(z) \hat{\mathbf{x}}_b(z) - \mathbf{K}_i \hat{\mathbf{i}}_n(z) - \mathbf{K}_s \hat{\mathbf{x}}_b(z) . \quad (6.5)$$

This relationship is depicted in figure 6.5. The last term $\mathbf{K}_s \mathbf{x}_b$ in this expression is not really necessary since it does not contribute to the cross-coupling parameters but simplifies the input-output relationship between cross-coupling and reference force.

The reason for the choice of the reference force is quite obvious. A “perfect controller” would compensate all forces acting on the rotor. With the assumption that the magnetic bearing force and the cross-coupling force are the only

forces acting on the rotor, the equation of motion is

$$\mathbf{M}_b \ddot{\mathbf{x}}_b = \mathbf{f}_{nb}(t) + \mathbf{f}_{MB}(t) .$$

A perfect controller would make

$$\mathbf{f}_{MB}(t) = -\mathbf{f}_{nb}(t)$$

and, with the additional assumption $T_{MB} = 0$, we get

$$\mathbf{f}_{ref}(t) = \mathbf{f}_{nb}(t) .$$

Of course, the controller is not perfect (if it were, no additional cross-coupling control would be needed). Further, additional forces act on the rotor, and $T_{MB} > 0$. So, instead of a perfect controller, we demand that

$$\hat{\mathbf{f}}_{ref}(z) \approx \hat{\mathbf{f}}_{nb}(z)$$

in the relevant frequency range where

$$\hat{\mathbf{f}}_{nb}(z) = \mathcal{Z}(\mathbf{f}_{nb}(kT_s)) .$$

We consider three inputs into the system for the analysis of the errors in the reference force. First, the cross-coupling force $\mathbf{f}_{nb}(t)$. Second, some additional external force $\mathbf{f}_b(t)$. And third, the cross-coupling control current $\hat{\mathbf{i}}_n(z)$. Because $\mathbf{f}_{nb}(t)$ and $\mathbf{f}_b(t)$ are not discrete-time input signals, the relationship between $\mathbf{f}_{nb}(t)$, $\mathbf{f}_b(t)$, and $\hat{\mathbf{f}}_{ref}(z)$ cannot exactly be described with a z -transfer matrix. So we use the following approximations. For the sake of simplicity, we define

$$\mathbf{G}_{x/f}(s) = \left[s^2 \mathbf{M}_b + s \mathbf{G}_b - \mathbf{K}_{f/x}(s) \right]^{-1}$$

with

$$\mathbf{G}_{x/i}(s) = \mathbf{G}_{x/f}(s) \mathbf{K}_{f/i}(s) \quad \text{and} \quad \mathbf{G}_{x/i}(z) \cong \mathbf{G}_{f/i}(z) \mathbf{K}_{f/i}(z) .$$

\mathbf{N}_b is not included in $\mathbf{G}_{x/i}(z)$ and $\mathbf{G}_{x/f}(z)$ because $\hat{\mathbf{f}}_{nb}$ is regarded as an "external" force. Written in the frequency domain, the reference force is approximately

$$\hat{\mathbf{f}}_{ref}(z) \cong \mathbf{T}_{ref}(z) \left(\hat{\mathbf{f}}_{nb}(z) + \hat{\mathbf{f}}_b(z) \right) + (\mathbf{T}_{ref}(z) \mathbf{K}_{f/i}(z) - \mathbf{K}_i) \hat{\mathbf{i}}_n(z)$$

and the inverse position filter

$$\mathbf{F}_x^{-1}(z) := \mathbf{T}_{ref}^{-1}(z) . \quad (6.8)$$

Usually $\mathbf{T}_{ref}(z)$ is not invertible. So, instead of applying $\mathbf{F}_x^{-1}(z)$ on the reference force, we apply $\mathbf{F}_x(z)$ on the measured rotor position

$$\hat{\mathbf{x}}_{ref}(z) = \mathbf{F}_x(z) \hat{\mathbf{x}}_b(z)$$

for the use in the estimation algorithm; this relationship is depicted in figure 6.6. With the usage of the two filters, the errors in the on-line estimation algorithm are reduced, but this causes additional computation load.

6.5. Adaptive Cross-Coupling Control (ACCC)

The concept of the adaptive cross-coupling control is very simple. With the estimate of the cross-coupling matrix $\tilde{\mathbf{N}}_b$, a compensating cross-coupling force is applied to the rotor. The additional cross-coupling control current is

$$\mathbf{i}_n = \mathbf{K}_i^{-1} \tilde{\mathbf{N}}_b \mathbf{x}_b .$$

The combination of the on-line estimation and the additional cross-coupling control is called "Adaptive Cross-Coupling Control" (ACCC). The resulting reference force is

$$\hat{\mathbf{f}}_{ref}(z) = (\mathbf{K}_i \mathbf{R}(z) - \tilde{\mathbf{N}}_b - \mathbf{K}_s) \hat{\mathbf{x}}_b(z) .$$

For the continuous-time controlled simple model described by equation (5.7), the resulting cross-coupling stiffness matrix becomes

$$\mathbf{N}_{res} = \mathbf{N}_b - \tilde{\mathbf{N}}_b .$$

This is just an approximation for the complex model with discrete-time control.

6.6. 2DoF Model with Adaptive Cross-Coupling Control

First the 2DoF case of the simple model is considered, to get some basic understanding of the adaptive control algorithm. The 2DoF case is very similar to

the 4DoF case with a single unknown parameter, which has been investigated by the author et al. in [HSS02, Hir03b].

For a 2DoF model described by equation (5.8), we can use the stability analysis described in section 6.2 to get an analytical stability limit of the system. With $\omega_x = \omega_y = \omega_0$ and $\xi_x = \xi_y = \xi$, we can assume that the unstable orbit of the autonomous system is a forward circular whirl with the angular frequency ω_0 , that is

$$\mathbf{x}_c = \varepsilon \begin{bmatrix} \cos \omega_0 t \\ \sin \omega_0 t \end{bmatrix} \quad \dot{\mathbf{x}}_c = \varepsilon \omega_0 \begin{bmatrix} -\sin \omega_0 t \\ \cos \omega_0 t \end{bmatrix}.$$

Inserting this trajectory into the energy equation (6.1) yields instability if

$$\dot{E} = -\varepsilon \omega_0^2 2\xi \omega_0 + \varepsilon \omega_0 \frac{n}{m} > 0,$$

i.e. the system is unstable for

$$n > 2\xi \omega_0^2 m = 2\xi k = n_{crit}. \quad (6.9)$$

Although we have derived this relationship by assuming a specific motion trajectory of the system, the difference between this expression and the numerically calculated stability limit has turned out of the same order of magnitude as the numerical accuracy.

For the parameter estimation algorithm, we have to write the cross-coupling force

$$\mathbf{f}_n(t) = - \begin{bmatrix} 0 & n \\ -n & 0 \end{bmatrix} \begin{bmatrix} x_c(t) \\ y_c(t) \end{bmatrix}$$

in the form

$$\mathbf{f}_n(t) = \begin{bmatrix} -y_c(t) \\ x_c(t) \end{bmatrix} n = \mathbf{X}(t) n.$$

Inserting this into the estimation algorithm, the parameter vector \mathbf{n} degrades to a scalar n , the signal matrix $\mathbf{X}(t)$ degrades to a vector, and the gain matrix \mathbf{P} degrades to a scalar. The on-line parameter estimation algorithm for the 2DoF model according to equation (6.2) and (6.3) is

$$\begin{aligned} \frac{d}{dt} \tilde{n}(t) &= p(t) - f_{refx}(t) y_c(t) + \tilde{n}(t) y_c^2(t) + f_{refy}(t) x_c(t) - \tilde{n}(t) x_c^2(t) \\ \frac{d}{dt} p(t) &= \lambda(t) p(t) - p^2(t) (x_c^2(t) + y_c^2(t)) \end{aligned}$$

with the forgetting factor

$$\lambda(t) = \lambda_0 \left(1 - \frac{|p(t)|}{K_0} \right)$$

and the reference force

$$\begin{bmatrix} f_{refx} \\ f_{refy} \end{bmatrix} = \begin{bmatrix} (k_i p_P - k_s) x_c + k_i p_D \dot{x}_c - k_i i_{nx} \\ (k_i p_P - k_s) y_c + k_i p_D \dot{y}_c - k_i i_{ny} \end{bmatrix} = \begin{bmatrix} k x_c + c \dot{x}_c - \tilde{n} y_c \\ k y_c + c \dot{y}_c + \tilde{n} x_c \end{bmatrix}.$$

6.7. Simulation Results 2DoF Model

First, four parameters have to be chosen. The initial value on $\tilde{n}(t)$ is set to zero, since we have no a-priori knowledge of the parameter $n(t)$. The least-squares estimator can be interpreted in a Kalman filter framework, with $p(t)$ as the estimation variance ($P(t)$ as the covariance matrix in the multi parameter case) [Lju87, SL91]. When instability occurs, the difference between estimated and actual parameter is larger than the critical value of n , that is

$$|n(t) - \tilde{n}(t)| > n_{crit}.$$

The gain $p(t)$ should be high enough to cope with this situation and should be in the same order of magnitude than n_{crit}^2 . So the upper bound K_0 of $p(t)$ is set to n_{crit}^2 and the initial value of $p(t)$ is also set to n_{crit}^2 . The chosen parameters are

$$\lambda_0 = 100 \quad K_0 = (2\zeta k)^2 \quad p(0) = K_0 \quad \tilde{n}(0) = 0.$$

The simulations are carried out for a completely continuous system. In order to realize the PD controller, we "measure" the rotor velocity instead of differentiating the measured position. Of course, this is only possible with additional velocity sensors³ in a real application, but is easy to accomplish in simulation. The applied integration algorithm is a fixed step algorithm based on an explicit Runge-Kutta (4,5) formula, the Dormand-Price pair. The name of this algorithm is ode5 in Simulink®. The step size is set to 10 μ s.

3 The dynamic behavior of velocity sensors has to be very good, i.e. the relevant time constants have to be much higher than the time constants of the system.

6.7.1. Autonomous 2DoF System with Nonzero Initial Conditions

The simulation results for the 2DoF system with ACCC are plotted in figure 6.7. There is no external excitation in the system, the only source of vibration is a nonzero initial condition of $x_c(0) = 0.1 \mu\text{m}$.

The applied cross-coupling parameter $n(t)/n_{crit}$ is plotted together with the estimated parameter $\tilde{n}(t)/n_{crit}$ in figure 6.7a. The grey background indicates the stable region. This means that the difference between $n(t)$ and $\tilde{n}(t)$ is smaller than n_{crit} when $\tilde{n}(t)$ is inside this region; then the system is stable in a quasi-static sense. In figure 6.7b, the gain $p(t)/K_0$ is plotted. The division by K_0 results in a maximum value of $p(t)/K_0 = 1$. Additionally to the gain, the ratio of the estimated parameter to the applied parameter $\tilde{n}(t)/n(t)$ and the stable region for this ratio is included in the figure.

In figure 6.7c, the first element of the reference force vector $\mathbf{f}_{ref}(t)$ and of the actual cross-coupling force $\mathbf{f}_n(t)$ can be seen. The grey region in this figure is magnified and shown in figure 6.7d. The rotor position itself is not drawn, but the qualitative behavior can also be seen in the reference force.

The applied cross-coupling parameter $n(t)$ is increased from zero to a value of about four times the critical value n_{crit} . In the beginning ($t \leq 0.11$ s), the estimated parameter $\tilde{n}(t)$ does not follow the applied parameter $n(t)$ (fig. 6.7a), but as soon as an unstable whirl develops, the estimation starts and $\tilde{n}(t)$ moves inside the stable region. As the unstable whirl disappears, the estimation stops and starts again when the unstable whirl reappears.

The behavior of the gain $p(t)$ is interesting. As long as there is no unstable whirl, the gain stays at its upper bound (fig. 6.7b); the estimation algorithm is not persistently excited. As the unstable whirl and with it the estimation starts, the gain $p(t)$ decreases, the estimation algorithm is persistently excited, and the forgetting rate is increased, as new information becomes available.

In figure 6.7c and figure 6.7d, the reference force and the cross-coupling force are plotted. It is astonishing how small the difference is. There is only a little phase lag between the actual and the reference force. In order to see the reason for the small reference force error, we look at the different contributions to the error according to equation (6.6). With the transfer functions of equation (6.6), we are able to calculate the transfer error from the force \mathbf{f}_n and the compensation error from the current \mathbf{i}_n ; there is no external force and no corresponding error. These errors together with the actual cross-coupling force $\mathbf{f}_n(t)$ are shown in figure 6.8. Since the system is continuous, we can

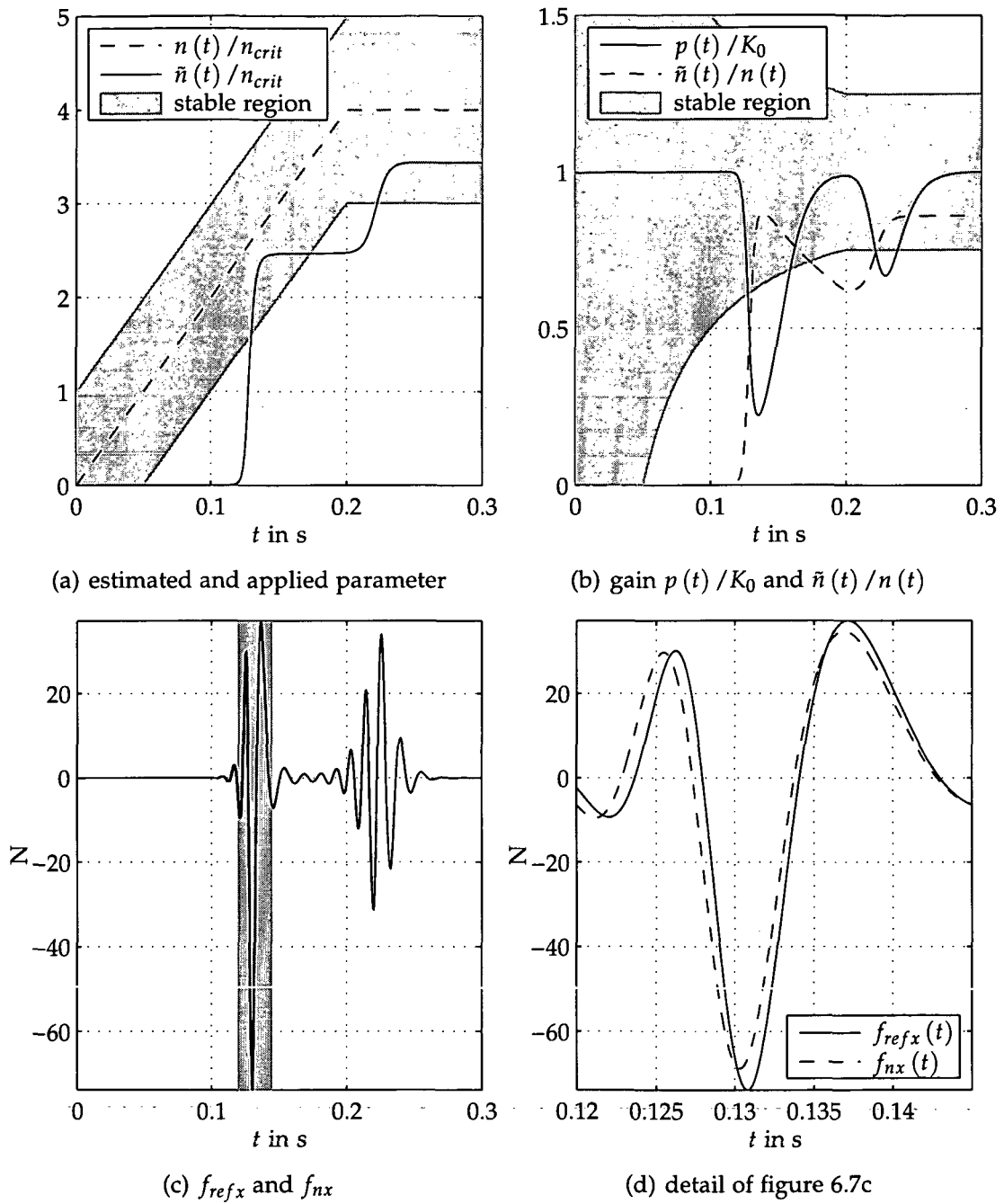


Figure 6.7.: The adaptive control for the 2DoF system with nonzero initial conditions

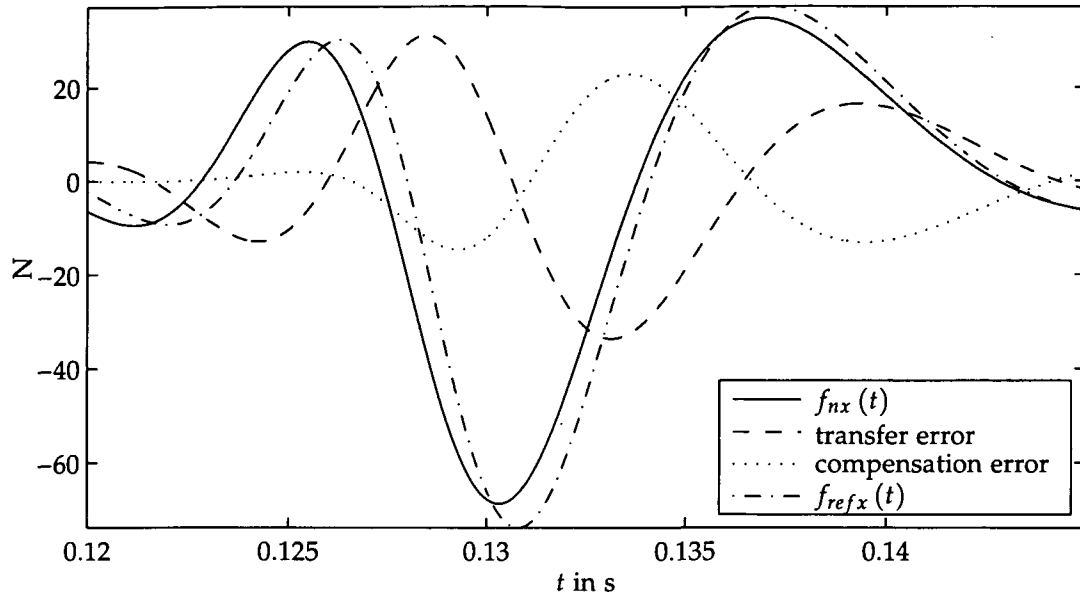


Figure 6.8.: The various errors included in the reference force

sum up the signals from figure 6.8 to get exactly the reference force $f_{ref}(t)$.

It is surprising that the transfer error associated with the difference between $T_{ref}(s)$ and the identity matrix is rather high. The compensation error (associated with the difference between the cross-coupling control force and its backlash on the reference force) partially compensates the transfer error.

6.7.2. 2DoF System with Noise Excitation

In the second simulation case, we set the initial conditions to zero and add white noise with a standard deviation of $1 \mu\text{m}$ to the measured rotor position. Now, the estimated parameter $\tilde{n}(t)$ follows the applied value more closely (fig. 6.9a) and the gain $p(t)$ is much lower (fig. 6.9b) which indicates high persistent excitation. In figure 6.9c the rotor position x_c and in 6.9d the control current i_x are plotted.

A comparison between the reference force and the actual cross-coupling force would not be very useful, because the reference force is too noisy for interpretation. In figure 6.10, the same simulation is carried out as before, but this time the maximum forgetting rate λ_0 is set ten times higher, i.e. $\lambda_0 = 1000$. The estimation still works well, but we see that the gain $p(t)$ is now higher than before and the estimated parameter $\tilde{n}(t)$ is shakier. The rotor

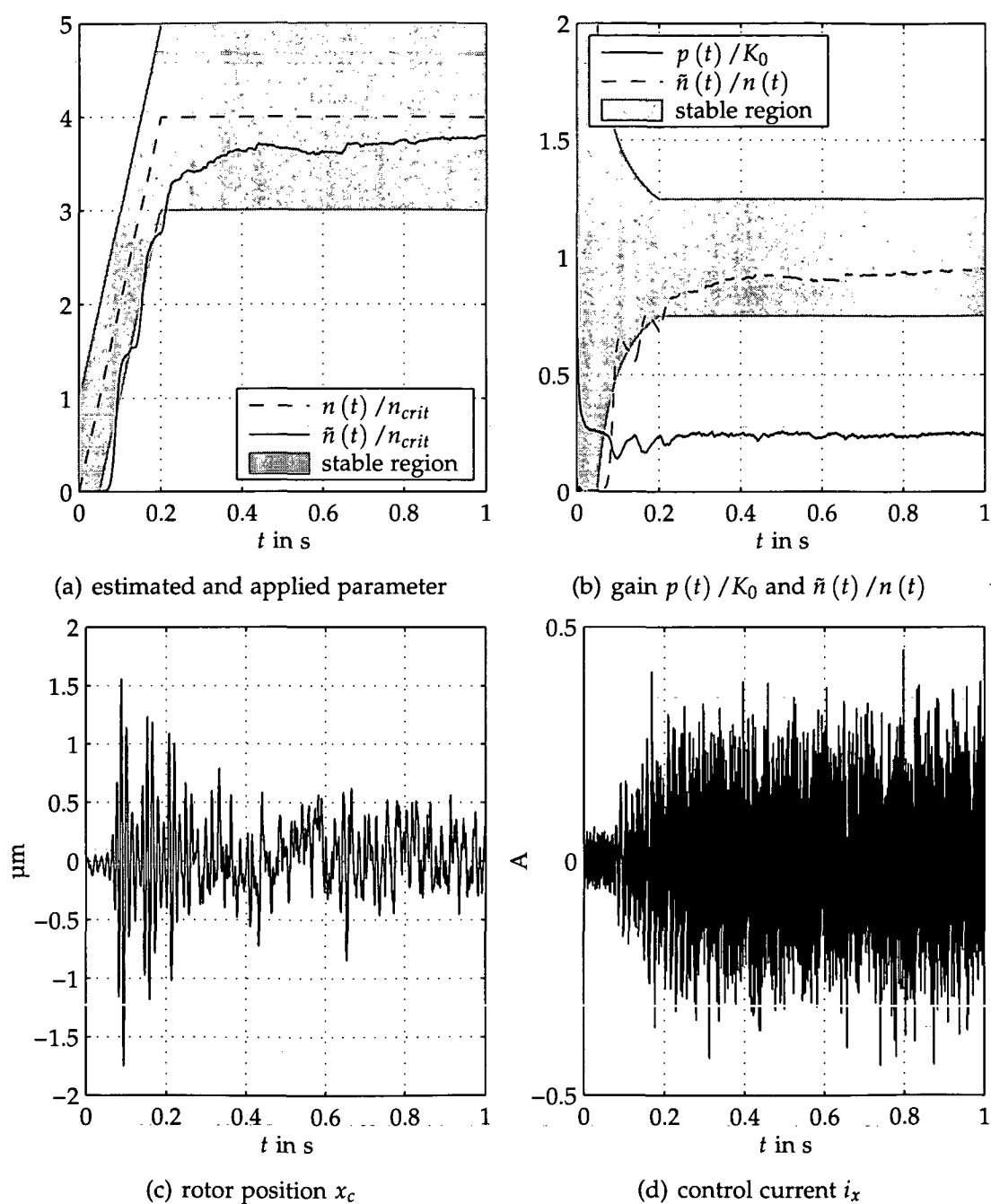


Figure 6.9.: The adaptive control for the 2DoF system with measurement noise and maximum forgetting rate $\lambda_0 = 100$

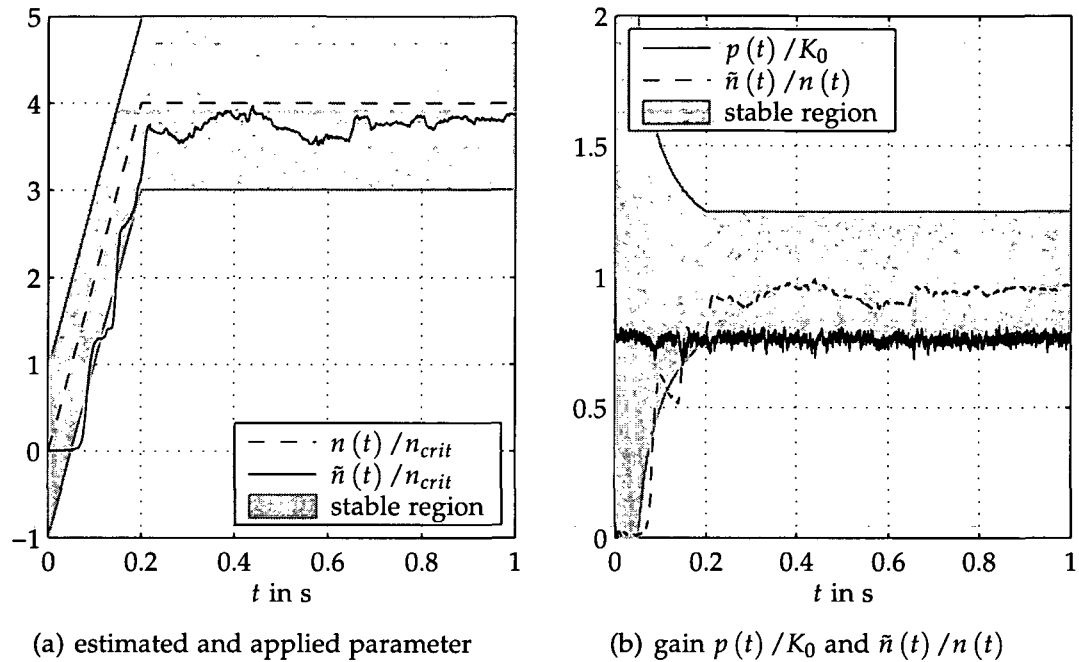


Figure 6.10.: The adaptive control for the 2DoF system with measurement noise and maximum forgetting rate $\lambda_0 = 1000$

displacement (not shown) is similar to the version with $\lambda_0 = 100$, but the amplitude is lower. However, for a higher measurement noise level, the high forgetting rate will lead to a very high variation of the estimated parameter.

In table 6.1, the results of six simulation runs with different values for $n(t)$ and λ_0 are combined. Contrary to the earlier simulation results, where the parameter $n(t)$ starts at zero and increases to a final value, the value of $n(t)$ is kept constant for this simulations to ensure a better comparability.

Table 6.1.: Comparison of different parameters for the 2DoF simulation model

n/n_{crit}	λ_0	ACCC		No ACCC	
		stnd (x_c) μm	stnd (i_x) A	stnd (x_c) μm	stnd (i_x) A
0	100	0.055	0.0255	0.055	0.0255
0.99	100	0.084	0.0268	0.301	0.0281
4	100	0.543	0.126	unstable	
4	1000	0.286	0.111	unstable	

It becomes clear that even when there is no cross-coupling excitation (i.e. $n(t) = 0$) the ACCC does not degrade performance significantly. For a value of n close to the critical value n_{crit} , the ACCC already reduces the rotor vibrations compared to the situation without adaptive cross-coupling control.

6.7.3. 2DoF System with Unbalance Excitation

As demonstrated in subsection 6.7.2, noise input does not degrade the performance of the adaptive control algorithm. A second important class of disturbances beside noise are harmonic disturbances. Especially mass unbalance excitation, which is a rotational speed synchronous harmonic excitation, is very important in rotor dynamics.

Slow Estimator Oscillations

The simulation results for the 2DoF model with adaptive control and unbalance excitation are shown in figure 6.11. The parameter values for the unbalance excitation are $\Omega = 2094$ rad/s and $e = 1.58$ μm , which corresponds to a rotational speed of 20000 r/min, an unbalance force amplitude of 200 N, and a center of gravity velocity of 3.31 mm/s. The estimated parameter $\tilde{n}(t)$ shows now an oscillatory behavior. This is due to the fact that the unbalance excitation leads to an external error in the reference force (see equation (6.6)), which is misinterpreted as a higher cross-coupling parameter than the actually applied $n(t)$. The difference between $|\tilde{n}(t) - n(t)|$ is higher than n_{crit} (\tilde{n}/n_{crit} is outside the stable region in figure 6.11a) and the system is unstable in a quasi-static sense. With this, an unstable whirl develops (as can be seen in the peaks of the rotor position in figure 6.11c). As the unstable whirl increases, the cross-coupling force vector $\mathbf{f}_n(t)$ also increases in magnitude and the external force error—which is constant—gets smaller in comparison to the actual cross-coupling force. With that, the estimation gets better and the system is stabilized again.

The gain $p(t)$ is much lower than in the simulations before (fig. 6.11b), which also results in a higher forgetting rate. The position x_c and the control current i_x are plotted in figures 6.11c and 6.11d. The horizontal lines indicate the amplitudes of x_c and i_x without adaptive control and cross-coupling excitation ($n(t) = 0$). The adaptive control in conjunction with unbalance excitation leads to a very high vibration level of the rotor position as well as of the control current.

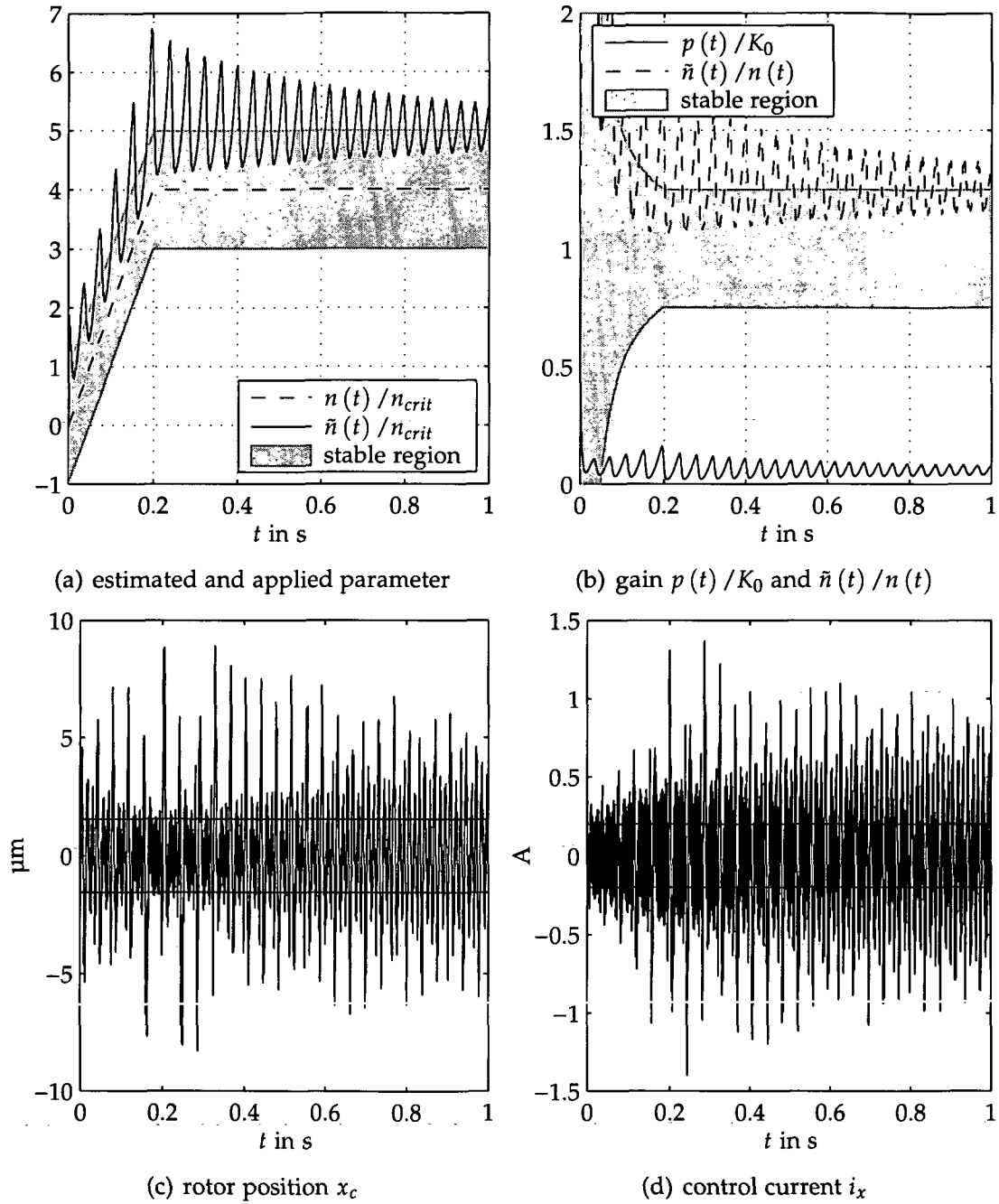


Figure 6.11.: The adaptive control for the 2DoF system with unbalance excitation $\Omega = 2094$ rad/s, $e = 1.58$ μm

We note that the oscillation frequency of the estimated parameter $\tilde{n}(t)$ is not directly related to the rotational speed and the frequency of the unbalance excitation. Of course, there is a relationship, but the oscillation frequency of $\tilde{n}(t)$ is not a multitude of the rotational speed. The influence of the unbalance excitation on the estimation algorithm will be discussed in section 6.8.

The parameters λ_0 and $K_0 = p(0)$ have an important influence on the oscillation frequency of $\tilde{n}(t)$. This is shown in figures 6.12 and 6.13 where λ_0 is set to $\lambda_0 = 10$ and the upper bound of $p(t)$ is set to $K_0 = n_{crit}^2/100$ respectively. Both parameter changes have a similar effect; the oscillation frequency of $\tilde{n}(t)$ is decreased. The gain in 6.12b is very low while in 6.13b it is at its upper bound. The difference between figure 6.12b and figure 6.13b may seem very striking, but in absolute numbers $p(t)$ and $\lambda(t)$ are in the same order of magnitude for both cases, only the qualitative course is different.

So far we have seen that the estimated parameter $\tilde{n}(t)$ oscillates and the parameters of the estimation algorithm influence the oscillation. The oscillation frequency is low compared to the rotational frequency. A typical example is shown in figure 6.14, together with the discrete Fourier transform of the estimated parameter and the rotor position. The time interval of one second is taken for the DFT, so that the frequency resolution is 1 Hz. The signal is multiplied with a Hanning window divided by the mean value of the window. This normation to a window mean value of one keeps the peak value of a frequency spike close to the real value of the corresponding Fourier coefficient, while the "energy" of the spike is higher than the energy of the actual frequency, since the spike is broader.⁴

The spectrum of $\tilde{n}(t) - n(t)$ is shown in figure 6.14b. The first harmonic of $\tilde{n}(t)$ is at 24 Hz and we can see the next three harmonics in the figure. Above the rotational frequency of 433 Hz we see some small peaks. The natural frequency of the system $\omega_0 = 500.8 \text{ rad/s} \triangleq 79.71 \text{ Hz}$ does not appear at all. In figure 6.14d, the harmonics of the estimator oscillations appear as sidebands of the natural frequency, which is the peak at 80 Hz. Of course, the rotational frequency also appears in the rotor position signal.

⁴ Usually window functions are defined such that the area under their Fourier transform is one. A multiplication with a window function in the time domain broadens and decreases peaks in the frequency domain; the energy content of the peak is preserved. The rectangular window is an exception.

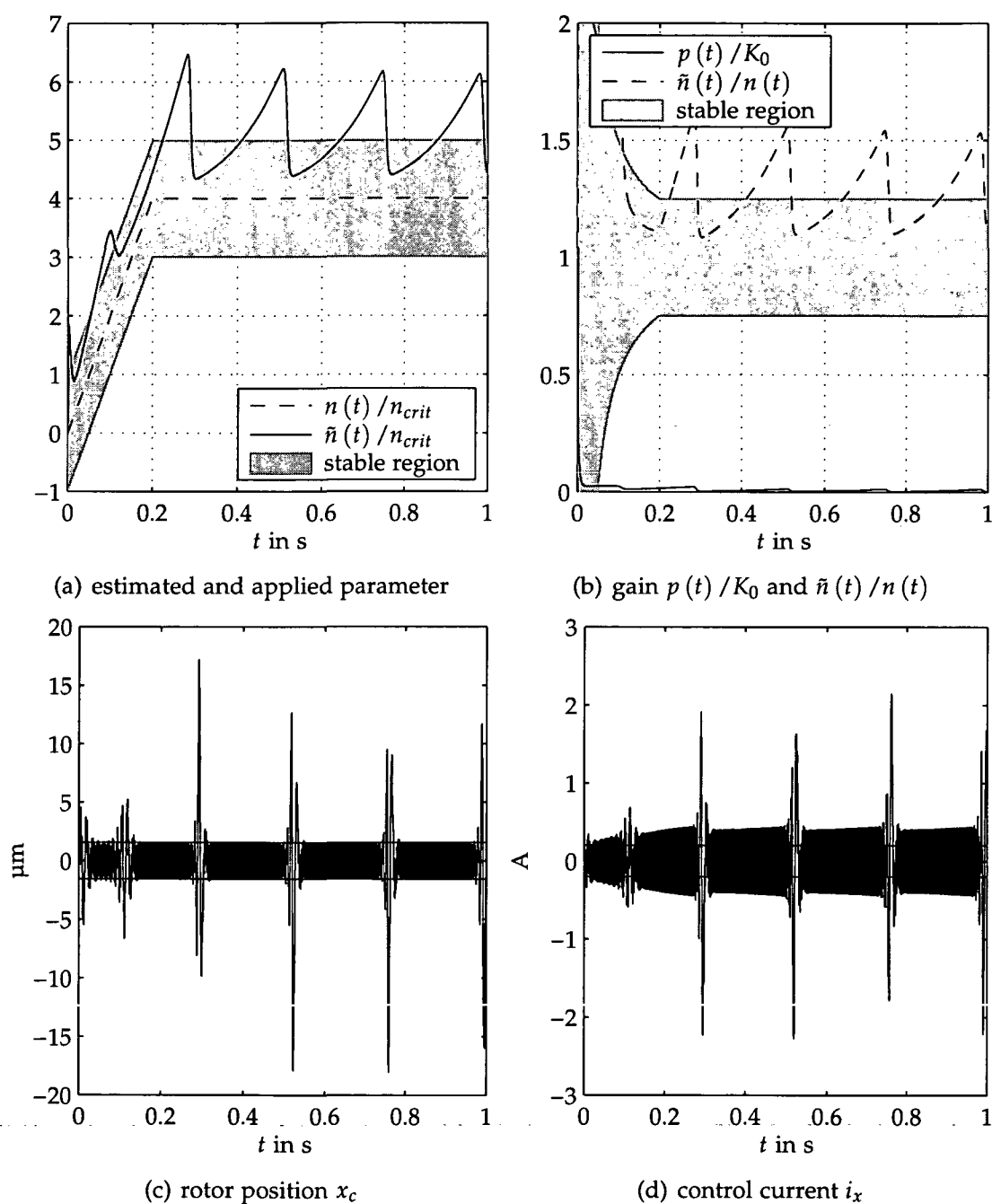


Figure 6.12.: The adaptive control for the 2DoF system with unbalance excitation $\Omega = 2094$ rad/s, $e = 1.58$ μm , and $\lambda_0 = 10$

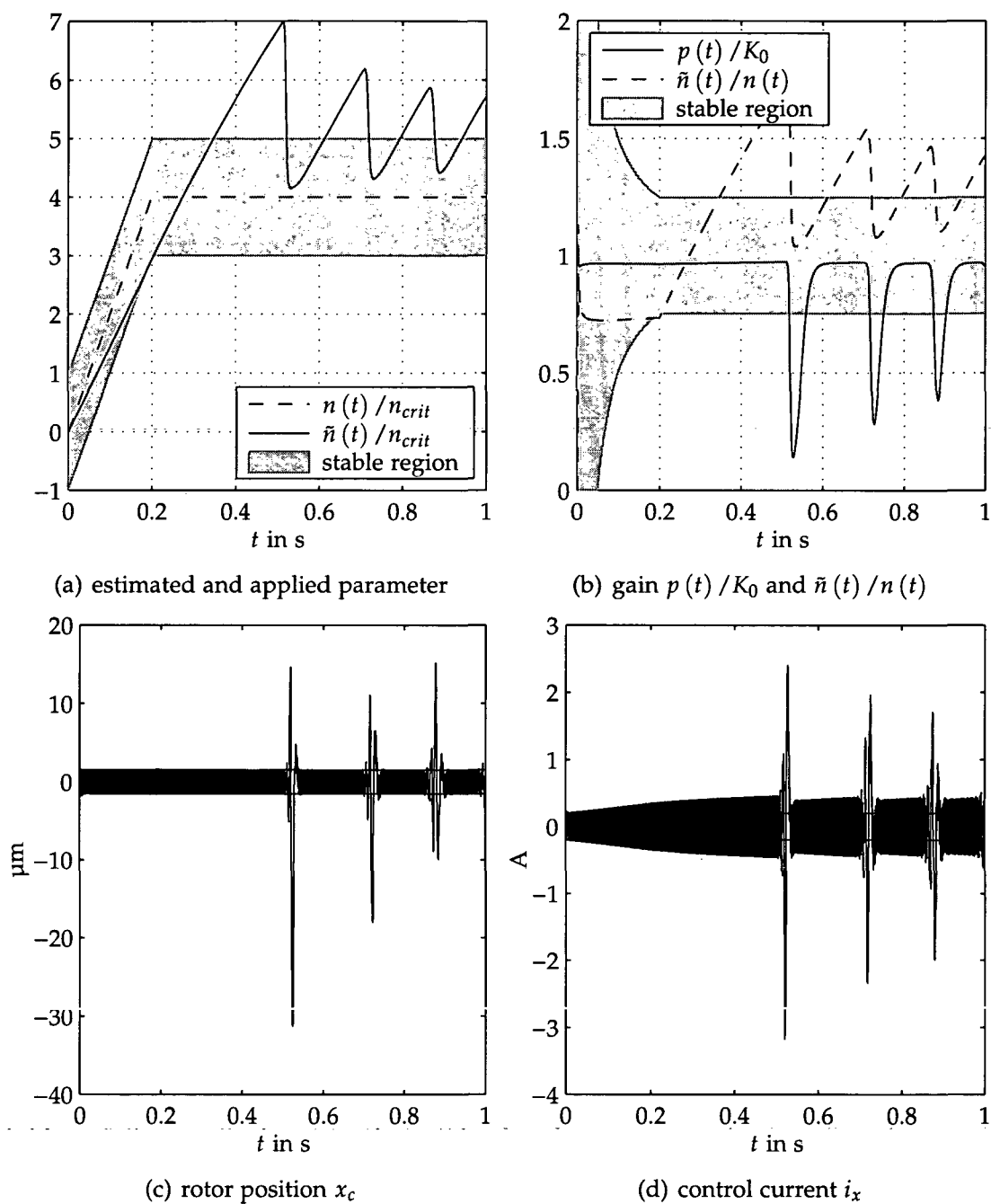


Figure 6.13.: The adaptive control for the 2DoF system with unbalance excitation $\Omega = 2094 \text{ rad/s}$, $e = 1.58 \mu\text{m}$, and $K_0 = (2\zeta k)^2 / 100$

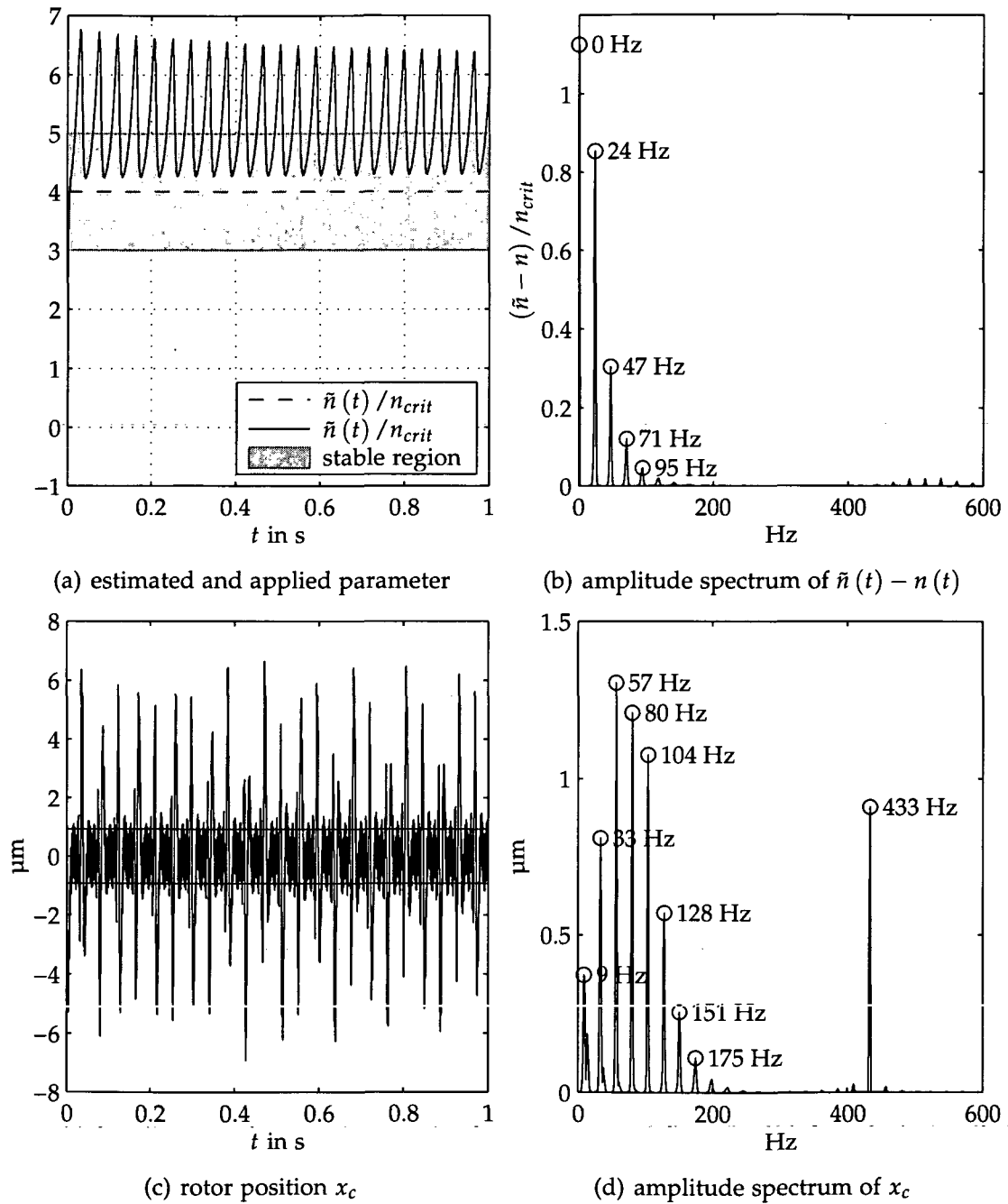


Figure 6.14.: The adaptive control for the 2DoF system with unbalance excitation $\Omega \triangleq 433$ Hz, $e = 0.94 \mu m$

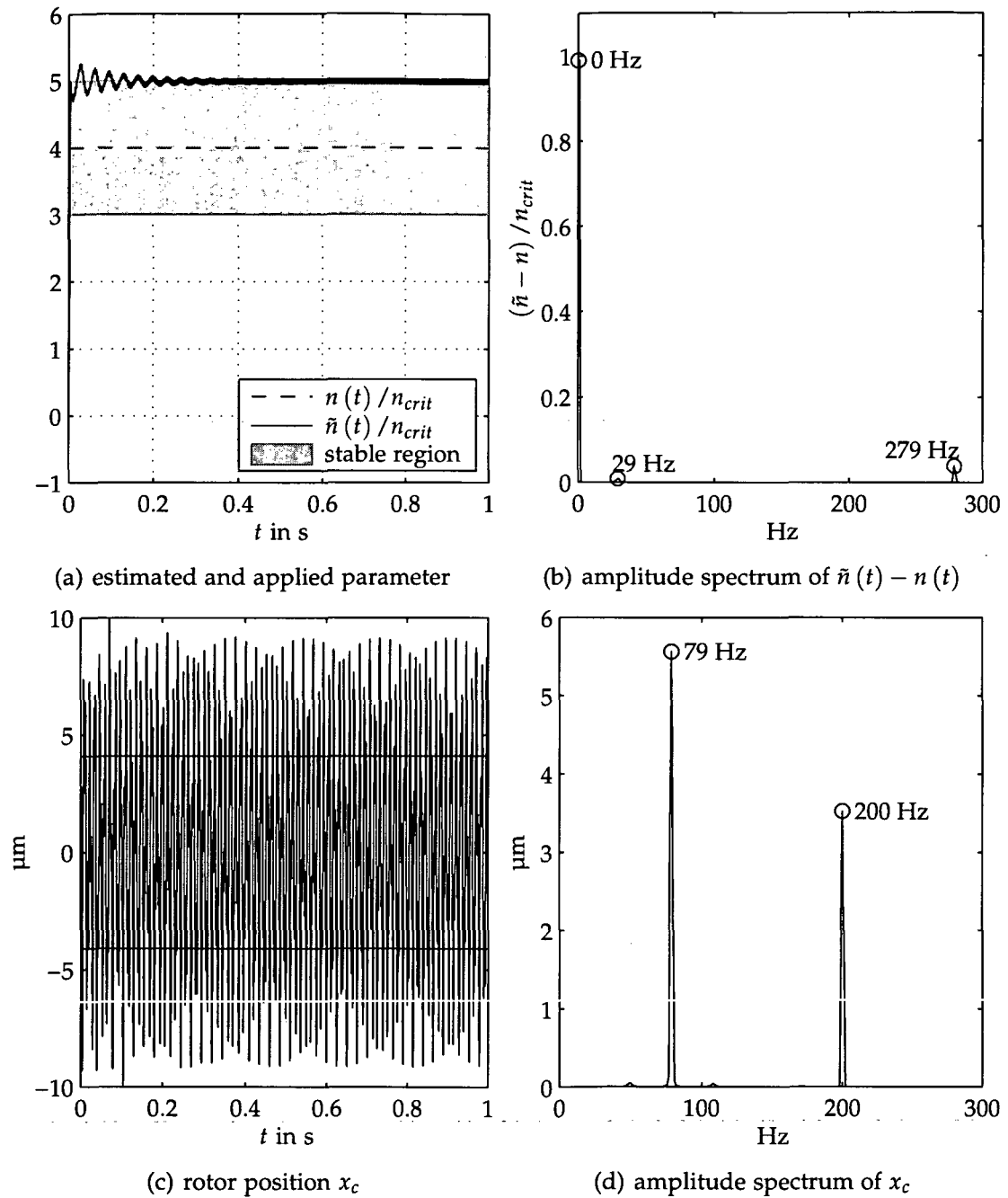


Figure 6.15.: The adaptive control for the 2DoF system with unbalance excitation $\Omega \cong 200$ Hz, $e = 4.4 \mu\text{m}$

Fast Estimator Oscillations

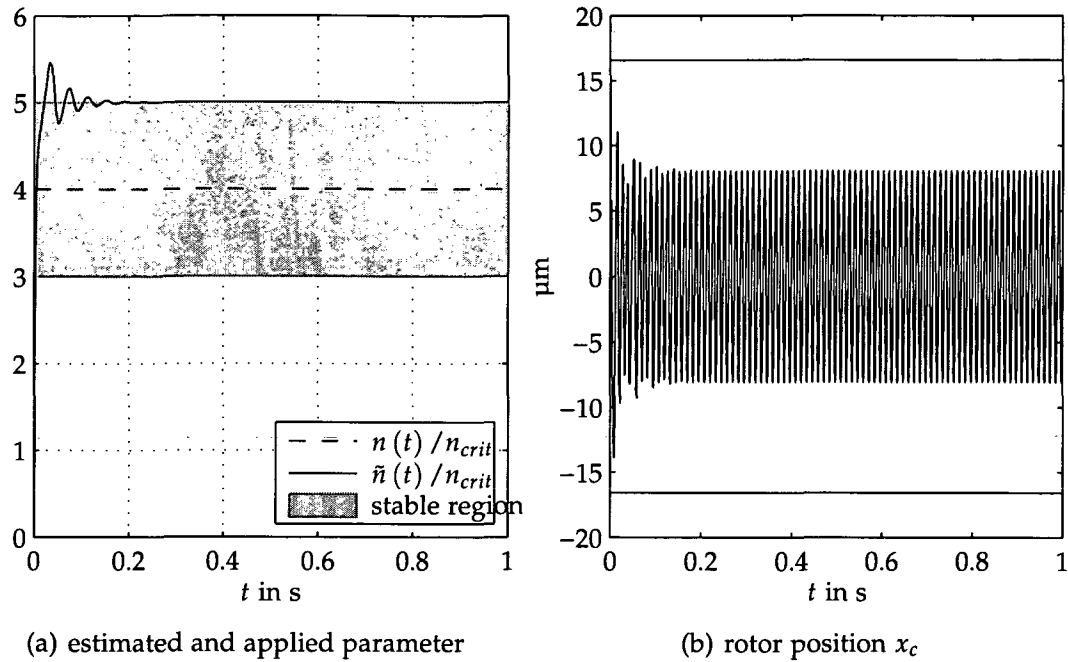


Figure 6.16.: The adaptive control for the 2DoF system with unbalance excitation $\Omega = \omega_0$, $e = 27.7 \mu\text{m}$

For a lower rotational speed of 200 Hz, a quite different behavior can be observed, as shown in figure 6.15. The “slow oscillation” of $\tilde{n}(t)$ rapidly wears off and only a very fast oscillation remains. The DFT shows that the frequency of this oscillation is the rotational frequency plus the natural frequency of the system. This oscillation is also harmonic since no high-orders are present. The mean value of the estimated parameter is approximately $n + n_{crit}$. In the rotor oscillations, we have only a component with the natural frequency and a component with the rotational frequency. The amplitude of the rotor vibration is higher than for the case $n = 0$, which is marked by the horizontal lines in figure 6.15c.

When the rotational speed is further decreased to match the natural frequency an interesting effect is recognized (see fig. 6.16). After all transients have decayed, the high frequency oscillation also disappears and the estimated cross-coupling parameter \tilde{n} is $n + n_{crit}$. Looking at the rotor vibration, we see that the amplitude is reduced dramatically, even compared to the system without cross-coupling excitations, which is marked by the horizontal

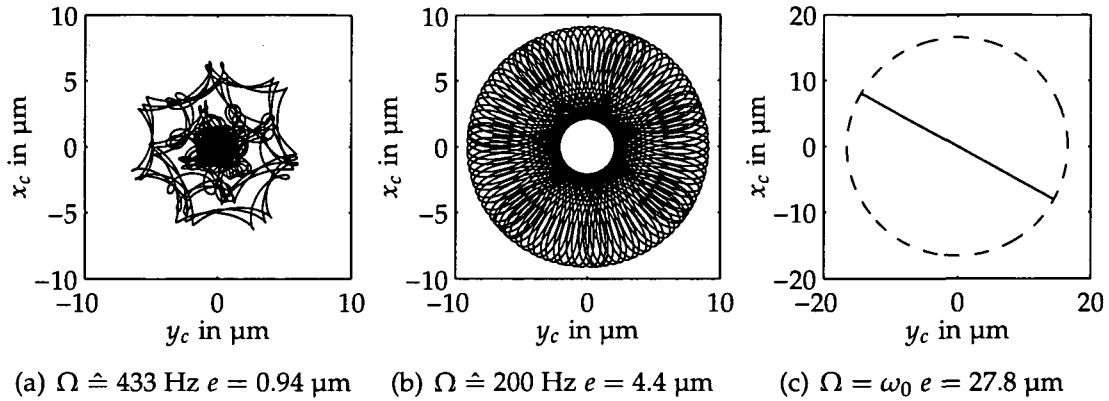


Figure 6.17.: Rotor orbits for the simulations in the figures 6.14, 6.15, and 6.16

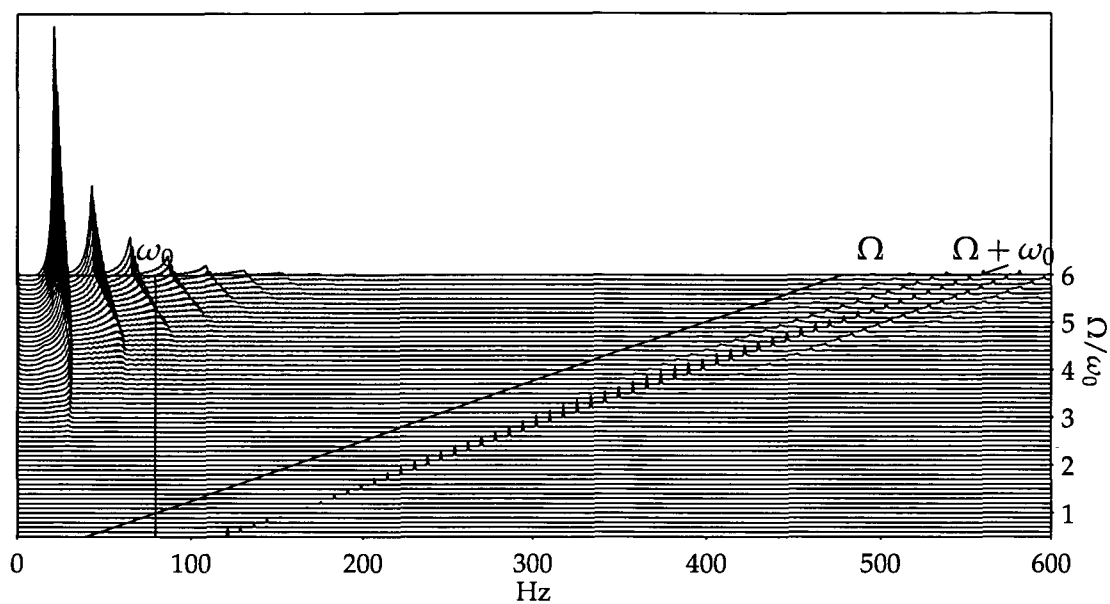
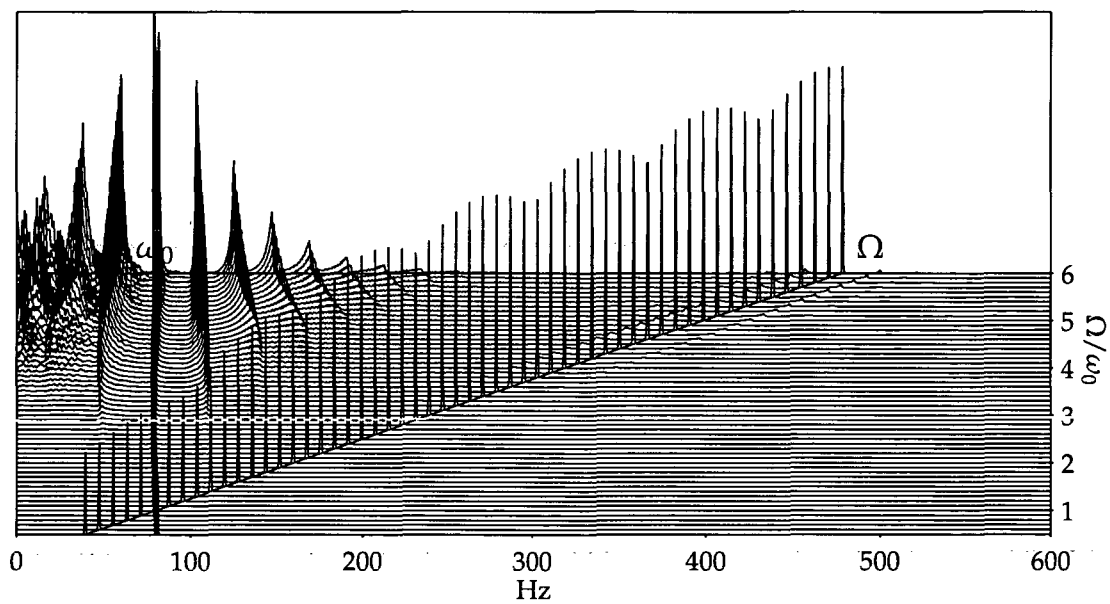
lines again. An explanation for this effect can only be found by looking at the actual rotor orbits given in figure 6.17. It only appears that the rotor orbit is smaller than the orbit without cross-coupling excitation, which is drawn as a dashed circle. The orbit itself has degraded to a line, and the amplitude of the x coordinate is a projection of this line on the x -axis. The actual angle between the "orbit" and the coordinate axes depends on the initial conditions. When the rotational speed is lower than the natural frequency this phenomenon disappears and the situation is similar as in figure 6.15.

Waterfall plots

In order to investigate the occurrence of fast or slow oscillations, the rotational frequency is varied from $0.5\omega_0$ to $6\omega_0$, and the DFTs of $\tilde{n} - n$ and x_c are carried out. The results are plotted in a so-called "waterfall-diagram". To reduce the influence of transients, the simulations are carried out for 3 s; the DFT is taken from the last 2.62 s which results in a frequency resolution of 0.38 Hz. The unbalance amplitude is chosen in a way that the rotor vibration amplitude would be $10 \mu\text{m}$ in the case $n = 0$ in the whole rotational speed range. The applied parameter n is kept constant at a value of $n = 4 n_{crit}$. Additionally to the DFT results, the lines for the natural frequency ω_0 and the rotational frequency Ω are plotted in figure 6.18.

We can see in figure 6.18a that the low frequency oscillation of the estimated value $\tilde{n}(t)$ only appear for higher values of Ω , whereas the high frequency oscillations appear in the whole range of Ω and have the frequency $\Omega + \omega_0$.

The waterfall plot of the rotor vibrations is shown in figure 6.18b. The oscillations with the natural frequency exist for the whole range of Ω . As soon as

(a) Waterfall plot of $\tilde{n}(t) - n(t)$ (b) Waterfall plot of the rotor position x_c Figure 6.18.: Waterfall plots for a variation of the rotational frequency Ω

the low frequency estimator oscillations start, the sidebands of the natural frequency oscillations appear. Although the amplitude of the speed synchronous oscillations with the frequency Ω should be constant, however, the peaks in figure 6.18b are not constant. A reason for that is mainly the limited frequency resolution of the DFT.

Finally, we should note that, for different parameters or a discrete version of the system, the waterfall plots may be very different from the plots as shown here.

6.8. Analysis of the 2DoF System with Unbalance Excitation

6.8.1. Analytic Solution of the On-Line Estimator for a Constant Whirl Radius

Finding an analytic solution for the 2DoF model with adaptive control and unbalance excitation is probably impossible. However, if we only investigate the estimation algorithm without the adaptive control, and if we assume a circular whirl motion with constant radius X , i.e.

$$\begin{bmatrix} x_c \\ y_c \end{bmatrix} = X \begin{bmatrix} \cos \Omega t \\ \sin \Omega t \end{bmatrix},$$

and furthermore a constant circulating reference force with an amplitude F and a phase lag ϕ between the reference force and the rotor displacements, i.e.

$$\begin{bmatrix} f_{refx} \\ f_{refy} \end{bmatrix} = F \begin{bmatrix} \cos (\Omega t + \phi) \\ \sin (\Omega t + \phi) \end{bmatrix},$$

then a solution can be found. The above assumptions are valid for an unbalance excited stable rotor when all transients have decayed.

The solution of the differential equations for

$$p(0) = K_0, \tilde{n}(0) = 0 \text{ and } \lambda(t) = \lambda_0 \left(\frac{|p|}{K_0} - 1 \right)$$

are

$$p(t) = \lambda_0 \frac{K_0}{\lambda_0 + X^2 K_0 (1 - e^{-\lambda_0 t})}$$

$$\tilde{n}(t) = \frac{F \sin \phi}{X} \left(1 - \left(\frac{\lambda_0 e^{-\lambda_0 t}}{\lambda_0 + X^2 K_0 (1 - e^{-\lambda_0 t})} \right)^{\frac{X^2 K_0}{\lambda_0 + X^2 K_0}} \right).$$

It is interesting that the frequency Ω does not appear in this solution. The final value of $\tilde{n}(t)$ then is

$$\lim_{t \rightarrow \infty} \tilde{n}(t) = \frac{F \sin \phi}{X}. \quad (6.10)$$

This result is exactly the perpendicular component of the reference force vector \mathbf{f}_{ref} on the rotor position vector \mathbf{x} . Since \mathbf{f}_{ref} and \mathbf{x} rotate with the same angular speed around the origin, the perpendicular component of \mathbf{f}_{ref} on \mathbf{x} is constant and the estimated parameter $\tilde{n}(t)$ approaches a steady value. The speed of convergence cannot be expressed by such a simple equation. However, at the initial time $t = 0$ the convergence speed is

$$\dot{\tilde{n}}(t)|_{t=0} = K_0 X^2 \frac{F \sin \phi}{X}.$$

For $t > 0$, λ_0 also influences the convergence speed.

6.8.2. Prediction of Estimator Oscillations

The obvious result of equation (6.10) for the final value of $\tilde{n}(t)$ leads to a prediction method of estimator oscillations in the adaptive control case. If we assume that the only external excitations are the unbalance forces and the system is stable, we can assume that a steady state solution of \mathbf{x} will be a harmonic oscillation with the same frequency Ω as the frequency of \mathbf{f}_{ub} .

The reference force in the 2DoF case is

$$\begin{bmatrix} \hat{f}_{refx}(s) \\ \hat{f}_{refy}(s) \end{bmatrix} = \begin{bmatrix} k_i p_F - k_s + k_i p_D s & 0 \\ 0 & k_i p_F - k_s + k_i p_D s \end{bmatrix} \begin{bmatrix} \hat{x}_c(s) \\ \hat{y}_c(s) \end{bmatrix} - \begin{bmatrix} \tilde{n} \hat{y}_c(s) \\ -\tilde{n} \hat{x}_c(s) \end{bmatrix}.$$

For the sake of convenience, we will use a complex notation (see section A.1.1)

$$x_c(t) + jy_c(t)$$

instead of the displacement vector \mathbf{x} . The complex cross-coupling force is then written in the form

$$f_{nx} + jf_{ny} = jn(x_c + jy_c)$$

and the complex reference force is

$$f_{refx}(t) + j f_{refy}(t) = (k_i p_P - k_s + k_i p_D j\Omega + j\tilde{n}) (x_c(t) + jy_c(t)) .$$

From equation (6.10), we know that $\tilde{n}(t)$ converges to the orthogonal part of f_{ref} on x divided by the length of x . In complex notation, this can be written as

$$\lim_{t \rightarrow \infty} \tilde{n}(t) = \lim_{t \rightarrow \infty} \operatorname{Re} \left(\frac{f_{refx} + j f_{refy}(t)}{j(x_c(t) + jy_c(t))} \right)$$

if $\lim_{t \rightarrow \infty} \tilde{n}(t)$ exists. By canceling $(x_c + jy_c)$ we get a complex equation for the final value $\lim_{t \rightarrow \infty} \tilde{n}(t)$ of $\tilde{n}(t)$

$$\lim_{t \rightarrow \infty} \tilde{n}(t) = \operatorname{Re} \left(\frac{k_i p_P - k_s + k_i p_D j\Omega}{j} \right) + \lim_{t \rightarrow \infty} \tilde{n}(t) ,$$

which obviously has the solution $\lim_{t \rightarrow \infty} \tilde{n}(t) = \infty$ as long as

$$\operatorname{Re} \left(\frac{k_i p_P - k_s + k_i p_D j\Omega}{j} \right) \neq 0 .$$

This means that for the proposed adaptive control algorithm there is no steady state solution for $\tilde{n}(t)$ under the assumption of harmonic rotor oscillations.

When we use the compensation current and the reference position filters as described in subsection 6.4.1 the situation is different. For the 2DoF model the current filter $F_i(s)$ (equation (6.7)) and the position filter $F_x(s)$ (equation (6.8)) are diagonal transfer matrices, that is ⁵

$$F_i(s) = \begin{bmatrix} k_i F_i(s) & 0 \\ 0 & k_i F_i(s) \end{bmatrix} \quad \text{and} \quad F_x(s) = \begin{bmatrix} F_x(s) & 0 \\ 0 & F_x(s) \end{bmatrix} ,$$

we get the following equation for the limit value of the parameter estimate;

$$\lim_{t \rightarrow \infty} \tilde{n}(t) = \lim_{t \rightarrow \infty} \operatorname{Re} \left(\frac{k_i p_P - k_s + k_i p_D j\Omega + F_i(j\Omega) j \tilde{n}(t)}{j F_x(j\Omega)} \right) .$$

This can be solved for $\lim_{t \rightarrow \infty} \tilde{n}(t)$ and the result is

$$\lim_{t \rightarrow \infty} \tilde{n}(t) = \frac{\operatorname{Re} \left(\frac{k_i p_P + k_i p_D j\Omega - k_s}{j F_x(j\Omega)} \right)}{\operatorname{Re} \left(1 - \frac{F_i(j\Omega)}{F_x(j\Omega)} \right)} . \quad (6.11)$$

⁵ The current coefficient k_i is included in the matrix F_i to be compatible with the definition given by equation (6.7).

We note that neither the rotor vibration amplitude nor the unbalance amplitude influences this solution. There is no solution for $F_i(j\Omega) = F_x(j\Omega)$. It is possible, however, to use $F_i(s)$ or $F_x(s)$ alone. F_i and F_x are chosen according to equation (6.7) and (6.8), thus $F_i(s)$ and $F_x(s)$ are given by

$$F_i(s) = F_x(s) = T_{ref}(s) = \frac{k_i p_P - k_s + k_i p_D s}{s^2 m + k_i p_P - k_s + k_i p_D s} = \frac{\omega_0^2 + 2D\omega_0 s}{s^2 + 2D\omega_0 s + \omega_0^2}. \quad (6.12)$$

The limit value of the parameter estimate given by equation (6.11), when either F_i or F_x is used, is plotted in figure 6.19a together with the results for $i_n = 0$ (no adaptive control). If there is no adaptive control the usage of F_x does not change the limit value of $\tilde{n}(t)$; the curve in figure 6.19a for $i_n = 0$ is valid with and without F_x . Both filters are defined by equation (6.12).

Additional to the results for the continuous-time 2DoF, the results for a discrete-time PD controller are shown in figure 6.19b. Although we have not described the discrete PD controller for the 2DoF case, these results are important, since they are significantly different from the continuous PD controller results. Moreover, they are also important for the 4DoF case. Similar results have been found for the discrete-time controlled 2DoF system in [Hir03a],

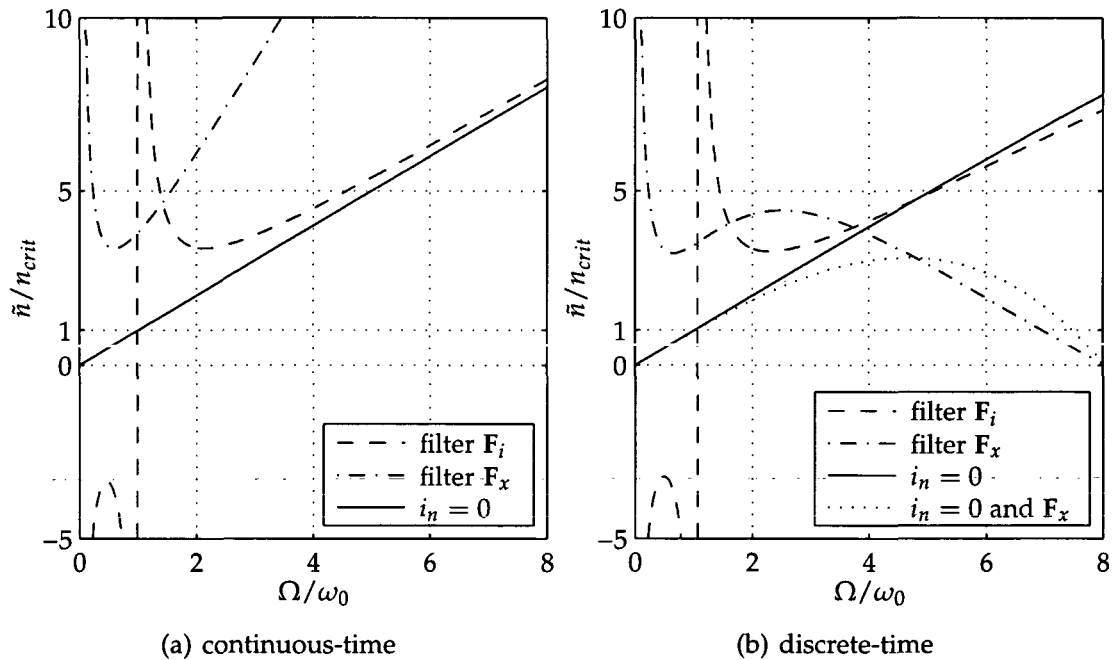


Figure 6.19.: Steady state value of \tilde{n} in the case of unbalance excitation

with the additional assumption that the stable rotor oscillations with cross-coupling are similar to the oscillations without cross-coupling.

When the predicted limit value of $\lim_{t \rightarrow \infty} \tilde{n}(t)$ in figure 6.19 is outside the stable region, that is $|\lim_{t \rightarrow \infty} \tilde{n}(t) - n(t)| \geq n_{crit}$, an oscillatory behavior in the estimated parameter $\tilde{n}(t)$ like in section 6.7.3 can be expected. If $|\lim_{t \rightarrow \infty} \tilde{n}(t) - n(t)| < n_{crit}$, there should be no oscillatory behavior, because the unbalance excitation drives the estimated value $\tilde{n}(t)$ into the stable region.

Three simulations are carried out to clarify the meaning of the results plotted in figure 6.19. Figure 6.20 shows the simulation result for the system with compensation current filter F_i , when we choose the applied cross-coupling intensity $n(t)$ to go exactly to the predicted value of $\lim_{t \rightarrow \infty} \tilde{n}(t) = 3.367 n_{crit}$ for $\Omega = 2\omega_0$. We see that the "prediction" is excellent, as $\tilde{n}(t)$ converges to the exact value of $n(t)$. Because the system is stabilized ($n(t) - \tilde{n}(t) = 0$), the rotor vibration has the same amplitude as it would have without cross-coupling excitation, which is indicated by the two horizontal lines.

After 0.5 s, the applied parameter $n(t)$ jumps back to zero. The estimated parameter $\tilde{n}(t)$ follows the applied parameter; the estimation is still working. After the jump, we have a high frequency oscillation of the estimated parame-

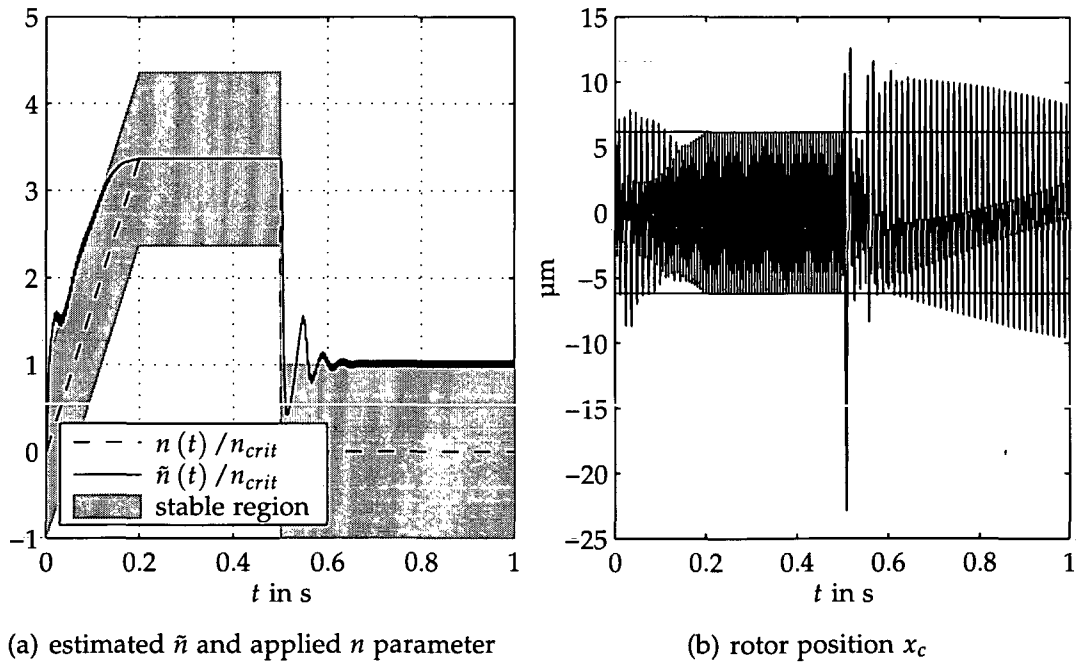


Figure 6.20.: The adaptive control with compensation current filter $F_i(s)$ for the 2DoF system with unbalance excitation $\Omega = 2\omega_0$

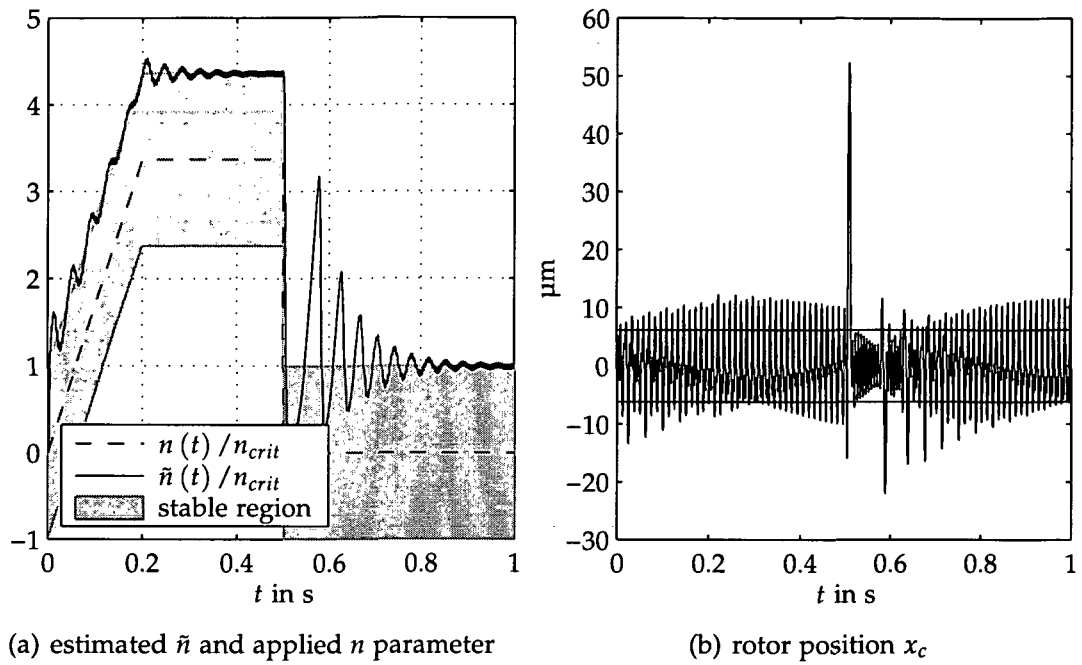


Figure 6.21.: The adaptive control without filters for the 2DoF system with unbalance excitation $\Omega = 2\omega_0$

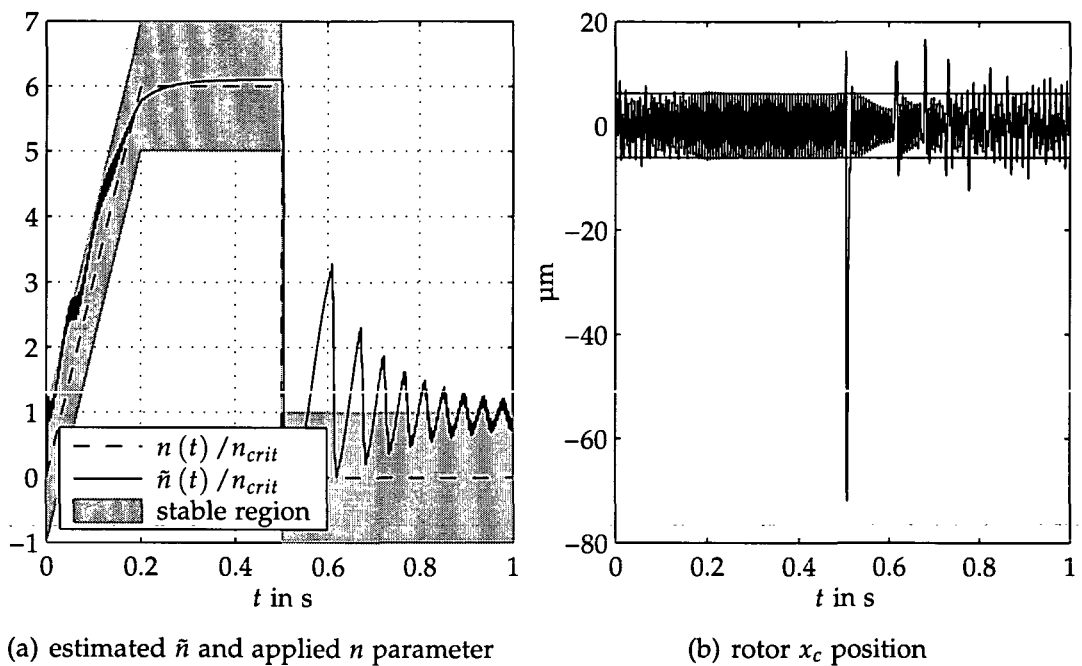


Figure 6.22.: The adaptive control with position filter $F_x(s)$ for the 2DoF system with unbalance excitation $\Omega = 2\omega_0$

ter $\tilde{n}(t)$, similar to figure 6.15. This is not a result of the usage of the filter, but a result of the chosen parameter set.

In figure 6.21, the same simulation is carried out without any filter. Compared to the simulation with filter $F_i(s)$, the estimated parameter always oscillates with a high frequency around the value $n(t) + n_{crit}$. The jump itself induces a low frequency oscillation of $n(t)$ with a higher amplitude than before, but it decays quickly.

Figure 6.22, shows an example for the usage of the position filter $F_x(s)$. All parameters are the same as before, only the maximum value of the applied cross-coupling stiffness is now $6n_{crit}$. We have a similar behavior as in figure 6.20 before the jump, while the situation after the jump looks like in figure 6.21.

6.9. Simulation Results 4DoF System

For the simulation of the 4DoF case, we use the nonlinear AMB model including amplifier saturation (see section 3.2) and the discrete-time PID controller (see section 5.4). This has an important consequence; the rotor position as well as the magnetic bearing forces are limited, and this may result in a system where the center position of the rotor is locally asymptotically stable but not globally, since the magnetic bearing force is not sufficient to stabilize large orbits.

For the on-line parameter estimation algorithm, a discrete-time version has to be found in order to be "compatible" with the PID controller. A possibility would be to use the discrete least-squares algorithm described in section A.5.2. However, it is computationally easier to use the forward difference quotient to get a simple discrete-time approximation of the continuous-time algorithm given by equations (6.2) and (6.3). The resulting estimation algorithm is

$$\begin{aligned}\tilde{\mathbf{n}}(k+1) &= \tilde{\mathbf{n}}(k) + T_s \mathbf{P}(k) \mathbf{X}^T(kT_s) (\mathbf{f}_n(kT_s) - \mathbf{X}(kT_s) \tilde{\mathbf{n}}(k)) \\ \mathbf{P}(k+1) &= \mathbf{P}(k) (1 + \lambda(kT_s) T_s) - T_s \mathbf{P}(k) \mathbf{X}^T(kT_s) \mathbf{X}(kT_s) \mathbf{P}(k) .\end{aligned}$$

No matrix inversion is needed in contrast to the discrete least-squares algorithm given by equations (A.3) and (A.4). The sample time for the estimation algorithm is set to the same value as the sample time for the PID algorithm.

As in section 6.7, we have to choose the parameters of the estimator. For equal parameter values n_1 to n_3 , the system gets unstable approximately for $n_1 = n_2 = n_3 > 3 \text{ MN/m}$. Analogous to section 6.7 we choose the upper

bound K_0 of the norm of the gain matrix $\mathbf{P}(t)$ to be $(3 \text{ MN/m})^2$ and the initial value of $\mathbf{P}(t)$ is set to $\mathbf{I} (3 \text{ MN/m})^2$. The chosen parameters are:

$$\lambda_0 = 100 \quad K_0 = (3 \text{ MN/m})^2 \quad \mathbf{P}(0) = \mathbf{I} (3 \text{ MN/m})^2 \quad \tilde{\mathbf{n}}(0) = \mathbf{0}.$$

The used integration algorithm is a fixed step algorithm based on an explicit Runge-Kutta (4,5) formula, the Dormand-Price pair. The name of this algorithm is ode5 in Simulink®. The step size is 10 μs .

6.9.1. Autonomous 4DoF System with Nonzero Initial Conditions

The simulation results for the autonomous system with nonzero initial conditions are plotted in figure 6.23. The behavior of the system is quite similar to the 2DoF Model in figure 6.7. A difference in the graphical representation is that it is not possible to plot the stability limit of the system without adaptive control and the stable region of the estimated parameters, since the stability depends on three independent parameters.

The applied and the estimated parameters in figure 6.23a are not marked separately. However, they can be recognized, by their different behavior. At first the parameter $n_2(t)$ increases from 0 to 20 MN/m, then $n_1(t)$ increases from 0 to 15 MN/m, and finally $n_3(t)$ increases from 0 to 10 MN/m. It takes some time until the changes in the applied parameters affect the estimated parameters. It is interesting that \tilde{n}_1 and \tilde{n}_2 have approximately the same value, as long as the applied parameter $n_1(t)$ starts to rise and with it the estimated parameter \tilde{n}_1 . The norm of the gain matrix $\|\mathbf{P}(t)\|$ is exceeding its "upper bound" K_0 for a short time interval. An explanation for this phenomenon is the discrete-time approximation of the continuous-time estimation algorithm.

6.9.2. 4DoF System with Noise Excitation

Figure 6.24 shows the response of the system to white noise with a standard deviation of 1 μm added to the measured rotor position. The vibration of the rotor position x_A , shown in figure 6.24b, is quite high with a standard deviation of 2.589 μm . This is mainly the result of the high noise amplification of the PID controller. The estimated parameters in figure 6.24a also show a very shaky behavior, but the system is still stable.

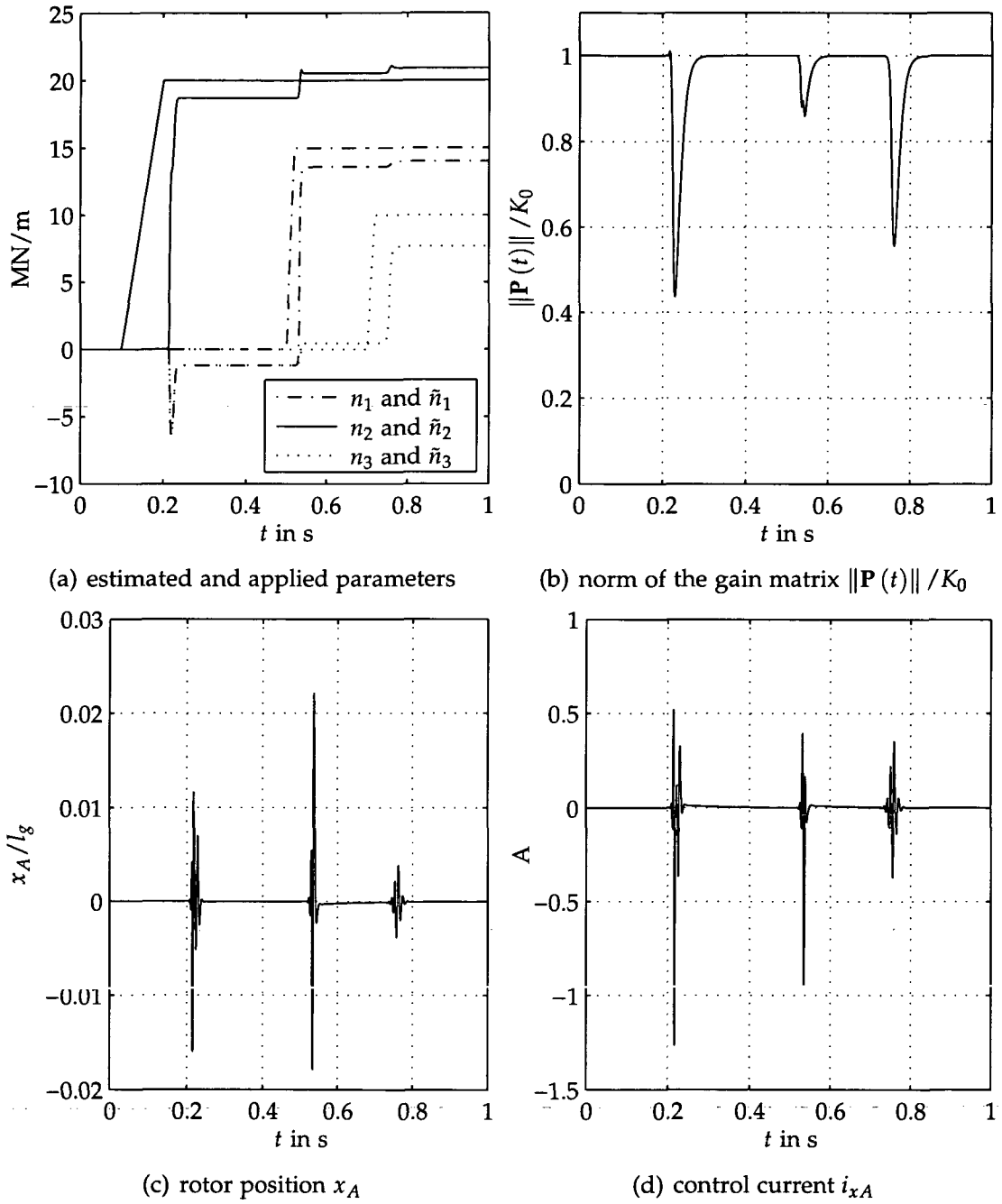


Figure 6.23.: The adaptive control for the 4DoF system with nonzero initial conditions

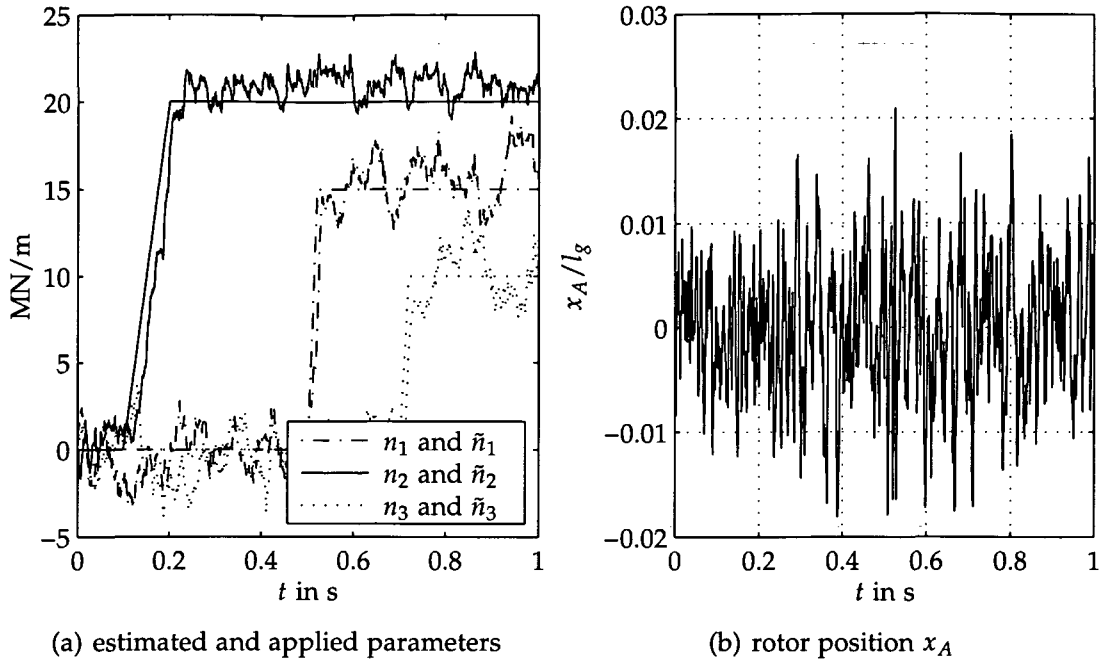


Figure 6.24.: The adaptive control for the 4DoF system with measurement noise

6.9.3. 4DoF System with Unbalance Excitation

Figure 6.25 shows the simulation result for unbalance excitation with a rotational speed of $\Omega = 2094$ rad/s and an unbalance radius of $e = 1$ μm . The same unbalance excitation is applied to the rotor in figure 6.26 with additional measurement noise with a standard deviation of 2.589 μm . The simulations are carried out for a period of 3 s to observe the development of the unstable whirls.

As in the 2DoF case, the estimated parameters $\tilde{n}_{1,2,3}$ oscillate. They induce an unstable whirl as they increase and they stabilize the system again as they decrease. The oscillation frequency is much lower than in the 2DoF case, which is not necessarily a result of the expansion to four degrees of freedom, since several other parameters have changed too.

In the next four figures 6.27 to 6.30, we see simulation results for two different rotational speeds and two different applied cross-coupling parameters. In figure 6.27 and figure 6.28, the rotor rotates with $\Omega \cong 90$ Hz. K_0 is set to

$$K_0 = 1000 (3 \text{ MN/m})^2$$

because, for the low rotational frequency, a higher K_0 value is needed to keep the rotor whirl magnitude inside the region where the maximum magnetic

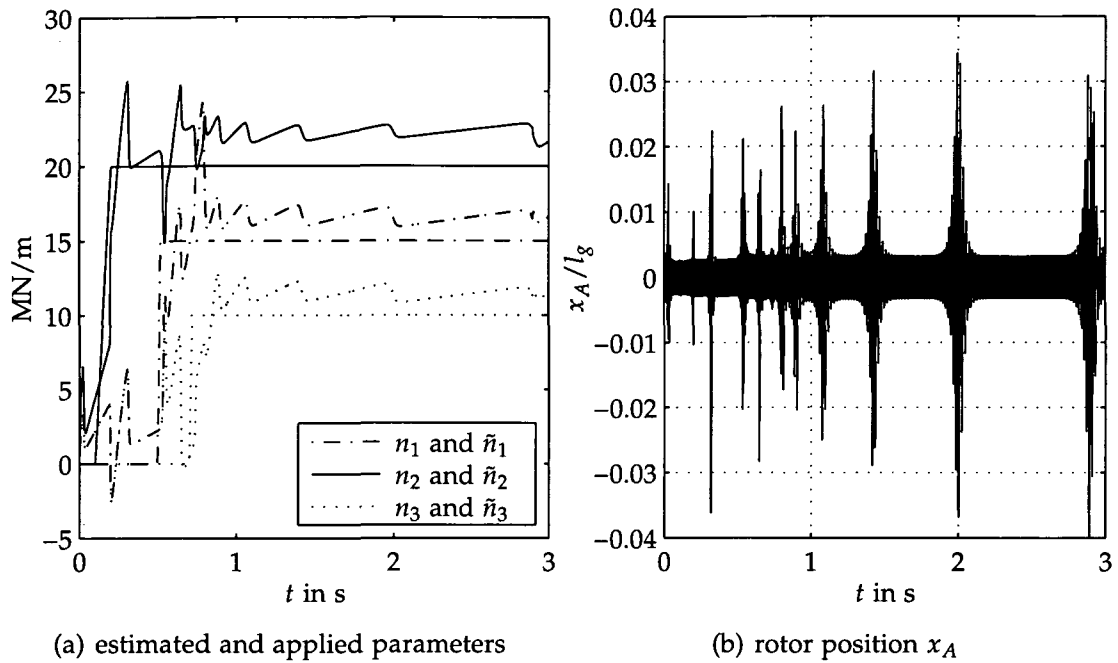


Figure 6.25.: The adaptive control for the 4DoF system with unbalance excitation $\Omega = 2094 \text{ rad/s}$, $e = 1 \mu\text{m}$

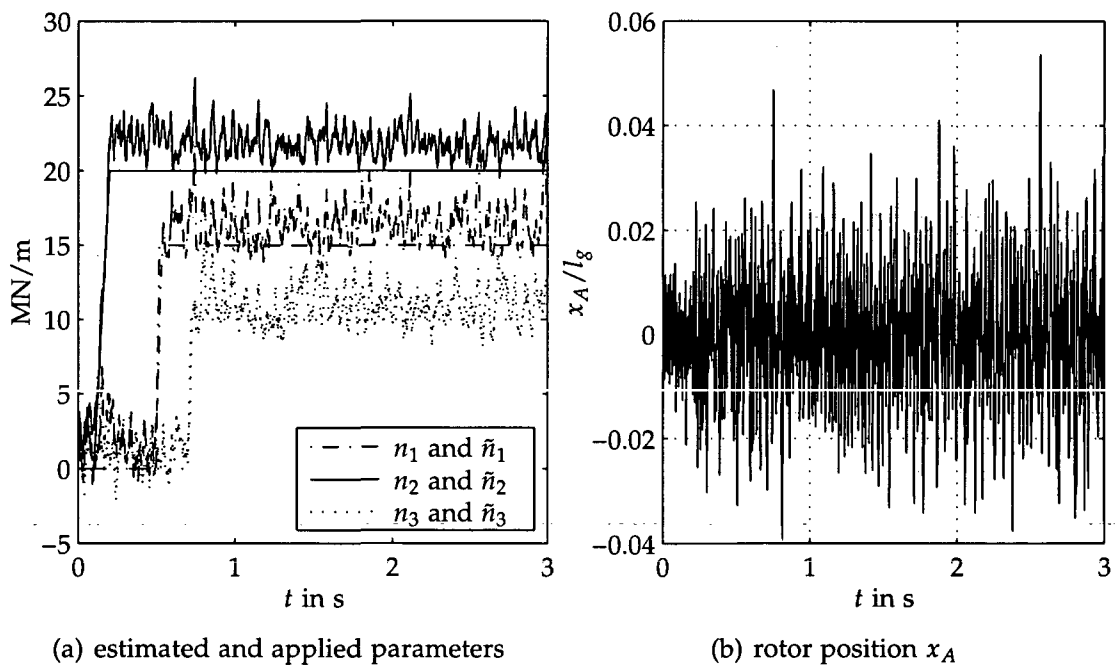


Figure 6.26.: The adaptive control for the 4DoF system with unbalance excitation $\Omega = 2094 \text{ rad/s}$, $e = 1 \mu\text{m}$, and measurement noise

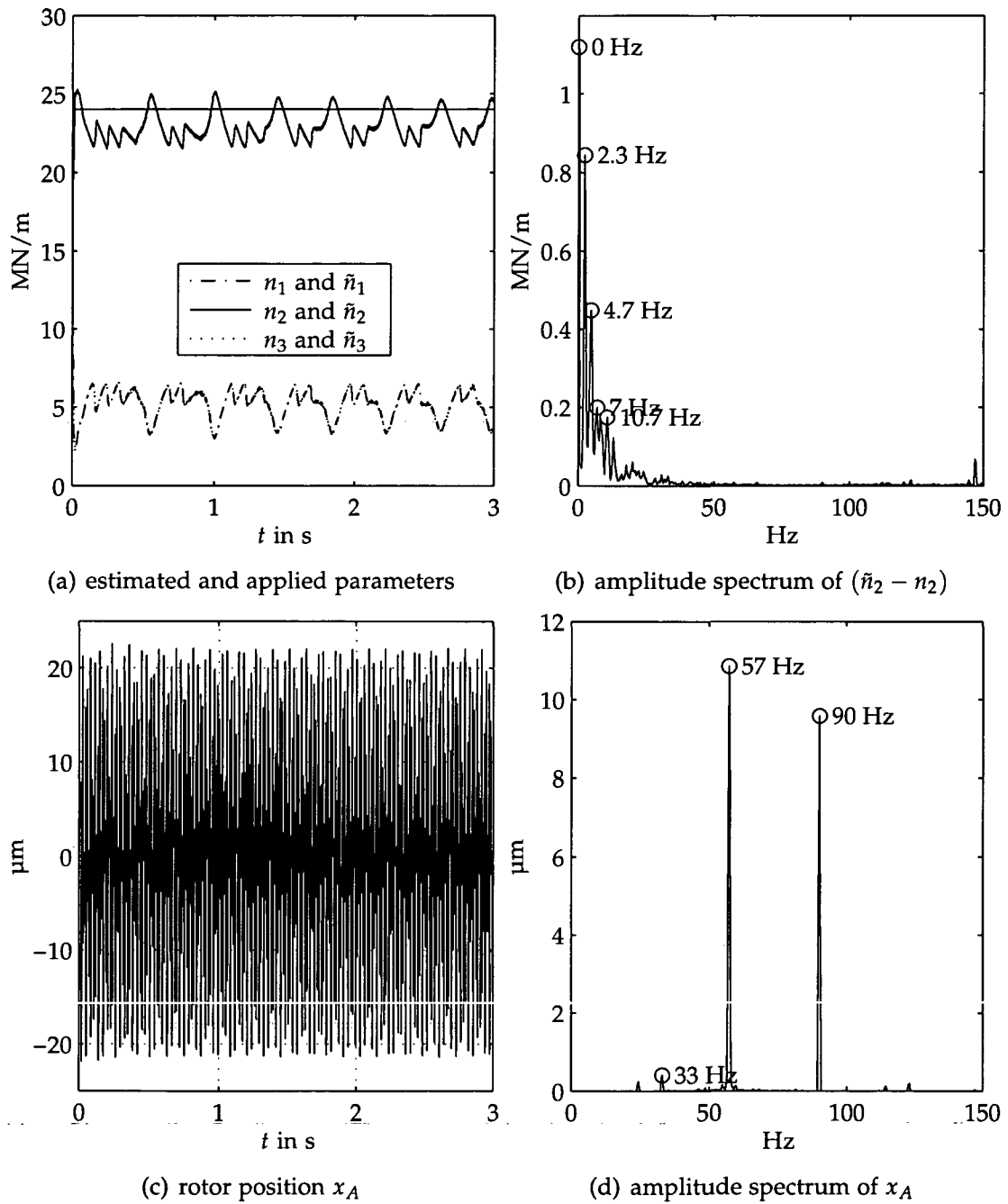


Figure 6.27.: The adaptive control for the 4DoF system with unbalance excitation $\Omega \triangleq 90$ Hz, $e = 21.7 \mu\text{m}$, $n_2 = 24$ MN/m, and $n_1 = n_3 = 0$

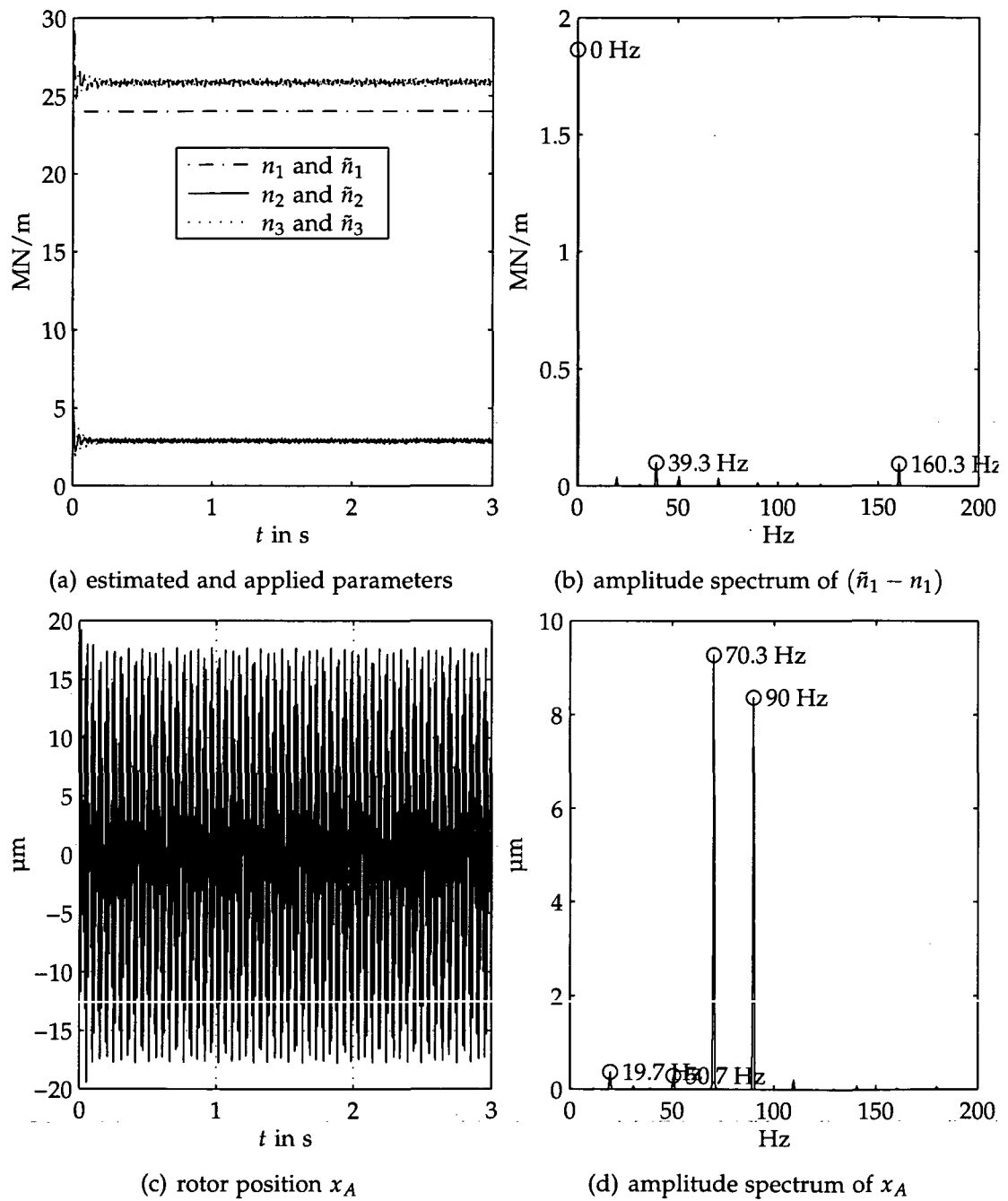


Figure 6.28.: The adaptive control for the 4DoF system with unbalance excitation $\Omega \hat{=} 90$ Hz, $e = 21.7 \mu\text{m}$, $n_1 = 24$ MN/m, and $n_2 = n_3 = 0$

bearing force is larger than the maximum cross-coupling force. The value of the applied cross-coupling parameters is set to $n_2 = 24$ MN/m and $n_1 = n_3 = 0$, and the result is depicted in figure 6.27. The resulting oscillation of the estimated parameters (fig. 6.27a) is quite slow with a frequency of about 2.3 Hz. This is also visible in figure 6.27b, which shows the DFT of $\hat{n}_2(t) - n_2$. The DFT is calculated for the 3 s simulation period so that the frequency resolution is 0.33 Hz. A Hanning window, normed to a mean value of one, is used to reduce leakage and transient effects. In the amplitude spectrum of the rotor position x_A , there are two peaks with 57 Hz and the rotational speed of 90 Hz. It is interesting that no mechanical natural frequency appears in the rotor vibration.

In figure 6.28, we see the simulation results with the same parameters, except that n_1 is now set to 24 MN/m and $n_2 = n_3 = 0$. The 2.3 Hz oscillation in the estimated parameters has vanished completely and there is a constant offset between the estimated and the applied parameters superposed with a small oscillation. The rotor vibration in figure 6.28d is similar to the results as obtained earlier, except that the first spike is at a higher frequency of 70.3 Hz.

Figures 6.29 and 6.30, show the simulation results when the rotor rotates with $\Omega = 2094 \text{ rad s}^{-1} \hat{=} 333.33 \text{ Hz}$. In figure 6.29, again $n_2 = 24$ MN/m and $n_1 = n_3 = 0$; and in figure 6.30, $n_1 = 24$ MN/m and $n_2 = n_3 = 0$. The results are quite different from each other. It is interesting that in both cases the mechanical natural frequencies do not appear in the rotor vibration spectra.

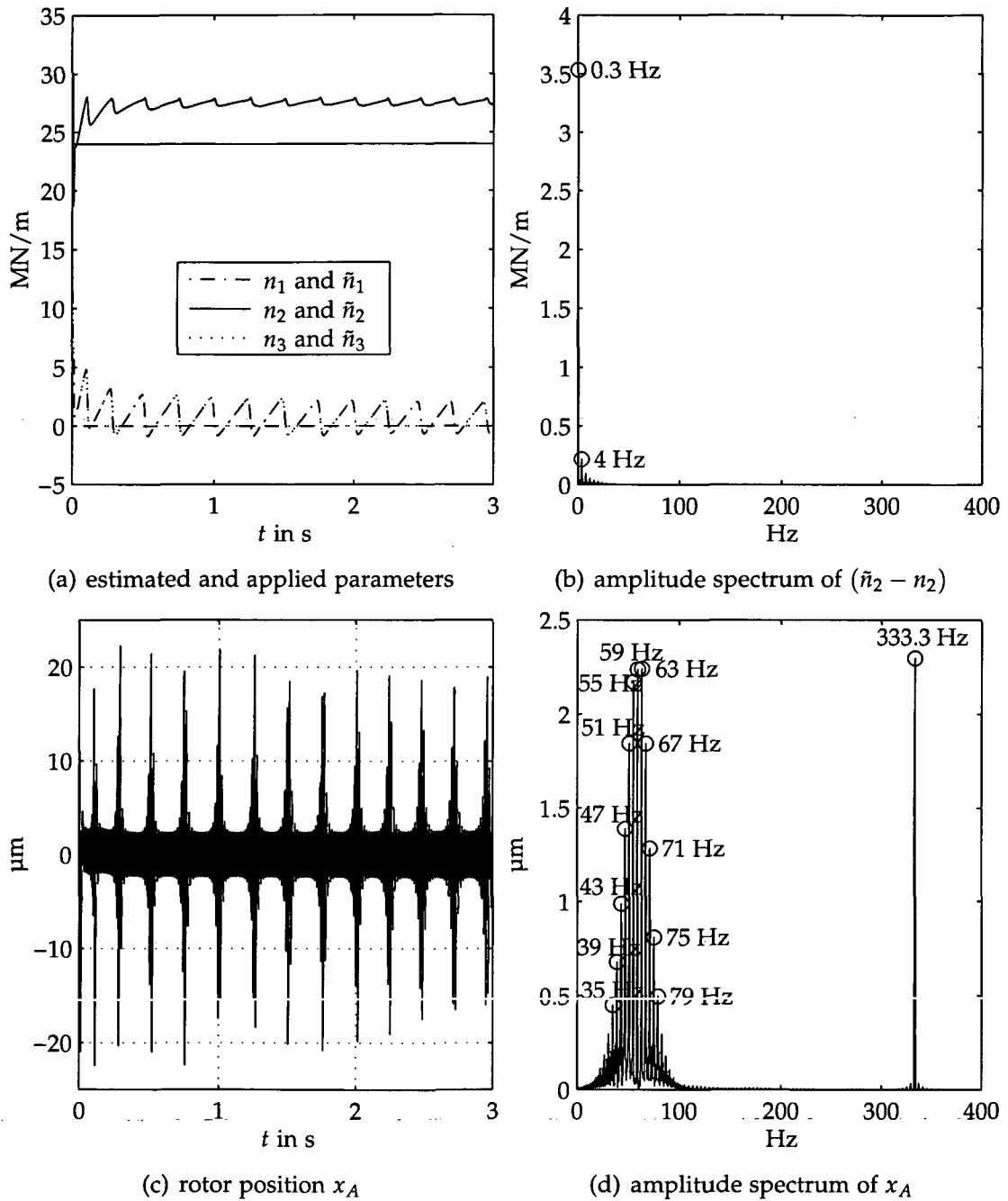


Figure 6.29.: The adaptive control for the 4DoF system with unbalance excitation $\Omega \hat{=} 333.3$ Hz, $e = 1.6$ μm , $n_2 = 24$ MN/m , and $n_1 = n_3 = 0$

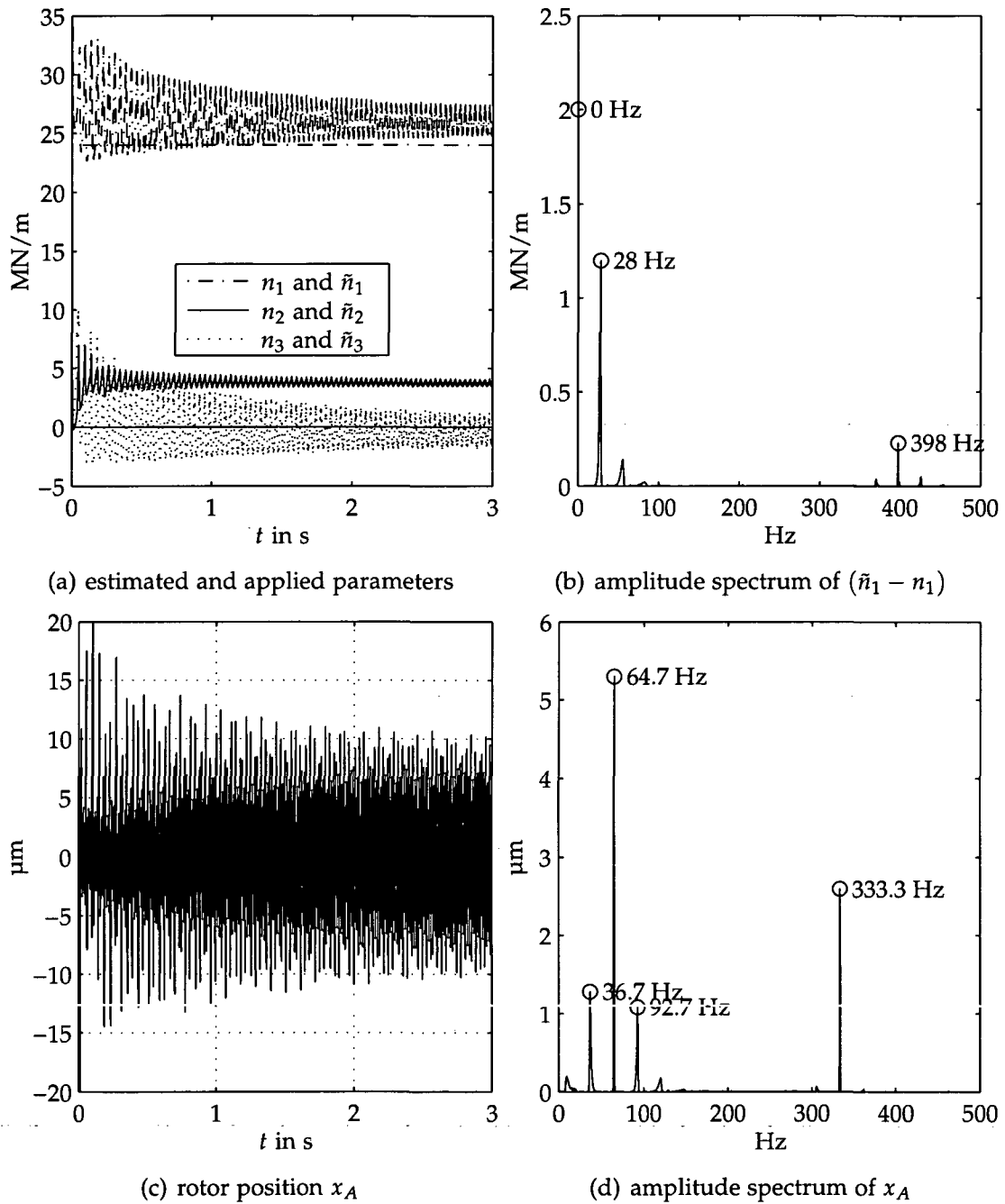


Figure 6.30.: The adaptive control for the 4DoF system with unbalance excitation $\Omega \triangleq 333.3 \text{ Hz}$, $e = 1.6 \mu\text{m}$, $n_1 = 24 \text{ MN/m}$, and $n_2 = n_3 = 0$

7. Unbalance Control

7.1. Introduction

Although in some applications controllers are designed particularly with regard to harmonic disturbances (e.g. mass unbalance excitation), this kind of design is usually not called unbalance control. In this thesis, the term "unbalance control" is reserved solely to any kind of control, which, based on the knowledge of the mass unbalance excitation frequency (i.e. the rotational speed), tries to influence the response to and only to the unbalance excitation. There are three possible goals of unbalance control with active magnetic bearings:

1. Displacement nulling, i.e. to achieve a rotation of the rotor around its geometric center.
2. Force nulling, i.e. to achieve a rotation of the rotor around its inertial axis through the center of gravity, also called "force free" rotation or "adaptive balancing".
3. Current nulling, i.e. reduction of the AMB currents (sometimes referred to as "force free" because the AMB forces are reduced substantially).

All three goals have been subject to extensive research. In early papers by Haberman and Brunet [Hab84, HM84], current nulling is achieved with a simple notch filter centered at the rotational frequency inside the controller feedback loop. This rather simple approach may work well for a fixed rotational speed. However, if the rotational frequency changes, the system gets unstable for certain ranges of the speed of rotation [Kno91, Kno92a, Kno92b]. The other two goals can not be achieved by such an approach.

In [BS83], Burrows and Sahinkaya develop an open-loop control scheme for the displacement nulling of a flexible rotor. The basis of this approach is the algebraic equation

$$\hat{\mathbf{y}}_1 = \hat{\mathbf{T}}(\Omega) \hat{\mathbf{u}}_1 + \hat{\mathbf{d}}_1$$

where \hat{y}_1 is the vector of speed synchronous Fourier coefficients of the system response, \hat{T} is the system model matrix or system gain matrix for the rotational speed Ω , \hat{u}_1 is the vector of speed synchronous Fourier coefficients of the unbalance control signal, and \hat{d}_1 is the vector of speed synchronous Fourier coefficients of the free unbalance response. They use a least-squares approach to calculate the optimal control vector which minimizes a cost function calculated from the rotor displacements. The least-squares approach is needed, because the number of control force locations can be lower than the number of measurement locations for the rotor displacements and thus $\hat{T}(\Omega)$ is not a square matrix.

The optimal control vector is calculated from the free unbalance response for any rotational frequency. The authors propose that the free unbalance response could either be measured or calculated from an estimated mass unbalance distribution, but they do not explain the exact procedure that is used in the numerical simulations. However, there is no feedback of the actual rotor displacements and the control scheme can be viewed as an open-loop scheme. Still, the rotational frequency has to be known (measured) to calculate the optimal control vector. Another subject of their research is the sensitivity of the optimum response and the optimum force locations. Numerical simulation results are given to show the feasibility of the approach.

In [BS88], the same authors give experimental results for the control of synchronous vibrations of a flexible rotor with the help of a magnetic bearing. The used procedure is not explained in detail, but seems to be the same as in [BSC89], where the calculation of the optimal control vector is expanded to an adaptive calculation of a new control vector from an old control vector. It seems that this adaptation is only carried out in a single step and not periodically. Additional to the unbalance control, the system matrix \hat{T} itself is identified by applying test signals and measuring the responses. The identified system parameters are used to calculate the optimal control vector. Again, this control is viewed as open-loop control, but this is not thoroughly correct, because the measured rotor vibrations are at least once fed back to the control vector calculation. Experimental results are given and the used test rig is explained in detail. In [BSTS88, Bur91], the earlier results are resumed. In these papers, it is described that an FFT (Fast Fourier Transform) is used to calculate the speed synchronous components of the measured signals, while in the earlier papers they used the term "Fourier coefficients" which can be calculated much easier. The adaptation of the control vector is carried out as long as the rotor vibration is larger than the desired limit or the rotational

speed changes. Thus, the term open-loop control is only valid when the rotor vibration is inside these limits.

Knospe et al. have started their research at unbalance control in 1991 with [KHS91b]. They compare current nulling with a notch filter with displacement nulling by the open-loop control method from Burrows et al. and gave experimental result for the open-loop control. Contrary to the approach by Burrows et al. the optimal control vector is not calculated but manually adjusted for the first critical speed. They describe the open-loop experimental results more explicitly in [KHS91a] and the problems with the notch filter in [Kno91]. In [HKS91], the same authors describe that the open-loop scheme can also be used to compensate sensor run-outs at low frequencies and foundation vibrations (force nulling). Again the control vector is determined after several minutes of manual adjustment. In [Kno92b, Kno92a], Knospe uses the structured singular value to study the stability and robustness of a 22 mass station model of a high speed compressor with a notch filter and an alternative filter for current nulling included in the feedback loop. He draws the conclusion that poor robustness and, in some cases, even nominal instability results due to excessive phase lag below the notch center frequency; only open-loop control would not alter the stability properties of the nominal feedback controller. In [KHMA92], the authors use the open-loop scheme with manually tuned control vectors to achieve, current nulling, force nulling, and displacement nulling.

The first publication of this research group describing adaptive open-loop control where the optimal control vector *is actually calculated* is [KHFW93]. The authors suggest two methods to find an estimate of the system matrix $\hat{T}(\Omega)$ and the optimal control vector from the Fourier coefficients of the measured rotor vibrations \hat{y}_1 . The third method uses an off-line calculated estimate of the system matrix \hat{T} and the measured rotor vibrations to calculate the optimal control vector. All three methods are adaptive methods which need the measurement of the rotor vibrations at every control update step. Thus, the term open-loop control is not longer correct. The last one of the three control methods is the most important one, since model on-line estimation of the the other methods may lead to numerical problems.

This adaptive open-loop control scheme with an off-line calculated or estimated system matrix \hat{T} is explained in detail in [KHFW94]. There, a set of system matrices for different operational speeds are estimated and a linear interpolation is used to calculate the system matrix $\hat{T}(\Omega)$ for operational speeds between the ones used for the model estimation. The authors also give

criteria for the stability of the system with adaptive open-loop control. The control scheme is applied on a test rig and 30 s run-ups from 1500 r/min to 5000 r/min are carried out. The research of this group up to this point is summarized in [KHFW95] and the most important version of the adaptive open-loop control is called "recursive gain scheduled algorithm".

Then, the work of this group has concentrated on the robustness of the adaptive open-loop control. Various papers have emerged from this research, for example [KTF95, KT96, KTF97, KT97a, KT97b, KTL97]. Only two more recent papers are not focused on robustness. In [KFHW97], Knospe et al. describe the implementation of the adaptive open-loop control scheme on a DSP and in [BK00, BK01] Betschon et al. describe an alternative method for the calculation of the system matrix from off-line computed parameters which minimizes the computational and memory requirements imposed on the hardware.

In 1980, Shaw [Sha80] independently develops the same adaptive open-loop control scheme for the control of helicopter rotor blades at harmonics of the rotor frequency such that unsteady airloads are canceled. In Shaw's thesis, this control method is referred to as "higher harmonic control". It is never viewed to be an open-loop control scheme but a discrete-time control algorithm with special blocks for the transition from discrete-time Fourier coefficients to continuous-time signals and vice versa. With the paradigm of discrete-time control algorithms, all well established methods for discrete-time systems can be used and so the stability condition of the higher harmonic control algorithm is already described in [Sha80]. Shaw also suggests a Kalman filter algorithm for estimating the system matrix \hat{T} on-line during the harmonic control operation. To honor this first researcher the Shaw-Burrows-Knospe algorithm is called "discrete harmonic control (DHC)" throughout this thesis. It should be pointed out that the underlying Fourier coefficient calculation process can be worked out in both discrete-time and continuous-time.

Shaw's work has ignited substantial research of harmonic disturbance compensation in the control of helicopters. A good review of the developments based on Shaws algorithm is given by Hall and Wereley in [HW89]. Hall and Wereley show that the higher harmonic control can be viewed as a discrete-time version of a continuous-time algorithm and that this continuous-time version can be described as a classic linear time invariant system. For $\hat{T} = 1$, this algorithm represents a notch filter. Hall and Wereley state that by implementing the DHC algorithm in continuous-time significant improvements in gain and phase margins can be achieved. The continuous-time version of the DHC algorithm is called continuous harmonic control (CHC) throughout this

thesis.

The DHC algorithm can be used with discrete-time and continuous-time systems; the only difference is in the calculation of the Fourier coefficients. The CHC algorithm is only described in continuous-time by Hall and Wereley. A discrete-time version of the CHC can be found in a different field of science, the adaptive signal filtering. Glover [Glo77] applies the so-called adaptive noise cancelling to sinusoidal interferences. With the special least-mean-squares (LMS) algorithm for the filter weight adaptation procedure, the adaptive noise cancelling filter is approximately a discrete-time linear time-invariant system. In the book by Widrow and Stearns [WS85], the adaptive filter approach is used to build an unusual notch filter which offers easy control of bandwidth, an infinite null, and the capability of adaptively tracking the exact frequency and phase of the disturbance. This algorithm gives a discrete-time version for the CHC and $\hat{T} = 1$. The so-called filtered- x LMS algorithm is also included in the book by Widrow and Stearns; this approach inspired Na and Park [NP97] for their unbalance control algorithm for a SISO system. It is similar to the discrete-time version of the CHC for a general system matrix \hat{T} , but the actual application is much more complicated. An interesting review of some of these control concepts is given by Sievers and von Flotow in [SF90, SF92].

Quite recently, Shi et al. have used the filtered- x LMS algorithm for displacement and current nulling. They distinguish between a "direct method" which is described in [SZL02a] and an "indirect method" which is described in [SZL02b]. In the direct method the quantity to be minimized is measured and the output of the filtered- x LMS algorithm is used as a control input to minimize this quantity. Therefore, it is almost identical to the CHC control. However, the authors do not use the system model matrix \hat{T} to acquire a stable and fast unbalance control algorithm, but instead they use an arbitrarily chosen constant. In the indirect method a performance measure which is an indirect function of the quantity to be minimized is used; this makes it easier to apply the original filtered- x LMS by Widrow and Stearns to the unbalance control problem. Both methods are summarized and experimental results are given in [SZQ03].

Herzog et al. independently derive the continuous-time version of the CHC in the often cited paper [HBGL96] and the earlier work [LH94], but they use it only for current nulling and choose to name the algorithm "generalized notch filter" which has led to many misunderstandings. Kugi et al. [KHS⁺98, KHS⁺00] also use a similar control algorithm for the compensation of roll

eccentricity in rolling mills. Kugi shows in [Kug01] that, if the system fulfills certain conditions, no further information about the plant is needed for the algorithm to be stable.

There several other publications describing different types of unbalance control algorithms. A few of these papers are cited here, for example the works of Beale et al. [BSLC92b, BSLC92a, SBLC94] describe an algorithm similar to the DHC based on a synchronous energy calculation. Lum et al. [LCB96] and von Löwis et al. [LR00] used an on-line identification of the location of the mass center. Setiawan et al. discuss the compensation of both mass unbalance excitation and sensor runout in [SMMS99, SM00, SMM01a, SMM01c, SMM01b, SMM02].

7.2. Ideal Unbalance Control of a Single-DoF Mass Rotor

For a better understanding of the three possible unbalance control goals, a single-degree-of-freedom lumped mass rotor supported by an active magnetic bearing is investigated. The rotor with mass m and displacement x is governed by the following equation of motion

$$m \ddot{x}(t) = f_{MB}(t) + f_{ub}(t)$$

with the magnetic bearing force f_{MB} and the unbalance excitation force f_{ub} . The magnetic bearing force can be described with the linear relationship

$$f_{MB}(t) = k_i i_x(t) + k_s x(t)$$

with the current i_x , the current coefficient k_i and the position coefficient k_s . The unbalance excitation is purely harmonic, i.e.

$$f_{ub}(t) = \hat{f}_{ub} \cos \Omega t ,$$

which will result in a purely harmonic current, magnetic bearing force and rotor position

$$\begin{aligned} x(t) &= \hat{x} \cos \Omega t + \varphi_x \\ i_x(t) &= \hat{i}_x \cos \Omega t + \varphi_i \\ f_{MB}(t) &= \hat{f}_{MB} \cos \Omega t + \varphi_f . \end{aligned}$$

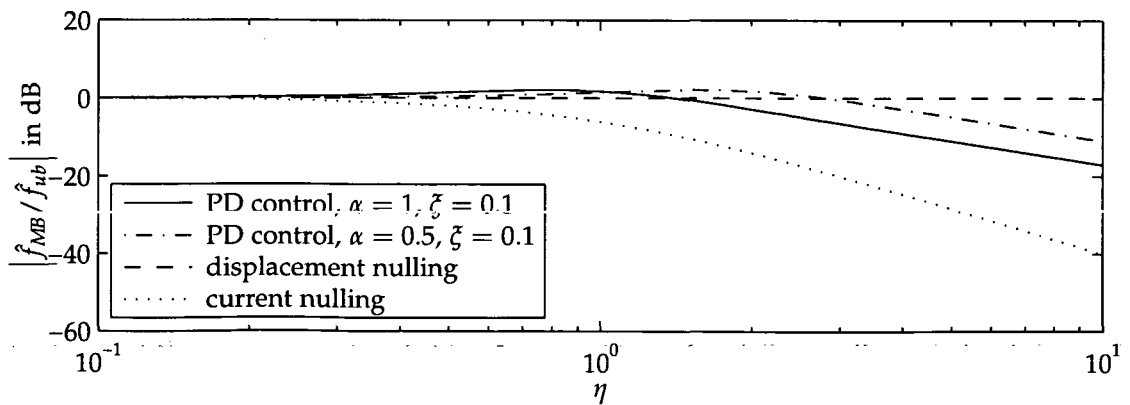
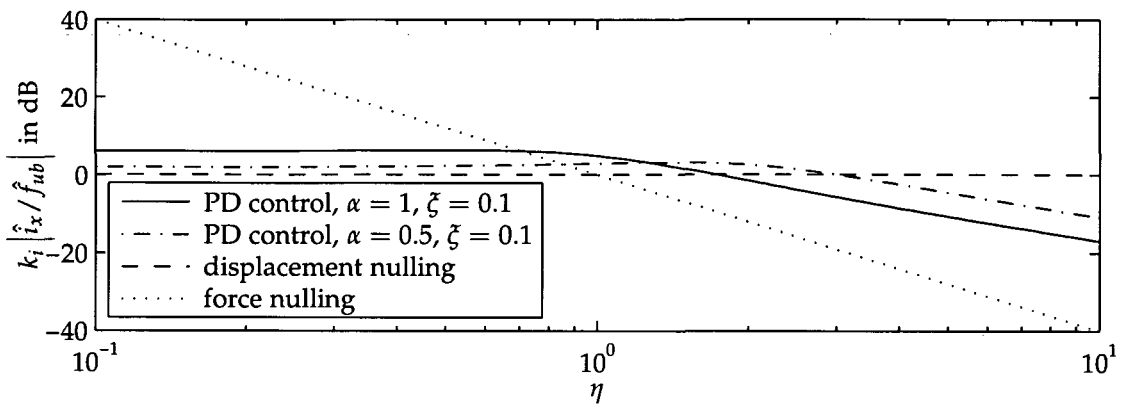
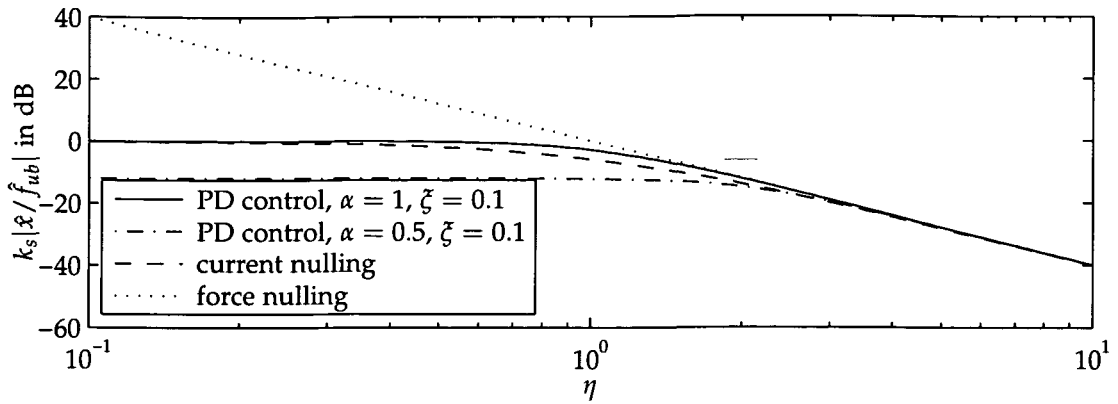


Figure 7.1.: Nondimensional relationship between the speed synchronous harmonics of a single degree of freedom rotor for various control methods

Table 7.1.: PD and unbalance control algorithms

	PD Control	displ. null.	current null.	force null.
control law	$i_x = -P_D \dot{x} - P_P x$	$i_x = -\frac{f_{ub}}{k_i}$	$i_x = 0$	$i_x = -\frac{k_s}{k_i} x$
$k_s \left \frac{\hat{x}}{\hat{f}_{ub}} \right $	$\frac{\alpha^2}{\sqrt{(1-\alpha^2\eta^2)^2 + 4\xi^2\alpha^2\eta^2}}$	0	$\frac{1}{\eta^2+1}$	$\frac{1}{\eta^2}$
$k_i \left \frac{\hat{i}_x}{\hat{f}_{ub}} \right $	$\sqrt{\frac{(1+\alpha^2)^2 + 4\xi^2\alpha^2\eta^2}{(1-\alpha^2\eta^2)^2 + 4\xi^2\alpha^2\eta^2}}$	1	0	$\frac{1}{\eta^2}$
$\left \frac{\hat{f}_{MB}}{\hat{f}_{ub}} \right $	$\sqrt{\frac{1+4\xi^2\alpha^2\eta^2}{(1-\alpha^2\eta^2)^2 + 4\xi^2\alpha^2\eta^2}}$	1	$\frac{1}{\eta^2+1}$	0

In table 7.1, the control algorithms for a PD controller and the three unbalance control concepts are given together with the solutions for displacement, current and force. It should be pointed out that this control algorithms and solutions are only valid for the harmonic excitation and the corresponding harmonic solutions. The results are given in nondimensional parameters with the following abbreviations

$$\begin{aligned}
 k &:= (k_i P_P - k_s) & \xi &:= \frac{k_i P_D}{2\sqrt{km}} & \omega_0 &:= \sqrt{\frac{k}{m}} \\
 \omega_s &:= \sqrt{\frac{k_s}{m}} & \alpha &:= \sqrt{\frac{k_s}{k}} = \frac{\omega_s}{\omega_0} & \eta &:= \frac{\Omega}{\omega_s}
 \end{aligned}$$

The parameter α gives the ratio of the position coefficient k_s to the resulting "stiffness" k of the PD controlled magnetic bearing. A PD controller with a value of $\alpha = 1$ is referred to as natural control in [STB93].

The amplitude response for x , i_x , and f_{MB} for all three control laws is shown in figure 7.1. Two curves are given for the PD control, both with a damping ratio of $\xi = 0.1$, the first one for a value of $\alpha = 0.5$ and the second one for a value of $\alpha = 1$. The displacement, current, and force nulling laws are ideal in this calculation, so that e.g. the displacement nulling does not appear in the displacement amplitude response plot. A quasi static run-up curve would look different though, because the unbalance amplitude is proportional to the squared rotational speed.

Figure 7.1c shows that the current nulling also reduces the magnetic bearing force dramatically, compared to the PD control. So the term "force free" rotation is somewhat justifiable.

7.3. Discrete Harmonic Control (DHC, Adaptive Open-Loop Control)

7.3.1. Harmonic Response of a Linear Time Invariant System

Harmonic Response of a Continuous-Time System

One fact that makes the suppression of harmonic disturbances very easy is that for a linear time invariant system the response to a harmonic excitation can be computed from an algebraic equation. The relationship between the output $\mathbf{y}(t)$ of the system and the input $\mathbf{u}(t)$ of the system can be described using a Laplace transfer matrix $\mathbf{G}(s)$. It is assumed that the disturbance $\mathbf{d}(t)$ may be represented as acting on the output. The resulting equation in the Laplace domain is

$$\hat{\mathbf{y}}(s) = \mathbf{G}(s) \hat{\mathbf{u}}(s) + \hat{\mathbf{d}}(s) .$$

For a purely harmonic input $\mathbf{u}(t)$ with angular frequency Ω , that is

$$\mathbf{u}(t) = \hat{\mathbf{u}}_{1c} \cos \Omega t + \hat{\mathbf{u}}_{1s} \sin \Omega t ,$$

and a purely harmonic disturbance $\mathbf{d}(t)$ on the output, that is

$$\mathbf{d}(t) = \hat{\mathbf{d}}_{1c} \cos \Omega t + \hat{\mathbf{d}}_{1s} \sin \Omega t ,$$

the steady state response after all transients have decayed is given by

$$\mathbf{y}(t) = \hat{\mathbf{y}}_{1c} \cos \Omega t + \hat{\mathbf{y}}_{1s} \sin \Omega t .$$

The amplitude of the cosine and sine waves can be also viewed as Fourier coefficients corresponding to the frequency Ω of a signal consisting of more than one harmonic. The Fourier coefficients are combined to a vector $\hat{\mathbf{y}}_1 = [\hat{\mathbf{y}}_{1c}^T \ \hat{\mathbf{y}}_{1s}^T]^T$ and the relationship between input and output can be described by

$$\begin{bmatrix} \hat{\mathbf{y}}_{1c} \\ \hat{\mathbf{y}}_{1s} \end{bmatrix} = \begin{bmatrix} \operatorname{Re}(\mathbf{G}(j\Omega)) & \operatorname{Im}(\mathbf{G}(j\Omega)) \\ -\operatorname{Im}(\mathbf{G}(j\Omega)) & \operatorname{Re}(\mathbf{G}(j\Omega)) \end{bmatrix} \begin{bmatrix} \hat{\mathbf{u}}_{1c} \\ \hat{\mathbf{u}}_{1s} \end{bmatrix} + \begin{bmatrix} \hat{\mathbf{d}}_{1c} \\ \hat{\mathbf{d}}_{1s} \end{bmatrix}$$

or

$$\hat{\mathbf{y}}_1 = \hat{\mathbf{T}}(\Omega) \hat{\mathbf{u}}_1 + \hat{\mathbf{d}}_1 .$$

The matrix $\hat{\mathbf{T}}(\Omega)$ is called "influence coefficient matrix".

Harmonic Response of a Discrete-Time System

For discrete-time systems, the equations for a harmonic input signals are very similar to the continuous-time ones. For a discrete-time system with sample time T_s and z -transfer matrix $\mathbf{G}(z)$, the relationship between input and output can be given as

$$\hat{\mathbf{y}}(z) = \mathbf{G}(z) \hat{\mathbf{u}}(z) + \hat{\mathbf{d}}(z) .$$

For a purely harmonic input

$$\mathbf{u}(k) = \hat{\mathbf{u}}_{1c} \cos \Omega T_s k + \hat{\mathbf{u}}_{1s} \sin \Omega T_s k$$

and corresponding disturbance $\mathbf{d}(k)$, the output is

$$\mathbf{y}(k) = \hat{\mathbf{y}}_{1c} \cos \Omega T_s k + \hat{\mathbf{y}}_{1s} \sin \Omega T_s k$$

where the vector of Fourier coefficients $\hat{\mathbf{y}}_1$ of the output is related to the vector of Fourier coefficients of input and disturbance by

$$\begin{bmatrix} \hat{\mathbf{y}}_{1c} \\ \hat{\mathbf{y}}_{1s} \end{bmatrix} = \begin{bmatrix} \operatorname{Re}(\mathbf{G}(e^{j\Omega T_s})) & \operatorname{Im}(\mathbf{G}(e^{j\Omega T_s})) \\ -\operatorname{Im}(\mathbf{G}(e^{j\Omega T_s})) & \operatorname{Re}(\mathbf{G}(e^{j\Omega T_s})) \end{bmatrix} \begin{bmatrix} \hat{\mathbf{u}}_{1c} \\ \hat{\mathbf{u}}_{1s} \end{bmatrix} + \begin{bmatrix} \hat{\mathbf{d}}_{1c} \\ \hat{\mathbf{d}}_{1s} \end{bmatrix} .$$

Basically we have the same equation as in the continuous-time case

$$\hat{\mathbf{y}}_1 = \hat{\mathbf{T}}(\Omega) \hat{\mathbf{u}}_1 + \hat{\mathbf{d}}_1 ,$$

the only difference is the calculation of $\hat{\mathbf{T}}(\Omega)$.

7.3.2. Discrete Harmonic Control Algorithm (DHC)

It has been shown that the harmonic response of a linear time invariant system can be described by

$$\hat{\mathbf{y}}_1 = \hat{\mathbf{T}}(\Omega) \hat{\mathbf{u}}_1 + \hat{\mathbf{d}}_1 . \quad (7.1)$$

When $\hat{\mathbf{T}}(\Omega)$ is a square matrix, an open-loop control law is given by the optimal control vector $\hat{\mathbf{u}}_{1,opt}$

$$\hat{\mathbf{u}}_{1,opt} = -\hat{\mathbf{T}}^{-1}(\Omega) \hat{\mathbf{d}}_1 .$$

Only the knowledge of the influence coefficient matrix $\hat{\mathbf{T}}$ and the disturbance vector $\hat{\mathbf{d}}_1$, but no feedback of measured quantities is needed. However, when

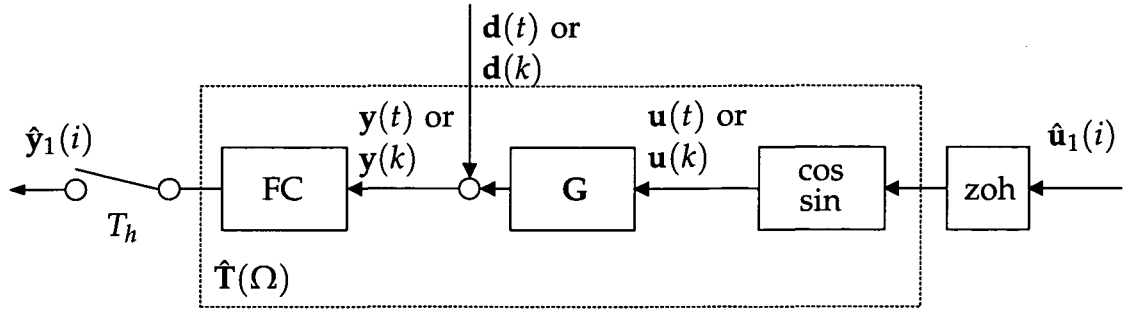


Figure 7.2.: A continuous-time or discrete-time system prepared for discrete harmonic control

either the matrix $\hat{\mathbf{T}}$ or the disturbance vector $\hat{\mathbf{d}}_1$ is not exactly known or changing, $\hat{\mathbf{y}}_1$ will not be zero.

In order to develop a feedback controller that eliminates the harmonic components in $\mathbf{y}(t)$, the steady state equation (7.1) is expanded to a sequence of steady states, i.e.

$$\hat{\mathbf{y}}_1(i) = \hat{\mathbf{T}}(\Omega) \hat{\mathbf{u}}_1(i-1) + \hat{\mathbf{d}}_1(i), \quad (7.2)$$

where

$$\mathbf{u}(t) = \hat{\mathbf{u}}_{1c}(i) \cos \Omega t + \hat{\mathbf{u}}_{1s}(i) \sin \Omega t \quad \text{for} \quad iT_h \leq t < (i+1)T_h$$

for continuous-time systems and

$$\mathbf{u}(k) = \hat{\mathbf{u}}_{1c}(i) \cos \Omega T_s k + \hat{\mathbf{u}}_{1s}(i) \sin \Omega T_s k \quad \text{for} \quad iT_h \leq kT_s < (i+1)T_h$$

for discrete-time systems. What these equations stand for in an actual system is depicted in figure 7.2. The underlying linear time invariant (LTI) system can be discrete-time or continuous-time. From the output of the system \mathbf{y} , the Fourier coefficients are calculated in the block FC and sampled with a sampling time T_h .¹ The result is a sequence of Fourier coefficients $\hat{\mathbf{y}}_1(i)$. The control vector \mathbf{u} is calculated from the sequence of Fourier coefficients $\hat{\mathbf{u}}_1(i)$ by a zero order hold block and a multiplication with $\cos \Omega t$ and $\sin \Omega t$ or $\cos \Omega T_s k$ and $\sin \Omega T_s k$ respectively. Equation (7.2) suggests that the system reaches the steady state within the harmonic sampling time T_h . This quasi-steady approach is only valid when T_h is much larger than the typical settling time of the system \mathbf{G} and the sampling time T_s if applicable. It should be

¹ The sampling procedure and Fourier calculation procedure are separated here, although they could be lumped together.

pointed out that in the literature equation (7.2) is usually written with $\hat{y}_1(i)$ and $\hat{u}_1(i)$. This is not correct, because at the measurement time point iT_h we measure the reaction of \hat{y} to the last control value $\hat{u}(i-1)$.

The control algorithm proposed by Shaw [Sha80] can be written as

$$\hat{u}_1(i) = \hat{u}_1(i-1) + \hat{A}\hat{y}_1(i) . \quad (7.3)$$

This is simply an integrating controller with a gain matrix \hat{A} . Since it is a discrete control algorithm it is called discrete harmonic control (DHC) throughout this thesis. Inserting the control law equation (7.3) into equation (7.2), the system with discrete harmonic control can be described with the discrete difference equation

$$\begin{aligned} \hat{u}_1(i) &= (\mathbf{I} + \hat{A}\hat{T}) \hat{u}_1(i-1) + \hat{A}\hat{d}_1(i) \\ \hat{y}_1(i) &= \hat{T} \hat{u}_1(i-1) + \hat{d}_1(i) . \end{aligned} \quad (7.4)$$

Again the literature is inconsistent in the usage of $\hat{u}_1(i+1)$, $\hat{u}_1(i)$, $\hat{u}_1(i-1)$. The important point is that $\hat{u}_1(i)$ is calculated from the last control vector $\hat{u}_1(i-1)$ and the actual measurement $\hat{y}_1(i)$ and is applied *immediately on the system*.

The discrete harmonic control (DHC) is a linear discrete-time control algorithm with sample time T_h and a special measurement/sampling procedure to generate the Fourier coefficients. In rotor dynamics literature, the term "adaptive open-loop control" is used for this kind of control, which is not a very helpful paradigm, because it makes the analysis more complicated. The term open-loop should point out that the discrete harmonic control does not influence the stability of the underlying control loop, but this is actually a side-effect of the quasi-static assumption.

When the quasi-static assumption is valid, the system with discrete harmonic control equation (7.4) is stable, if and only if all eigenvalues of $\mathbf{I} + \hat{A}\hat{T}$ lie within the unit circle. A weaker condition is that the maximum singular value of $\mathbf{I} + \hat{A}\hat{T}$ is smaller than one,

$$\bar{\sigma}(\mathbf{I} + \hat{A}\hat{T}) < 1 .$$

The advantage is that the maximum singular value of a matrix also gives an induced matrix norm such that

$$\bar{\sigma}(\mathbf{A}) = \max_{\mathbf{x} \in \mathbb{C}^n} \frac{\|\mathbf{A}\mathbf{x}\|}{\|\mathbf{x}\|} .$$

This implies that the maximum singular value of $I + \hat{A}\hat{T}$ can be interpreted as the convergence speed of the algorithm. We should note that this induced matrix norm is a "worst case" convergence speed.

If the system equation (7.4) is stable and the disturbance vector is constant

$$\hat{d}_1(i) = \hat{d}_1 = \text{const.}$$

there exist final values of $\hat{y}_1(i)$ and $\hat{u}_1(i)$

$$\lim_{i \rightarrow \infty} \hat{y}_1(i) = (-\hat{T}(\hat{A}\hat{T})^{-1}\hat{A} + I)\hat{d}_1$$

$$\lim_{i \rightarrow \infty} \hat{u}_1(i) = -(\hat{A}\hat{T})^{-1}\hat{A}\hat{d}_1.$$

For square matrices \hat{A} and \hat{T} , this simplifies to

$$\lim_{i \rightarrow \infty} \hat{y}_1(i) = 0 \quad \lim_{i \rightarrow \infty} \hat{u}_1(i) = -\hat{T}^{-1}\hat{d}_1.$$

This result implies that regardless of the value of \hat{A} the DHC controlled system converges to $y = 0$, as long as the system is stable; the choice of \hat{A} is only relevant for the stability and the convergence speed, and the final value of y is determined by the integrating action of the controller.

If \hat{T} is a square matrix, the optimum choice for the matrix $\hat{A}(\Omega)$ is

$$\hat{A}(\Omega) := -\hat{T}^{-1}(\Omega)$$

so that all eigenvalues of $I + \hat{A}\hat{T}$ are zero and the DHC is a dead-beat control which means that $\hat{y}_1(i)$ is reduced in one discrete time step T_h to zero.

For non-square \hat{T} , a weighted pseudo-inverse can be used instead of the inverse of \hat{T}

$$\hat{A}(\Omega) := -(\hat{T}^T W \hat{T})^{-1} \hat{T}^T W$$

where W is a weighting matrix. This approach is equivalent to applying the DHC to a new system output \hat{y}_1^* where

$$\hat{y}_1^* := \hat{T}^T W \hat{y}_1$$

In this thesis, only square matrices \hat{T} are considered, so the implications of a non-square \hat{T} are not described here, and the reader is referred to the literature by Knospe et al. (e.g. [KHFW95]) and Burrows et al. (e.g. [BS83]).

7.3.3. Calculation of Fourier Coefficients

The basic equation for calculating the Fourier coefficients of the measured system output y is simply an integration of the signal multiplied with a sine and cosine wave of frequency Ω , i.e.

$$y_{1c}(i) = \frac{2}{T_i} \int_{iT_h - T_i}^{iT_h} y(\tau) \cos \Omega \tau d\tau \quad y_{1s}(i) = \frac{2}{T_i} \int_{iT_h - T_i}^{iT_h} y(\tau) \sin \Omega \tau d\tau. \quad (7.5)$$

The integration time T_i has to be an (approximate) integer multiple of the period $2\pi/\Omega$. In DHC control, the integration time has to be smaller or equal than the step time of the DHC control;

$$T_i \leq T_h.$$

It may be useful to choose the integration time T_i significantly smaller than T_h in order to minimize the effect of transients on the Fourier coefficients, since they may violate the quasi-static assumption.

For an actual implementation in a discrete-time controller environment, a discrete-time version has to be used

$$y_{1c}(i) = \frac{2}{N_i} \sum_{\kappa=iN_h - N_i}^{iN_h} y(\kappa T_s) \cos \Omega T_s \kappa \quad (7.6)$$

$$y_{1s}(i) = \frac{2}{N_i} \sum_{\kappa=iN_h - N_i}^{iN_h} y(\kappa T_s) \sin \Omega T_s \kappa$$

where

$$N_i := \frac{T_i}{T_s} \quad \text{and} \quad N_h := \frac{T_h}{T_s}.$$

Additional to the conditions of the continuous-time case, the integration time T_i has to be an integer multiple of the sampling time T_s . This condition usually violates the condition that the integration time should be an integer multiple of the period $2\pi/\Omega$. Therefore, an error results in the Fourier coefficients. All simulations in this thesis are carried out with the discrete-time version of the Fourier coefficients calculation.

As a rough rule of thumb, the error of the Fourier coefficient in percent is the ratio of the sample time T_s to the integration time T_i in percent, as long as T_i is the nearest integer multiple of $2\pi/\Omega$. Of course, this is only valid for $T_s \ll \pi/\Omega$. Additional white noise with a low signal-to-noise ratio may increase the error significantly.

7.3.4. Application to a Magnetic Bearing System

The DHC can be used to achieve all three design goals: current, displacement, or force nulling. The only difference is the measured quantity to be minimized and the corresponding influence coefficient matrix. A problem in achieving the force nulling goal arises from the fact that the magnetic bearing force cannot be measured directly. Instead of measuring the force, it can be calculated from the measured bearing current and rotor positions. Another way is to use the current nulling approach and additionally compensate for the position coefficient matrix as shown in [Siv02].

There are more or less two choices for the harmonic control input, namely the additional magnetic bearing current vector \mathbf{i}_h for harmonic control and the additional rotor position vector \mathbf{x}_h . There is a-priori no special advantage or disadvantage of one choice. However, if the DHC is used together with the ACCC, the DHC control output should not interfere with the ACCC, which is usually allowed by the choice of either \mathbf{i}_h or \mathbf{x}_h (for details see chapter 8). Another issue is that for one of the control input choices the elements of the matrix $\hat{\mathbf{A}}$ can be approximated by simple functions and thus computation time and computation memory can be reduced.

For the practical implementation of the discrete harmonic control, the computational load and the needed memory space of the DSP are limited. An on-line calculation of the inverse influence coefficient matrix is usually too time consuming and an off-line calculation and storing the values of $\hat{\mathbf{A}}(\Omega)$ for a table of Ω -values needs much memory.

The first step to reduce the amount of necessary memory is to store only the upper half of $\hat{\mathbf{A}}(\Omega)$. When we use the following abbreviations

$$\hat{\mathbf{T}} = \begin{bmatrix} \hat{\mathbf{T}}_R & \hat{\mathbf{T}}_J \\ -\hat{\mathbf{T}}_J & \hat{\mathbf{T}}_R \end{bmatrix}$$

we can use the matrix inversion theorem A.2 in appendix A.1 for the calculation of $\hat{\mathbf{T}}^{-1}$. With $\Delta = \hat{\mathbf{A}} = \hat{\mathbf{T}}_R + \hat{\mathbf{T}}_J \hat{\mathbf{T}}_R^{-1} \hat{\mathbf{T}}_J$, we get

$$\begin{bmatrix} \hat{\mathbf{T}}_R & \hat{\mathbf{T}}_J \\ -\hat{\mathbf{T}}_J & \hat{\mathbf{T}}_R \end{bmatrix}^{-1} = \begin{bmatrix} \Delta^{-1} & -\Delta^{-1} \hat{\mathbf{T}}_J \hat{\mathbf{T}}_R^{-1} \\ \Delta^{-1} \hat{\mathbf{T}}_J \hat{\mathbf{T}}_R^{-1} & \Delta^{-1} \end{bmatrix}. \quad (7.7)$$

So the inverse of $\hat{\mathbf{T}}$ has the same structure as $\hat{\mathbf{T}}$ itself. Since $\hat{\mathbf{A}}$ should be an approximation of $\hat{\mathbf{T}}^{-1}$ we assume that

$$\hat{\mathbf{A}} = \begin{bmatrix} \hat{\mathbf{A}}_R & \hat{\mathbf{A}}_J \\ -\hat{\mathbf{A}}_J & \hat{\mathbf{A}}_R \end{bmatrix}.$$

The second step is to use the symmetry of $G(z)$. If we neglect the gyroscopic effect², $G(z)$ has the same structure as the mass matrix \mathbf{M}_b (4.4) and the controller matrices \mathbf{P}_P (5.4), \mathbf{P}_I (5.5), and \mathbf{P}_D (5.6)—this is that half of the elements are equal to zero—because there is no coupling between x and y coordinates. When we further assume that the rotor bearing system is symmetric with respect to the x - and y -direction (isotropic bearings), some elements of $G(z)$ are equal to each other and we obtain the following scheme for the elements of the real and imaginary parts of $\hat{\mathbf{T}}(\Omega) = G(e^{j\Omega T_s})$ as well as for the elements of $\hat{\mathbf{A}}_R$ and $\hat{\mathbf{A}}_I$

$$\hat{\mathbf{A}}_R = \begin{bmatrix} A & 0 & B & 0 \\ 0 & \pm A & 0 & \pm B \\ B & 0 & A & 0 \\ 0 & \pm B & 0 & \pm A \end{bmatrix} \quad \hat{\mathbf{A}}_I = \begin{bmatrix} C & 0 & D & 0 \\ 0 & \pm C & 0 & \pm D \\ D & 0 & C & 0 \\ 0 & \pm D & 0 & \pm C \end{bmatrix} \quad (7.8)$$

There are only four independent variables in $\hat{\mathbf{A}}(\Omega)$, which have to be stored. The \pm sign of some parameters indicate that for the use of \mathbf{i}_h as control input the variables have different sign (a consequence of the NNSS-configuration of the AMBs) and for the use of \mathbf{x}_h as input variable the coefficients have equal signs. A further reduction of memory space can be achieved by approximating the variables A to D depending on Ω by a polynomial or a rational function.

Figure 7.3 shows the effect of the various approximations on the maximum singular value of $\mathbf{I} + \hat{\mathbf{A}}\hat{\mathbf{T}}$ over Ω for the displacement nulling case. The harmonic control input $\mathbf{x}_h(kT_s)$ is added to the measurement vector to minimize $\mathbf{x}_b(t)$. Therefore the influence coefficient matrix $\hat{\mathbf{T}}$ is calculated from the frequency response of $-\mathbf{T}_o(z)$. The matrix $\hat{\mathbf{A}}$ is calculated by neglecting the gyroscopic effect and assuming a symmetric rotor, which results in only four independent elements (see equation (7.8)). The highest curve shows the maximum singular value for the actual influence coefficient matrix $\hat{\mathbf{T}}$ and the DHC gain matrix $\hat{\mathbf{A}}$. The maximum singular value is different from zero, because we neglected the gyroscopic effect, assumed a symmetric system, and approximated the resulting coefficients by a polynomial. In order to see how much each approximation contributes to the increase in $\bar{\sigma}$ we gradually improve the gain matrix $\hat{\mathbf{A}}$ and/or omit³ the gyroscopic effect in $\hat{\mathbf{T}}$. The second

2 The nonconservative cross-coupling is also neglected, because it is a-priori unknown and handled separately by the adaptive control.

3 It is not possible to include the gyroscopic effect and use the symmetry assumption in $\hat{\mathbf{A}}$. Therefore the gyroscopic effect is omitted in $\hat{\mathbf{T}}$ which is equivalent to including it in $\hat{\mathbf{A}}$.

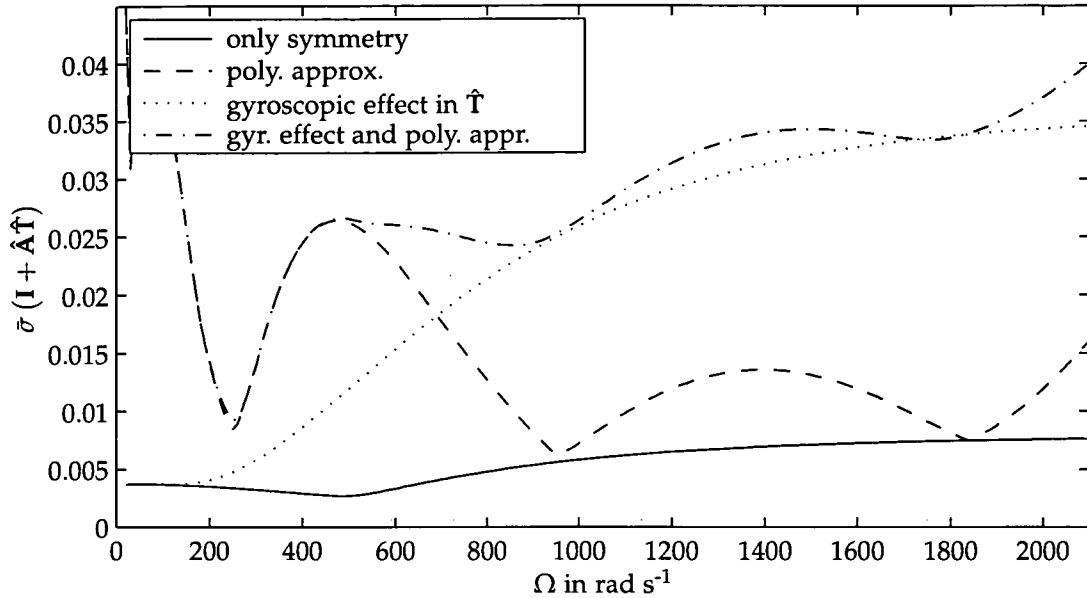


Figure 7.3.: Maximum singular value of $I + \hat{A}\hat{T}$ for control input x_h and harmonically controlled variable x_b (\hat{T} calculated from $-T_o(z)$)

curve shows the maximum singular value when the coefficients are not approximated by polynomials. It is obvious that for low rotational speeds the polynomial approximation is the main reason for the deviation of $\bar{\sigma}$ from zero. The third curve shows $\bar{\sigma}$ when the gyroscopic effect is omitted in \hat{T} and the symmetry assumption as well as the polynomial approximation is used. The lowest curve is calculated for \hat{T} without gyroscopic effect and the "symmetric" \hat{A} . The amount by which $\bar{\sigma}$ is larger than zero can be interpreted as the convergent speed decrease due to the symmetry assumption.

Although the highest curve represents the actual system, the convergence speed is best predicted by the third curve, where the gyroscopic effect is omitted in the calculation of the influence coefficient matrix \hat{T} . Since the center of gravity is almost at the mid-span position between the two bearings, the mass unbalance forces are not exciting tilting motions; the gyroscopic effect is not important for the actual unbalance control, while $\bar{\sigma}$ gives a worst case limit of the convergence rate. It should be pointed out that in the whole rotational speed range from $\Omega = 200 \text{ rad s}^{-1}$ to $\Omega = 2100 \text{ rad s}^{-1}$ the maximum singular value $\bar{\sigma}$ is smaller than 0.04, which means in the worst case a reduction of 96% in a single time step of the DHC algorithm

The robustness of the DHC algorithm is very good, since it tolerates quite

large deviations of $\hat{\mathbf{A}}$ from $\hat{\mathbf{T}}^{-1}$. However, if the simple model of the AMB/Rotor system with $T_{MB} = 0$ and continuous PID control is used to calculate $\hat{\mathbf{A}}$, the relatively high phase lag between this model and the actual simulation model makes the DHC controlled system unstable. This can be prevented by multiplying the matrix $\hat{\mathbf{A}}$ with a factor lower than one, which stabilizes the DHC controlled system but decreases the convergence speed. This method has been used in the first papers of the author [HSS02, HS02, Hir03b].

7.3.5. Simulation Results for Displacement Nulling

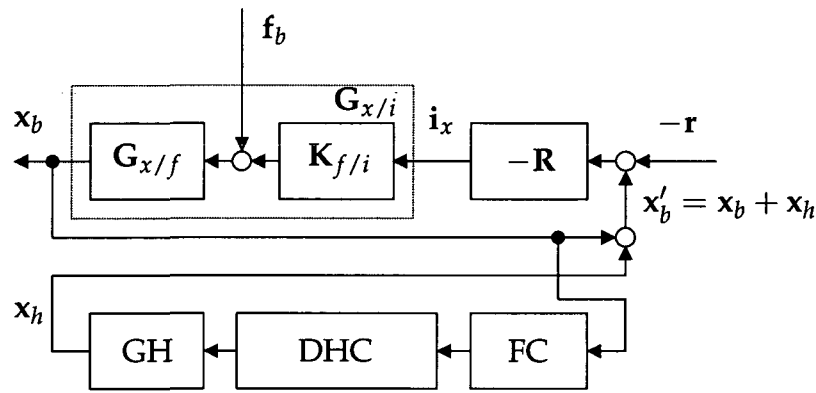


Figure 7.4.: Block diagram of the displacement nulling discrete harmonic control

Figure 7.4 shows the block diagram of the displacement nulling DHC scheme. The block FC stands for the calculation of the Fourier coefficients, DHC for the discrete harmonic control algorithm and GH for the generation of the actual harmonic control input. As in the previous sections, $\mathbf{K}_{f/i}$ for the control current to magnetic bearing force transfer matrix, $\mathbf{G}_{x/f}$ is the force to rotor displacement transfer matrix, $\mathbf{G}_{x/i}$ is the control current to rotor displacement transfer matrix, \mathbf{R} is the PID controller transfer matrix, \mathbf{r} is the reference rotor displacement vector (usually zero), and \mathbf{f}_b is the disturbance force vector in bearing coordinates (including unbalance force) acting on the rotor.

The implementation of the displacement nulling with discrete harmonic control is straight forward. Since we want to minimize \mathbf{x}_b with the control input \mathbf{x}_h , we need the input-output relationship between these two to calculate $\hat{\mathbf{T}}$ and $\hat{\mathbf{A}}$. From equation (5.2) we get

$$\hat{\mathbf{x}}_b(z) = -\mathbf{T}_o(z) \hat{\mathbf{x}}_h(z)$$

and the matrix $\hat{\mathbf{A}}$ is

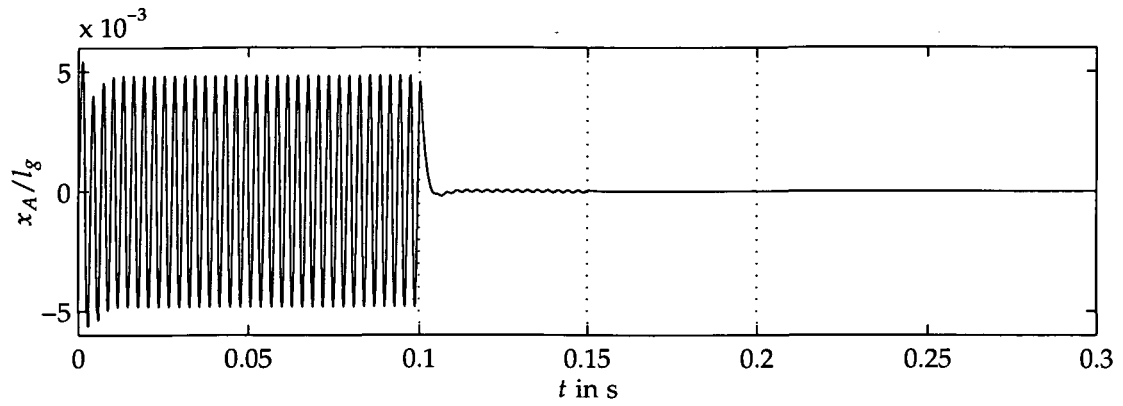
$$\hat{\mathbf{A}}(\Omega) = \begin{bmatrix} \text{Re}(\mathbf{T}_o(e^{j\Omega T_s})) & \text{Im}(\mathbf{T}_o(e^{j\Omega T_s})) \\ -\text{Im}(\mathbf{T}_o(e^{j\Omega T_s})) & \text{Re}(\mathbf{T}_o(e^{j\Omega T_s})) \end{bmatrix}^{-1}.$$

This matrix is brought into the form of equation (7.8) (all coefficients have the same sign) and the matrix elements are approximated by a second order polynomial.

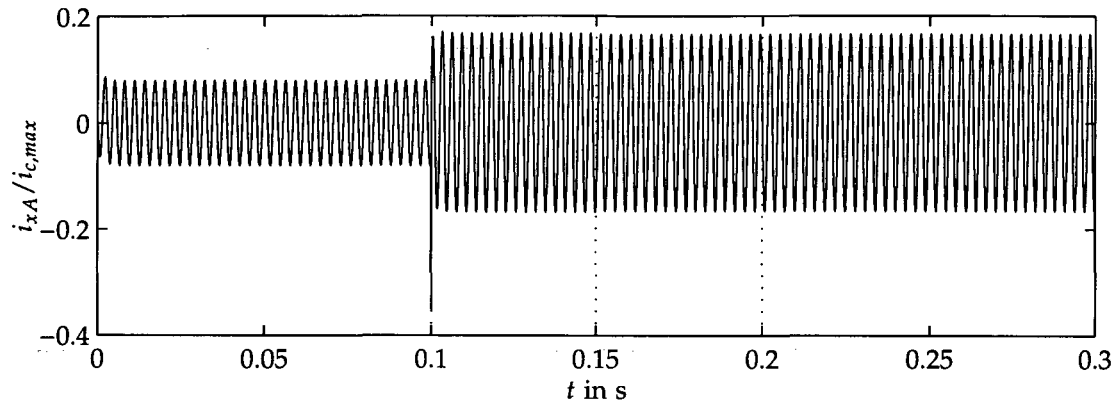
In figure 7.5, we see the simulation results for DHC controlled rotor at a rotational speed of $\Omega = 2094 \text{ rad/s} \triangleq 20000 \text{ r/min}$, an unbalance radius of $e = 2 \mu\text{m}$, a DHC sample time of $T_h = 0.05 \text{ s}$ and an integration time $T_i \cong 10 \frac{2\pi}{\Omega}$. T_h is chosen rather large, so that the quasi-static assumption holds and the Fourier coefficients are calculated for approximately ten oscillation periods. The adaptive control starts at $t = 2T_h$. The points of time $2T_h$, $3T_h$ and $4T_h$ are marked by dotted vertical lines in figure 7.5. As in all following simulation the rotor displacement x_A , the control current $i_x A$, and the actual magnetic bearing force f_{xA} are plotted relative to the nominal maximum values given in table 2.2.

With the start of the DHC control the harmonic control variable x_h jumps from zero to a value defined by the Fourier coefficients of the DHC output. This jump is amplified by the differential part of the PID controller and we can see a rather high peak in the control current (figure 7.5b). However, the low pass behavior of the magnetic bearing smoothes this peak and it is comparatively small in the actual magnetic bearing force as can be seen in figure 7.5c. The rotor vibrations are reduced in one single step by 99%, which is a little bit faster than predicted by the maximum singular value as plotted in figure 7.3; the DHC control works at its maximum speed. There is only one possibility to make the unbalance control faster with respect to the actual time that the DHC needs to reduce the unbalance vibration: the time T_h has to be reduced.

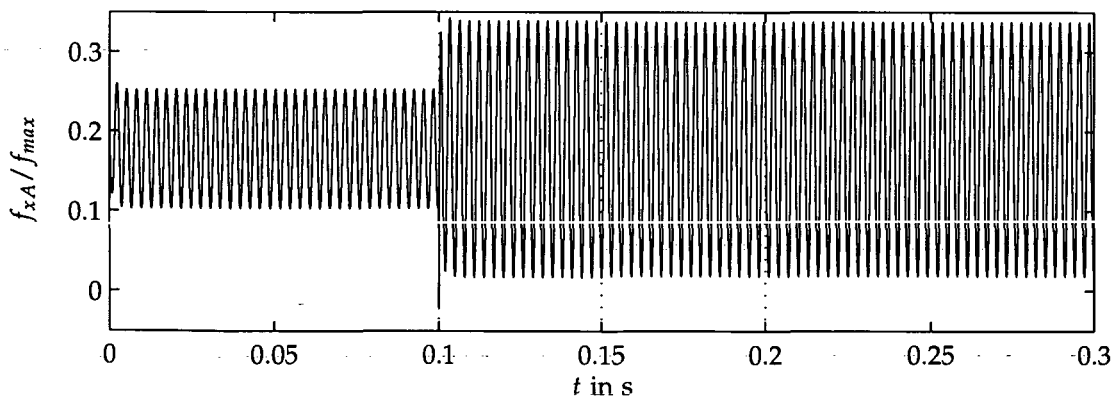
Figure 7.6 shows the result for $T_h = 0.01 \text{ s}$ and $T_i \cong 2\pi/\Omega$. The reduction of the sample time T_h violates the quasi-static assumption as can be seen in figure 7.6a. After the start of the algorithm, the response on the DHC does not reach a steady state in one time step T_h . Coincidentally the DHC is not unstable and is able to reduce the rotor vibrations in an additional time step. Although the DHC algorithm is now faster with respect to the actual time t (while it is slower with respect to the needed discrete steps), we are on dangerous grounds. The steady state assumption is violated and the stability and convergence of the algorithm cannot be guaranteed anymore.



(a) rotor displacement

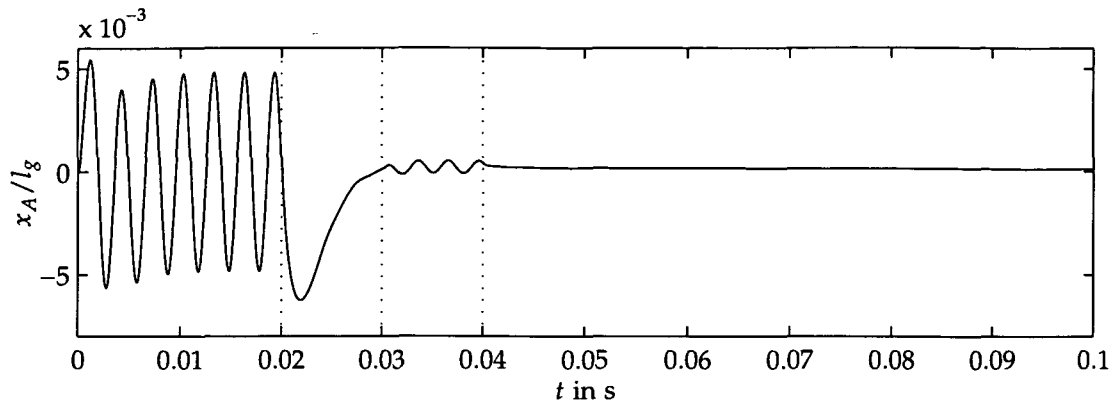


(b) control current

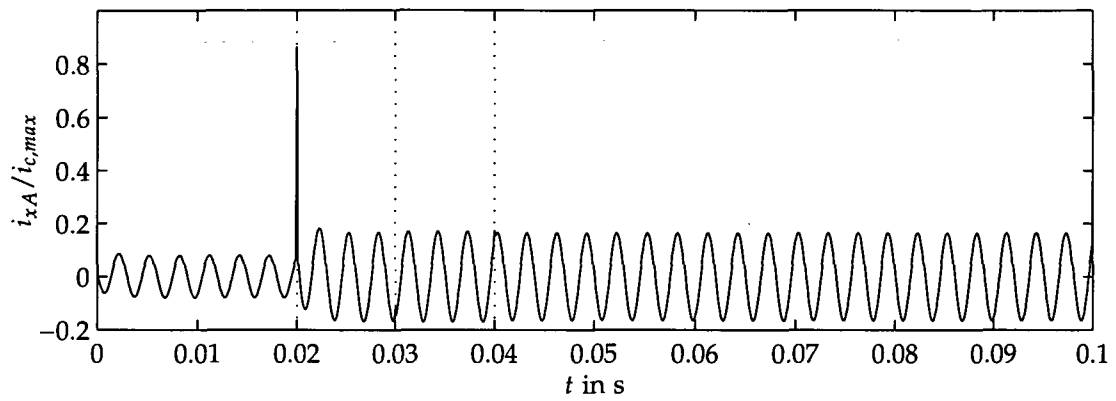


(c) magnetic bearing force

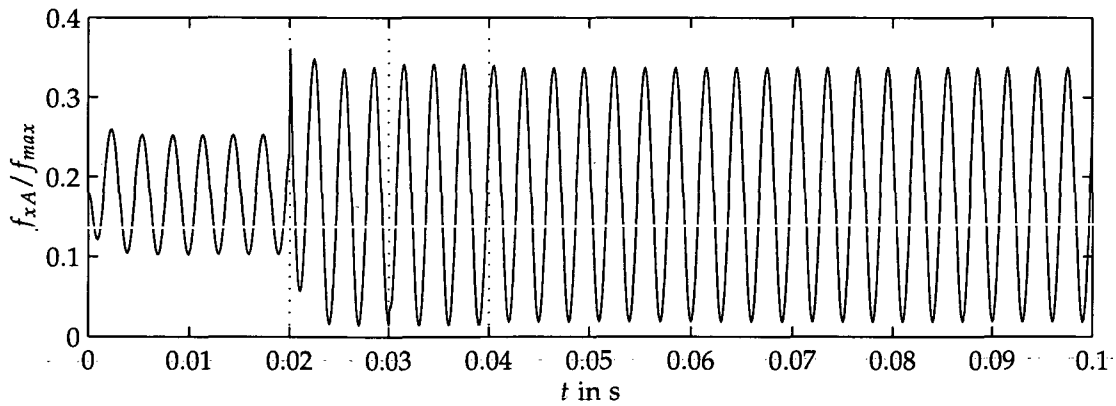
Figure 7.5.: Displacement nulling with DHC algorithm for a rotational speed of $\Omega = 2094 \text{ rad/s} \hat{=} 20000 \text{ r/min}$, a DHC sample time of $T_h = 0.05 \text{ s}$, and an integration time $T_i \cong 10 \frac{2\pi}{\Omega}$



(a) rotor displacement

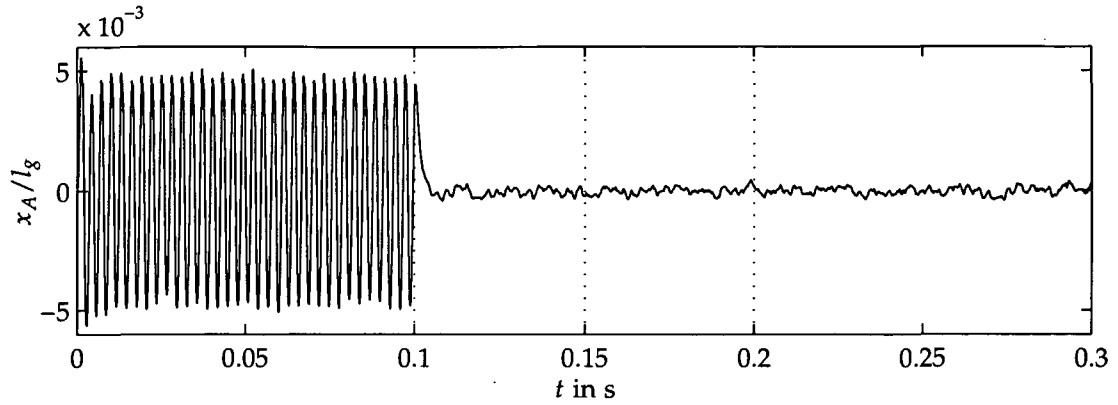


(b) control current

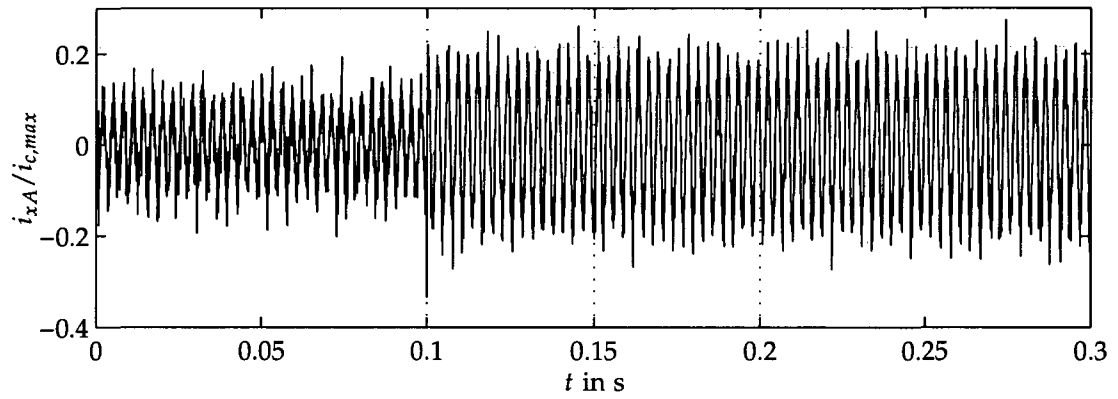


(c) magnetic bearing force

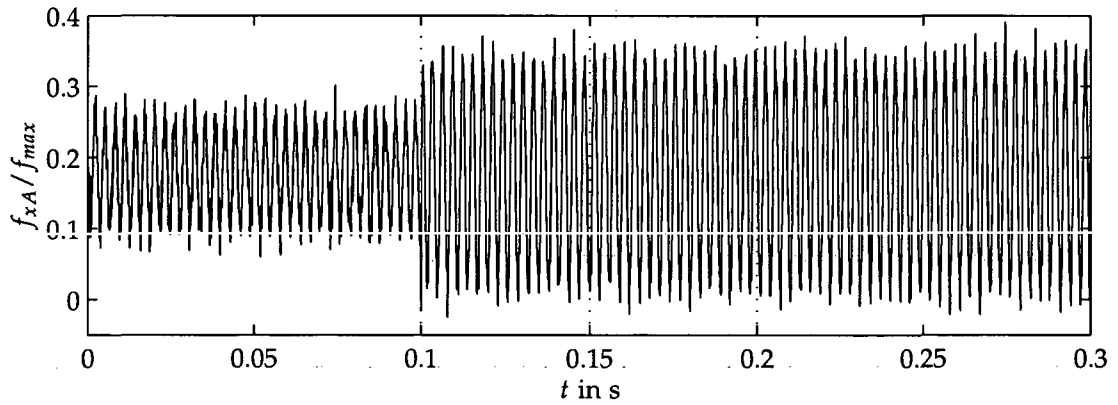
Figure 7.6.: Displacement nulling with DHC algorithm for a rotational speed of $\Omega = 2094 \text{ rad/s} \hat{=} 20000 \text{ r/min}$, a DHC sample time of $T_h = 0.01 \text{ s}$, and an integration time $T_i \hat{=} \frac{2\pi}{\Omega}$



(a) rotor displacement



(b) control current



(c) magnetic bearing force

Figure 7.7.: Displacement nulling with DHC algorithm for a rotational speed of $\Omega = 2094 \text{ rad/s} \cong 20000 \text{ r/min}$, added measurement noise, a DHC sample time of $T_h = 0.05 \text{ s}$, and an integration time $T_i \cong 10 \frac{2\pi}{\Omega}$

Finally, for the displacement nulling DHC control simulation, measurement noise with a standard variation of $0.1 \mu\text{m}$ is added to the measured rotor position x_b . The resulting rotor vibration is shown in figure 7.7. The measurement noise does not influence the performance of the DHC, since the noise has almost no effect on the Fourier coefficients.

7.3.6. Simulation Results for Current Nulling

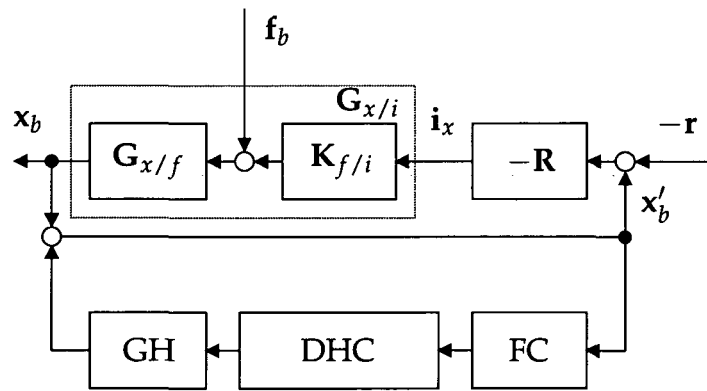


Figure 7.8.: Block diagram of the current nulling discrete harmonic control

For the current nulling control aim, it would be possible to use the same procedure as before; measure the control current and add a compensation signal x_h or i_h . However, for the adaptive cross-coupling control the control current as well as the rotor position have to be free of harmonic components. Instead of compensating the unbalance directly in the control current, we compensate it in the rotor position vector

$$x'_b = x_b + x_h,$$

which is used as the input for the stabilizing controller and the ACCC. Thus, the control signal of the DHC is added to x'_b which results in the system shown in figure 7.8. There is no additional harmonic disturbance between the measurement and the controller. An elimination of the harmonics in the rotor position x'_b also eliminates the harmonics in the control currents i_x .

In equation (5.2) the input-output relationship between x'_b and x_h is given by

$$\hat{x}'_b(z) = S_o(z) \hat{x}_h(z)$$

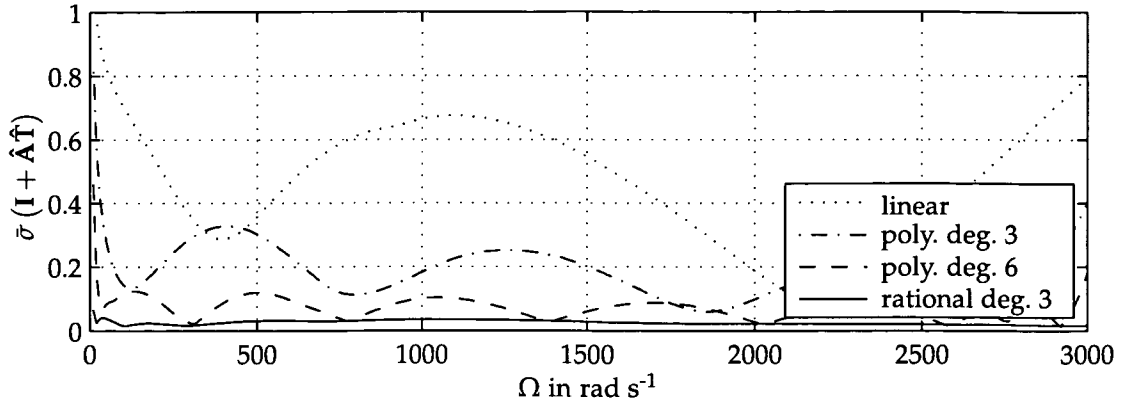


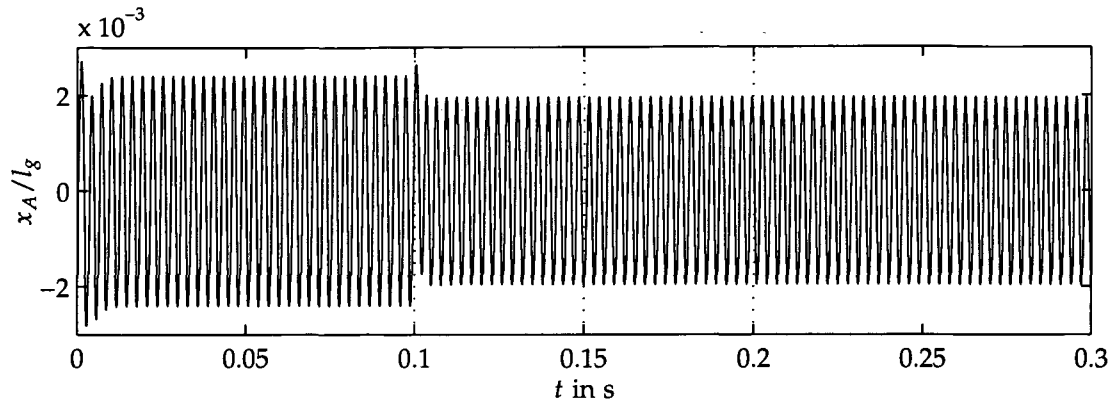
Figure 7.9.: Maximum singular value of $\mathbf{I} + \hat{\mathbf{A}}\hat{\mathbf{T}}$; The nonzero elements of \mathbf{A} are polynomial approximations of the elements of $\hat{\mathbf{T}}^{-1}$.

so that $\hat{\mathbf{A}}$ is calculated from $\mathbf{S}_o(z)$. Unfortunately, a polynomial approximation of the coefficients of the matrix $\hat{\mathbf{A}}$ is not very good in the sense of a low maximum singular value $\bar{\sigma}$ of $\mathbf{I} + \hat{\mathbf{A}}\hat{\mathbf{T}}$. This is shown in figure 7.9 where $\bar{\sigma}$ is plotted over the rotational frequency Ω for various polynomial approximations. Therefore, rational functions with polynomials of degree three as numerators and denominators, that is

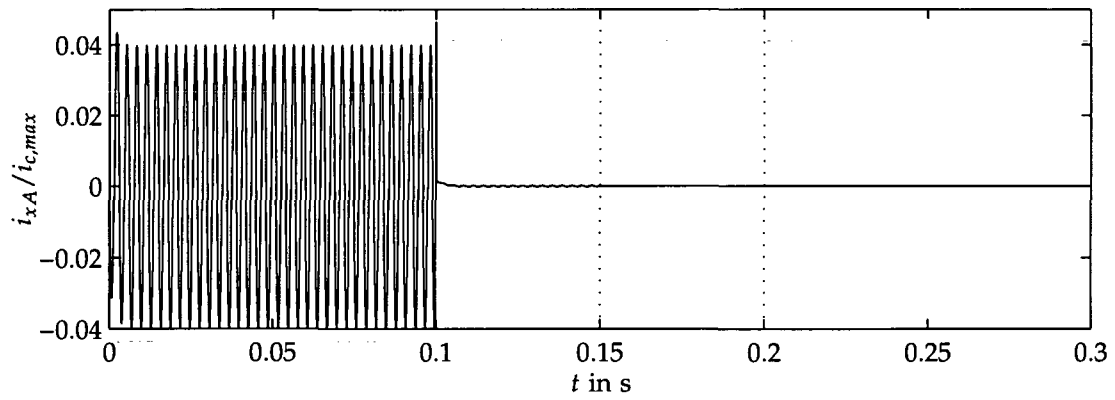
$$A(\Omega) = \frac{a_0 + a_1\Omega + a_2\Omega^2 + a_3\Omega^3}{b_0 + b_1\Omega + b_2\Omega^2 + b_3\Omega^3},$$

are used to approximate the elements of $\hat{\mathbf{A}}$. The resulting $\bar{\sigma}$ is also shown in figure 7.9.

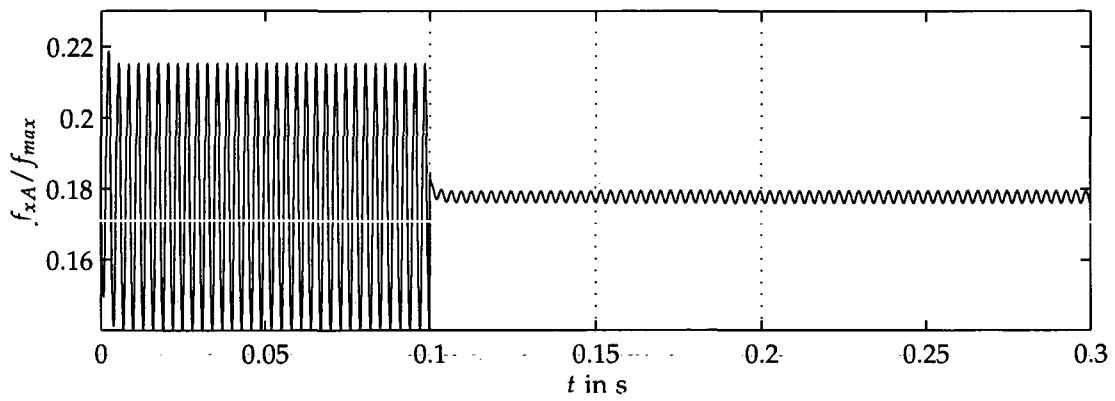
In figure 7.10, we see the simulation results for the DHC current nulling controlled rotor, at a rotational speed of $\Omega = 2094 \text{ rad/s} \hat{=} 20000 \text{ r/min}$, a DHC sample time of $T_h = 0.05 \text{ s}$ and an integration time $T_i \cong 20\pi/\Omega$. Again the vibration level is reduced substantially, this time at a rate of about 99% in a single time step $T_h = 0.05 \text{ s}$. Further, the magnetic force level is reduced to about 5% and even the rotor vibration is reduced to about 81% compared with no DHC application; the current nulling scheme causes a lower vibration level than the discrete-time PID controller for rotational speeds significantly higher than the first natural mechanical frequency.



(a) rotor displacement



(b) control current



(c) magnetic bearing force

Figure 7.10.: Current nulling with DHC algorithm for a rotational speed of $\Omega = 2094 \text{ rad/s} \cong 20000 \text{ r/min}$, a DHC sample time of $T_h = 0.05 \text{ s}$, and an integration time $T_i \cong 10 \frac{2\pi}{\Omega}$

This equation is purely algebraic, since $K_{f/i}(s)$ and $K_{f/x}(s)$ have the same poles and no zeros.

In the current nulling case, the elimination of the harmonics in the measured rotor vibrations has already been used to achieve the elimination in the control current. After a few time steps the harmonics in the measured rotor vibrations have been eliminated and the negative DHC control output $-x_h$ has been equal to the harmonics in the actual rotor vibrations x_b . If we use the same scheme with an additional compensation path from the DHC to the control current, that is

$$\mathbf{i}_h = \mathbf{K}_i^{-1} \mathbf{K}_s \mathbf{x}_h ,$$

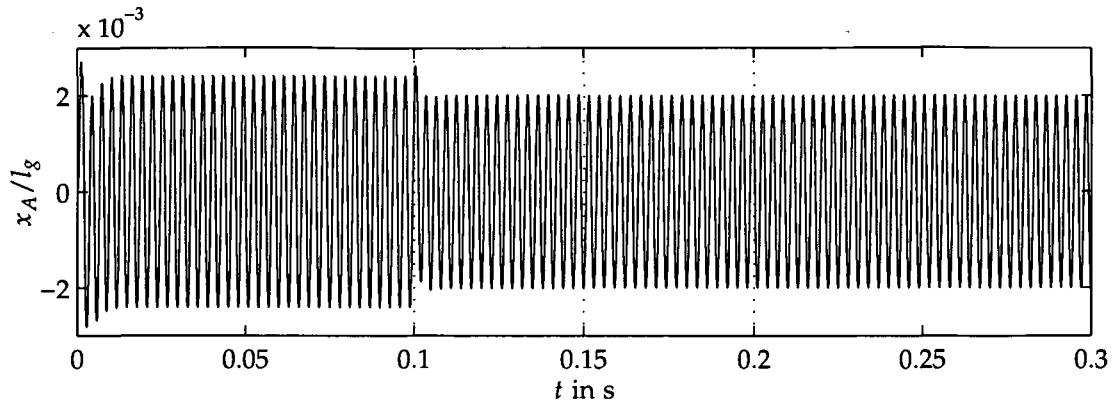
we can achieve a significant reduction in the harmonics of the control current. This scheme is shown in figure 7.11. Due to the additional current input, we also get a different transfer function for the calculation of $\hat{\mathbf{A}}$. The relationship between $\hat{\mathbf{x}}'_b$ and the DHC control output $\hat{\mathbf{x}}_h$ is (see equation (5.2))

$$\begin{aligned} \hat{\mathbf{x}}'_b(z) &= \mathbf{S}_o(z) \hat{\mathbf{x}}_h(z) + \mathbf{S}_o(z) \mathbf{G}_{x/i}(z) \hat{\mathbf{i}}_h(z) \\ &= \left(\mathbf{S}_o(z) + \mathbf{S}_o(z) \mathbf{G}_{x/i}(z) \mathbf{K}_i^{-1} \mathbf{K}_s \right) \hat{\mathbf{x}}_h(z) . \end{aligned}$$

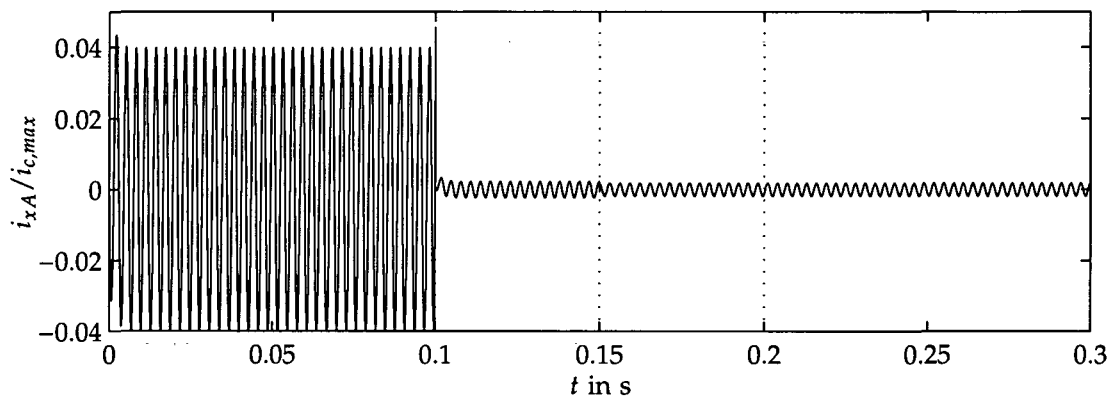
The compensation in the magnetic bearing force is not perfect, since the compensation signal is discrete-time and the rotor vibration effect is continuous-time. An additional error in the modelling of \mathbf{K}_i and \mathbf{K}_s will increase the residual harmonics in the AMB force and the resulting force amplitude may even be higher than in the original case.

A further problem is the approximation of the elements of $\hat{\mathbf{A}}$ with rational functions. The approximation of the matrix elements itself is quite good, but since the force nulling scheme produces high rotor vibration amplitudes in the low frequency region (see fig. 7.1a) the coefficients of $\hat{\mathbf{A}}$ are also very large in the low frequency range. An approximation procedure which minimizes the overall matrix element error produces large values for the maximum singular value $\bar{\sigma}$ of $\mathbf{I} + \hat{\mathbf{A}}\hat{\mathbf{T}}$. Since the rotor vibration is limited, the force nulling should only take place in the higher frequency range where the resulting rotor vibration as well as the coefficients of $\hat{\mathbf{A}}$ are rather small. In this region, the approximation procedure usually leads to a small singular value $\bar{\sigma}$ of $\mathbf{I} + \hat{\mathbf{A}}\hat{\mathbf{T}}$. The actual optimization is carried out in the range from $\Omega = 100$ rad/s to 3000 rad/s.

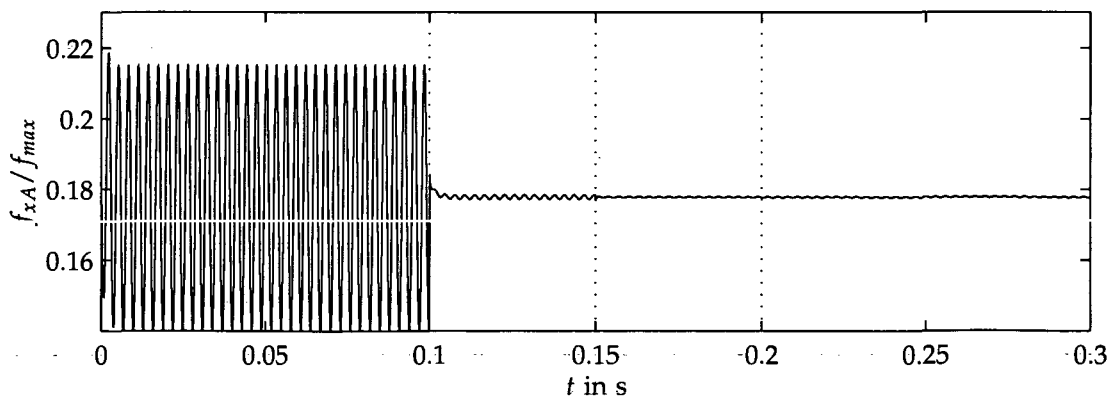
Figure 7.12 shows the simulation results, again at a rotational speed of $\Omega = 2094$ rad/s $\hat{=} 20000$ r/min, a DHC sample time of $T_h = 0.05$ s, and an



(a) rotor displacement

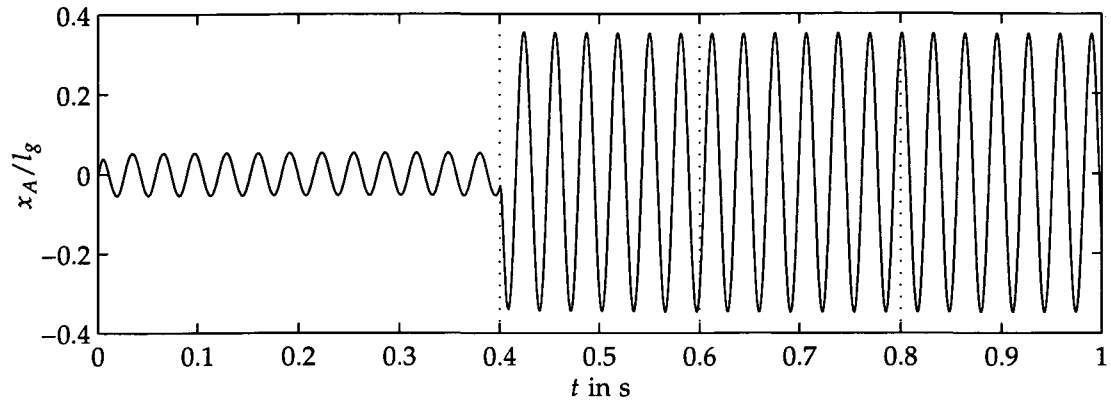


(b) control current

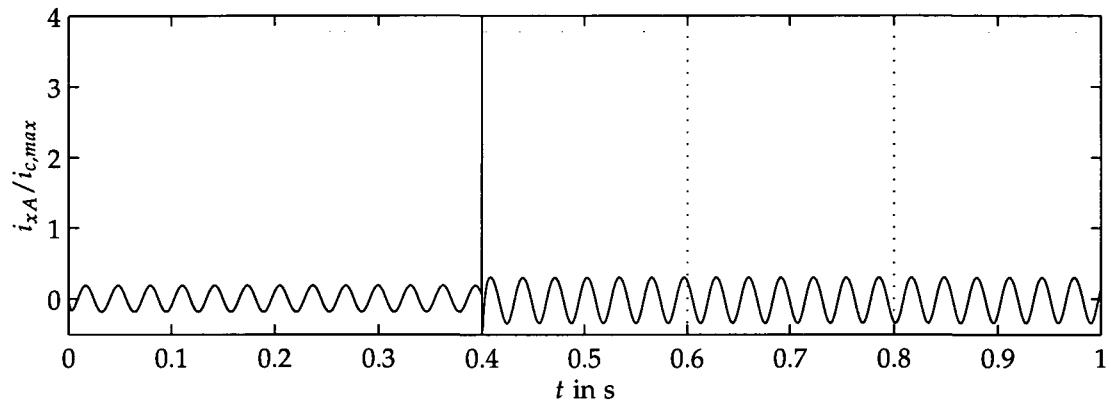


(c) magnetic bearing force

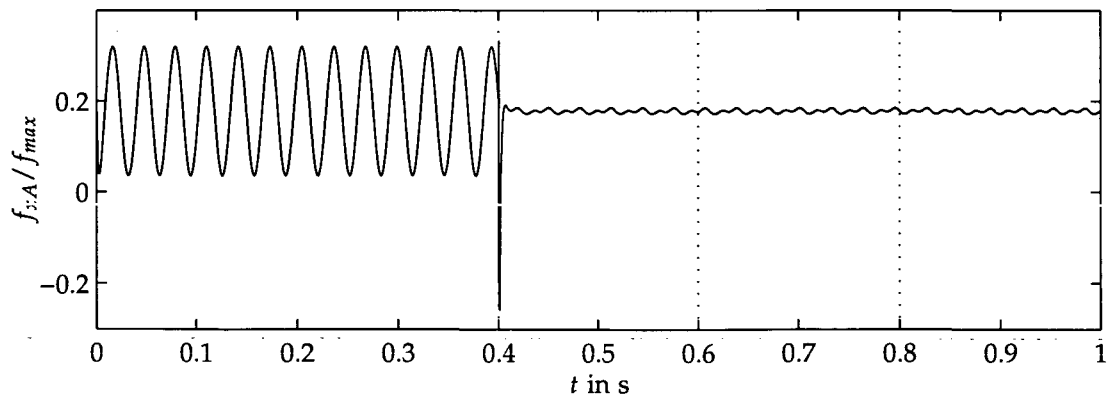
Figure 7.12.: Force nulling with DHC algorithm for a rotational speed of $\Omega = 2094 \text{ rad/s} \cong 20000 \text{ r/min}$, a DHC sample time of $T_h = 0.05 \text{ s}$, and an integration time $T_i \cong 10 \frac{2\pi}{\Omega}$



(a) rotor displacement



(b) control current



(c) magnetic bearing force

Figure 7.13.: Force nulling with DHC algorithm for a rotational speed of $\Omega = 200$ rad/s, a DHC sample time of $T_h = 0.2$ s, and an integration time $T_i \cong 5 \frac{2\pi}{\Omega}$

integration time $T_i \cong 10 \frac{2\pi}{\Omega}$. The magnetic bearing force is reduced very fast, but there is a residual force oscillation. Since K_i and K_s are exactly known in the simulation this can be viewed as an optimal case. Any further attempt to reduce the remaining oscillation is probably not worth the effort, because in reality the uncertainties in K_i and K_s will contribute much more to a residual oscillation than the difference between discrete-time and continuous-time input signals.

To show that the algorithm also works for low frequency oscillations, a further simulation is carried out with a rotational frequency of $\Omega = 200 \text{ rad/s} \cong 1910 \text{ r/min}$. To get a larger rotor vibration amplitude the unbalance radius is set to $e = 170 \text{ }\mu\text{m}$. The result is shown in figure 7.13. The algorithm works similar to the earlier cases. It is interesting that there are nonlinear effects due to the rather large rotor vibrations in the remaining force oscillation (fig. 7.13c). The control current exceeds the maximum allowed current at $t = 0.4 \text{ s}$, as we see in figure 7.13b. However the actual magnetic bearing current is smaller, since the underlying current controller is taking care of the limitations, and the coil current cannot follow the control current immediately.

7.4. Continuous Harmonic Control

The discrete harmonic control equation (7.3) can also be written as

$$\hat{\mathbf{u}}_1(i) = \hat{\mathbf{A}} (\hat{\mathbf{y}}_1(i) + \hat{\mathbf{y}}_1(i-1) + \hat{\mathbf{y}}_1(i-2) + \dots + \hat{\mathbf{y}}_1(1)) ,$$

which emphasizes the integrating nature of this controller. We insert the continuous calculation of the Fourier coefficients equation (7.5), set the integration time of the Fourier coefficients to the DHC sample time, i.e. $T_i = T_h$, and obtain

$$\hat{\mathbf{u}}_1(i) = \hat{\mathbf{A}} \frac{2}{T_h} \left(\int_{(i-1)T_h}^{iT_h} \begin{bmatrix} \bar{\mathbf{y}}(\tau) \cos \Omega \tau \\ \mathbf{y}(\tau) \sin \Omega \tau \end{bmatrix} d\tau + \dots + \int_0^{T_h} \begin{bmatrix} \bar{\mathbf{y}}(\tau) \cos \Omega \tau \\ \mathbf{y}(\tau) \sin \Omega \tau \end{bmatrix} d\tau \right) .$$

This can be simplified to

$$\hat{\mathbf{u}}_1(i) = \hat{\mathbf{A}} \frac{2}{T_h} \int_0^{iT_h} \begin{bmatrix} \bar{\mathbf{y}}(\tau) \cos \Omega \tau \\ \mathbf{y}(\tau) \sin \Omega \tau \end{bmatrix} d\tau .$$

This equation suggests an alternative implementation of the DHC algorithm. The whole adaptive or recursive process can be moved to the Fourier coefficients calculation part, and the discretization is done afterwards by sampling

with sample time T_h . The only drawback of this implementation is that T_i has to be the same as T_h and therefore T_h must be a multiple of the period of rotation $2\pi/\Omega$.

However, it is not really clear why the control vector $\hat{\mathbf{u}}_1$ should be sampled at all. The elimination of the sampling procedure leads to

$$\mathbf{u}(t) = \begin{bmatrix} \mathbf{I} \cos \Omega t & \mathbf{I} \sin \Omega t \end{bmatrix} \hat{\mathbf{A}} 2\mu \int_0^t \begin{bmatrix} \mathbf{y}(\tau) \cos \Omega \tau \\ \mathbf{y}(\tau) \sin \Omega \tau \end{bmatrix} d\tau. \quad (7.9)$$

This control algorithm is called "continuous harmonic control" (CHC) in this thesis. The gain factor μ is introduced here to be able to adjust the convergence speed. A direct comparison between DHC and CHC is achieved for (see [HW89])

$$\mu = \frac{1}{T_h}. \quad (7.10)$$

When we repeat the derivation of the CHC from the DHC with the discrete-time calculation of the Fourier coefficients equation (7.6), we get a discrete-time version of the CHC algorithm, i.e.

$$\mathbf{u}(k) = \begin{bmatrix} \mathbf{I} \cos \Omega k T_s & \mathbf{I} \sin \Omega k T_s \end{bmatrix} \hat{\mathbf{A}} 2T_s \mu \sum_{\kappa=0}^{k-1} \begin{bmatrix} \mathbf{y}(\kappa T_s) \cos \Omega T_s \kappa \\ \mathbf{y}(\kappa T_s) \sin \Omega T_s \kappa \end{bmatrix}, \quad (7.11)$$

for the discrete case.⁴ Both continuous-time (7.9) and discrete-time (7.11) versions are called continuous harmonic control. All simulations are carried out with the discrete-time version.

7.4.1. Stability Analysis

Continuous-Time CHC

For the continuous-time system, the stability analysis of the CHC algorithm is rather easy. The control vector $\mathbf{u}(t)$ in equation (7.9) satisfies the following differential equation [HBGL96]

$$\ddot{\mathbf{u}}(t) + \Omega^2 \mathbf{u}(t) = 2\mu (\hat{\mathbf{A}}_R \dot{\mathbf{y}}(t) + \Omega \hat{\mathbf{A}}_J \mathbf{y}(t))$$

⁴ To make the implementation easier, the summation is carried out from $\kappa = 0$ to $k - 1$ which makes almost no difference for small sample times.

or, written in the Laplace domain,

$$\hat{\mathbf{u}}(s) = \frac{2\mu}{s^2 + \Omega^2} (s\hat{\mathbf{A}}_R + \Omega\hat{\mathbf{A}}_J) \hat{\mathbf{y}}(s) . \quad (7.12)$$

So, basically the CHC algorithm behaves like a linear time invariant system of differential equations.⁵ When the transfer matrix described by equation (7.12) is included in the PID controlled system, the poles of the complete system can be calculated. For $\mu = 0$, the control loop is open and the additional poles from the CHC algorithm are located at $j\Omega$. A classical root locus curve with μ as parameter can be drawn. In [HW89] and [HBGL96], the authors come to the conclusion that, for $\hat{\mathbf{A}} = \hat{\mathbf{T}}^{-1}$, the root locus in μ of these additional poles has an angle of departure of 90° , i.e. they move in the left half plane for increasing μ ; the additional CHC poles are always stable for small μ when $\hat{\mathbf{A}}$ is chosen in the described way. There is no general rule how the other poles of the system react. Since we assume that the system without CHC control is stable and therefore the poles are in the left half plane, a small μ exists that the root locus starting from these poles stay in the left half plane. However, for increasing μ some poles may move to the right half plane, so that the upper bound of μ is set by the behavior of the system. This corresponds to the condition for the DHC algorithm that T_h should be greater than the relevant time constants of the system (quasi-static assumption).

Discrete-Time CHC

The approach by Hall et al. [HW89] and Herzog et al. [HBGL96] for the continuous-time version of the CHC suggest that the discrete-time version of the CHC can also be expressed as a linear time invariant system. Widrow et al. [WS85] developed the so-called LMS-algorithm for adaptive signal processing. This LMS-algorithm together with sinusoidal reference inputs is exactly the same as the discrete-time CHC control with $\hat{\mathbf{A}} = \mathbf{I}$. Glover [Glo77] and Widrow et al. [WS85] show that the path from $\mathbf{y}(k)$ to $\mathbf{u}(k)$ is linear and time-invariant. This analysis is extended here for an arbitrary $\hat{\mathbf{A}}_R$ and $\hat{\mathbf{A}}_J$.

In equation (7.11), we set the input $\mathbf{y}(k)$ to be a unit pulse at discrete-time $k = m$, that is

$$\mathbf{y}(k) = \mathbf{1} \delta(k - m)$$

⁵ The same result is achieved by Laplace transforming equation (7.9).

where $\delta(k)$ is a unit pulse at $k = 0$

$$\delta(k) = \begin{cases} 1 & \text{for } k = 0 \\ 0 & \text{for } k \neq 0 \end{cases}.$$

The response on this unit pulse is

$$\mathbf{u}(k) = \begin{bmatrix} \mathbf{I} \cos \Omega k T_s & \mathbf{I} \sin \Omega k T_s \end{bmatrix} \begin{bmatrix} \hat{\mathbf{A}}_R & \hat{\mathbf{A}}_J \\ -\hat{\mathbf{A}}_J & \hat{\mathbf{A}}_R \end{bmatrix} 2T_s \mu \begin{bmatrix} 1 \cos \Omega m T_s \\ 1 \sin \Omega m T_s \end{bmatrix} \sigma(k - m - 1) \quad (7.13)$$

where $\sigma(k)$ is the unit step function

$$\sigma(k) = \begin{cases} 0 & \text{for } k < 0 \\ 1 & \text{for } k \geq 0 \end{cases}.$$

Equation (7.13) can be simplified to

$$\mathbf{u}(k) = 2T_s \mu [\hat{\mathbf{A}}_R \cos \Omega T_s (k - m) - \hat{\mathbf{A}}_J \sin \Omega T_s (k - m)] \sigma(k - m - 1).$$

Note that the right hand side of this equation is a function only of $(k - m)$ and is thus a true impulse response. If the impulse time m is set equal to zero, the unit impulse response is

$$\mathbf{u}(k) = 2T_s \mu [\hat{\mathbf{A}}_R \cos \Omega T_s k - \hat{\mathbf{A}}_J \sin \Omega T_s k] \sigma(k - 1)$$

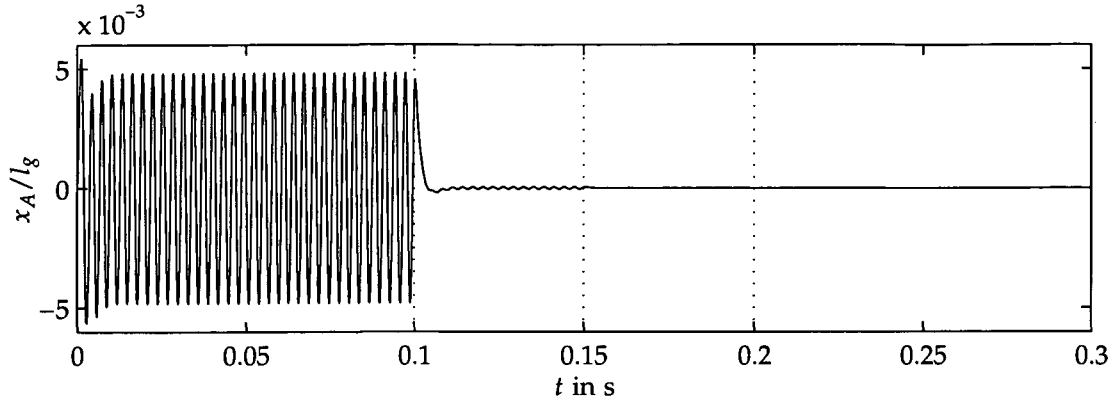
and the z-transfer matrix is the z-transform of the impulse response, that is

$$\hat{\mathbf{u}}(z) = \frac{2T_s \mu}{z^2 - 2z \cos \Omega T_s + 1} (\hat{\mathbf{A}}_R (z \cos \Omega T_s - 1) - \hat{\mathbf{A}}_J z \sin \Omega T_s) \hat{\mathbf{y}}(z). \quad (7.14)$$

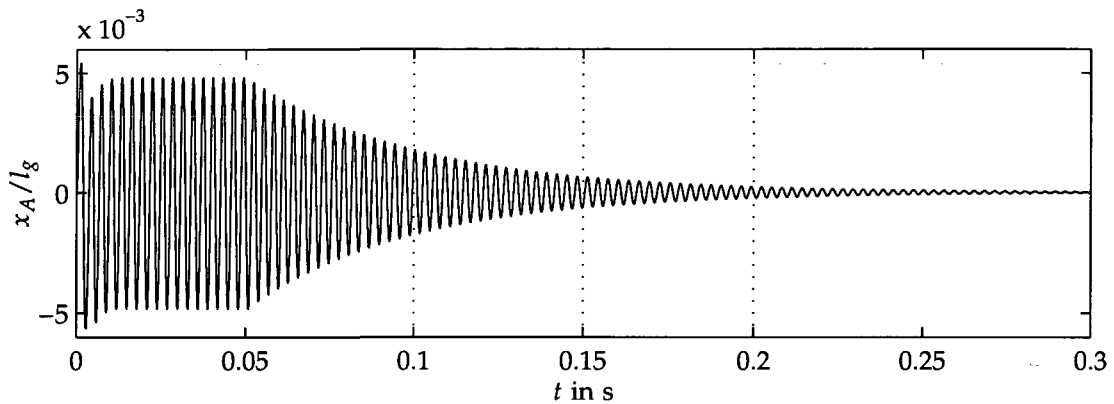
The transfer matrix described by equation (7.14) can be included in the stability analysis of the complete PID controlled system.

7.4.2. Comparison of DHC and CHC for Displacement Nulling

To compare the discrete harmonic control and the continuous harmonic control, we use the same parameters as in figure 7.5 and 7.6 and simulate again with CHC. In order to compare the results, we choose μ from equation (7.10). The result is compared with the previous result in figure 7.14.



(a) rotor displacement for DHC control



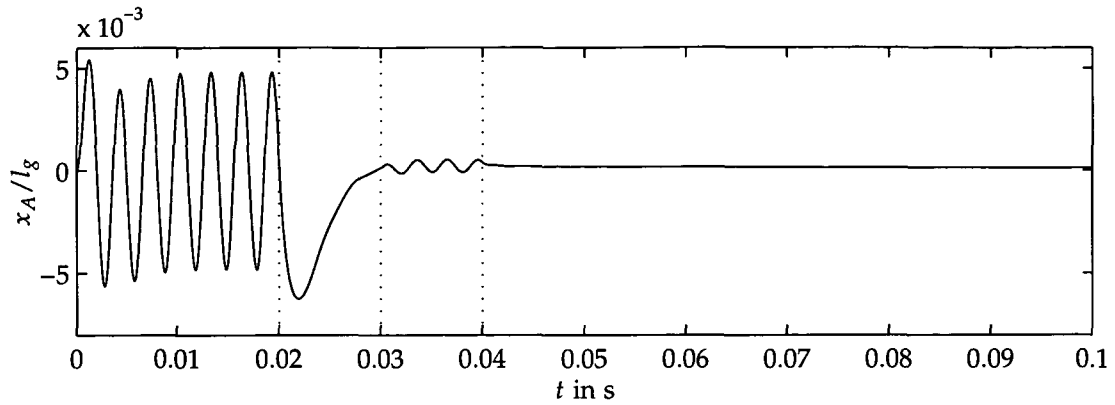
(b) rotor displacement for CHC control

Figure 7.14.: Displacement nulling with DHC algorithm and CHC algorithm; $\Omega = 2094 \text{ rad/s} \triangleq 20000 \text{ r/min}$, $T_h = 0.05 \text{ s}$, and $\mu = 1/T_h$

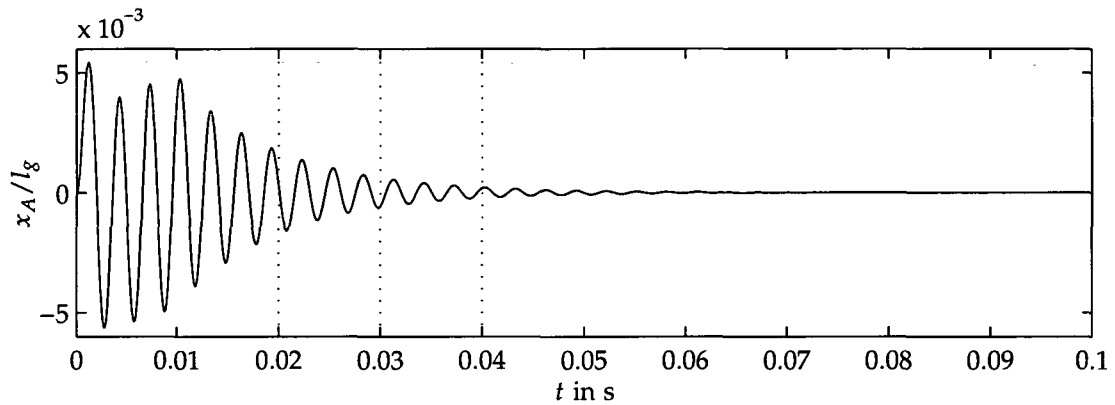
Both algorithms start after 0.05 s. The DHC needs one discrete step to calculate the Fourier coefficients and then diminishes the rotor vibrations in almost a single step. The CHC can immediately start with the vibration reduction, but it takes longer to diminish the vibration completely. This result may lead to the conclusion that the CHC is slower than the DHC.

However, if we try to speed up both algorithms the situation changes. In figure 7.15, we repeat the simulation of figure 7.5 and compare it with the according CHC result. Now both algorithms have almost the same speed, because the DHC no longer shows a dead beat behavior. The steady state assumption of the DHC algorithm is not longer valid and the stability of the algorithm cannot be guaranteed.

The advantages of the CHC algorithms become even clearer when the rota-



(a) rotor displacement for DHC control

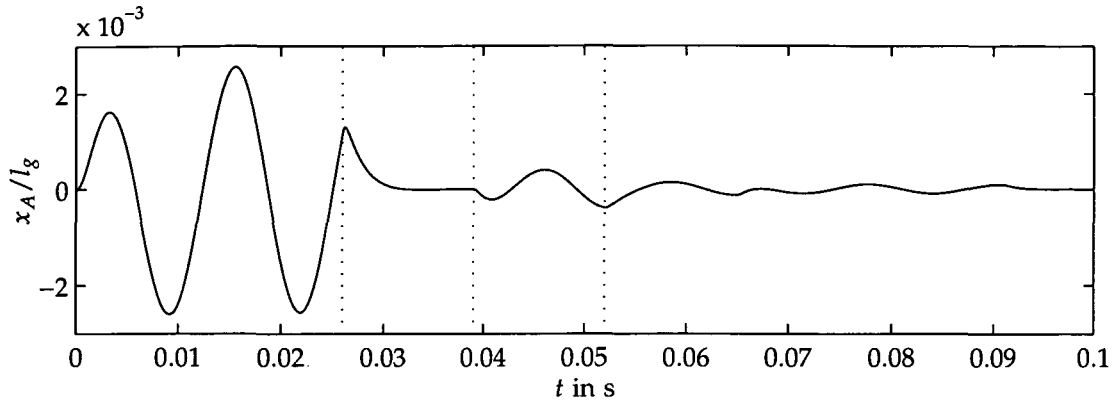


(b) rotor displacement for CHC control

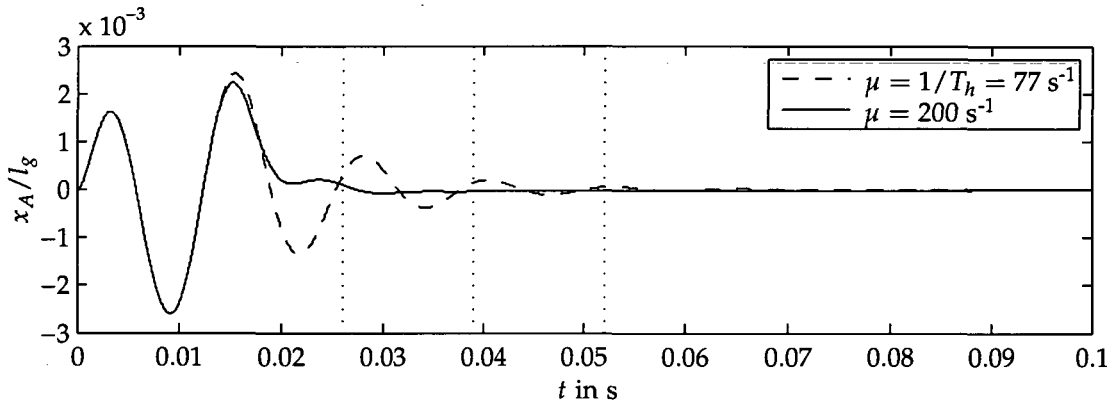
Figure 7.15.: Displacement nulling with DHC algorithm and CHC algorithm; $\Omega = 2094 \text{ rad/s} \hat{=} 20000 \text{ r/min}$, $T_h = 0.01 \text{ s}$, and $\mu = 1/T_h$

tional speed and therefore the frequency of the unbalance excitation is lower. For $\Omega \hat{=} 79 \text{ Hz}$, the sample time of the DHC has to be set quite high with $T_h = 0.013 \text{ s}$ because it has to be at least one rotational period. The result is shown in 7.16a. The DHC takes quite a long time because the steady state assumption is not fulfilled. When the corresponding CHC is used with a parameter of $\mu = 77 \text{ s}^{-1}$, this is shown in figure 7.16b as the dotted line, the unbalance vibrations are reduced faster than with DHC. However, there is no strict limitation of μ while T_h is limited to be larger than the duration of one period. So μ is increased to a value of $\mu = 200 \text{ s}^{-1}$ and the result is shown as the solid line in figure 7.16b. With the higher value of μ , the unbalance vibration is diminished even faster than before.

In conclusion, the CHC algorithm is easier to handle than the DHC algo-



(a) rotor displacement for DHC control



(b) rotor displacement for CHC control

Figure 7.16.: Displacement nulling with DHC algorithm and CHC algorithm; $\Omega \triangleq 79$ Hz, $T_h = 0.013$ s, $\mu = 1/T_h = 77$ s⁻¹, and $\mu = 200$ s⁻¹

rithm because there is no need for a sophisticated calculation of Fourier coefficients, especially with changing excitation frequency. The CHC is slower when $\mu = 1/T_h$ and the steady state assumption is true, but μ can be set to much higher values and usually reaches the same speed as the DHC algorithm. For low excitation frequencies, the DHC is limited to a sample time that is equal or greater than the duration of one unbalance period while for the CHC the only limitation is the stability of the system. The work of Sivich [Siv02] suggests that the robustness of the CHC algorithm is usually higher than the robustness of DHC algorithm. The main advantages of the DHC algorithm are: it is easier to understand, the steady state assumption allows an easy stability and robustness test, and it can easily be used to on-line identify the influence coefficient matrix $\hat{\mathbf{T}}$.

8. Combination of Unbalance and Cross-Coupling Control

8.1. Introduction

In the sections 6.7.3 and 6.9.3, the negative influence of harmonic excitations on the adaptive cross-coupling control can be seen. A possible solution of this problem is to add the compensation current filter and the position filter to the calculation of the reference force for the adaptive control as in the 2DoF case. Another possibility is to filter out the harmonic components from the reference force and the measured rotor position. However, when the DHC or the CHC algorithm is used in order to achieve any of the three unbalance control goals, this can be done in a way which also eliminates the harmonic components in the signals for the on-line estimator. Therefore, DHC and CHC not only have the ability to diminish unbalance vibrations but may also eliminate the negative effects of unbalance excitations on the ACCC.

Matsushita et al. [MTY⁺88, MTY⁺90] have already controlled unbalance as well as cross-coupling excitations, but the unbalance control algorithm described is similar to the cross-coupling control algorithm and has nothing to do with more advanced algorithms. Steinschaden has done some preliminary investigations based on the simulation model of Lang which are incorporated in the paper by the author et al. [HSS02]. To the knowledge of the author, this and the other publications by the author et al. [HS02, Hir03b] are the only ones considering unbalance control and cross-coupling control at the same time.

8.2. Simulation Results for DHC and Adaptive Cross-Coupling Control

8.2.1. Displacement Nulling and ACCC

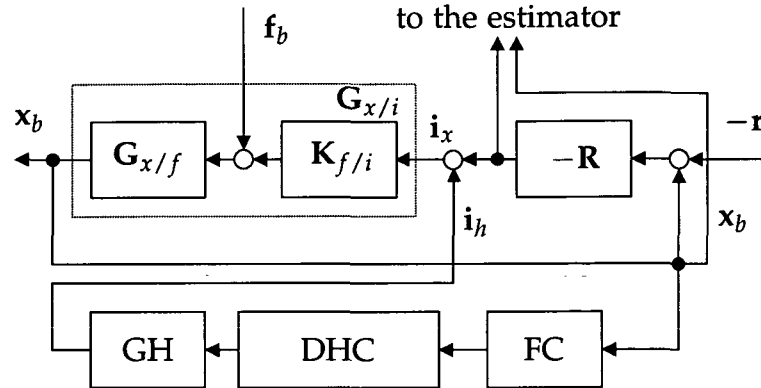


Figure 8.1.: Block diagram of the displacement nulling discrete harmonic control that is compatible with the adaptive cross-coupling control

In section 7.3.5, we have described how to use the DHC algorithm to minimize the speed synchronous rotor vibrations with x_h as control variable, see figure 7.4. Unfortunately, this approach is incompatible with the adaptive cross-coupling control, because the compensation signal x_h is included in the rotor position signal x'_b . So the DHC would diminish the rotor vibrations, but the ACCC would still get harmonic signal components included in the reference force from the DHC.

Instead of x_h a compensation current i_h is used; the according block diagram is shown in figure 8.1. With this variant, the signals for the estimator are free of harmonic components. According to equation (5.2) the influence of i_h on x_b can be described with

$$\hat{x}_b(z) = S_o(z) G_{x/i}(z) \hat{i}_h(z) .$$

So the coefficients of the matrix \hat{A} are calculated from $S_o G_{x/i}$. Figure 8.2 shows the maximum singular value of $I + \hat{A}\hat{T}$ for different methods of calculating the coefficients of \hat{A} . It is easy to see that at least a polynomial with a degree of three has to be used for the calculation of the coefficients of \hat{A} .

The performance of the DHC algorithm does not depend on the specific choice of the control variable. In figure 8.3, we see the simulation result for the

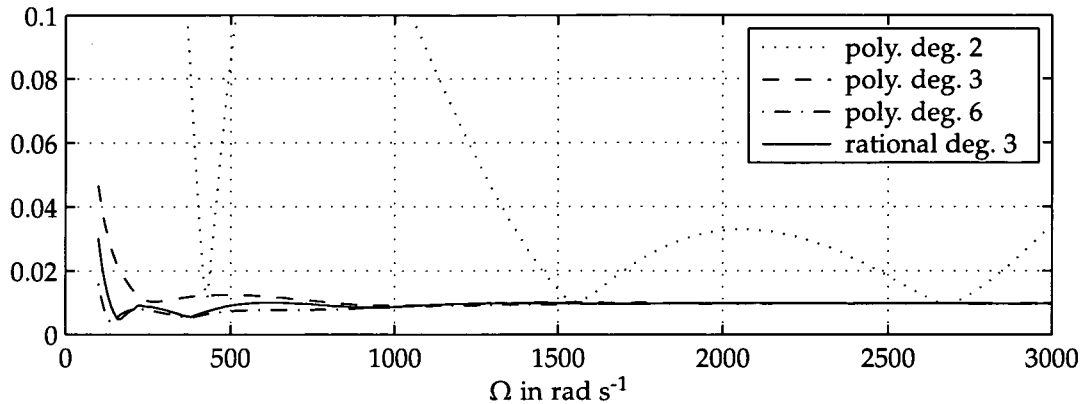


Figure 8.2.: Maximum singular value of $I + \hat{A}\hat{T}$; The nonzero elements of \hat{A} are polynomial approximations of the elements of \hat{T}^{-1}

DHC combined with the ACCC for a rotor without cross-coupling excitation $n_1 = n_2 = n_3 = 0$.

The DHC algorithm starts at $t = 0.5$ s and the first two discrete steps are shown as dotted vertical lines in figure 8.3.

At first, we have the same situation as before and the unbalance whirl influences the adaptive cross-coupling control. Since there is no applied cross-coupling excitation we can only see the estimated parameters \tilde{n}_1 , \tilde{n}_2 and \tilde{n}_3 in figure 8.3a. \tilde{n}_1 and \tilde{n}_3 have almost the same value, so that they appear as a single line in the plot. As the DHC control starts, the algorithm is able to reduce the unbalance excitation in a single discrete step. With the disappearance of the harmonic vibrations, the large estimator oscillations are also diminished and the rotor vibrations disappear completely.

The conclusion that the two algorithms do not influence each other in a negative way is not really surprising. The cross-coupling excited whirls are in the frequency region of the mechanical natural frequencies while the unbalance whirls are speed synchronous whirls. However, if the rotational frequency is also close to the natural frequencies a higher level of interaction will most likely occur.

In figure 8.4, we see the simulation result when only the DHC is active. The on-line estimation is still included but the ACCC loop is not closed. We also see that for a rotational speed at the natural frequency of the rotor the DHC can achieve displacement nulling in a single step. When the ACCC loop is closed, the situation is different. In figure 8.4, the DHC takes significantly more steps to reduce the rotor vibrations. This is due to the interaction of the

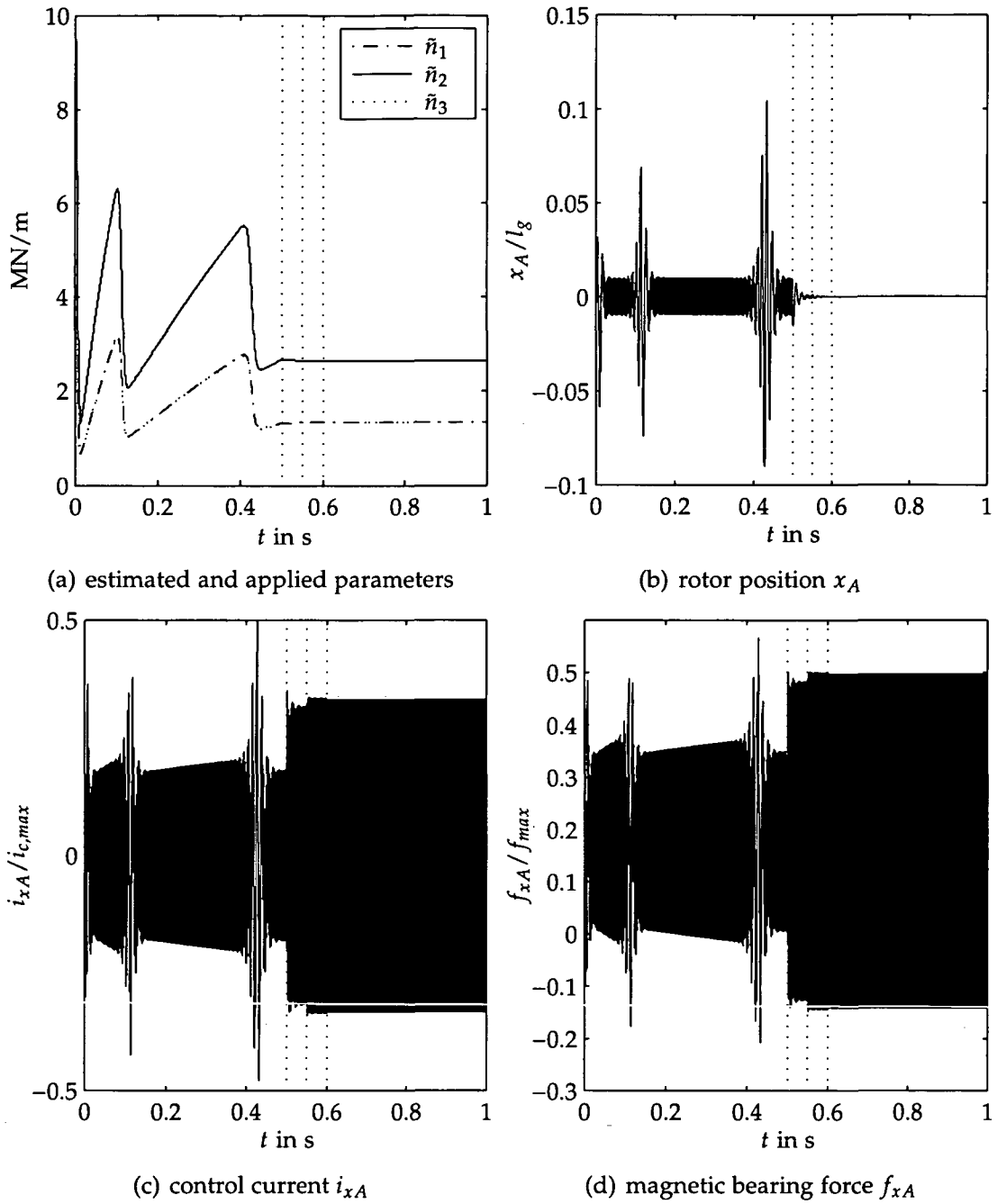


Figure 8.3.: 4DoF system with no cross-coupling excitation $n_1 = n_2 = n_3 = 0$ and ACCC; unbalance excitation $\Omega \doteq 333.3$ Hz, $e = 4$ μm , and DHC

two algorithms at approximately the same frequency.

The first two simulations with ACCC and DHC are carried out for applied values of $n_1 = n_2 = n_3 = 0$. An increase of these values also increases the required magnetic bearing force to stabilize the rotor. Therefore the maximum controllable unbalance amplitude is decreased.

The next simulation, shown in figure 8.6, is carried out for the same parameters as in the simulations in figure 6.25 with additional unbalance control. The DHC starts at 1.5 s and immediately decreases the unbalance vibrations. With the unbalance vibrations, the oscillations in the estimated cross-coupling parameters and the "unstable" whirls also disappear. In figure 8.7, measurement noise with a standard deviation of $0.2 \mu\text{m}$ is added to the system. The behavior of the system is similar to the situation without noise.

The last simulation with displacement nulling by DHC and ACCC is carried out for the same parameters as in figure 6.30. Again the DHC eliminates the estimator oscillations as the unbalance vibrations disappear.

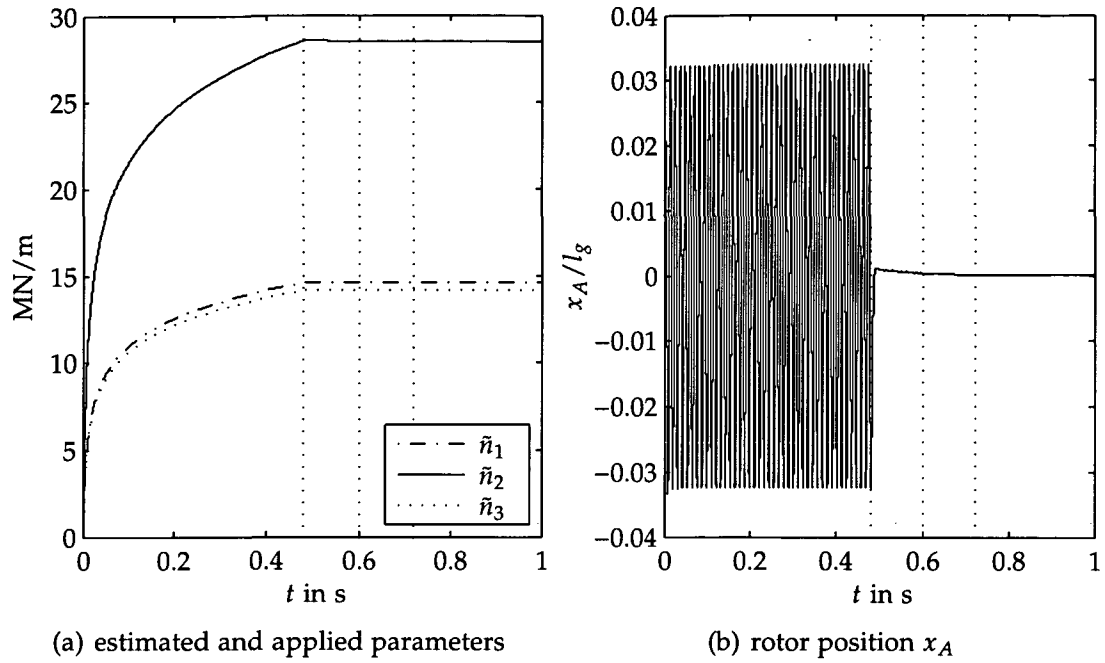


Figure 8.4.: 4DoF system with no cross-coupling excitation and ACCC loop not closed; unbalance excitation $\Omega \triangleq 89$ Hz, $e = 22$ μm , and DHC

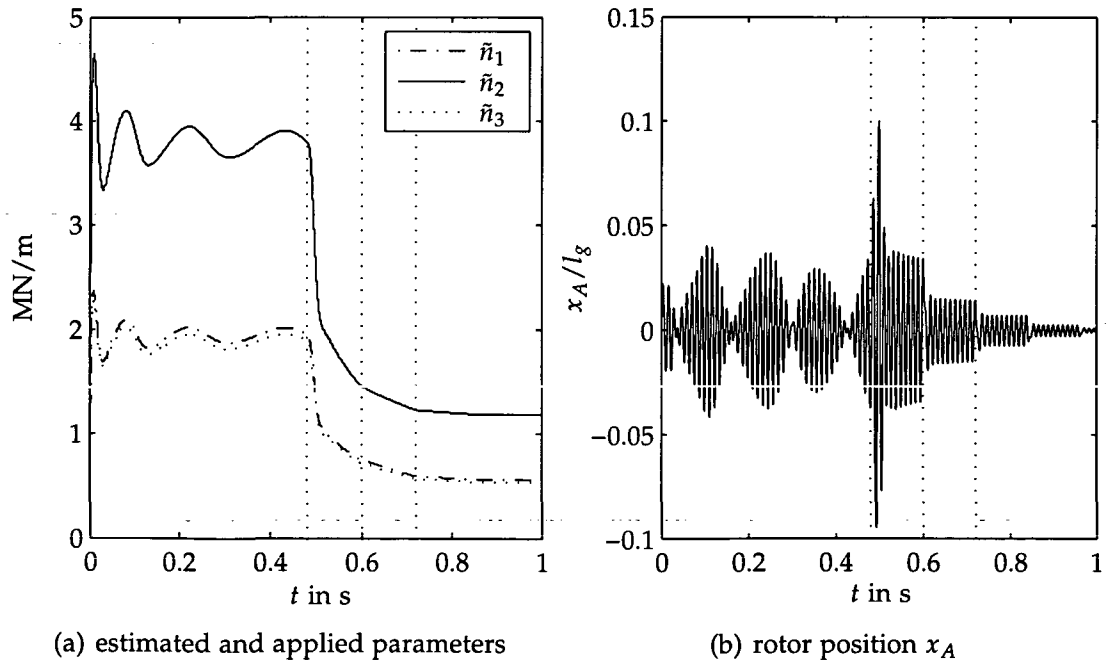


Figure 8.5.: 4DoF system with no cross-coupling excitation $n_1 = n_2 = n_3 = 0$ and active ACCC; unbalance excitation $\Omega \triangleq 89$ Hz, $e = 22$ μm , and DHC

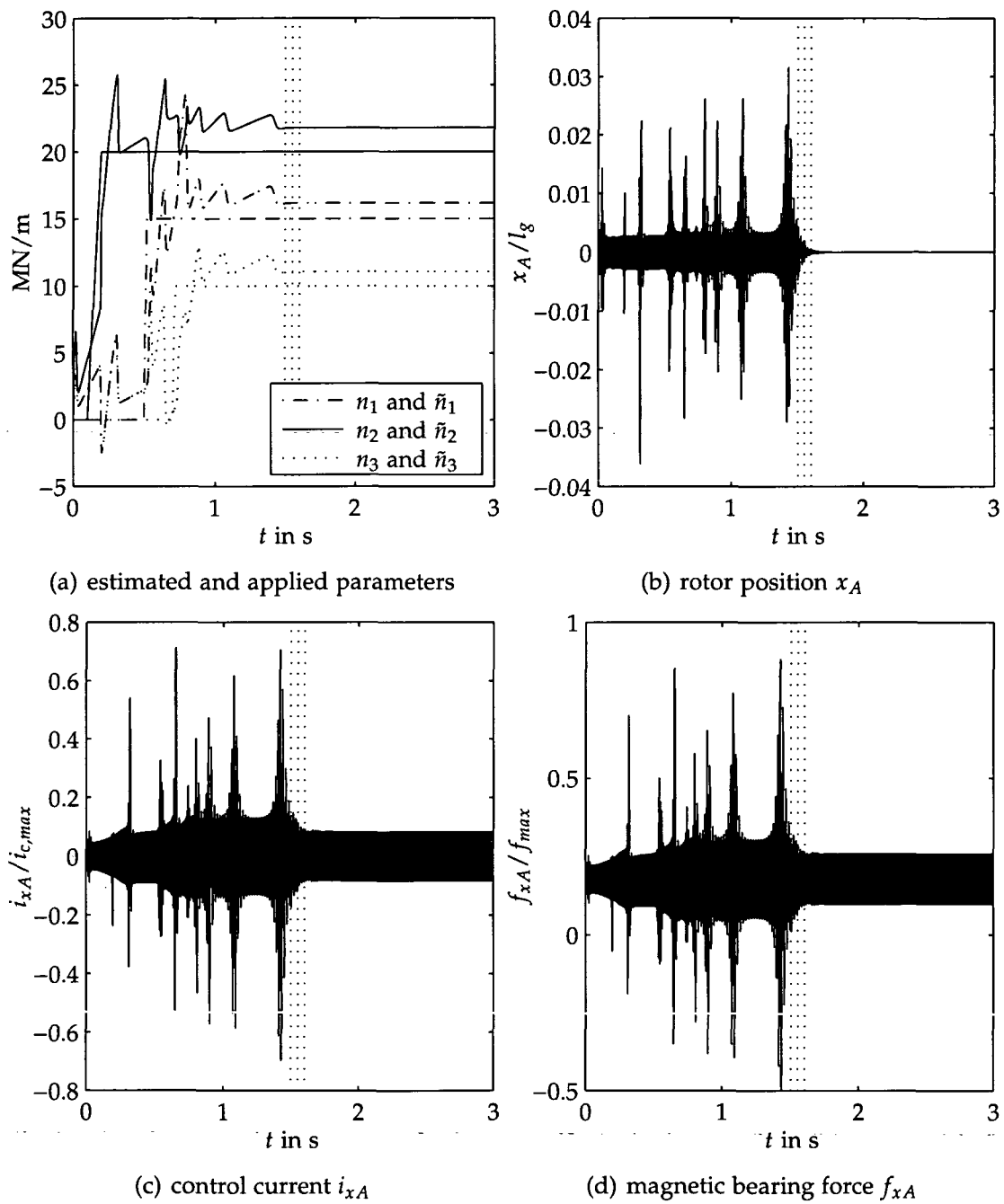


Figure 8.6.: 4DoF system with cross-coupling excitation $n_1 = 15 \text{ MN/m}$, $n_2 = 20 \text{ MN/m}$, $n_3 = 10 \text{ MN/m}$ and ACCC; unbalance excitation $\Omega \triangleq 333.3 \text{ Hz}$, $e = 1 \text{ }\mu\text{m}$, and DHC

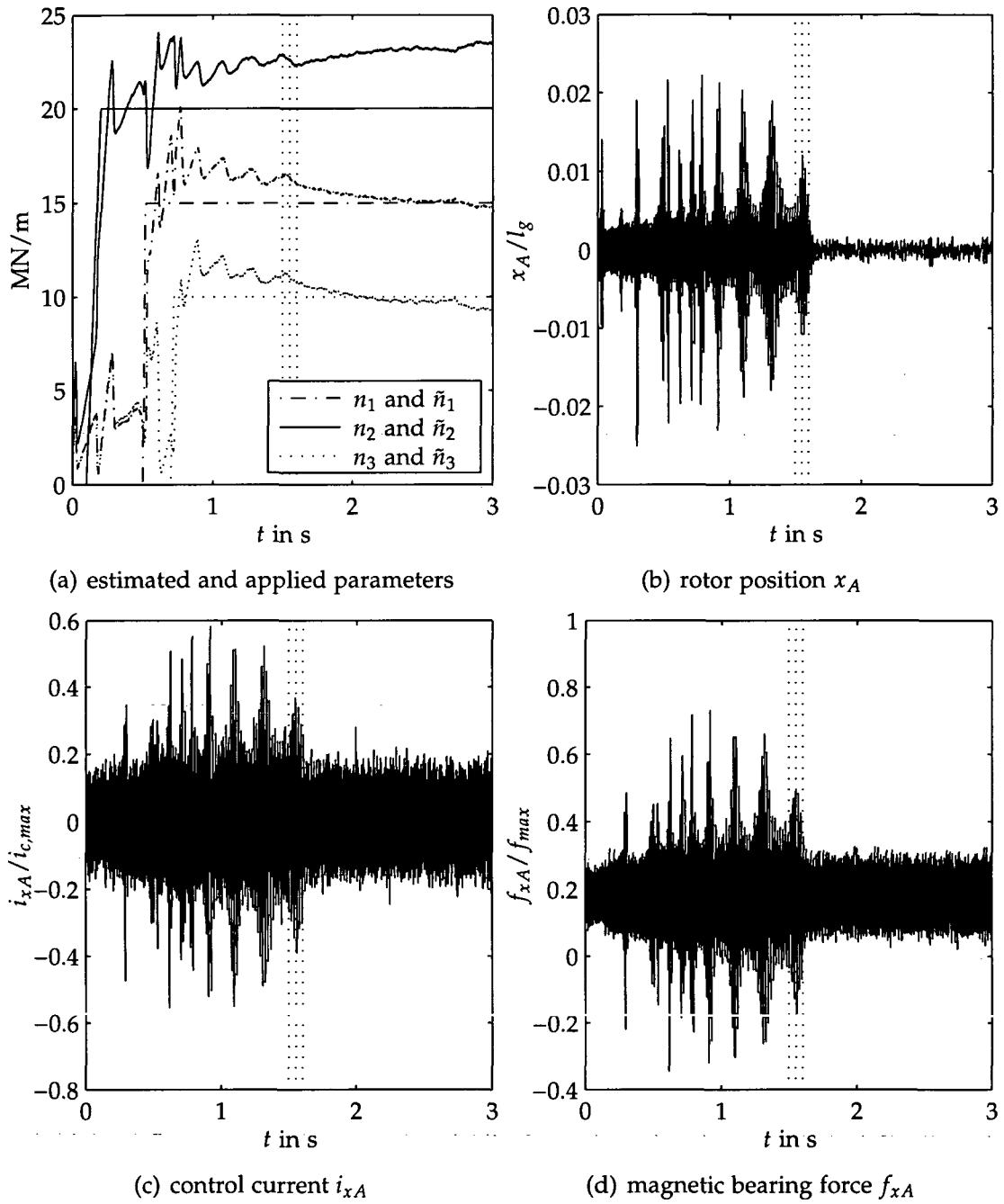


Figure 8.7.: 4DoF system with cross-coupling excitation $n_1 = 15$ MN/m, $n_2 = 20$ MN/m, $n_3 = 10$ MN/m and ACCC; unbalance excitation $\Omega \hat{=} 333.3$ Hz, $e = 1$ μ m, and DHC; measurement noise

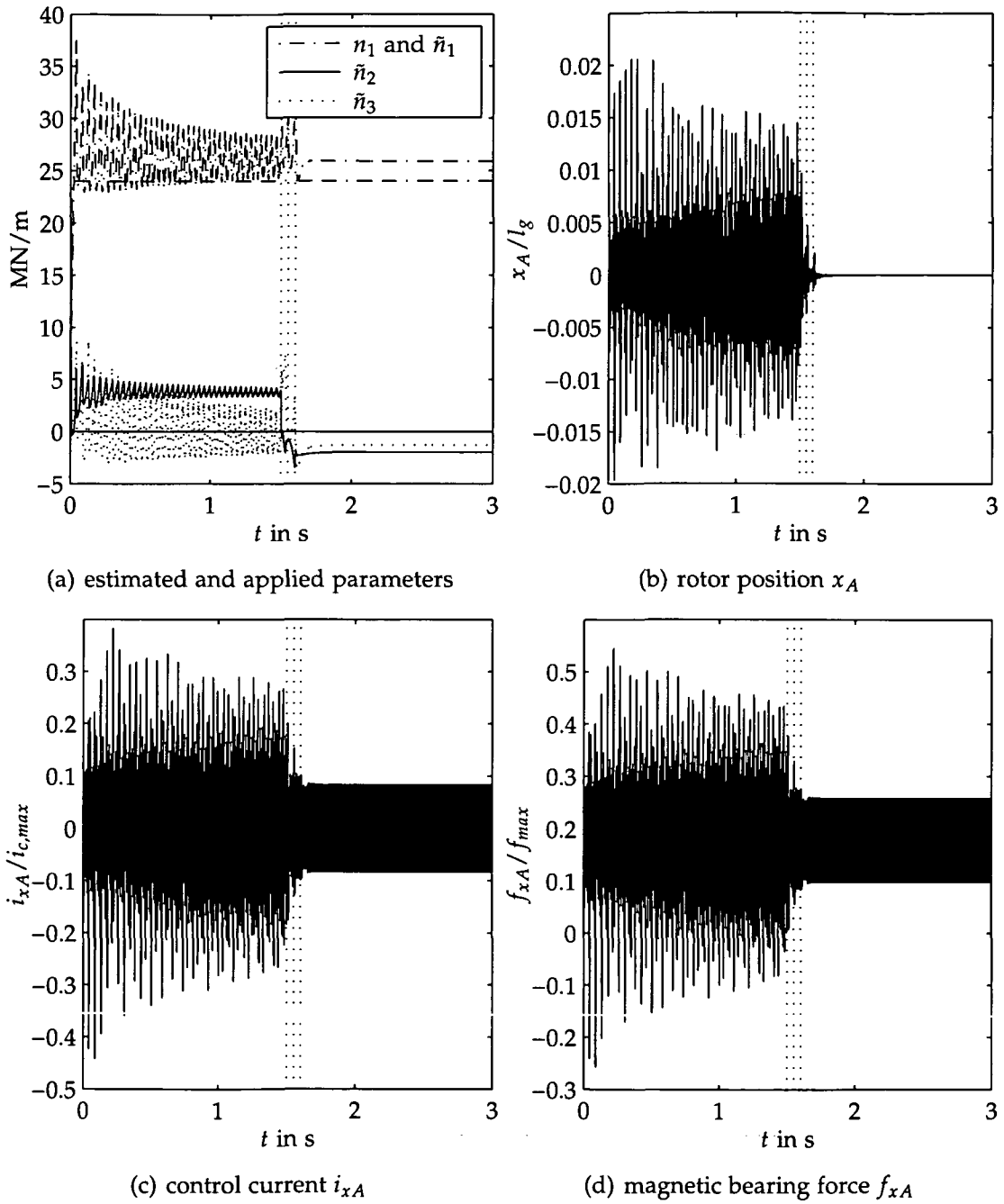


Figure 8.8.: 4DoF system with cross-coupling excitation $n_1 = 15 \text{ MN/m}$, $n_2 = n_3 = 0$ and ACCC; unbalance excitation $\Omega \doteq 333.3 \text{ Hz}$, $e = 1 \text{ }\mu\text{m}$, and DHC; measurement noise

8.2.2. Current Nulling and ACCC

In section 7.3.6, it is shown that the DHC algorithm is able to eliminate the speed synchronous components in the magnetic bearing currents. The chosen control input \mathbf{x}_h is also suitable to work together with the ACCC algorithm. The DHC minimizes the harmonic components in \mathbf{x}'_b . Since \mathbf{x}'_b is also used for the PID controller and therefore also in the estimator reference force, the estimated parameters \tilde{n}_1 to \tilde{n}_3 are no longer influenced by the unbalance vibrations.

However, for the cross-coupling compensation part in the ACCC, there are two possible choices for the used rotor vibration signal, either \mathbf{x}_b or \mathbf{x}'_b , i.e.

$$\mathbf{i}_n = -\tilde{\mathbf{N}}\mathbf{x}_b(t) \quad \text{or} \quad \mathbf{i}_n = -\tilde{\mathbf{N}}\mathbf{x}'_b = -\tilde{\mathbf{N}}(\mathbf{x}_b(t) + \mathbf{x}_h(t)) .$$

If \mathbf{x}_b is used, the cross-coupling forces are compensated and the system is stabilized. However, since there is still a speed synchronous rotor vibration, we also have speed synchronous magnetic bearing currents due to the cross-coupling compensation. Since the rotor vibration may be higher with current nulling, the resulting magnetic bearing currents may be even higher than without current nulling.

If \mathbf{x}'_b is used, the harmonic components are also compensated in the cross-coupling compensation part of the ACCC. This has the effect that the compensation current \mathbf{i}_n is also free from harmonic components as long as the DHC succeeds. Unfortunately, this has the effect that the actual cross-coupling forces due to the unbalance vibrations are not compensated and an unstable whirl may develop.

Both choices have their benefits. With \mathbf{x}_b , the ACCC is more reliable but the speed synchronous harmonics in \mathbf{i}_x are not zero; with \mathbf{x}'_b the ACCC/DHC combination is able to decrease the harmonics in \mathbf{i}_x to zero but may not succeed to do so. When the rotational speed of the rotor is close to one of the mechanical natural frequencies, the current nulling scheme causes problems since the DHC strongly interferes with the ACCC. With the choice $\mathbf{i}_n = -\tilde{\mathbf{N}}\mathbf{x}_b(t)$, the system is usually still stable but the DHC does not converge, while with the choice $\mathbf{i}_n = -\tilde{\mathbf{N}}\mathbf{x}'_b(t)$ the system is usually unstable.¹

The next three figures show the simulation results for a rotational frequency of $\Omega \triangleq 333.3$ Hz and an unbalance radius of $e = 1$ μm . In all three cases,

¹ Unstable means that no stable whirl develops and the rotor crashes into the housing. Since the linearized cross-coupling forces are not limited, there exists no other stable limit cycle. In a real system, the cross-coupling forces are limited and stable high amplitude limit cycles might occur.

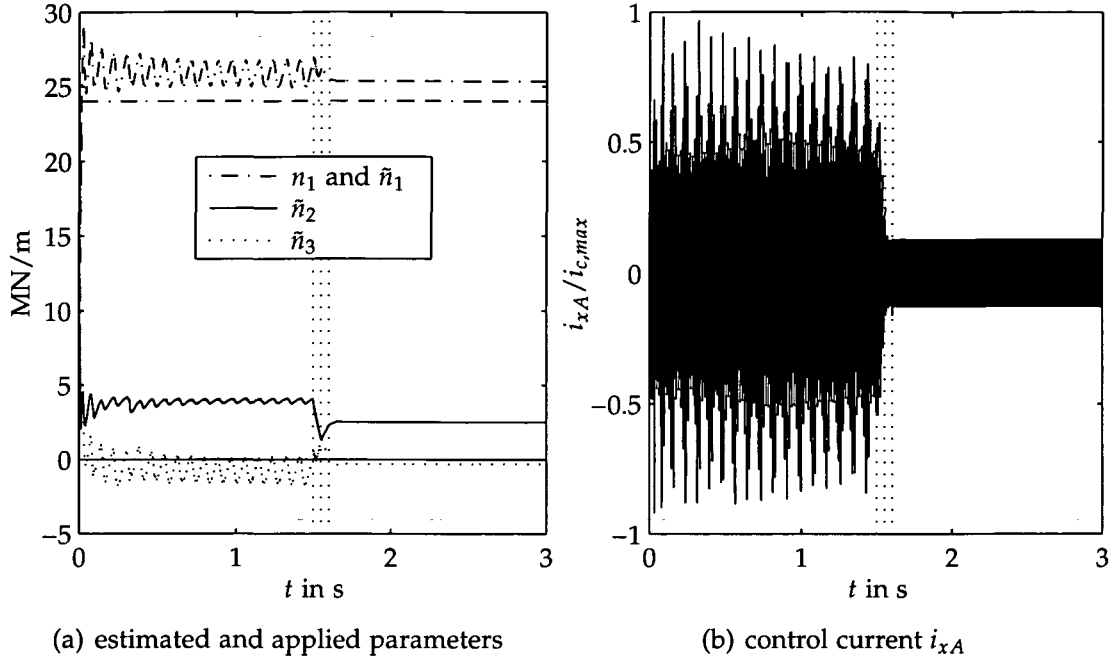


Figure 8.9.: 4DoF system with $n_1 = 24$ MN/m, $n_2 = n_3 = 0$; ACCC with $i_n = \tilde{N}x_b$; unbalance excitation $\Omega \cong 333.3$ Hz and DHC

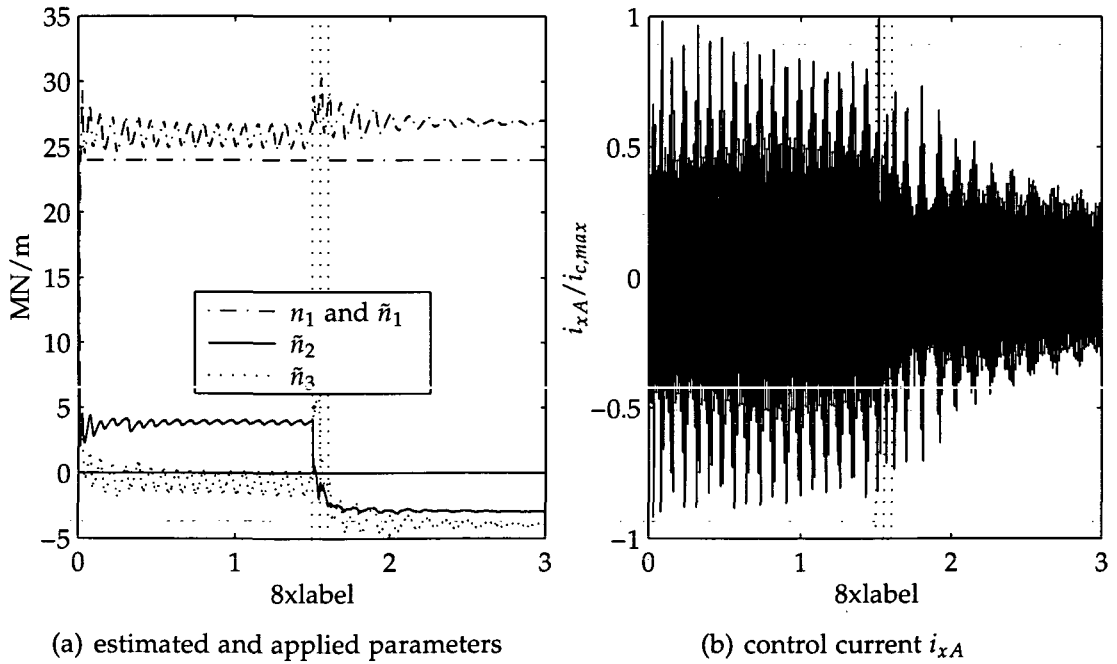


Figure 8.10.: 4DoF system with $n_1 = 24$ MN/m, $n_2 = n_3 = 0$; ACCC with $i_n = -\tilde{N}x'_b$; unbalance excitation $\Omega \cong 333.3$ Hz, $e = 1$ μm , and DHC

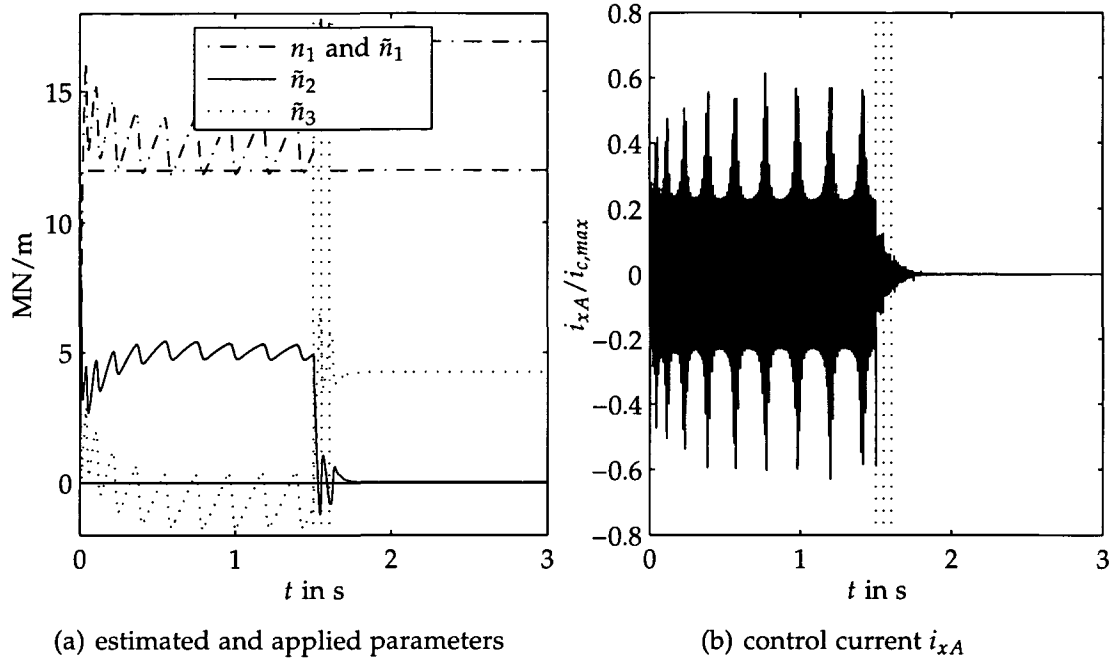


Figure 8.11.: 4DoF system with $n_1 = 12$ MN/m, $n_2 = n_3 = 0$; ACCC with $\mathbf{i}_n = -\tilde{\mathbf{N}}\mathbf{x}'_b$; unbalance excitation $\Omega \triangleq 333.3$ Hz, $e = 1$ μm , and DHC

the applied cross-coupling parameters n_2 and n_3 are set to zero and only n_1 is greater than zero. In figure 8.9, n_1 is set to $n_1 = 24$ MN/m and for the adaptive control $\mathbf{i}_n = -\tilde{\mathbf{N}}\mathbf{x}_b(t)$ is used. The DHC is able to reduce the harmonic components in the PID controller current but not in the total controller currents. However, the oscillations in the estimated parameters disappear. In figure 8.10, we have the same parameter values as before, but instead of \mathbf{x}_b we use \mathbf{x}'_b in the adaptive controller. In this case, the DHC can neither diminish the harmonics in the controller current nor prevent the oscillation in the estimated parameters. However, if the applied cross-coupling parameter n_1 is decreased to $n_1 = 12$ MN/m, the choice of $\mathbf{i}_n = -\tilde{\mathbf{N}}\mathbf{x}'_b(t)$ leads to a complete disappearance of the harmonics in \mathbf{i}_x as shown in figure 8.11.

8.2.3. Force Nulling and ACCC

The force nulling scheme as used in section 7.3.7 is just an extension of the current nulling scheme. Therefore, the force nulling has basically the same implications on the ACCC as the current nulling. Since the force nulling is of lesser importance in practice than the other two schemes, we will just show

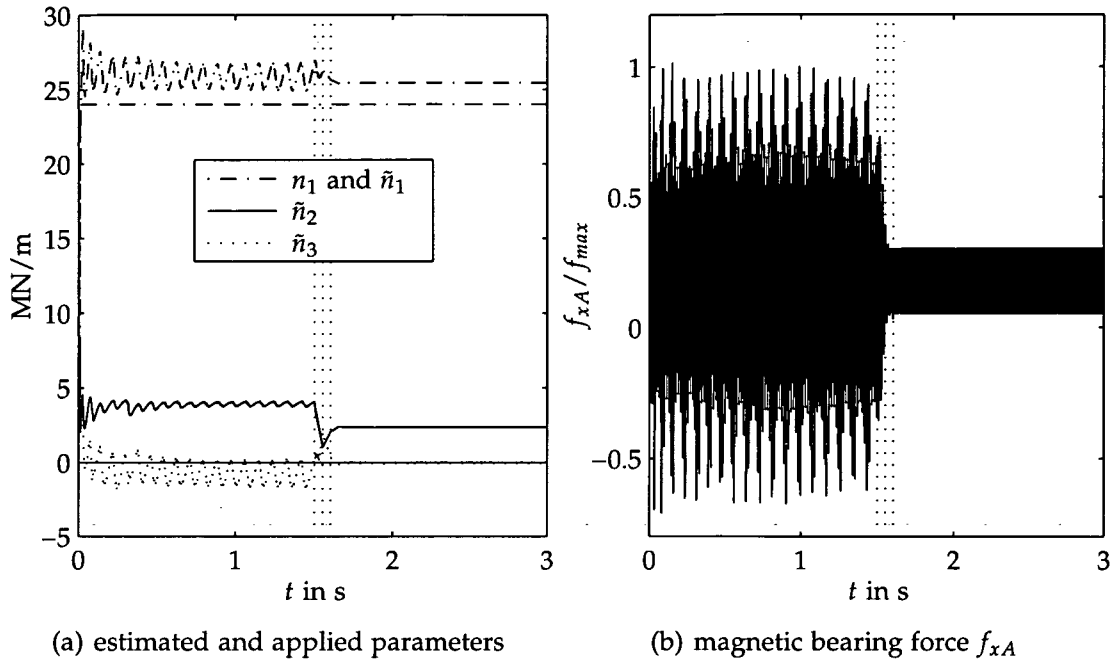


Figure 8.12.: 4DoF system with $n_1 = 24$ MN/m, $n_2 = n_3 = 0$; ACCC with $\mathbf{i}_n = -\tilde{\mathbf{N}}\mathbf{x}_b$; unbalance excitation $\Omega \hat{=} 333.3$ Hz, $e = 1$ μm , and DHC

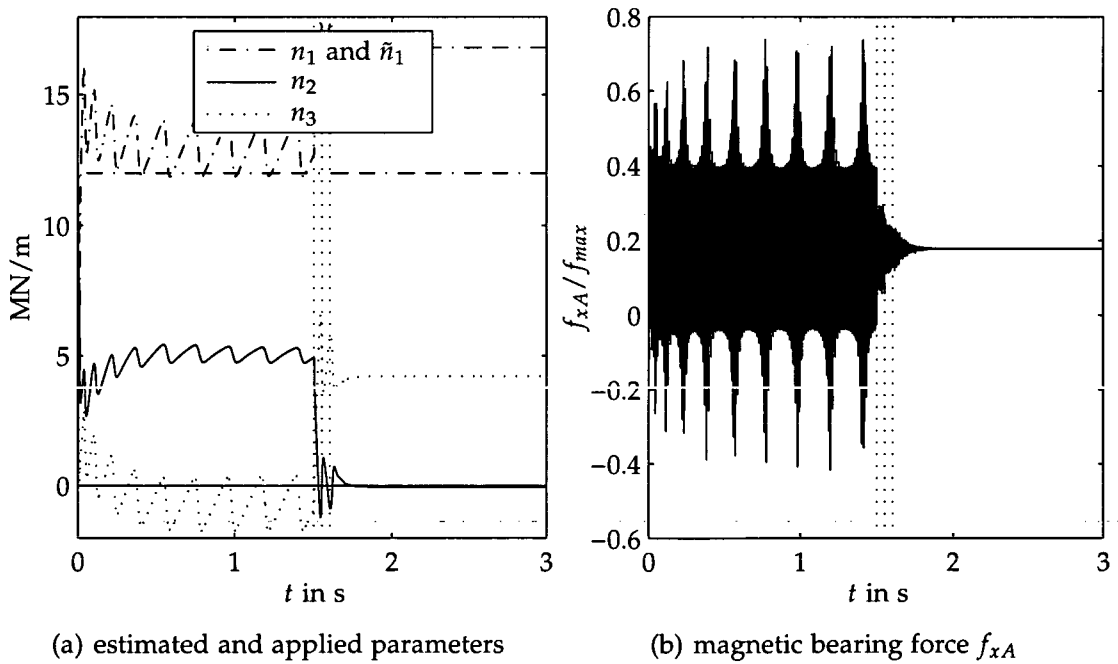


Figure 8.13.: 4DoF system with $n_1 = 12$ MN/m, $n_2 = n_3 = 0$; ACCC with $\mathbf{i}_n = -\tilde{\mathbf{N}}\mathbf{x}'_b$; unbalance excitation $\Omega \hat{=} 333.3$ Hz, $e = 1$ μm , and DHC

the simulation results for the same parameter sets as in figure 8.10 and 8.11. The results are shown in figure 8.12 and 8.13, respectively.

8.3. Simulation Results for CHC and Adaptive Cross-Coupling Control

8.3.1. Displacement Nulling and ACCC

The combination of the CHC control scheme with the ACCC is very similar to the combination of ACCC with DHC. Therefore, only two simulation results of the displacement nulling scheme are given as a "proof of concept". For the first simulation, we use the same parameters as in figure 8.6 and a CHC gain factor of $\mu = 100 \text{ s}^{-1}$ (see (7.10)). The result is given in figure 8.14. There is not much difference between the DHC in figure 8.6 and the CHC in figure 8.14, except the convergence speed is a little bit higher with the chosen parameters.

The second simulation in this section shows the influence of measurement noise. Again the parameters of an earlier simulation as shown in figure 8.7 are used to test the CHC. The measurement noise is white noise with a standard deviation of $0.2 \text{ }\mu\text{m}$. Again the continuous harmonic control behaves almost exactly the same as the discrete harmonic control.

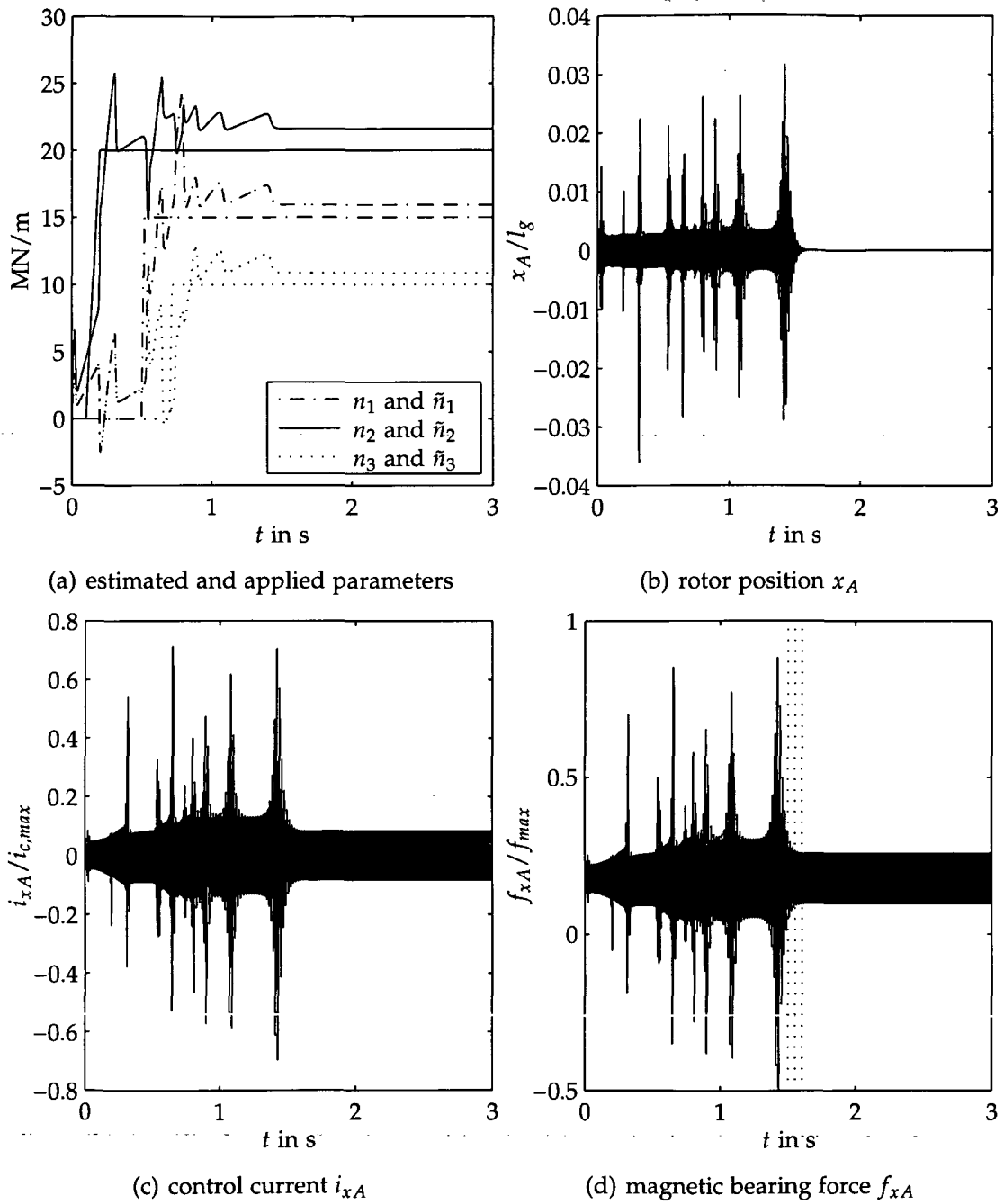


Figure 8.14.: 4DoF system with cross-coupling excitation $n_1 = 15 \text{ MN/m}$, $n_2 = 20 \text{ MN/m}$, $n_3 = 10 \text{ MN/m}$ and ACCC; unbalance excitation $\Omega \triangleq 333.3 \text{ Hz}$, $e = 1 \mu\text{m}$, and CHC

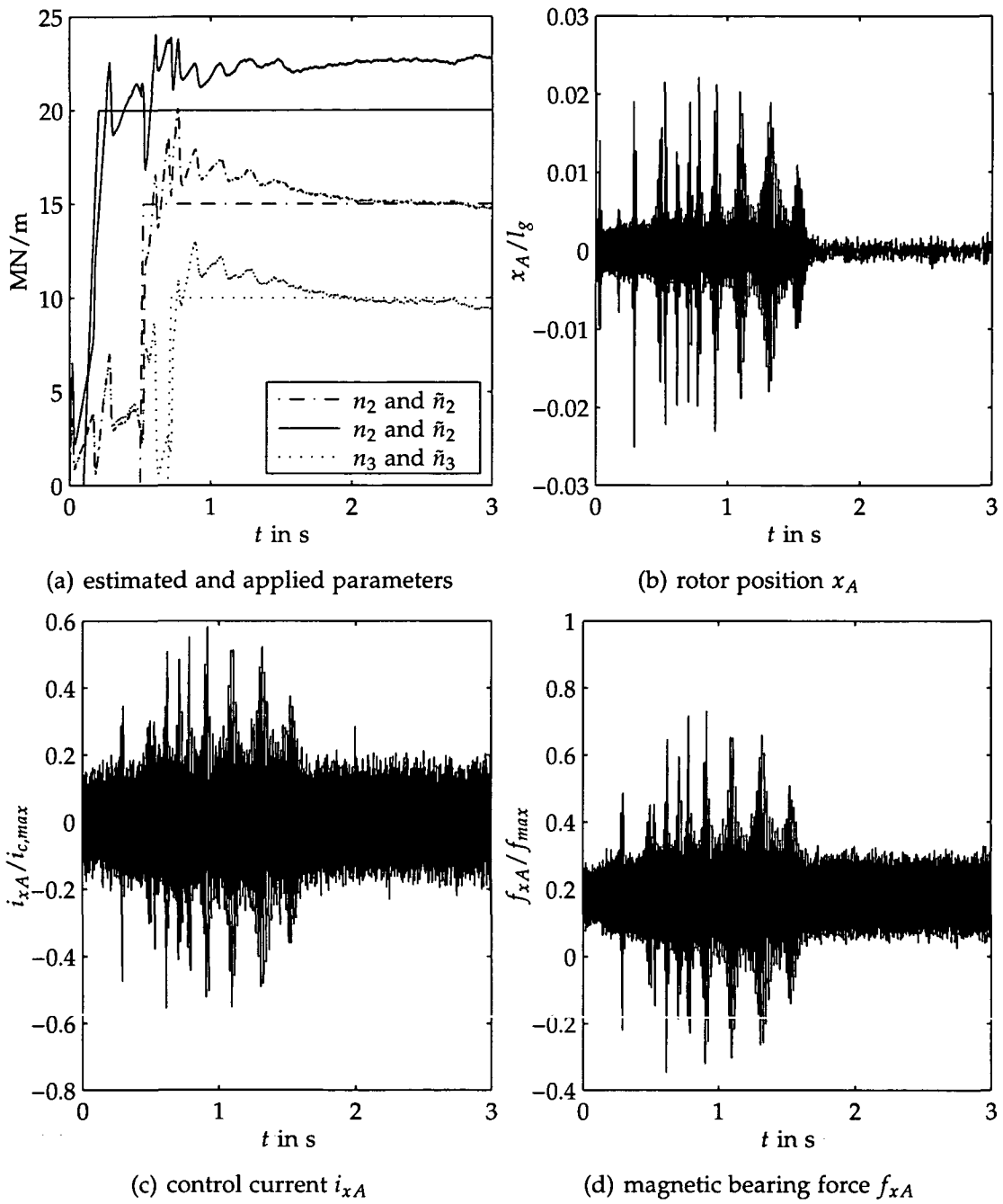


Figure 8.15.: 4DoF system with cross-coupling excitation $n_1 = 15$ MN/m, $n_2 = 20$ MN/m, $n_3 = 10$ MN/m and ACCC; unbalance excitation $\Omega \hat{=} 333.3$ Hz, $e = 1$ μ m and CHC; measurement noise

8.3.2. Rotor Run-Ups

The last two simulations show a rotor run-up for a realistic system. We use displacement nulling, because it seems to be the most realistic unbalance control goal and we use the CHC algorithm, because it is very well suited for changing rotational speed. For the DHC, we would either have to choose a discrete sample time which works with low rotational frequencies as well as with high ones. This would result in a reduced convergence speed for the higher speed range. Alternatively, we could adjust the sampling time which makes the programming more complicated.

For the applied cross-coupling parameters, we choose a configuration with two cross-coupling forces at each end of the rotor and one in the center of the rotor. The cross-coupling stiffness close to the bearing A is called n_a with z -coordinate z_{na} , close to B is n_b with z_{nb} , and close to the center of gravity is n_c with z_{nc} . From section 4.4 we get for the three cross-coupling parameters

$$\begin{aligned} n_1 &= \left(\frac{z_{na}-z_B}{z_A-z_B} \right)^2 n_a + \left(\frac{z_{nb}-z_B}{z_A-z_B} \right)^2 n_b + \left(\frac{z_{nc}-z_B}{z_A-z_B} \right)^2 n_c \\ n_2 &= -\frac{(z_{na}-z_B)(z_{na}-z_A)}{(z_A-z_B)^2} n_a - \frac{(z_{nb}-z_B)(z_{nb}-z_A)}{(z_A-z_B)^2} n_b - \frac{(z_{nc}-z_B)(z_{nc}-z_A)}{(z_A-z_B)^2} n_c \\ n_3 &= \left(\frac{z_{na}-z_A}{z_A-z_B} \right)^2 n_a + \left(\frac{z_{nb}-z_A}{z_A-z_B} \right)^2 n_b + \left(\frac{z_{nc}-z_A}{z_A-z_B} \right)^2 n_c \end{aligned}$$

with

$$z_{na} = z_A - 46 \text{ mm} = -285 \text{ mm}$$

$$z_{nb} = z_B - 46 \text{ mm} = 195 \text{ mm}$$

$$z_{nc} = 20 \text{ mm} ,$$

the resulting cross-coupling parameters n_1 to n_3 are calculated to

$$n_1 = 1.2009 * n_a + 0.009184 * n_b + 0.21198 * n_c$$

$$n_2 = -0.10502 * n_a + 0.086649 * n_b + 0.24843 * n_c$$

$$n_3 = 0.009184 * n_a + 0.81752 * n_b + 0.29115 * n_c .$$

We assume that the cross-coupling parameters n_a to n_b depend on the rotor angular speed Ω in the following way

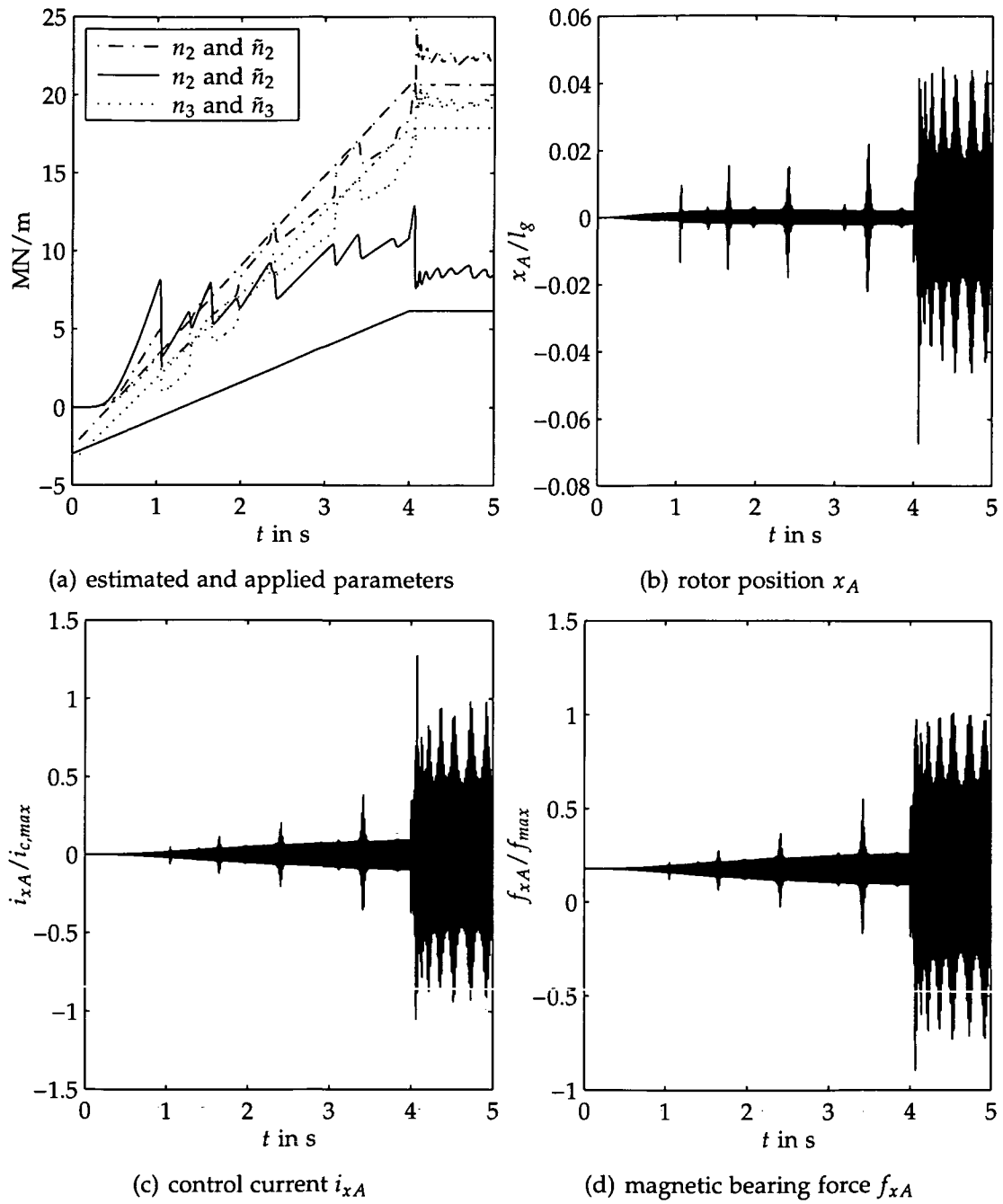
$$n_a = n_c = 6 \text{ kN s/m} * \Omega \quad n_b = 18 \text{ kN s/m} * \Omega - 12 \text{ MN/m}$$

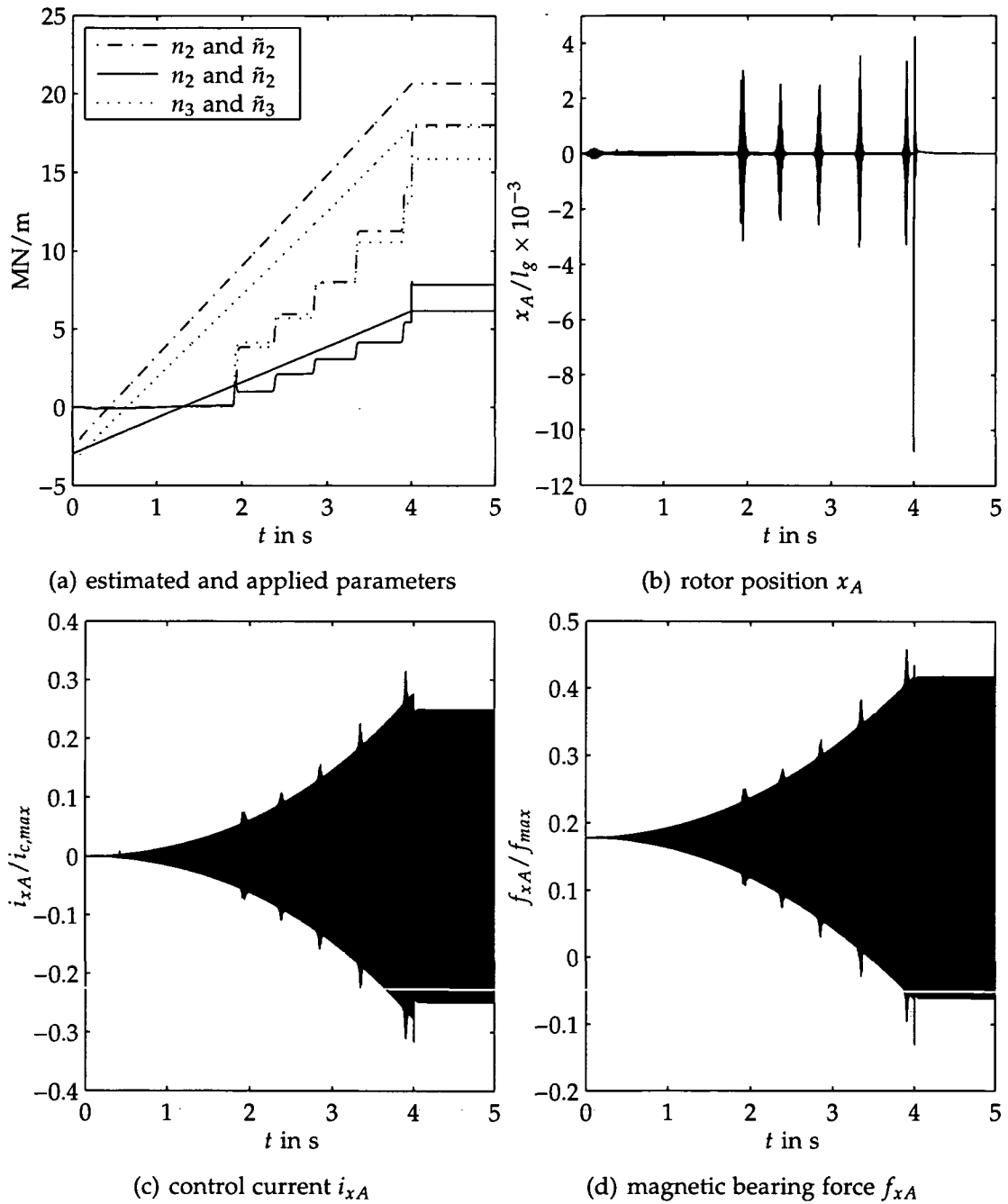
for Ω in rad s^{-1} . Although there is no evidence that real sources of cross-coupling excitation behave like this, the assumption of linear dependency on the rotational speed is realistic, see [Nor93].

For the simulations, we increase the rotational speed from 0 to 20000 r/min in 4 s with a constant acceleration rate of 83.33 Hz/s. The unbalance radius is $e = 3 \mu\text{m}$. The first simulation, shown in figure 8.16, is the reference case where we use the ACCC to stabilize the system with no unbalance control present. During the run-up we see the characteristic oscillations in the estimated cross-coupling parameter values and the corresponding peaks in the rotor vibration. After 4 s the rotational frequency reaches the steady state value and the rotor vibration increases dramatically since a steady state harmonic excitation is very bad for the estimator performance.

The second simulation, shown in figure 8.17, is now carried out with CHC displacement nulling. The rotor vibration level is substantially reduced by the CHC, but not completely eliminated, because the additional unbalance force due to acceleration and the changing excitation frequency degrades the CHC performance. Since the rotor vibration is reduced, the information for the estimator is also reduced. The peaks in the rotor vibrations indicate "unstable" whirls and the steps in the estimated parameters correspond to these peaks, since they are the only source of information for the estimator.

The third simulation, shown in figure 8.18, combines ACCC and CHC, with white measurement noise of a standard deviation $0.2 \mu\text{m}$ is added to the measured rotor position. The noise improves the estimation process and the peaks in the rotor vibrations disappear while the estimated parameters \hat{n}_j are closer to the applied parameters n_j . At $\Omega \triangleq 20000 \text{ r/min}$ a peak in the rotor vibration can be recognized, due to the abrupt end of the rotor acceleration phase. In figure 8.19, we see the rotor vibration of the three run-up simulations, plotted in the equal scales for easier comparison.

Figure 8.16.: Rotor run-up with ACCC; unbalance radius $e = 3 \mu\text{m}$

Figure 8.17.: Rotor run-up with ACCC and CHC; unbalance radius $e = 3 \mu\text{m}$

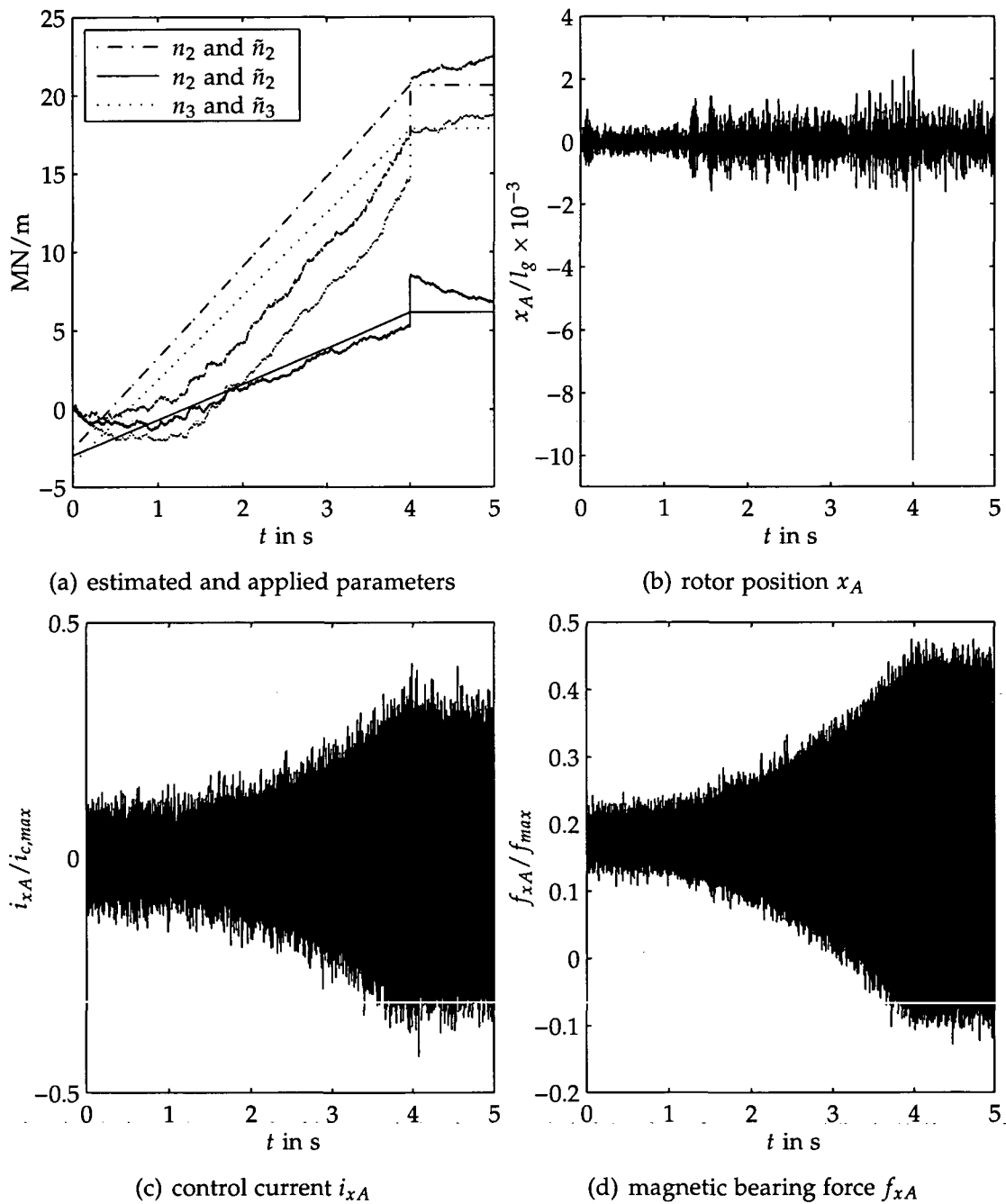


Figure 8.18.: Rotor run-up with ACCC and CHC; unbalance radius $e = 3 \mu\text{m}$; measurement noise standard deviation $0.2 \mu\text{m}$

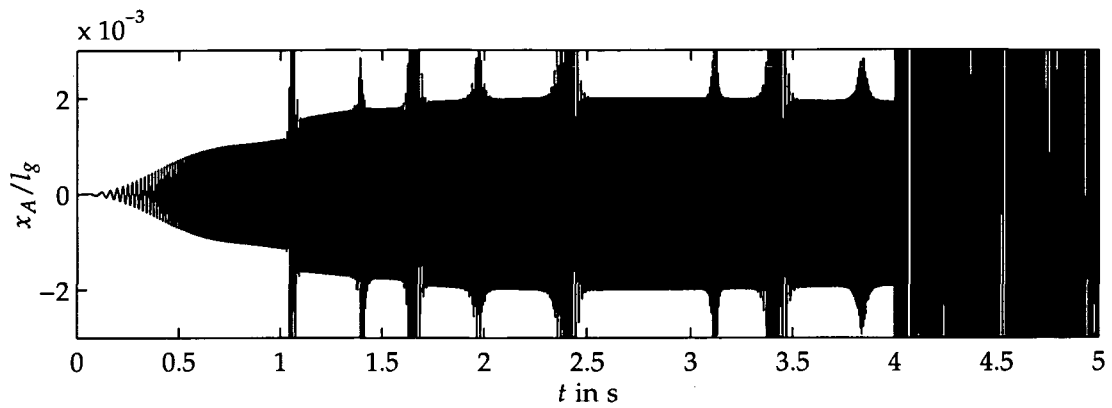
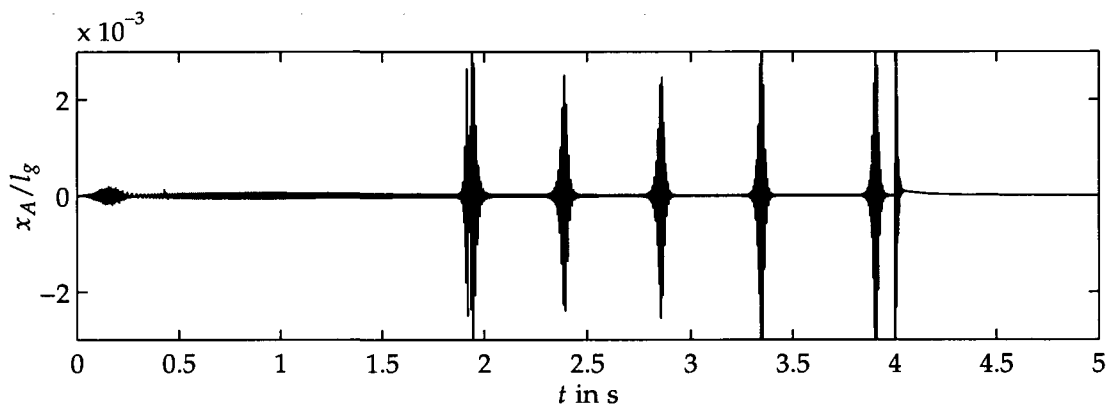
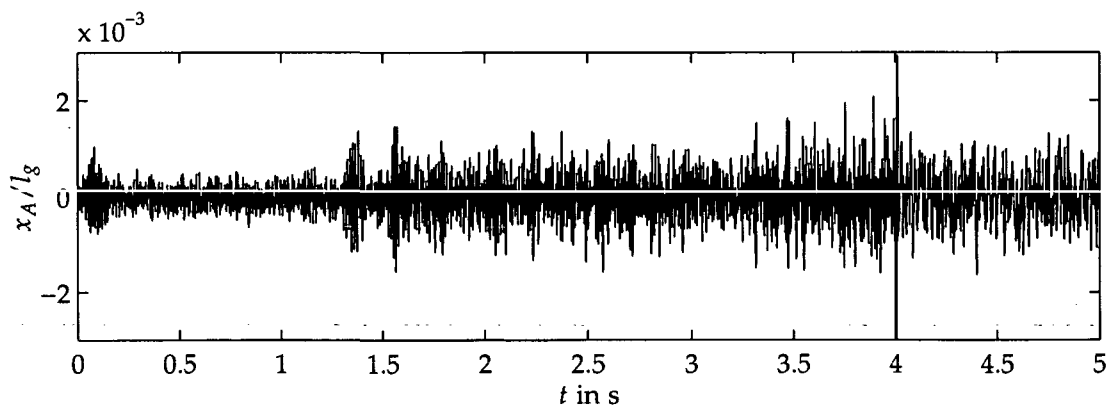
(a) rotor position x_A ; ACCC(b) rotor position x_A ; ACCC with CHC(c) rotor position x_A ; ACCC with CHC and measurement noise

Figure 8.19.: Comparison of the rotor vibrations for the three run-up simulations

9. Conclusions and Outlook

This dissertation consists of two parts. The first part describes the modelling of the magnetic bearing rotor system. Although this should be a well known process, the implications of using a current controlled magnetic bearing with an underlying current controller as described cannot—to the author's knowledge—be found in the literature. The differences between a conventional approach and the approach used here may significantly influence the behavior of the magnetic bearing rotor system. Using PWM controlled power electronic is another issue and the justification of a linear model has been found in control theory literature. The other sections of the modelling part, where the model of the rotor and the combination of magnetic bearings with the rotor are derived, are straight-forward and not really new results, but necessary for the understanding of the following chapters.

The second part of this thesis describes the control of the rotor supported by active magnetic bearings. The basic stabilizing controller is a simple PID controller which has already been used by Lang [Lan97]. However, the system is analyzed with discrete-time methods which is a substantial progress and makes it possible to increase the sampling time by a factor of more than six. The stabilizing controller itself is not substantially improved compared to Lang, although it is not considered by the author to be the best possible design. A H_2 approach (Kalman filter based observer together with an LQR control) has been tested, but is not included in the thesis since it has not provided enough initial robustness to work together with the ACCC algorithm. A more carefully designed H_2 or H_∞ approach would probably be able to overcome the limitations of the PID control and provide enough robustness to work with the ACCC control, but is beyond the scope of this thesis.

In chapter 6, a thorough stability analysis of the rigid rotor with an arbitrary distribution of cross-coupling forces along the rotor is carried out. The ACCC control is derived from theoretical considerations and the behavior is studied for a two degrees of freedom system as well as for a four degrees of freedom system. Special effort is made to explain the behavior of the ACCC control with harmonic excitation and analytical solutions for the two degrees

of freedom system are found.

In chapter 7, the discrete harmonic control, which is known in rotor dynamics literature as adaptive open-loop control, is derived from theoretical considerations. The name open-loop control is misleading and so throughout this thesis the term discrete harmonic control (DHC) is used. The three possible control goals—displacement nulling, current nulling, and force nulling—are defined and the DHC algorithm is used to achieve these goals. Furthermore, special considerations are taken to reduce the necessary time and memory space for the actual calculation of the required influence coefficient matrix.

With help of helicopter control literature, it has been shown that there is a continuous form of the DHC algorithm, which is naturally called “continuous harmonic control” throughout this thesis. The only paper in rotor dynamics literature [HBGL96] in which basically this CHC control algorithm is described unfortunately has not described the equivalence with the DHC control and has only been used for current nulling as an advancement of the notch filter scheme. Therefore, the introduction of CHC control and its application for displacement and force nulling can be viewed as a progress in the field of rotor dynamics.

In chapter 8 of this thesis, the unbalance and adaptive cross-coupling control algorithms are combined. It is shown that all three unbalance control goals can be achieved with the DHC algorithm together with the ACCC, and that the influence of unbalance excitation on the ACCC is minimized. Run-up simulations are carried out of a rotor with displacement nulling CHC and ACCC, which show a very good behavior of the two algorithms for fast changing rotational speeds.

There are many directions of further research in which the present work can be extended. One important topic is, of course, experimental work. In the authors opinion, however, it would not be of a very high scientific value to build up an experimental setup just to prove that the CHC, DHC and ACCC algorithms work, because this is already proven by the simulation studies, carried out in this thesis. So, in order to learn something new, the control algorithms should be tested on a machine with a real source of cross-coupling excitation, like e.g. annular seals, to see how the ACCC algorithm handles an excitation, which behaves in the linearized way as described in this thesis for small vibration amplitudes, while it behaves different for large vibration amplitudes.

Another possibility to get at least a feeling what might be the problems with real-world nonlinear cross-coupling excitations would be to do a numer-

ical simulation with a nonlinear model of a cross-coupling excitation, e.g. for a journal bearing utilizing the short bearing assumption. Also a linearized model may be helpful where further knowledge about the dependency of the cross-coupling parameters on the operational conditions is included.

The nonlinear behavior of the ACCC algorithm itself, when applied to a linear cross-coupling excitation, could also be investigated. There are many modern methods which could be utilized, for example, numerical path-following methods to acquire bifurcation diagrams. However, the parameter space is of high dimension and general statements, which are not only valid for a very small set of parameters, might be difficult to acquire.

A. Appendix

A.1. Some Concepts of Linear Algebra, Rotor Dynamics and Controller Design

Theorem A.1 (Push-Through Identity) *For regular matrices A and B , the following equation holds*

$$(I + AB)^{-1} AB = A (I + BA)^{-1} B = AB (I + AB)^{-1} .$$

Theorem A.2 (Matrix Inversion) *Let A be a square matrix as follows*

$$A := \begin{bmatrix} A_{11} & A_{12} \\ A_{21} & A_{22} \end{bmatrix}$$

where A_{11} and A_{22} also are square matrices. If A is nonsingular then

$$\begin{bmatrix} A_{11} & A_{12} \\ A_{21} & A_{22} \end{bmatrix}^{-1} = \begin{bmatrix} A_{11}^{-1} + A_{11}^{-1} A_{12} \Delta^{-1} A_{21} A_{11}^{-1} & -A_{11}^{-1} A_{12} \Delta^{-1} \\ -\Delta^{-1} A_{21} A_{11}^{-1} & \Delta^{-1} \end{bmatrix}$$

with $\Delta := A_{22} - A_{21} A_{11}^{-1} A_{12}$ (A is nonsingular if and only if Δ is nonsingular) and

$$\begin{bmatrix} A_{11} & A_{12} \\ A_{21} & A_{22} \end{bmatrix}^{-1} = \begin{bmatrix} \hat{\Delta}^{-1} & -\hat{\Delta}^{-1} A_{12} A_{22}^{-1} \\ -A_{22}^{-1} A_{21} \hat{\Delta}^{-1} & A_{22}^{-1} + A_{22}^{-1} A_{21} \hat{\Delta}^{-1} A_{12} A_{22}^{-1} \end{bmatrix}$$

with $\hat{\Delta} := A_{11} - A_{12} A_{22}^{-1} A_{21}$ (A is nonsingular if and only if $\hat{\Delta}$ is nonsingular). The matrix Δ ($\hat{\Delta}$) is called Schur complement of A_{11} (A_{22}) in A .

A.1.1. Complex Notation for 2DoF Rotor Dynamics

It may be convenient to describe the two degrees of freedom as a single complex number, i.e. instead of

$$\mathbf{x} = \begin{bmatrix} x(t) \\ y(t) \end{bmatrix} \quad \text{we use} \quad x(t) + jy(t) .$$

Two matrix multiplications can be carried out on this

$$\begin{bmatrix} a & 0 \\ 0 & a \end{bmatrix} \begin{bmatrix} x(t) \\ y(t) \end{bmatrix} = \begin{bmatrix} ax(t) \\ ay(t) \end{bmatrix} \quad \text{is equivalent to} \quad a(x(t) + jy(t)) \quad \text{for } a \in \mathbb{R}$$

and

$$\begin{bmatrix} 0 & -a \\ a & 0 \end{bmatrix} \begin{bmatrix} x(t) \\ y(t) \end{bmatrix} = \begin{bmatrix} -ay(t) \\ ax(t) \end{bmatrix} \quad \text{is equivalent to} \quad ja(x(t) + jy(t)) \quad \text{for } a \in \mathbb{R}.$$

With the additional assumption that $x(t)$ and $y(t)$ are describing a constant orbit with constant rotational speed Ω , amplitude \hat{x} , and phase lag between $x(t)$ and $y(t)$ of 90° (cartesian coordinate system), that is

$$x(t) = \hat{x} \cos(\Omega t + \varphi) \quad y(t) = \hat{x} \sin(\Omega t + \varphi),$$

we can find the solution of

$$\begin{bmatrix} \hat{a}(s) \\ \hat{b}(s) \end{bmatrix} = \begin{bmatrix} G(s) & 0 \\ 0 & G(s) \end{bmatrix} \begin{bmatrix} \hat{x}(s) \\ \hat{y}(s) \end{bmatrix}$$

(after all transients have decayed) by

$$a(t) + jb(t) = G(j\Omega)(x(t) + jy(t)).$$

A.2. Discrete-Time (Digital) Control

A.2.1. Discrete-Time State Space

Today almost every controller is implemented as digital control. Still many people design their controllers as continuous systems and approximate these continuous systems through a discrete-time system by a forward Euler method, i.e.

$$\begin{aligned} \dot{x}(t) = f(x(t), u(t)) &\approx x((k+1)T_s) = x(kT_s) + T_s f(x(kT_s), y(kT_s)) \\ y(t) = g(x(t), u(t)) &\approx y(kT_s) = g(x(kT_s), y(kT_s)). \end{aligned}$$

Although this method works for many control tasks, there are many disadvantages:

- It is only an approximation. The lower the sample time T_s is chosen, the better is the approximation. If the sample time is too high the control will not work. So people tend to choose the sample time as low as possible, which also imposes a high bandwidth demand on the measurement equipment and a high demand for calculation speed on the digital equipment.
- The approximation of an optimal continuous-time control algorithm is probably not optimal for the discrete system.
- Not every possible discrete-time control algorithm has a continuous-time equivalent.
- Although the continuous-time system is stable, the discrete-time approximation may be unstable.
- The discrete-time approximation of connected continuous-time systems may be significantly different to the connection of their discrete-time approximations.

The first step of designing a digital controller is to convert the physical continuous-time model of the plant to a discrete-time model. This can be achieved by assuming a zero order hold block at the system inputs, which converts the discrete-time series to a continuous-time step function and sample block at the system outputs, which converts the continuous system outputs to a discrete-time series.

If the plant can be described by linear differential equations, i.e.

$$\begin{aligned}\dot{\mathbf{x}}(t) &= \mathbf{A} \mathbf{x}(t) + \mathbf{B} \mathbf{u}(t) \\ \mathbf{y}(t) &= \mathbf{C} \mathbf{x}(t) + \mathbf{D} \mathbf{u}(t) ,\end{aligned}$$

the resulting system can be described by a linear difference equation

$$\begin{aligned}\mathbf{x}(k+1) &= e^{\mathbf{A}T_s} \mathbf{x}(k) + \int_0^{T_s} e^{\mathbf{A}\tau} \mathbf{B} d\tau \mathbf{u}(k) \\ &= \mathbf{A}_d \mathbf{x}(k) + \mathbf{B}_d \mathbf{u}(k) \\ \mathbf{y}(kT_s) &= \mathbf{C} \mathbf{x}(k) + \mathbf{D} \mathbf{u}(k) .\end{aligned}$$

This difference equation is the starting point for many state-space control algorithms like pole placement method (including dead beat controllers) and

linear quadratic optimal control. The problem is that for these kind of controllers the states have to be known. In most cases, not all of the states can be measured directly and so the states estimators are used e.g. Kalman estimators or dead beat estimators.

A.2.2. z-Transform

Analogous to the Laplace transform for the continuous systems, there exists the z-transform for discrete-time systems. For a linear discrete-time system, the so-called z-transfer function can be found, which describes the input-output behavior, that is

$$\mathbf{y}(z) = \mathbf{G}(z) \mathbf{u}(z)$$

$$\mathbf{G}(z) := \mathbf{C}(z\mathbf{I} - \mathbf{A}_d)^{-1} \mathbf{B}_d + \mathbf{D}.$$

The frequency response to an input series

$$u_k = \cos \omega k T_s$$

can be found with

$$y_k = \left| G(e^{j\omega T_s}) \right| \cos \left(\omega k T_s + \arg G(e^{j\omega T_s}) \right).$$

The z-transfer function is BIBO-stable (Biased Input Biased Output), if and only if, the poles of this function are inside the unit circle.

A.2.3. q-Transform (Tustin Approximation)

The z-transfer function is a little bit difficult to use. The stability tests are different from the ones for the Laplace transfer function and the frequency response spectrum is also difficult to calculate; therefore controller design methods based on Bode plots are virtually impossible. However, with the bilinear transformation (Tustin approximation)

$$z = \frac{1 + q \frac{T_s}{2}}{1 - q \frac{T_s}{2}}$$

and its inverse

$$q = \frac{2}{T_s} \frac{z - 1}{z + 1}$$

the so-called q -transfer function $G^\#(q)$

$$G^\#(q) = G(z) \Big|_{z = \frac{1+q\frac{T_s}{2}}{1-q\frac{T_s}{2}}}$$

can be found which has some interesting features (see [GHS91]).

- Every point inside the unit circle of the z -plane is mapped to the left open half-plane of the q -plane.
- Every point on the unit circle of the z -plane is mapped to the imaginary axis of the q -plane.
- The region outside the unit circle of the z -plane is mapped to the right open half-plane of the q -plane.
- The frequency response to an input series

$$u_k = \cos \Omega T_s k$$

can be found with

$$y_k = \left| G^\#(jw) \right| \cos \left(\Omega k T_s + \arg G^\#(jw) \right)$$

with the transformed frequency w

$$w = \frac{2}{T_s} \tan \left(\Omega \frac{T_s}{2} \right) .$$

- For a discrete-time transfer function $G(z)$ of a sampled continuous-time transfer function $G(s)$, the approximation

$$G^\#(jw) \approx G(j\Omega) \quad \text{for} \quad |\Omega T_s| \ll 1$$

is valid.

These features make it possible to use all the stability tests and most control design methods for Laplace transfer functions also for the discrete-time $G^\#(q)$ transfer function with no or little changes.

We note that

$$\frac{\hat{y}(z)}{\hat{u}(z)} = \frac{T_s z + 1}{2 z - 1} \quad y(n) = \frac{1}{2} \left(T_s \sum_{i=0}^{n-1} u(i) + T_s \sum_{i=1}^n u(i) \right)$$

is a discrete-time approximation of an integrator applying the right-side rule,

$$\frac{\hat{y}(z)}{\hat{u}(z)} = T_s \frac{1}{z-1} \quad y(n) = T_s \sum_{i=0}^{n-1} u(i) = y(n-1) + T_s u(n-1)$$

is a discrete-time approximation of an integrator applying the trapezoid rule and

$$\frac{\hat{y}(z)}{\hat{u}(z)} = T_s \frac{z}{z-1} \quad y(n) = T_s \sum_{i=1}^n u(i) = y(n-1) + T_s u(n)$$

is a discrete-time approximation of an integrator applying the left-side rule. The inverse of this integrator is the only useful approximation of a differentiator

$$\frac{\hat{y}(z)}{\hat{u}(z)} = \frac{1}{T_s} \frac{z-1}{z} \quad y(n) = \frac{u(n) - u(n-1)}{T_s}.$$

A.3. The Reluctance Network AMB-Model

The governing equations of the reluctance network model are developed with the help of the graph theory. Only a short excerpt can be given in this thesis.

At first we search for a "tree" of the network. This is a part of the network without any loops and where the addition of a single other component of the network will add a loop to the tree. The components of the network that do not belong to the tree are the so-called "gates". There exists a linear relationship between the independent gate fluxes and the tree fluxes

$$\phi_T = A \phi_G.$$

This is a relationship which is based on the topology of the network and it is valid for any kind of network and network components, as long as Kirchhoff's laws are valid.

Now we choose the tree in such a way that all network elements are included in the tree, and the gates are virtual network elements which represent the magneto motive force in each loop. If we assume: a material without magnetic hysteresis, and a linear relationship between the flux through one network element and the magnetic potential drop along this element, we can find a linear relationship between the tree fluxes and the tree magnetic potentials which is

$$\Theta_T = \mathcal{R}_T(x, y) \phi_T,$$

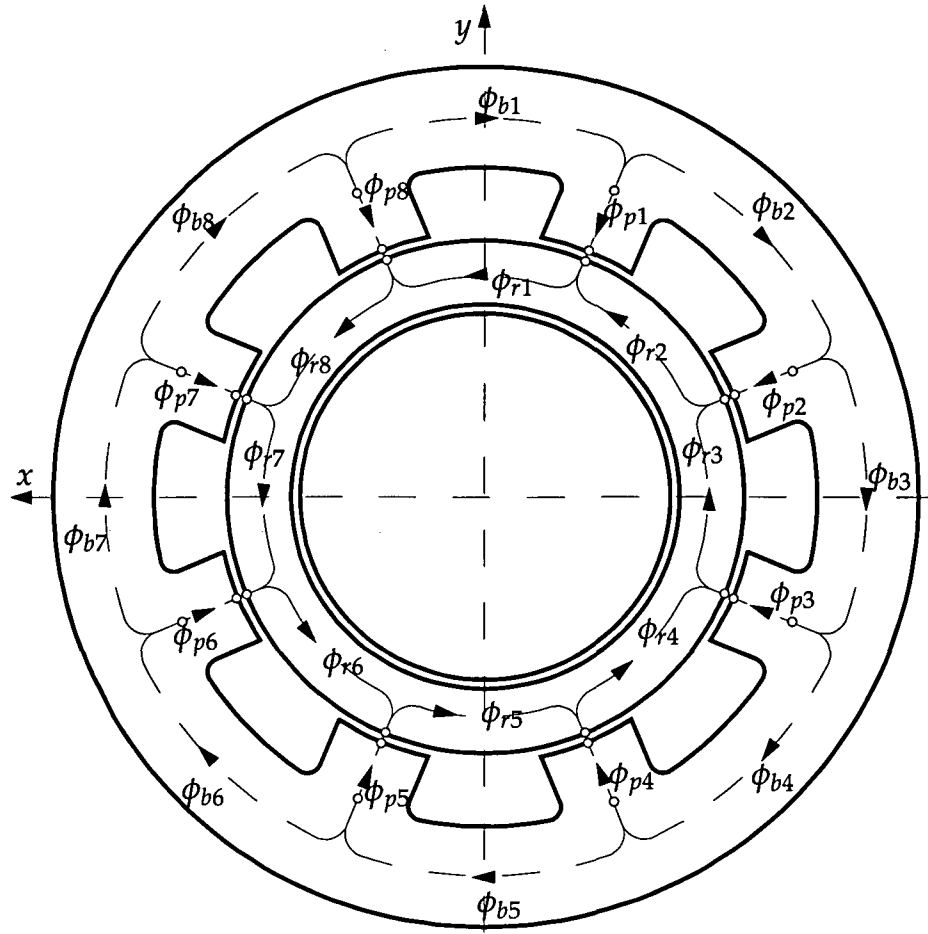


Figure A.1.: The actuator model for the reluctance network

where \mathcal{R}_T is the diagonal matrix of the magnetic reluctances of the network tree elements. The relationship between magnetic potential at the gates Θ_G and the gate fluxes ϕ_G is given by

$$\begin{matrix} \Theta_G & = & \mathcal{R}(x,y) & \phi_G \\ [9 \times 1] & & [9 \times 9] & [9 \times 1] \end{matrix},$$

where \mathcal{R} is the gate reluctance matrix,

$$\begin{matrix} \mathcal{R}(x,y) & := & \mathbf{A}^T & \mathcal{R}_T(x,y) & \mathbf{A} \\ [9 \times 9] & & [9 \times 32] & [32 \times 32] & [32 \times 9] \end{matrix}.$$

For the four actuator AMB used in this thesis (figure A.1), the gate reluctance

matrix is

$$\mathcal{R}(x, y) = \begin{bmatrix} \mathcal{R}_A + \mathcal{R}_{g1} + \mathcal{R}_{g2} & -\mathcal{R}_p - \mathcal{R}_{g2} & 0 & 0 & 0 & 0 & 0 & -\mathcal{R}_p - \mathcal{R}_r - \mathcal{R}_{g1} & -\mathcal{R}_r \\ -\mathcal{R}_p - \mathcal{R}_{g2} & \mathcal{R}_A + \mathcal{R}_{g2} + \mathcal{R}_{g3} & \ddots & 0 & 0 & 0 & 0 & -\mathcal{R}_r & -\mathcal{R}_r \\ 0 & -\mathcal{R}_p - \mathcal{R}_{g3} & \ddots & \ddots & 0 & 0 & 0 & -\mathcal{R}_r & -\mathcal{R}_r \\ 0 & 0 & \ddots & \ddots & \ddots & 0 & 0 & -\mathcal{R}_r & -\mathcal{R}_r \\ 0 & 0 & 0 & \ddots & \ddots & \ddots & 0 & -\mathcal{R}_r & -\mathcal{R}_r \\ 0 & 0 & 0 & 0 & \ddots & \ddots & -\mathcal{R}_p - \mathcal{R}_{g7} & -\mathcal{R}_r & -\mathcal{R}_r \\ 0 & 0 & 0 & 0 & 0 & \ddots & \mathcal{R}_A + \mathcal{R}_{g7} + \mathcal{R}_{g8} & -\mathcal{R}_p - \mathcal{R}_r - \mathcal{R}_{g8} & -\mathcal{R}_r \\ -\mathcal{R}_p - \mathcal{R}_r - \mathcal{R}_{g1} & -\mathcal{R}_r & -\mathcal{R}_r & -\mathcal{R}_r & -\mathcal{R}_r & -\mathcal{R}_r & -\mathcal{R}_p - \mathcal{R}_r - \mathcal{R}_{g8} & \mathcal{R}_A + 6\mathcal{R}_r + \mathcal{R}_{g8} + \mathcal{R}_{g1} & 7\mathcal{R}_r \\ -\mathcal{R}_r & -\mathcal{R}_r & -\mathcal{R}_r & -\mathcal{R}_r & -\mathcal{R}_r & -\mathcal{R}_r & -\mathcal{R}_r & 7\mathcal{R}_r & 8\mathcal{R}_r \end{bmatrix}$$

where

$$\mathcal{R}_A := \mathcal{R}_b + 2\mathcal{R}_p + \mathcal{R}_r.$$

It is worth to note that the matrix $\mathcal{R}(x, y)$ is symmetric. For the gate fluxes, we can find

$$\phi_G = \mathcal{R}(x, y)^{-1} \Theta_G = \mathcal{P}(x, y) \Theta_G$$

with

$$\mathcal{P}(x, y) = \mathcal{R}(x, y)^{-1}.$$

The magnetic motoric force Θ_G at the gates can be calculated with

$$\Theta_G = \mathbf{N} \mathbf{i}$$

where \mathbf{N} is the coil matrix given by

$$\mathbf{N} := \begin{bmatrix} 1 & 0 & 0 & 0 \\ -\frac{1}{2} & -\frac{1}{2} & 0 & 0 \\ 0 & 1 & 0 & 0 \\ 0 & -\frac{1}{2} & -\frac{1}{2} & 0 \\ 0 & 0 & 1 & 0 \\ 0 & 0 & -\frac{1}{2} & -\frac{1}{2} \\ 0 & 0 & 0 & 1 \\ -\frac{1}{2} & 0 & 0 & -\frac{1}{2} \\ 0 & 0 & 0 & 0 \end{bmatrix} N_w$$

and \mathbf{i} is the coil current vector given by

$$\mathbf{i} := [i_1 \ i_2 \ i_3 \ i_4]^T.$$

The relationship between the gate fluxes and the coil currents is given with

$$\phi_G = \mathcal{P}(x, y) \mathbf{N} \mathbf{i}.$$

To calculate the fluxes in the poles, we use again the linear relationship between the gate fluxes and the tree fluxes to calculate the tree fluxes. We select the pole fluxes from the tree by multiplication with a selection matrix \mathbf{S}_p . The pole fluxes are

$$\phi_p = \mathbf{S}_p \mathbf{A} \phi_G$$

$$\phi_p = \mathbf{S}_p \mathbf{A} \mathcal{P}(x, y) \mathbf{N} \mathbf{i} = \mathcal{P}_p(x, y) \mathbf{i}.$$

The magnetic bearing forces are calculated with

$$F_x = \phi_p^T \mathbf{X}_F \phi_p \quad F_y = \phi_p^T \mathbf{Y}_F \phi_p$$

where

$$\mathbf{X}_F := \frac{1}{2\mu_0} \begin{bmatrix} A_1 \cos \alpha_1 & & & \\ & A_2 \cos \alpha_2 & & \\ & & \ddots & \\ & & & A_8 \cos \alpha_8 \end{bmatrix}$$

$$\mathbf{Y}_F := \frac{1}{2\mu_0} \begin{bmatrix} A_1 \sin \alpha_1 & & & \\ & A_2 \sin \alpha_2 & & \\ & & \ddots & \\ & & & A_8 \sin \alpha_8 \end{bmatrix}.$$

(\mathbf{X}_F and \mathbf{Y}_F are calculated from bearing geometry.)

Now we can describe the complete system. With the applied voltage vector

$$\mathbf{u} = [u_1 \ u_2 \ u_3 \ u_4]^T,$$

we have the system of differential algebraic equations

$$\mathbf{u} = \mathbf{N}_u \frac{d}{dt} \phi_p + \mathbf{R} \mathbf{i}$$

$$[4 \times 1] = [4 \times 8] [8 \times 1] + [4 \times 4] [4 \times 1]$$

$$\begin{aligned}\phi_p &= \mathcal{P}_p(x, y) \mathbf{i} \\ [8 \times 1] &= [8 \times 4] [4 \times 1]\end{aligned}$$

to describe the system. Since DAEs are very difficult to simulate we can simplify the system by assuming that the number of windings in each coil is equal. Then we define the vector of flux sums

$$\phi_S := \begin{bmatrix} \phi_{p1} + \phi_{p2} \\ \phi_{p3} + \phi_{p4} \\ \phi_{p5} + \phi_{p6} \\ \phi_{p7} + \phi_{p8} \end{bmatrix},$$

$$\begin{aligned}\phi_S &= \mathbf{S}_S \mathcal{P}_P(x, y) \mathbf{N} \mathbf{i} \\ &= \mathcal{P}_I(x, y) \mathbf{i}.\end{aligned}$$

With the inverse of $\mathcal{P}_I(x, y)$, we can calculate the coil currents from ϕ_S

$$\mathbf{i} = \mathcal{P}_I^{-1} \phi_S = \mathcal{R}_I(x, y) \phi_S.$$

The differential equations are

$$\mathbf{u} = \mathbf{N} \frac{d}{dt} \phi_S + \mathbf{R} \mathbf{i} = \mathbf{N} \frac{d}{dt} \phi_S + \mathbf{R} \mathcal{R}_I(x, y) \phi_S.$$

A.4. Change in the Total Energy of a System with Cross-Coupling Excitation

The system of differential equations of second order

$$\mathbf{M} \ddot{\mathbf{x}} + \mathbf{D} \dot{\mathbf{x}} + \mathbf{K} \mathbf{x} + \mathbf{N} \mathbf{x} = \mathbf{0}$$

can be transformed to a system of differential calculated of first order, that is

$$\dot{\mathbf{z}} = \mathbf{A} \mathbf{z},$$

with

$$\mathbf{z} = \begin{bmatrix} \dot{\mathbf{x}} \\ \mathbf{x} \end{bmatrix} \quad \text{and} \quad \mathbf{A} = \begin{bmatrix} -\mathbf{M}^{-1} \mathbf{D} & -\mathbf{M}^{-1} (\mathbf{K} + \mathbf{N}) \\ \mathbf{I} & \mathbf{0} \end{bmatrix}.$$

The total energy in the system is given by

$$V = \frac{1}{2} \begin{bmatrix} \dot{x} \\ x \end{bmatrix}^T \begin{bmatrix} \mathbf{M} & \mathbf{0} \\ \mathbf{0} & \mathbf{K} \end{bmatrix} \begin{bmatrix} \dot{x} \\ x \end{bmatrix} = \mathbf{z}^T \mathbf{P} \mathbf{z}.$$

V also is a candidate for a Lyapunov function of the system. The change in the total energy is

$$\dot{V} = \mathbf{z}^T (\mathbf{A}^T \mathbf{P} + \mathbf{P} \mathbf{A}) \mathbf{z}$$

where

$$\mathbf{A}^T \mathbf{P} + \mathbf{P} \mathbf{A} = -\mathbf{Q}$$

is the famous *Lyapunov equation*. With

$$\mathbf{A}^T = \begin{bmatrix} -\mathbf{M}^{-1} \mathbf{D} & \mathbf{I} \\ -(\mathbf{K} - \mathbf{N}) \mathbf{M}^{-1} & \mathbf{0} \end{bmatrix}$$

$$\mathbf{A}^T \mathbf{P} = \frac{1}{2} \begin{bmatrix} -\mathbf{M}^{-1} \mathbf{D} & \mathbf{I} \\ -(\mathbf{K} - \mathbf{N}) \mathbf{M}^{-1} & \mathbf{0} \end{bmatrix} \begin{bmatrix} \mathbf{M} & \mathbf{0} \\ \mathbf{0} & \mathbf{K} \end{bmatrix} = \frac{1}{2} \begin{bmatrix} -\mathbf{D} & \mathbf{K} \\ -\mathbf{K} + \mathbf{N} & \mathbf{0} \end{bmatrix}$$

$$\mathbf{P} \mathbf{A} = \frac{1}{2} \begin{bmatrix} \mathbf{M} & \mathbf{0} \\ \mathbf{0} & \mathbf{K} \end{bmatrix} \begin{bmatrix} -\mathbf{M}^{-1} \mathbf{D} & -\mathbf{M}^{-1} (\mathbf{K} + \mathbf{N}) \\ \mathbf{I} & \mathbf{0} \end{bmatrix} = \frac{1}{2} \begin{bmatrix} -\mathbf{D} & -\mathbf{K} - \mathbf{N} \\ \mathbf{K} & \mathbf{0} \end{bmatrix},$$

we get

$$\mathbf{A}^T \mathbf{P} + \mathbf{P} \mathbf{A} = \begin{bmatrix} -\mathbf{D} & -\frac{1}{2} \mathbf{N} \\ \frac{1}{2} \mathbf{N} & \mathbf{0} \end{bmatrix}$$

and for the change in the total energy

$$\begin{aligned} \dot{V} &= \begin{bmatrix} \dot{x} \\ x \end{bmatrix}^T \begin{bmatrix} -\mathbf{D} & -\frac{1}{2} \mathbf{N} \\ \frac{1}{2} \mathbf{N} & \mathbf{0} \end{bmatrix} \begin{bmatrix} \dot{x} \\ x \end{bmatrix} = -\dot{x}^T \mathbf{D} \dot{x} - \frac{1}{2} \dot{x}^T \mathbf{N} x + \frac{1}{2} x^T \mathbf{N} \dot{x} \\ &= -\dot{x}^T \mathbf{D} \dot{x} + x^T \mathbf{N} \dot{x}. \end{aligned}$$

A.5. Least-Squares Estimation

A.5.1. Projection Theorem

Definition A.3 (Inner Product, see [ZDG96, Sch97a]) Let \mathcal{X} be a vector space over \mathbb{C} . An inner product on \mathcal{X} is a complex valued function

$$\langle \cdot, \cdot \rangle : \mathcal{X} \times \mathcal{X} \rightarrow \mathbb{C}$$

such that for any $x, y, z \in \mathcal{X}$ and $\alpha, \beta \in \mathbb{C}$

1. $\langle x, \alpha y + \beta z \rangle = \alpha \langle x, y \rangle + \beta \langle x, z \rangle$
2. $\langle x, y \rangle = \overline{\langle y, x \rangle}$ (conjugate complex)
3. $\langle x, x \rangle > 0$ if $x \neq 0$

Theorem A.4 (Projection Theorem, see [Sch97a]) Let \mathcal{X} be a Hilbert space with the inner product $\langle \cdot, \cdot \rangle : \mathcal{X} \times \mathcal{X} \rightarrow \mathbb{R}$ and the norm $\|x\| = \sqrt{\langle x, x \rangle}$, and let \mathcal{V} be a linear closed subspace of \mathcal{X} .¹ Then for each vector $x \in \mathcal{X}$ exists a unique vector $v_0 \in \mathcal{V}$ such that

$$\|x - v_0\| \leq \|x - v\|$$

for all $v \in \mathcal{V}$. v_0 is the unique vector such that $\langle v, x - v_0 \rangle = 0$ for all $v \in \mathcal{V}$, or $x - v_0$ is orthogonal on all $v \in \mathcal{V}$.

The usefulness becomes clear if we look at the equation

$$y = Wa + e \tag{A.1}$$

where y is the so-called output vector, W is the so-called signal matrix, and e is an additional error vector. Now we search for a vector \tilde{a} which is an “optimal” estimate for a when y and W are known. The “optimal” estimate \tilde{a} should be a solution of equation (A.1) such that $\|e\|$ is a minimum.

y is element of the vector space $\mathcal{X} = \mathbb{R}^m$ and the column vectors of W span the closed subspace $\mathcal{V} = \text{span}\{w_1, w_2, \dots, w_n\}$. The optimal vector v_0 such that

$$\|y - v_0\| \leq \|y - v\|$$

is given by

$$\langle w_i, y - v_0 \rangle = 0 \quad \text{for all } i = 1, \dots, n.$$

Since $v_0 \in \mathcal{V}$ we can write

$$\begin{aligned} \langle w_i, y - W\tilde{a} \rangle &= 0 & \text{for all } i = 1, \dots, n \\ \langle w_i, y - w_1\tilde{a}_1 - w_2\tilde{a}_2 - \dots - w_n\tilde{a}_n \rangle &= 0 & \text{for all } i = 1, \dots, n \end{aligned}$$

¹ The definition of a Hilbert space can be found in [ZDG96].

or

$$\underbrace{\begin{bmatrix} \langle \mathbf{w}_1, \mathbf{w}_1 \rangle & \cdots & \langle \mathbf{w}_1, \mathbf{w}_n \rangle \\ \vdots & \ddots & \vdots \\ \langle \mathbf{w}_n, \mathbf{w}_1 \rangle & \cdots & \langle \mathbf{w}_n, \mathbf{w}_n \rangle \end{bmatrix}}_{\mathbf{G}} \begin{bmatrix} \tilde{a}_1 \\ \vdots \\ \tilde{a}_n \end{bmatrix} = \begin{bmatrix} \langle \mathbf{w}_1, \mathbf{y} \rangle \\ \vdots \\ \langle \mathbf{w}_n, \mathbf{y} \rangle \end{bmatrix} .$$

If \mathbf{G} is invertible, the optimal solution of $\tilde{\mathbf{a}}$ is

$$\tilde{\mathbf{a}} = \mathbf{G}^{-1} \begin{bmatrix} \langle \mathbf{w}_1, \mathbf{y} \rangle \\ \vdots \\ \langle \mathbf{w}_n, \mathbf{y} \rangle \end{bmatrix} .$$

A.5.2. Discrete Least-Squares

Standard Least-Squares

Let $\mathbf{y}(k) \in \mathbb{R}^m([0, k])$ be a discrete-time output vector which is given by

$$\mathbf{y}(k) = \mathbf{W}(k) \mathbf{a} + \mathbf{d}(k) .$$

where $\mathbf{W}(k) \in \mathbb{R}^{m \times n}([0, k])$ is the a discrete-time signal matrix, \mathbf{a} is the unknown parameter vector, $\mathbf{d}(k)$ is the error vector, $k \in \mathbb{N}$, and \mathbb{R}^m is the Hilbert space of vector valued discrete-time functions.² The optimal estimate $\tilde{\mathbf{a}}_k$ for \mathbf{a} , based on the past values of \mathbf{W} and \mathbf{y} , at the discrete time k is defined by

$$\|\mathbf{y}(k) - \mathbf{W}(k) \tilde{\mathbf{a}}_k\| \leq \|\mathbf{y}(k) - \mathbf{W}(k) \mathbf{a}\| \quad \text{for all } \mathbf{a} \in \mathbb{R}^n$$

with

$$\|\mathbf{x}\| := \sqrt{\langle \mathbf{x}, \mathbf{x} \rangle} \quad \text{and} \quad \langle \mathbf{x}(k), \mathbf{y}(k) \rangle := \sum_{i=1}^k \mathbf{x}^T(i) \mathbf{y}(i) .$$

The solution for the optimal estimate $\tilde{\mathbf{a}}_k$ is

$$\tilde{\mathbf{a}}_k = \mathbf{P}(k) \left(\sum_{i=1}^k \mathbf{W}^T(i) \mathbf{y}(i) \right)$$

² The usage of k as the end of the definition interval of $\mathbf{y}(k)$ and the point at which $\mathbf{y}(k)$ has a special value is a little bit sloppy.

where

$$\mathbf{P}(k) = \left(\sum_{i=1}^k \mathbf{W}^T(i) \mathbf{W}(i) \right)^{-1}.$$

A recursive definition of this algorithm is given by

$$\mathbf{P}^{-1}(k) = \mathbf{P}^{-1}(k-1) + \mathbf{W}^T(k) \mathbf{W}(k)$$

$$\tilde{\mathbf{a}}_k = \tilde{\mathbf{a}}_{k-1} + \mathbf{P}(k) \mathbf{W}^T(k) (\mathbf{y}(k) - \mathbf{W}(k) \tilde{\mathbf{a}}_{k-1}).$$

Least-Squares with Exponential Forgetting

For time varying systems, it is convenient to use a weighted inner product with $\lambda_d(k) \leq 1$

$$\langle \mathbf{x}(k), \mathbf{y}(k) \rangle := \sum_{i=1}^k \left(\prod_{j=i+1}^k \lambda_d(j) \right) \mathbf{x}^T(i) \mathbf{y}(i)$$

to get the same result as in [Lju87]. The name exponential forgetting is chosen in analogy with the continuous least-squares algorithm from [SL91] and due to the fact that

$$\prod_{j=i+1}^k \lambda_d(j) = e^{\sum_{j=i+1}^k \log \lambda_d(j)}.$$

The optimal $\tilde{\mathbf{a}}_k$ based on measurements until k is

$$\tilde{\mathbf{a}}_k = \mathbf{P}(k) \left(\sum_{i=1}^k \left(\prod_{j=i+1}^k \lambda_d(j) \right) \mathbf{W}^T(i) \mathbf{y}(i) \right) \quad (\text{A.2})$$

with the gain matrix

$$\mathbf{P}(k) = \left(\sum_{i=1}^k \left(\prod_{j=i+1}^k \lambda_d(j) \right) \mathbf{W}^T(i) \mathbf{W}(i) \right)^{-1};$$

a recursive definition of this algorithm is

$$\mathbf{P}^{-1}(k) = \lambda_d(k) \mathbf{P}^{-1}(k-1) + \mathbf{W}^T(k) \mathbf{W}(k) \quad (\text{A.3})$$

$$\tilde{\mathbf{a}}_k = \tilde{\mathbf{a}}_{k-1} + \mathbf{P}(k) \mathbf{W}^T(k) (\mathbf{y}(k) - \mathbf{W}(k) \tilde{\mathbf{a}}_{k-1}). \quad (\text{A.4})$$

Applying the matrix inversion lemma

$$(\mathbf{A} + \mathbf{BCD})^{-1} = \mathbf{A}^{-1} - \mathbf{A}^{-1}\mathbf{B} \left(\mathbf{DA}^{-1}\mathbf{B} + \mathbf{C}^{-1} \right)^{-1} \mathbf{DA}^{-1}$$

and taking $\mathbf{A} = \lambda_d(k) \mathbf{P}^{-1}(k-1)$, $\mathbf{B} = \mathbf{D}^T = \mathbf{W}^T(k)$ and $\mathbf{C} = \mathbf{I}$, we get

$$\begin{aligned} \mathbf{P}(k) &= \left[\lambda_d(k) \mathbf{P}^{-1}(k-1) + \mathbf{W}^T(k) \mathbf{W}(k) \right]^{-1} \\ &= \mathbf{P}(k-1) \frac{\mathbf{I} - \mathbf{W}^T(k) [\mathbf{W}(k) \mathbf{P}(k-1) \mathbf{W}^T(k) + \lambda_d(k) \mathbf{I}]^{-1} \mathbf{W}(k) \mathbf{P}(k-1)}{\lambda_d(k)} \end{aligned}$$

which reduces the computational effort for calculating \mathbf{P} as long as $\mathbf{W}(k) \in \mathbb{R}^{m \times n}$ and $m < n$.

A.5.3. Continuous Least-Squares

The formulation of the continuous least-squares algorithm from Slotine and Lee [SL91] presented here cannot—to the author's knowledge—be found in the literature.

Standard Least-Squares

Let $\mathbf{y}(t) \in \mathbb{R}^m([0, t])$ be a continuous-time output vector which is given by

$$\mathbf{y}(t) = \mathbf{W}(t) \mathbf{a} + \mathbf{d}(t) .$$

where $\mathbf{W}(t) \in \mathbb{R}^{m \times n}([0, t])$ is the a continuous-time signal matrix, \mathbf{a} is the unknown parameter vector, $\mathbf{d}(t)$ is the error vector, and $\mathbb{R}^m([0, t])$ is the Hilbert space of vector valued continuous-time functions.³ With the inner product

$$\langle \mathbf{x}(t), \mathbf{y}(t) \rangle := \int_{r=0}^t \mathbf{x}^T(r) \mathbf{y}(r) \, dr$$

we get the same result as in [SL91] for the optimal estimate $\tilde{\mathbf{a}}_t$ of \mathbf{a} , based on the past values of \mathbf{W} and \mathbf{y} , at the time t . It is defined by

$$\tilde{\mathbf{a}}_t = \mathbf{P}(t) \left(\int_0^t \mathbf{W}^T(r) \mathbf{y}(r) \, dr \right) \quad (\text{A.5})$$

³ The usage of t as the end of the definition interval of $\mathbf{y}(t)$ and the time point at which $\mathbf{y}(t)$ has a special value is a little bit sloppy.

where

$$\mathbf{P}(t) = \left(\int_0^t \mathbf{W}^T(r) \mathbf{W}(r) dr \right)^{-1}.$$

The derivative of the inverse of the gain matrix \mathbf{P} is

$$\frac{d}{dt} \mathbf{P}^{-1}(t) = \mathbf{W}^T(t) \mathbf{W}(t). \quad (\text{A.6})$$

To avoid matrix inversions we can use the relationship

$$\frac{d}{dt} (\mathbf{P} \mathbf{P}^{-1}) = \mathbf{0} \quad \longrightarrow \quad \frac{d}{dt} \mathbf{P} = -\mathbf{P} \left(\frac{d}{dt} \mathbf{P}^{-1} \right) \mathbf{P}. \quad (\text{A.7})$$

Inserting equation (A.6) delivers

$$\frac{d}{dt} \mathbf{P} = -\mathbf{P} \mathbf{W}^T(t) \mathbf{W}(t) \mathbf{P}.$$

For a differential equation version, we are differentiating (A.5)

$$\frac{d}{dt} \mathbf{P}^{-1}(t) \tilde{\mathbf{a}}_t + \mathbf{P}^{-1}(t) \frac{d}{dt} \tilde{\mathbf{a}}_t = \mathbf{W}^T(t) \mathbf{y}(t).$$

The differential equation form is

$$\begin{aligned} \frac{d}{dt} \mathbf{P}(t) &= -\mathbf{P}(t) \mathbf{W}^T(t) \mathbf{W}(t) \mathbf{P}(t) \\ \frac{d}{dt} \tilde{\mathbf{a}}_t &= \mathbf{P}(t) \mathbf{W}^T(t) (\mathbf{y}(t) - \mathbf{W}(t) \tilde{\mathbf{a}}_t). \end{aligned}$$

Least-Squares with Exponential Forgetting

Slotine and Lee [SL91] also describe a least-squares estimator with exponential forgetting. If we use the inner product

$$\langle \mathbf{x}(t), \mathbf{y}(t) \rangle := \int_{r=0}^t e^{-\int_s^t \lambda(r) dr} \mathbf{x}^T(r) \mathbf{y}(r) ds$$

we get the same result

$$\mathbf{P}^{-1}(t) \tilde{\mathbf{a}}_t = \int_0^t e^{-\int_s^t \lambda(r) dr} \mathbf{W}^T(r) \mathbf{y}(r) ds \quad (\text{A.8})$$

with

$$\mathbf{P}(t) = \left(\int_0^t e^{-\int_s^t \lambda(r) dr} \mathbf{W}^T(r) \mathbf{W}(r) dr \right)^{-1}.$$

We note that, for $t = kT_s$ and the approximation

$$\int_{iT_s}^{kT_s} f(t) dt \approx \sum_{j=i+1}^k f(jT_s) T_s,$$

equation (A.8) is equal to equation (A.2). The relationship between the continuous and the discrete forgetting factor

$$\lambda(jT_s) = -\frac{1}{T_s} \ln \lambda_d(j).$$

For a differential equation version of the algorithm, we are differentiating (A.8)

$$\frac{d}{dt} \mathbf{P}^{-1}(t) \tilde{\mathbf{a}}_t + \mathbf{P}^{-1}(t) \frac{d}{dt} \tilde{\mathbf{a}}_t = -\lambda(t) \int_0^t e^{-\int_s^t \lambda(r) dr} \mathbf{W}^T(r) \mathbf{y}(r) ds + \mathbf{W}^T(t) \mathbf{y}(t).$$

By inserting the differential equation version of the inverse gain matrix

$$\frac{d}{dt} \mathbf{P}^{-1}(t) = -\lambda(t) \mathbf{P}^{-1}(t) + \mathbf{W}^T(t) \mathbf{W}(t)$$

we get

$$\begin{aligned} \mathbf{P}^{-1}(t) \frac{d}{dt} \tilde{\mathbf{a}}_t &= -\lambda(t) \underbrace{\left(\int_0^t e^{-\int_s^t \lambda(r) dr} \mathbf{W}^T(r) \mathbf{y}(r) ds - \mathbf{P}^{-1}(t) \tilde{\mathbf{a}}_t \right)}_{=0 \text{ equ. (A.8)}} \\ &\quad + \mathbf{W}^T(t) \mathbf{y}(t) - \mathbf{W}^T(t) \mathbf{W}(t) \tilde{\mathbf{a}}_t \end{aligned}$$

$$\mathbf{P}^{-1}(t) \frac{d}{dt} \tilde{\mathbf{a}}_t = \mathbf{W}^T(t) (\mathbf{y}(t) - \mathbf{W}(t) \tilde{\mathbf{a}}_t).$$

Together with equation (A.7) we get the differential equation version of the algorithm

$$\begin{aligned} \frac{d}{dt} \mathbf{P}(t) &= \lambda(t) \mathbf{P}(t) - \mathbf{P}(t) \mathbf{W}^T(t) \mathbf{W}(t) \mathbf{P}(t) \\ \frac{d}{dt} \tilde{\mathbf{a}}_t &= \mathbf{P}(t) \mathbf{W}^T(t) (\mathbf{y}(t) - \mathbf{W}(t) \tilde{\mathbf{a}}_t). \end{aligned}$$

Bibliography

- [Ack88] ACKERMANN, J.: *Abtastregelung*. Springer-Verlag, Berlin, Germany, 3rd edn. 1988.
- [ALA98] ANTILA, M., LANTTO, E., and ARKKIO, A.: *Determination of forces and linearized parameters of radial active magnetic bearings by finite element technique*. *IEEE Transactions on Magnetics*, vol. 34(3):pp. 684–694. May 1998.
- [ALT98] ANTILA, M., LANTTO, E., and TOMMILA, V.: *Determination of eddy current effects on radial active magnetic bearings based on a reluctance network and 1D eddy current model*. In ALLAIRE, P. E. and TRUMPER, D. L., eds., *Proc. of Sixth Int. Symp. on Magnetic Bearings*, pp. 204–213. Massachusetts Institute of Technology (MIT), Technomic Publ., Lancaster - Basel, Cambridge, Massachusetts. Aug. 5–7 1998.
- [AN99] AENIS, M. and NORDMANN, R.: *A precise force measurement in magnetic bearings for diagnosis purposes*. In GROOM, N. J. and BRITCHER, C. P., eds., *Proc. of Fifth Int. Symp. on Magnetic Suspension Technology*, pp. 397–409. NASA Langley Research Center, Santa Barbara, California. NASA Conf. Publ. No. 2000-210291. Dec. 1–3 1999.
- [Ant98] ANTILA, M.: *Electromechanical properties of radial active magnetic bearings*, PhD Thesis Helsinki University of Technology. No. 92 in Electrical Engineering Series. Acta Polytechnica Scandinavica, Espoo, Finland. 1998.
- [BB39] BEAMS, J. W. and BLACK, S. A.: *Electrically-Driven Magnetically-Supported Vacuum-Type Ultracentrifuge*. *Review of Scientific Instruments*, vol. 10:pp. 59–63. Feb. 1939.

- [BG97] BERRY, M. V. and GEIM, A. K.: *Of flying frogs and levitrons*. *European Journal of Physics*, vol. 18:pp. 307–313. 1997.
- [BK00] BETSCHON, F. and KNOSPE, C. R.: *Gain scheduled adaptive vibration control*. In SCHWEITZER, G., SIEGWART, R., LÖSCH, F., and BERKSUN, R., eds., *Proc. of Seventh Int. Symp. on Magnetic Bearings*, pp. 23–28. Int. Center for Magnetic Bearings, Eidgenössische Technische Hochschule (ETH) Zürich, Zurich, Switzerland. Aug. 23–25 2000.
- [BK01] BETSCHON, F. and KNOSPE, C. R.: *Reducing Magnetic Bearing Currents via Gain Scheduled Adaptive Control*. *IEEE/ASME Transactions On Mechatronics*, vol. 6(4):pp. 437–443. Dec. 2001.
- [Ble84] BLEULER, H.: *Decentralized control of magnetic rotor bearing systems*. Ph.D. thesis, Eidgenössische Technische Hochschule (ETH) Zürich, Zurich, Schweiz. Aug. 1984.
- [Bra39a] BRAUNBEK, W.: *Freies Schweben diamagnetischer Körper im Magnetfeld*. *Zeitschrift für Physik*, vol. 112:pp. 764–769. 1939.
- [Bra39b] BRAUNBEK, W.: *Freischwebende Körper im elektrischen und magnetischen Feld*. *Zeitschrift für Physik*, vol. 112:pp. 753–763. 1939.
- [BS83] BURROWS, C. R. and SAHINKAYA, M. N.: *Vibration Control of a multi-mode rotor-bearing system*. *Proceedings of the Royal Society London*, (A 386):pp. 77–94. 1983.
- [BS88] BURROWS, C. R. and SAHINKAYA, M. N.: *Control strategies for use with magnetic bearings*. In *Proc. of Fourth Int. Conf. on Vibrations in Rotating Machinery*, pp. 23–32. Institution of Mechanical Engineers (IMechE), Mechanical Engineering Publications Ltd., Edinburgh, U.K. IMechE Paper C273/88. Sep. 13–15 1988.
- [BSC89] BURROWS, C. R., SAHINKAYA, M. N., and CLEMENTS, S.: *Active vibration control of flexible rotors: an experimental and theoretical study*. *Proceedings of the Royal Society London*, (A 422):pp. 123–146. 1989.
- [BSLC92a] BEALE, S., SHAFAI, B., LARocca, P., and CUSSON, E.: *Adaptive forced balancing for magnetic bearing control systems*. In *Proc. of*

- the 31st Conf. on Decision and Control*, pp. 3535–3539. Tucson, Arizona, U.S.A. Dec. 1992.
- [BSLC92b] BEALE, S., SHAFAI, B., LARocca, P., and CUSson, E.: *Adaptive forced balancing for magnetic bearing systems*. In ALLAIRe, P. E., ed., *Proc. of Third Int. Symp. on Magnetic Bearings*, pp. 601–611. Technomic Publ., Lancaster - Basel, Alexandria, Virginia. Jul. 29–31 1992.
- [BSTS88] BURROWS, C. R., SAHINKAYA, M. N., TRAXLER, A., and SCHWEITZER, G.: *Design and Application of a Magnetic Bearing for Vibration Control and Stabilization of a Flexible Rotor*. In SCHWEITZER, G., ed., *Proc. of First Int. Symp. on Magnetic Bearings*, pp. 159–168. Eidgenössische Technische Hochschule (ETH) Zürich, Springer-Verlag, Zurich, Switzerland. Jun. 6–8 1988.
- [Bur91] BURROWS, C. R.: *An evaluation of some strategies for vibration control of flexible rotors*. In GROOM, N. J., ed., *Proc. of Int. Symp. on Magnetic Suspension Technology*, vol. 2, pp. 691–701. NASA Langley Research Center, Hampton, Virginia. NASA Conf. Publ. 3152. Aug. 19–23 1991.
- [BYM46] BEAMS, J. W., YOUNG, J. L., and MOORE, J. W.: *The Production of High Centrifugal Fields*. *Journal of Applied Physics*, vol. 17:pp. 886–890. Nov. 1946.
- [CCI+97] CARABELLI, S., CRIVELLI, A., IANNANTUONI, A., IPPOLITI, R., MADDALENO, F., and MUZZARELLI, M.: *A switching power amplifier for active magnetic suspensions*. In *Proc. of Seventh European Conf. on Power Electronics and Applications*. Trondheim, Norway. Sep. 1997.
- [Chi93] CHILDS, D.: *Turbomachinery Rotordynamics Phenomena, Modeling, and Analysis*. John Wiley & Sons, New York, USA. 1993.
- [Ear39] EARNSHAW, S.: *On the Nature of the Molecular Forces which regulate the Constitution of the Luminiferous Ether*. *Transactions of the Cambridge Philosophical Society*, vol. 7 - Part 1:pp. 97–112. Pitt Press, Cambridge. Parker J. W., London. Mar. 18 1839.

- [FGN96] FÖRCH, P., GÄHLER, C., and NORDMANN, R.: *AMB System for rotordynamic experiments: calibration results and control*. In MATSUMURA, F., OKADA, Y., FUJITA, M., and NAMERIKAWA, T., eds., *Proc. of Fifth Int. Symp. on Magnetic Bearings*, pp. 171–178. Kanazawa, Japan. Aug. 28–30 1996.
- [Gen93] GENTA, G.: *Vibration of Structures and Machines, Practical Aspects*. Springer-Verlag, New York, USA. 1993.
- [GF94] GÄHLER, C. and FÖRCH, P.: *A precise magnetic bearing exciter for rotordynamic experiments*. In SCHWEITZER, G., SIEGWART, R., and HERZOG, R., eds., *Proc. of Fourth Int. Symp. on Magnetic Bearings*, pp. 193–200. Int. Center for Magnetic Bearings, Eidgenössische Technische Hochschule (ETH) Zürich, Hochschulverlag, ETH Zürich, Zurich, Switzerland. Aug. 23–26 1994.
- [GG97] GIBBS, P. and GEIM, A.: *Is Magnetic Levitation Possible? The Physics and Relativity FAQ*, ©1992–2002. Mar. 1997.
URL <http://www.edu-observatory.org/physics-faq/>
- [GHS91] GAUSCH, F., HOFER, A., and SCHLACHER, K.: *Digitale Regelkreise*. Oldenbourg Verlag, München, Germany. 1991.
- [Glo77] GLOVER, J. R., JR: *Adaptive Noise Canceling Applied to Sinusoidal Interferences*. *IEEE Transactions on Acoustics, Speech and Signal Processing*, vol. ASSP-25(6):pp. 481–491. Dec. 1977.
- [GNP02] GASCH, R., NORDMANN, R., and PFÜTZNER, H.: *Rotordynamik*. Springer-Verlag, Berlin, Germany, 2nd edn. 2002.
- [Hab84] HABERMANN, H.: *Magnetische Lager. Techniques de l'ingenieur*, vol. 8. 1984.
- [HBGL96] HERZOG, R., BÜHLER, P., GÄHLER, C., and LARSONNEUR, R.: *Unbalance compensation using generalized notch filters in the multivariable feedback of magnetic bearings*. *IEEE Transactions on control systems technology*, vol. 4(5):pp. 580–586. Sep. 1996.
- [Hir01] HIRSCHMANNER, M.: *Magnetische Widerstandsnetzwerke mit MATLAB/SIMULINK berechnen und simulieren*. Seminarunterlagen S70 MATLAB/SIMULINK Einsatz, Anwendungen, En-

twicklungen, ARGE Simulation News (ARGESIM), Technische Universität Wien, Vienna, Austria. May 2001.

- [Hir03a] HIRSCHMANNER, M.: *Adaptive Kompensation von zirkulatorischen Anregungen am Beispiel eines 2FG-Rotors*. In IRRETIER, H., NORDMANN, R., and SPRINGER, H., eds., *SIRM 2003 - Schwingungen in rotierenden Maschinen VI*, pp. 61–69. Verlag Vieweg, Braunschweig - Wiesbaden, Darmstadt, Germany. ISBN 3-528-03956-6. Feb. 26–28 2003.
- [Hir03b] HIRSCHMANNER, M.: *Adaptive Vibration and Unbalance Control of a Rotor Supported by Active Magnetic Bearings*. In *Proc. in Applied Mathematics and Mechanics, GAMM - Conf. Augsburg 2002*. WILEY-VCH Verlag, Weinheim, Germany. 2003.
- [HKS91] HUMPHRIS, R. R., KNOSPE, C. R., and SUNDARAM, S.: *Dynamic balancing with open loop control of magnetic bearings*. In *Proc. of the 26th Intersociety Energy Conversion Engineering Conf. (IECEC-91)*. Boston, MA, U.S.A. Aug. 4–9 1991.
- [HM84] HABERMANN, H. and MAURICE, B.: *The Active Magnetic Bearing Enables Optimum Damping of Flexible Rotors*. ASME Paper 84-GT-117. 1984.
- [HS02] HIRSCHMANNER, M. and SPRINGER, H.: *Adaptive Vibration and Unbalance Control of a Rotor Supported by Active Magnetic Bearings*. In OKADA, Y. and NONAMI, K., eds., *Proc. of Eighth Int. Symp. on Magnetic Bearings*, pp. 483–488. Dynamics and Control Lab., Dept. of Mechanical Eng., Ibaraki University, Mito, Japan. Aug. 26–28 2002.
- [HSS02] HIRSCHMANNER, M., STEINSCHADEN, N., and SPRINGER, H.: *Adaptive Control of a Rotor Excited by Destabilizing Cross Coupling Forces*. In HAHN, E. and RANDALL, R., eds., *Proc. of Sixth Int. Conf. on Rotordynamics*, pp. 38–45. International Federation of the Theory of Mechanism and Machines (IFTOMM), UNSW Printing Services, Sydney, Australia. Sep. 30–Oct. 3 2002.
- [HW89] HALL, S. R. and WERELEY, N. M.: *Linear control issues in the higher harmonic control of helicopter vibrations*. In *Proc. 45th Annual Fo-*

rum of the American Helicopter Society, pp. 955–971. Boston, MA. May 1989.

- [KB92] KEOGH, P. S. and BURROWS, C. R.: *H-infinity controller design for active vibration control of a flexible rotor*. In *Proc. of Fifth Int. Conf. on Vibrations in Rotating Machinery*, pp. 131–140. Institution of Mechanical Engineers (IMEchE), Mechanical Engineering Publications Ltd., Bath, England. Sep. 7–10 1992.
- [KE94] KIENBERGER, A. and ECKER, H.: *Untersuchung von Regelkonzepten für einen magnetgelagerten Rotor mittels Simulation*. In KAMPE, G. and ZEITZ, M., eds., *Simulationstechnik, 9. Symp. in Stuttgart*, vol. 9 of *Fortschritte in der Simulationstechnik*, pp. 373–378. Arbeitsgemeinschaft Simulation (ASIM), Verlag Vieweg, Wiesbaden, Germany. Oct. 10–13 1994.
- [KFHW97] KNOSPE, C. R., FEDIGAN, S. J., HOPE, R. W., and WILLIAMS, R. D.: *A multitasking DSP implementation of adaptive magnetic bearing control*. *IEEE Transactions on control systems technology*, vol. 5(2):pp. 230–238. Mar. 1997.
- [KHFW93] KNOSPE, C. R., HOPE, R. W., FEDIGAN, S. J., and WILLIAMS, R. D.: *Adaptive On-Line Rotor Balancing Using Digital Control*. In *Proc. of MAG '93 - Magnetic Bearings, Magnetic Drives and Dry Gas Seals Conf. & Exhib.*, pp. 153–164. Technomic Publ., Lancaster - Basel, Alexandria, Virginia. Jul. 29–30 1993.
- [KHFW94] KNOSPE, C. R., HOPE, R. W., FEDIGAN, S. J., and WILLIAMS, R. D.: *New results in the control of rotor synchronous vibration*. In SCHWEITZER, G., SIEGWART, R., and HERZOG, R., eds., *Proc. of Fourth Int. Symp. on Magnetic Bearings*, pp. 119–124. Int. Center for Magnetic Bearings, Eidgenössische Technische Hochschule (ETH) Zürich, Hochschulverlag, ETH Zürich, Zurich, Switzerland. Aug. 23–26 1994.
- [KHFW95] KNOSPE, C. R., HOPE, R. W., FEDIGAN, S. J., and WILLIAMS, R. D.: *Experiments in the Control of Unbalance Response Using Magnetic Bearings*. *Mechatronics*, vol. 5(4):pp. 385–400. doi: 10.1016/0957-4158(95)00015-W. Elsevier Science, Great Britain. 1995.

- [KHMA92] KNOSPE, C. R., HUMPHRIS, R. R., MASLEN, E. H., and ALLAIRE, P. E.: *Active balancing of a high speed rotor in magnetic bearings*. In *Proc. of Rotordynamics t'92 Conf.* Venice, Italy. Apr. 28–30 1992.
- [KHS91a] KNOSPE, C. R., HUMPHRIS, R. R., and SUNDARAM, S.: *Flexible rotor balancing using magnetic bearings*. In *Proc. of Recent Advances in Active Control of Sound and Vibration Conf.* Virginia Polytechnic Institute and State University. Apr. 15–17 1991.
- [KHS91b] KNOSPE, C. R., HUMPHRIS, R. R., and SUNDARAM, S.: *Magnetic bearings for rotor unbalance response attenuation*. In *Proc. of MAG '91 - Magnetic Bearings, Magnetic Drives and Dry Gas Seals Conf. & Exhib.* Alexandria, Virginia. Mar. 13–15 1991.
- [KHS⁺98] KUGI, A., HAAS, W., SCHLACHER, K., AISTLEITNER, K., FRANK, H. M., and RIGLER, G. W.: *Active Compensation of Roll Eccentricity in Rolling Mills*. In *The 1998 IEEE Industry Applications Conf., Thirty-Third IAS Annual Meeting*, pp. 2199–2206. St. Louis, U.S.A. Oct. 12–15 1998.
- [KHS⁺00] KUGI, A., HAAS, W., SCHLACHER, K., AISTLEITNER, K., FRANK, H. M., and RIGLER, G. W.: *Active Compensation of Roll Eccentricity in Rolling Mills*. *IEEE Transactions on Industry Applications*, vol. 36(2):pp. 625–632. Mar./Apr. 2000.
- [Kie94] KIENBERGER, A.: *Simulation und Regelung eines magnetgelagerten Rotors*. Master's thesis, Vienna University of Technology, Vienna, Austria. Apr. 1994.
- [KMHW90] KEITH, F. J., MASLEN, E. H., HUMPHRIS, R. R., and WILLIAMS, R. D.: *Switching amplifier design for magnetic bearings*. In HIGUCHI, T., ed., *Proc. of Second Int. Symp. on Magnetic Bearings*, pp. 211–218. Institute of Industrial Science, University of Tokyo, Tokyo, Japan. Jul. 12–14 1990.
- [Kno91] KNOSPE, C. R.: *Stability and performance of notch filter control for unbalance response*. In GROOM, N. J., ed., *Proc. of Int. Symp. on Magnetic Suspension Technology*, pp. 181–205. NASA Langley Research Center, Hampton, Virginia. NASA Conf. Publ. No. 3152 Part 1. Aug. 19–23 1991.

- [Kno92a] KNOSPE, C. R.: *Reducing unbalance response with magnetic bearings*. In *Proc. of REVOLVE'92*. Calgary, Alberta, Canada. Apr. 29 1992.
- [Kno92b] KNOSPE, C. R.: *Robustness of unbalance response controllers*. In ALLAIRE, P. E., ed., *Proc. of Third Int. Symp. on Magnetic Bearings*, pp. 580–589. Technomic Publ., Lancaster - Basel, Alexandria, Virginia. Jul. 29–31 1992.
- [KT96] KNOSPE, C. R. and TAMER, S. M.: *Experiments in robust unbalance response control*. In MATSUMURA, F., OKADA, Y., FUJITA, M., and NAMERIKAWA, T., eds., *Proc. of Fifth Int. Symp. on Magnetic Bearings*, pp. 131–136. Kanazawa, Japan. Aug. 28–30 1996.
- [KT97a] KNOSPE, C. R. and TAMER, S. M.: *Experiments in robust control of rotor unbalance response using magnetic bearings*. *Mechatronics*, vol. 7(3):pp. 217–229. doi: 10.1016/S0957-4158(96)00047-5. Elsevier Science, Great Britain. 1997.
- [KT97b] KNOSPE, C. R. and TAMER, S. M.: *Robust adaptive control of unbalance response for a flexible rotor*. *JSME International Journal*, vol. 40(4):pp. 599–606. 1997.
- [KTF95] KNOSPE, C. R., TAMER, S. M., and FEDIGAN, S. J.: *Design of robust adaptive unbalance response controllers for rotors with magnetic bearings*. In *Proc. of 3rd Int. Symp. on Magnetic Suspension Technology*. NASA Langley Research Center, Tallahassee, Florida. Dec. 13–15 1995.
- [KTF97] KNOSPE, C. R., TAMER, S. M., and FITTRO, R.: *Rotor synchronous response control: approaches for addressing speed dependence*. *Journal of vibration and control*, vol. 3:pp. 435–458. 1997.
- [KTL97] KNOSPE, C. R., TAMER, S. M., and LINDLAU, J.: *New results in adaptive vibration control*. In *Proc. of MAG '97 - Industrial Conf. and Exhib. on Magnetic Bearings*, pp. 209–219. Technomic Publ., Lancaster - Basel, Alexandria, Virginia. Aug. 19–22 1997.
- [Kug01] KUGI, A.: *Non-linear Control Based on Physical Models*. Lecture Notes in Control and Information Sciences. Springer-Verlag, London, Great Britain. 2001.

- [KXM92] KNIGHT, J. D., XIA, H. Z., and McCAUL, E. B.: *Forces in Magnetic Journal Bearings: Nonlinear Computation and Experimental Measurement*. In ALLAIRE, P. E., ed., *Proc. of Third Int. Symp. on Magnetic Bearings*, pp. 441–450. Technomic Publ., Lancaster - Basel, Alexandria, Virginia. Jul. 29–31 1992.
- [Lan97] LANG, O.: *Vibration Control of a Self-Excited Rotor by Active Magnetic Bearings*. Ph.D. thesis, Vienna University of Technology, Austria. Jan. 1997.
- [LCB96] LUM, K.-Y., COPPOLA, V. T., and BERNSTEIN, D. S.: *Adaptive autocentering control for an active magnetic bearing supporting a rotor with unknown mass imbalance*. *IEEE Transactions on control systems technology*, vol. 4(5):pp. 587–597. Sep. 1996.
- [LGH98] LÖSCH, F., GÄHLER, C., and HERZOG, R.: μ -Synthesis Controller Design for a 3 MW Pump running in AMB's. In ALLAIRE, P. E. and TRUMPER, D. L., eds., *Proc. of Sixth Int. Symp. on Magnetic Bearings*, pp. 415–428. Massachusetts Institute of Technology (MIT), Technomic Publ., Lancaster - Basel, Cambridge, Massachusetts. Aug. 5–7 1998.
- [LGKK00] LIAO, M. F., GASCH, R., KOLK, O., and KLETSCHKOWSKI, T.: *Stability Improvement of Motion of a Rotor with an Active Control Method*. *Journal of Vibration and Control*, vol. 6(2):pp. 291–308. Feb. 2000.
- [LH94] LARSONNEUR, R. and HERZOG, R.: *Feedforward compensation of unbalance: new results and application experiences*. In *Proc. of IUTAM Symposium Active Control of Vibrations*, pp. 45–52. Bath, U.K. Sep. 1994.
- [Lju87] LJUNG, L.: *System Identification: Theory for the User*. Prentice Hall, Englewood Cliffs, New Jersey, USA. 1987.
- [LR00] VON LÖWIS, J. and RUDOLPH, J.: *Adaptive inertial autocentering of a rigid rotor with unknown imbalance supported by active magnetic bearings*. In SCHWEITZER, G., SIEGWART, R., LÖSCH, F., and BERKSUN, R., eds., *Proc. of Seventh Int. Symp. on Magnetic Bearings*, pp. 561–566. Int. Center for Magnetic Bearings, Eidgenössische Technische Hochschule (ETH) Zürich, Zurich, Switzerland. Aug. 23–25 2000.

- [LWS95] LANG, O., WASSERMANN, J., and SPRINGER, H.: *Adaptive Regelung von zirkulatorischen Kräften in rotierenden Maschinen mit Magnetlagern*. In HAMPEL, R., ed., *Proc. of 2nd Zittau Workshop Magnetic Bearing*, pp. 101–107. Hochschule für Technik, Wirtschaft und Sozialwesen Zittau/Görlitz (FH), Zittau, Germany. Wissenschaftliche Berichte, Heft 42, Nr. 1508-1516. Sep. 5–6 1995.
- [LWS96a] LANG, O., WASSERMANN, J., and SPRINGER, H.: *Adaptive Regelung eines magnetgelagerten Rotors*. Seminarunterlagen über Modellbildung und Simulation (MATLAB und SIMULINK), ARGE Simulation News (ARGESIM), Technische Universität, Vienna, Austria. Mar. 1996.
- [LWS96b] LANG, O., WASSERMANN, J., and SPRINGER, H.: *Adaptive Vibration Control of a Rigid Rotor Supported by Active Magnetic Bearings*. *Journal of Engineering for Gas Turbines and Power*, vol. 118(1):pp. 825–829. Transactions of The American Society of Mechanical Engineers (ASME). Jan. 1996.
- [Mas91] MASLEN, E. H.: *Magnetic Bearing Synthesis for Rotating Machinery*. Ph.D. thesis, University of Virginia, Virginia, U.S.A. Jan. 1991.
- [MB89] MUSZYNSKA, A. and BENTLY, D. E.: *Anti-swirl arrangements prevent rotor/seal instability*. *Journal of vibration, stress, and reliability in design*, vol. 111:pp. 156–162. 1989.
- [Mee96] MEEKER, D. C.: *Optimal Solutions to the Inverse Problem in Quadratic Magnetic Actuators*. Ph.D. thesis, University of Virginia, Virginia, U.S.A. May 1996.
- [MFB88] MUSZYNSKA, A., FRANKLIN, W., and BENTLY, D. E.: *Rotor active "anti-swirl" control*. *Journal of vibration, acoustics, stress, and reliability in design*, vol. 110:pp. 143–150. 1988.
- [MM94] MASLEN, E. H. and MEEKER, D. C.: *Bias Linearization and Decoupling for Active Magnetic Bearings: A Generalized Theory*. In SCHWEITZER, G., SIEGWART, R., and HERZOG, R., eds., *Proc. of Fourth Int. Symp. on Magnetic Bearings*, pp. 23–28. Int. Center

- for Magnetic Bearings, Eidgenössische Technische Hochschule (ETH) Zürich, Hochschulverlag, ETH Zürich, Zurich, Switzerland. Aug. 23–26 1994.
- [MM95] MASLEN, E. H. and MEEKER, D. C.: *Fault tolerance of magnetic bearings by generalized bias current linearization*. *IEEE Transactions on Magnetics*, vol. 31(3):pp. 2304–2314. May 1995.
- [MMN96] MEEKER, D. C., MASLEN, E. H., and NOH, M. D.: *An Augmented Circuit Model for Magnetic Bearings Including Eddy Currents, Fringing and Leakage*. *IEEE Transactions on Magnetics*, vol. 32(4):pp. 3219–3227. Jul. 1996.
- [MTY⁺88] MATSUSHITA, O., TAKAGI, M., YONEYAMA, M., SAITOH, I., NAGATA, A., and AIZAWA, M.: *Stabilization by cross stiffness control of electromagnetic damper for contained liquid rotor unstable vibration*. In *Proc. of Fourth Int. Conf. on Vibrations in Rotating Machinery*, pp. 77–84. Institution of Mechanical Engineers (IMechE), Mechanical Engineering Publications Ltd., Edinburgh, U.K. IMechE Paper C320/88. Sep. 13–15 1988.
- [MTY⁺90] MATSUSHITA, O., TAKAGI, M., YONEYAMA, M., YOSHIDA, T., and SAITOH, I.: *Control of rotor vibration due to cross stiffness effect of active magnetic bearing*. In LALANNE, M. and HENRY, R., eds., *Proc. of 3rd Int. Conf. on Rotordynamics*, pp. 515–519. International Federation of the Theory of Mechanism and Machines (IFTOMM), Éditions du Centre National de la Recherche Scientifique (CNRS), Lyon, France. Sep. 10–12 1990.
- [Mus88] MUSZYNSKA, A.: *Improvements in lightly loaded rotor/bearing and rotor/seal models*. *Journal of vibration, acoustics, stress, and reliability in design*, vol. 110:pp. 129–136. 1988.
- [NI96] NONAMI, K. and ITO, T.: *μ Synthesis of flexible rotor-magnetic bearing systems*. *IEEE Transactions on control systems technology*, vol. 4(5):pp. 503–512. Sep. 1996.
- [NMMK00] NOH, M. D., MONTIE, D. T., MASLEN, E. H., and KONDOLEON, A.: *A Simulation Model for the Analysis of Transient Magnetic Bearing Performance*. In SCHWEITZER, G., SIEGWART, R., LÖSCH, F., and

- BERKSUN, R., eds., *Proc. of Seventh Int. Symp. on Magnetic Bearings*, pp. 177–182. Int. Center for Magnetic Bearings, Eidgenössische Technische Hochschule (ETH) Zürich, Zurich, Switzerland. Aug. 23–25 2000.
- [Nor93] NORDMANN, R.: *Rotordynamische Kennzahlen von berührungslosen Dichtungen und Laufrädern – Grundsatzreferat*. In *Dämpfung und Nichtlinearität, Phänomene, Probleme und Lösungen*, no. 1082 in VDI-Berichte, pp. 249–276. Verein Deutscher Ingenieure, VDI-Verlag, Düsseldorf. Oct. 1993.
- [NP97] NA, H.-S. and PARK, Y.: *An adaptive feedforward controller for rejection of periodic disturbances*. *Journal of Sound and Vibration*, vol. 201(4):pp. 427–435. 1997.
- [NP00a] NA, U. J. and PALAZZOLO, A.: *Fault tolerance of magnetic bearings with material path reluctances and fringing factors*. *IEEE Transactions on Magnetics*, vol. 36(6):pp. 3939–3946. Nov. 2000.
- [NP00b] NA, U. J. and PALAZZOLO, A.: *Fault tolerant, decoupling control of magnetic bearings including material path reluctances*. In SCHWEITZER, G., SIEGWART, R., LÖSCH, F., and BERKSUN, R., eds., *Proc. of Seventh Int. Symp. on Magnetic Bearings*, pp. 213–218. Int. Center for Magnetic Bearings, Eidgenössische Technische Hochschule (ETH) Zürich, Zurich, Switzerland. Aug. 23–25 2000.
- [NP00c] NA, U. J. and PALAZZOLO, A.: *Optimized realization of fault-tolerant heteropolar magnetic bearings*. *Journal of vibration and acoustics*, vol. 122:pp. 209–221. Jul. 2000.
- [NP01] NA, U. J. and PALAZZOLO, A.: *The fault-tolerant control of magnetic bearings with reduced controller outputs*. *Journal of dynamic systems, measurement, and control*, vol. 123:pp. 219–224. Jun. 2001.
- [SBLC94] SHAFAI, B., BEALE, S., LARocca, P., and CUSSON, E.: *Magnetic bearing control systems and adaptive forced balancing*. *IEEE Control systems magazine*, vol. 14(2):pp. 4–13. Apr. 1994.
- [Sch] SCHULZ, A.: *Aktive Magnetlager mit hoher Betriebssicherheit*. PhD thesis, to appear.

- [Sch86] SCHIEHLEN, W.: *Technische Dynamik*. B. G. Teubner, Stuttgart, Germany. 1986.
- [Sch95] SCHRÖDER, U.: *Power Amplifiers for Magnetic Bearings*. In *Proc. of MAG '95 - Magnetic Bearings, Magnetic Drives and Dry Gas Seals Conf. & Exhib.*, pp. 63–76. Technomic Publ., Lancaster - Basel, Alexandria, Virginia. Aug. 10–11 1995.
- [Sch97a] SCHLACHER, K.: *Prozessautomatisierung 2*. Skriptum zur Vorlesung, Department of Automatic Control and Control Systems Technology, Linz, Austria. 1997.
- [Sch97b] SCHLAGER, G.: *Numerische Simulation von magnetischen Netzwerken in aktiven Magnetlagern*. Master's thesis, Vienna University of Technology, Vienna, Austria. Aug. 1997.
- [SF90] SIEVERS, L. A. and VON FLOTOW, A. H.: *Comparison and Extensions of Control Methods for Narrowband Disturbance Rejection*. In WARNAKA, G. E., RADCLIFFE, C., and VON FLOTOW, A. H., eds., *Active Noise and Vibration Control*, pp. 11–22. The American Society of Mechanical Engineers (ASME), Dallas, Texas, U.S.A. NCA-Vol. 8. Nov. 25–30 1990.
- [SF92] SIEVERS, L. A. and VON FLOTOW, A. H.: *Comparison and Extensions of Control Methods for Narrow-Band Disturbance Rejection*. *IEEE Transactions on Signal Processing*, vol. 40(10):pp. 2377–2391. Oct. 1992.
- [Sha80] SHAW, J.: *Higher harmonic blade pitch control : a system for helicopter vibration reduction*. Phd-thesis, Massachusetts Institute of Technology, U.S.A. Oct. 1980.
- [Siv02] SIVICH, H.: *Vergleich verschiedener Unwuchtkompensationsalgorithmen*. Master's thesis, Vienna University of Technology, Vienna, Austria. Dec. 2002.
- [SL76] SCHWEITZER, G. and LANGE, R.: *Characteristics of a magnetic rotor bearing for active vibration control*. In *Vibrations in Rotating Machinery*, pp. 301–308. Institution of Mechanical Engineers (IMechE), Mechanical Engineering Publications Ltd., Cambridge, England. IMechE Paper C239/76. Sep. 15–17 1976.

- [SL91] SLODINE, J.-J. E. and LI, W.: *Applied Nonlinear Control*. Prentice-Hall, Englewood Cliffs, New Jersey. Massachusetts Institute of Technology (MIT). 1991.
- [SM00] SETIAWAN, J. D. and MUKHERJEE, R.: *Variable magnetic stiffness approach for simultaneous sensor runout and mass unbalance compensation in active magnetic bearings*. In SCHWEITZER, G., SIEGWART, R., LÖSCH, F., and BERKSUN, R., eds., *Proc. of Seventh Int. Symp. on Magnetic Bearings*, pp. 549–554. Int. Center for Magnetic Bearings, Eidgenössische Technische Hochschule (ETH) Zürich, Zurich, Switzerland. Aug. 23–25 2000.
- [SMM01a] SETIAWAN, J. D., MUKHERJEE, R., and MASLEN, E. H.: *Adaptive compensation of sensor runout for magnetic bearings with uncertain parameters: theory and experiments*. *Journal of dynamic systems, measurement, and control*, vol. 123:pp. 211–218. Jun. 2001.
- [SMM01b] SETIAWAN, J. D., MUKHERJEE, R., and MASLEN, E. H.: *Adaptive Compensation of Sensor Runout for Magnetic Bearings With Uncertain Parameters: Theory and Experiments*. *Journal of Dynamic Systems, Measurement, and Control*, vol. 123:pp. 211–218. Jun. 2001.
- [SMM01c] SETIAWAN, J. D., MUKHERJEE, R., and MASLEN, E. H.: *Synchronous disturbance compensation in active magnetic bearings using bias current excitation*. In *IEEE/ASME Int. Conf. on Advanced Intelligent Mechatronics*, pp. 707–712. Como, Italy. Jul. 8–12 2001.
- [SMM02] SETIAWAN, J. D., MUKHERJEE, R., and MASLEN, E. H.: *Synchronous sensor runout and unbalance compensation in active magnetic bearings using bias current excitation*. *Journal of Dynamic Systems, Measurement, and Control*, vol. 124:pp. 14–24. Transactions of The American Society of Mechanical Engineers (ASME). Mar. 2002.
- [SMMS99] SETIAWAN, J. D., MUKHERJEE, R., MASLEN, E. H., and SONG, G.: *Adaptive compensation of sensor runout and mass unbalance in magnetic bearing systems*. In *Proc. of the 1999 IEEE/ASME Int. Conf. on Advanced Intelligent Mechatronics*, pp. 800–805. Atlanta, U.S.A. Sep. 19–23 1999.

- [SPS96] SCHMIDT, E., PLATTER, T., and SPRINGER, H.: *Force and Stiffness Calculations in Magnetic Bearings - Comparison between Finite Element Method and Network Theory*. In MATSUMURA, F., OKADA, Y., FUJITA, M., and NAMERIKAWA, T., eds., *Proc. of Fifth Int. Symp. on Magnetic Bearings*, pp. 259–264. Kanazawa, Japan. Aug. 28–30 1996.
- [SRBPRLA92] SIRA-RAMIREZ, H., BENSOUSSAN, D., PRADA-RIZZSO, M. T., and LISCHINSKY-ARENAS, P.: *On the design of Pulse Width Modulation Controllers for Linear Dynamical Systems*. In *Proc. of the 31st Conf. on Decision and Control*, vol. 2, pp. 1375–1380. Tucson, Arizona. Dec. 1992.
- [SSP98] SPRINGER, H., SCHLAGER, G., and PLATTER, T.: *A Nonlinear Simulation Model for Active Magnetic Bearing Actuators*. In ALLAIRE, P. E. and TRUMPER, D. L., eds., *Proc. of Sixth Int. Symp. on Magnetic Bearings*, pp. 189–203. Massachusetts Institute of Technology (MIT), Technomic Publ., Lancaster - Basel, Cambridge, Massachusetts. Aug. 5–7 1998.
- [STB93] SCHWEITZER, G., TRAXLER, A., and BLEULER, H.: *Magnetlager - Grundlagen, Eigenschaften und Anwendungen berührungsfreier, elektromagnetischer Lager*. Springer-Verlag, Berlin, Germany. 1993.
- [Ste96] STEINHARDT, H.: *Auslegung und Regelung eines elastischen Rotors in Magnetlagern*. Master's thesis, Vienna University of Technology, Vienna, Austria. Jan. 1996.
- [SW] SPRINGER, H. and WASSERMANN, J.: *Magnetlager: Theorie und Anwendung*. Lecture notes.
- [SZL02a] SHI, J., ZMOOD, R., and LIJIANG, Q.: *The Direct Method for Adaptive Feed-Forward Vibration Control of Magnetic Bearing Systems*. In *Proc. of the 7th Int. Conf. on Control, Automation, Robotics and Vision (ICARCV 2002)*, pp. 675–680. Singapore. Dec. 2–5 2002.
- [SZL02b] SHI, J., ZMOOD, R., and LIJIANG, Q.: *The Indirect Adaptive Feed-Forward Control in Magnetic Bearing Systems for Minimizing Selected Vibration Performance Measures*. In OKADA, Y. and NONAMI, K., eds., *Proc. of Eighth Int. Symp. on Magnetic Bearings*, pp.

- 223–228. Dynamics and Control Lab., Dept. of Mechanical Eng., Ibaraki University, Mito, Japan. Aug. 26–28 2002.
- [SZQ03] SHI, J., ZMOOD, R., and QIN, L.: *Synchronous disturbance attenuation in magnetic bearing systems using adaptive compensating signals*. *Control Engineering Practice*. doi: 10.1016/S0967-0661(03)00095-9. Elsevier Science, Great Britain, in print. available online May 29 2003.
- [UAC96] ULBRICH, H., AHAUS, G., and CYLLIK, A.: *Stabilization of Elastic Rotors with Fluid Components by Magnetic Bearings*. In MATSUMURA, F., OKADA, Y., FUJITA, M., and NAMERIKAWA, T., eds., *Proc. of Fifth Int. Symp. on Magnetic Bearings*, pp. 125–130. Kanazawa, Japan. Aug. 28–30 1996.
- [UCA97] ULBRICH, H., CYLLIK, A., and AHAUS, G.: *Stabilisierung von elastischen Rotoren mit Fluidanteilen durch Magnetlager*. In IRRETIER, H., NORDMANN, R., and SPRINGER, H., eds., *SIRM '97 - Schwingungen in rotierenden Maschinen IV*, pp. 48–60. Verlag Vieweg, Kassel, Germany. 1997.
- [UCA00] ULBRICH, H., CYLLIK, A., and AHAUS, G.: *Stabilization of centrifuges with instabilities due to fluid-structure interactions: various control approaches*. In *Proc. of 8th Int. Symp. on Transport Phenomena and Dynamics of Rotating Machinery, ISROMAC-8*, vol. II, pp. 886–891. Mar. 2000.
- [Ulb79] ULBRICH, H.: *Entwurf und Realisierung einer berührungsfreien Magnetlagerung für ein Rotorsystem*. Ph.D. thesis, Technische Universität München, Munich, Germany. Jun. 1979.
- [WJ96] WURMSDOBLER, P. and JÖRGL, H. P.: *State Space Adaptive Control for a Rigid Rotor Suspended in Active Magnetic Bearings*. In MATSUMURA, F., OKADA, Y., FUJITA, M., and NAMERIKAWA, T., eds., *Proc. of Fifth Int. Symp. on Magnetic Bearings*, pp. 185–190. Kanazawa, Japan. Aug. 28–30 1996.
- [WJS96] WURMSDOBLER, P., JÖRGL, H. P., and SPRINGER, H.: *State Space Adaptive Control for a Lumped Mass Rotor Excited by Nonconservative Cross-Coupling Forces*. In *Proc. of Eighth Workshop on Ro-*

tordynamic Instability Problems in High-Performance Turbomachinery. Turbomachinery Laboratory, Texas A&M University, College Station, Texas, U.S.A. May 6–8 1996.

- [WS85] WIDROW, B. and STEARNS, S. D.: *Adaptive Signal Processing*. Prentice Hall, Englewood Cliffs, New Jersey, USA. 1985.
- [Wur97a] WURMSDOBLER, P.: *State Space Adaptive Control for a Rigid Rotor Excited by Non-Conservative Cross-Coupling Forces*. *Int. Journal Automation Austria*, vol. 5(2):pp. 37–50. 1997.
- [Wur97b] WURMSDOBLER, P.: *State Space Adaptive Control for a Rigid Rotor Suspended in Active Magnetic Bearings*. Ph.D. thesis, Vienna University of Technology, Vienna, Austria. 1997.
- [Zam81] ZAMPIERI, D. E.: *Einfluss einer aktiven magnetischen Lagerung auf das dynamische Verhalten eines Rotors*. Ph.D. thesis, Universität Stuttgart, Stuttgart, Germany. 1981.
- [ZDG96] ZHOU, K., DOYLE, J. C., and GLOVER, K.: *Robust and Optimal Control*. Prentice Hall, Upper Saddle River, New Jersey, USA. 1996.

Lebenslauf

Persönliche Daten

Dipl.-Ing. Martin Hirschmanner
Keilgasse. 8/16
1030 Wien

Geb. am 14. 03. 1974 in Scheibbs
österreichischer Staatsbürger
ledig

Schulbildung

09/1980–06/1984 Volksschule in Leonding

09/1984–06/1992 Naturwissenschaftliches BRG Linz
Matura mit gutem Erfolg

Studium

10/1992–09/1998 Mechatronik an der Universität Linz

Diplomarbeit am Institut für Regelungstechnik in Zusammenarbeit mit der VA Stahl Linz AG, Abteilung Mechatronik über „Auslegung und Simulation des Nockenwalzgerüsts mit Probenmanipulator“

Wehrdienst

1/1999–09/1999 Stellungskommission Linz

Berufserfahrung

seit 01/2000 Universitätsassistent am Institut für Maschinendynamik und Messtechnik, Technische Universität Wien

Wien, 1. September 2003